Optical coherent feedback control of a mechanical oscillator

Inauguraldissertation

zur
Erlangung der Würde eines Doktors der Philosophie
vorgelegt der
Philosophisch-Naturwissenschaftlichen Fakultät
der Universität Basel

von

Maryse Ernzer

2024

Genehmigt von der Philosophisch-Naturwissenschaftlichen Fakultät
auf Antrag von
Erstbetreuer: Prof. Dr. Philipp Treutlein
Zweitbetreuer: Prof. Dr. Patrick Maletinsky
Externer Experte: Prof. Dr. Albert Schliesser

Basel, den 20. Juni 2023

Prof. Dr. Marcel Mayor
Dekan

Abstract

Coherent feedback is a quantum control technique that governs the behavior of a target system by employing closed-loop actuation based on a coherent interaction with a second quantum system, acting as a controller. This approach eliminates the need for any invasive measurements that are typically required in feedback control. Especially in optomechanics, where a light field coherently interacts with the mechanical degree of freedom of an oscillator, coherent feedback is expected to expand the range of control possibilities, promote the generation of non-classical states and allow for a reduction of noise. Despite the numerous theoretical proposals emphasizing the potential advantages of employing coherent feedback for optomechanical quantum control, experiments validating these proposals are still scarce.

In this thesis I present the implementation of a coherent feedback platform for a cavity optomechanical system. We demonstrate that a coherent feedback protocol involving an optical light beam interacting twice with a mechanical oscillator, thus forming an optical feedback loop with tunable parameters, opens up new avenues for controlling the mechanical state.

Our optomechanical setup consists in a nanomechanical membrane placed in a Fabry-Pérot optical cavity. The membrane, a thin sheet of silicon nitride embedded in a phononic shield, couples to the cavity light through radiation pressure. The cavity has one incoupling port that allows a coherent light field to drive a cavity mode. The light that has interacted with the membrane and escapes the cavity is then collected, delayed and phase shifted using an optical fiber and an auxiliary local oscillator beam. The polarization of the light beam is subsequently rotated before the beam is sent back to the cavity, allowing for a second interaction of the light with the mechanical oscillator in an orthogonal cavity mode. During the second interaction, the light beam, already containing the mechanical signal from the first interaction, implements an effective interaction of the mechanical oscillator with itself. The feedback parameters, given by the delay and phase in the feedback loop, strongly modify the nature of this self-interactions, making it possible to implement a damping or an amplifying force.

As a result, tuning the optical phase and delay between the two interactions enables us to control the motional state of the mechanical oscillator via its resonance frequency and damping rate. We show theoretically that this coherent feedback loop enables ground-state cooling even in the unresolved sideband regime, where the optical cavity linewidth is much larger than the mechanical frequency and which cannot be achieved by standard cooling techniques. Experimentally, we tune the feedback parameters and show modifications of the mechanical susceptibility that are enabled by the coherent feedback scheme. We demonstrate cooling of the mechanical mode to a state with $\bar{n}_{\mathrm{m}} = 4.89 \pm 0.14$ phonons (480 μK) in a 20 K environment. This result is below the theoretical limit of conventional dynamical backaction cooling in the unresolved sideband regime. Our feedback scheme is highly versatile, offering unprecedented opportunities for quantum control in a variety of optomechanical systems.

Contents

Introduction

Coherent Feedback

Feedback is a powerful technique in classical and quantum control used in many applications to stabilize and manipulate the behaviour of a system. It typically relies on measuring a parameter of the system and using that information to adjust a controller acting on it. By manipulating the state of the system in response to the measurement, feedback control can reduce the effects of disturbances and increase the stability of the system. Control theory has evolved into a vast field of research, ranging from air conditioning of a room to self-correcting drones. The process of measuring and adjusting is repeated continuously in a closed-loop feedback system, allowing the system to respond to changes and disturbances in its environment [1].

However, when considering feedback control of quantum systems, one has to consider the fact that the measurement itself produces an irreversible disturbance. non-destructive procedure. In the past decades, there has been an ongoing investigation into how to transfer the principles of feedback control to the quantum regime [2, 3, 4, 5, 6]. On the one hand, there are many examples where feedback based on measurement and classically processed signals, the so-called measurement-based feedback, reached remarkable milestones on quantum state control. Among others, quantum feedback based on measurements has achieved quantum-noise suppression [7, 8], produced quantum states like the mechanical ground state [9], led to quantum state tracking and steering [10, 11], prepared and stabilized non-classical states [12, 13, 14, 15], generated entanglement [16, 17] and performed quantum error correction [18, 19].

On the other hand, in recent years, coherent feedback has emerged as an alternative paradigm for state control of physical systems without introducing a measurement process and classical information being fed back [20, 5, 21, 6]. Typically, coherent feedback is implemented through an auxiliary physical system that acts as a reversible quantum controller. This system processes quantum signals without the need to convert them into classical signals through a measurement. Furthermore, the interaction between the controller and the target system serves as a feedback actuator, coherently driving the subject system towards a desired state [22]. A schematic comparing coherent feedback to measurement-based feedback is displayed in Fig. 1. These two different implementations of quantum control trigger the following interesting question: which tasks can be improved by coherent signal processing [23, 21]? This question is only beginning to be addressed, mostly in theoretical studies and in a few experiments. In fact, numerous theoretical works suggest that coherent feedback not only improves quantum control of physical systems but also outperforms and enables tasks that are unattainable with measurement-based feedback [22, 24, 25, 21]. It has been put forward that one of the advantages of coherent feedback relies on the absence of measurements, which enables the persistence of quantum coherence through the closed-loop feedback [20, 23].

As a first example, coherent feedback facilitates quantum noise evasion by establishing so-called anti-noise paths [26]. In case of a second system-controller interaction that exactly corresponds to the time-reversal of the first, the quantum noise associated with

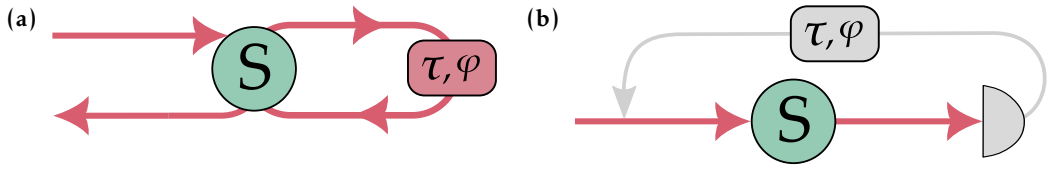

FIGURE 1: Sketch of feedback schemes, exerting a phase shift φ and a delay τ between the two interactions. **(a)**: Coherent feedback, where the feedback is implemented on the signal of the system S that is redirected for a second interaction with the system S. **(b)**: Measurement-based feedback, where the signal is detected in a measurement and processed classically to form a closed feedback loop.

the interaction can be completely cancelled [27]. This noise cancellation effect is particularly useful for quantum sensing and control tasks that require high accuracy and precision [26]. Besides cancelling the quantum noise through the interaction, coherent feedback also causes less disturbance to the system, as it avoids the decoherence and noise associated with measurements [20, 23].

Moreover, coherent feedback can exploit more information from a system, as it is capable of handling signals stored in non-commuting observables, instead of measuring one and completely discarding the other variable. In this way, the two non-commuting observables can be actively used, potentially leading to performance gains in quantum information processing and quantum control. For instance, one quadrature can be employed as a probe signal, and the orthogonal one for feedback [24]. This would allow coherent feedback to measure and manipulate multiple quantum properties of a system simultaneously [22, 6, 24, 28].

Furthermore, coherent feedback has been predicted to outperform measurement-based feedback in terms of the cooling efficiency in the quantum regime of low steady-state excitation number [24, 21, 29]. Indeed cooling can be associated to an extraction of entropy that coherent schemes can perform more efficiently. This advantage has been attributed to two features: first, the ability to avoid introducing noise related to a measurement of the quantum system, and second, the capability to follow more efficient paths in the state-space when preparing the desired state [25, 29].

Coherent feedback also possess the ability to generate non-classical states in systems where measurement-based feedback cannot. This has been demonstrated, for example, in optical systems that lack nonlinear dynamics, where feedback relying on detected photocurrents is unable to generate squeezed light, in contrast to all-optical feedback [22]. Moreover it has been theoretically demonstrated that feedback-based operation cannot achieve the specific tasks of back-action cancellation, or generation of quantum non-demolition variables and decoherence-free subspaces unless it is employing a coherent feedback scheme [21].

Experimentally, coherent feedback has demonstrated its potential to improve control over various physical systems [6], by enhancing optical squeezing [30] and optical entanglement generation using a non-degenerate optical parametric amplifier [31]. Coherent control has been used to implement sympathetic cooling of trapped ions, nanolevitated particles and hybrid spin-mechanical systems [32, 33, 34], and to stabilize entanglement between two superconducting qubits [35] or the qubit state of a diamond nitrogen-vacancy center [36].

Here we distinguish between two different kinds of coherent feedback: the first one is implemented using a direct interaction between the target and control system, and can

be applied to systems in direct vicinity to each other, coupling over a short distance [37, 38, 33, 39]. Alternatively, the interaction between the different systems can be mediated using a travelling light field in a cascaded fashion, applicable to all systems providing a strong light interface [27]. This offers a great versatility of coherent feedback schemes, and makes the implementation of all-optical feedback loops particularly interesting due to their ability to strongly couple multiple remote systems, effectively creating a quantum network [40]. That is why we focus on all-optical feedback schemes that process and perform the feedback entirely via a light field [22].

Optomechanical systems are a highly promising choice for such all-optical feedback schemes, thanks to their refined interface to light. Indeed, there are numerous theoretical proposals on how to implement coherent feedback on optomechanical systems for a broad range of applications such as the enhancement of entanglement [41, 42], enabling non-classical effects and reducing noise [6, 42], or improving cooling performance [24, 28, 42, 43]. However, experiments in this research area are still rare. The idea of implementing and exploring the possibilities of optical coherent feedback in an optomechanical setup thus arises naturally.

Optomechanics

Observing quantum phenomena with mesoscopic objects, as well as the broad range of applications offered by optomechanical systems have sparked a great deal of interest in such systems over the past decade [44]. Optomechanical systems are based on the interaction between a mechanically compliant element and an electromagnetic field. In most cases, the mechanical element is placed inside a cavity resonator where its motion is parametrically coupled to optical forces [45]. The optomechanical coupling, illustrated in Fig. 2 is realized through the radiation pressure force of photons impinging and reflecting off the mechanical oscillator, exerting a momentum kick that modifies the mechanical motion. Furthermore, the motion of the mechanical element inside the optical resonator modifies the resonance condition of the latter. In general this leads to a modification of the amplitude and phase of the outgoing light field. For a resonant drive, this results in a phase shift of the outgoing light field that depends on the mechanical displacement and provides us with the basic read-out mechanism of the mechanical vibrations.

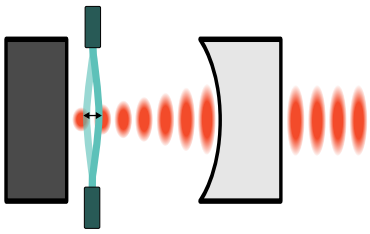

Figure 2: Sketch of the optomechanical coupling between a mechanical oscillator and the light field inside of an optically driven cavity. The light field exerts a radiation pressure force on the mechanical oscillator, and vice-versa, the vibrations of the mechanical oscillator modify the resonance condition of the cavity and thus modify the amplitude and phase of the outgoing light field.

The first optomechanical experiments emerged from the combined insights gained from laser cooling experiments on atomic systems with radiation pressure forces and the

measurable backaction effect of the light forces on macroscopic objects, specifically end-mirrors of an optical cavities in interferometric measurements [46, 47, 48, 49]. Since then, optomechanical systems have undergone a remarkable evolution: Initially, suspended mirrors were used to improve acoustic isolation from the environment and allowed to investigate some optomechanical properties [50, 51, 52, 52, 53]. This led to suspending sub-wavelength elements, such as silicon nitride membranes [54, 55], as well as levitated microspheres, nanoparticles or trapped atoms and ions [56, 57, 58, 59, 60] inside optical cavities. There is a whole range of structures fabricated out of highly stressed SiN, providing especially low bulk dissipations and convenient fabrication mechanisms for nanobeams or thin sheets called membranes. These components can be equipped with trampoline shapes, patterned phononic crystals or geometrical tapering to further reduce dissipation [61, 62, 63, 64, 65, 66].

Advances in fabrication techniques have led to fast reduction in the size of the produced solid-state optomechanical systems [44]. For example, micromechanical mirrors on cantilevers and beams were introduced [67, 68, 69], allowing for both higher mechanical frequencies and mechanical quality factors than their previous macroscopic counterparts. The introduction of microcavities consisting of microdisks and toroids, where the mechanical modes are given by the expansion of whispering-gallery modes, further increased achievable coupling strengths and mechanical frequencies, along with higher optical quality factors [70, 71, 72, 73]. Besides miniaturization, there is also a push towards integrating optomechanical systems into microchips. Optomechanical crystals that are created by overlapping a motional mode of a beam with the localized eletromagnetic mode in a photonic crystal cavity [74, 75, 76, 77], can be employed at cryogenic temperatures and offer some of the strongest optomechanical coupling rates realized in solid-state systems so far [78].

Many quantum technology applications require mechanical occupation numbers close to the ground state. However, mechanical oscillators are usually coupled to a thermal bath via their support, and their motion is dominated by thermal fluctuations. For this reason, mechanical cooling techniques are a rich research field by themselves [44, 79]. The pursuit of the quantum regime, where motion is dominated by the impact of the light instead of thermal noise, has led to elaborated designs of the internal dissipation mechanisms of the mechanical oscillators. A great effort has been invested in developing structure with reduced dissipation, that are compatible with a cryogenic applications [79, 45].

The design evolution of optomechanical systems has enabled them to enter the quantum regime, and they have become promising candidates for quantum technologies [79]. Indeed, optomechanics experiments have demonstrated quantum state control and readout [80, 9, 81], squeezed states of mechanical motion [82, 83] as well as squeezed states of the radiation field [84, 85, 86]. They also provide a platform for mechanical entanglement [87, 88, 89, 90], optomechanical entanglement [91, 92] as well as entanglement in the output fields and enabling Bell tests [93, 94]. Especially in the context of hybrid systems and quantum networks, the response of mechanical oscillators to a wide range of forces has led to their intense pursuit as transducers and frequency converters [95, 96, 97].

Modern nanomechanical oscillators offer great controllability via their optical interactions, which are strongly influenced by the design of the optical cavity. We distinguish two regimes for the cavity-mechanical parameters: the resolved sideband regime, where the cavity has a linewidth κ that is smaller than the mechanical resonance frequency

Ω_m, resulting in a small sideband resolution factor ($\kappa/\Omega_m \ll 1$). In this case, the cavity light can exert a strong control of the mechanical motion and enables beam-splitter interactions, resulting in coherent state-swaps between the mechanical and optical excitations, allowing for ground-state cooling of the mechanical mode [98, 99, 78, 100, 101]. Moreover, the optomechanical coupling can also lead to a parametric amplification interaction, resulting in the generation of entanglement between the optical and mechanical modes, a prerequisite for many quantum technology applications [44, 79].

However for many applications concerning quantum networks and hybrid systems, short delays and thus broad cavities are desirable [102]. The requirement of a fast cavity response places the optomechanical system in the unresolved sideband regime, where $\kappa/\Omega_m \gg 1$. The mechanical signal effectively couples to the travelling field outside of the cavity, with only a small delay generated by the cavity. Although the unresolved sideband regime offers possibilities for coupling setups of different nature, it also requires additional schemes to reduce the thermal occupation of the mechanical oscillator and prepare the mechanical mode in its motional ground state. This is because in the unresolved sideband regime, the standard method known as cavity dynamical backaction cooling is limited to a minimally achievable phonon number higher than the ground state. To address this difficulty, various schemes have been implemented, including the usage of non-classical input light states [103, 104], measurement-based feedback cooling (cold damping) [105, 9, 106, 107, 108], or sympathetic cooling [32, 109, 34].

Coherent Feedback in Optomechanics

Given the impressive capabilities of optomechanical systems and the wide range of control options provided by their interaction with light, they are an ideal platform for exploring all-optical feedback schemes. Consequently, there is a natural inclination to implement and investigate the possibilities of optical coherent feedback within the framework of optomechanical setups. As previously mentioned, coherent feedback holds promise for a wide range in applications of optomechanical systems, particularly those operating in the unresolved sideband regime. These applications include improving mechanical cooling [24, 28, 42, 43], enhancing entanglement, generating non-classical states, and cancelling noise [110, 111, 112, 42, 43].

We can categorize coherent feedback schemes based on their underlying working principle, distinguishing between the schemes applying the feedback to one cavity mode versus two different cavity modes. Most of the aforementioned theoretical proposals that suggest improvements for cooling mechanical oscillators use coherent feedback onto the same cavity mode, with the option of using additional passive elements such as auxiliary optical Fabry-Perot cavities [110, 111, 112, 42, 43]. In this case, the improvement relies on the modified impact of the cavity on the mechanics via an effective cavity linewidth.

Alternatively, to aim the coherent feedback directly at the mechanical oscillator, feedback can be generated via one optomechanical cavity driven in two different cavity modes, and corresponds to the scheme that we explore here.

In this thesis, I present experiments where we developed a continuous all-optical feedback loop using two orthogonal modes of an optical cavity containing a membrane in the middle, as illustrated in Fig. 3. The feedback scheme involves a coherent field driving the optomechanical cavity. We then collect the light leaking out after a first interaction with the mechanical membrane. This outgoing light beam is delayed by τ before coupling it back into the cavity with an orthogonal polarization. To achieve a tunable loop phase φ we also combine the outgoing light field with an auxiliary local oscillator. Together with

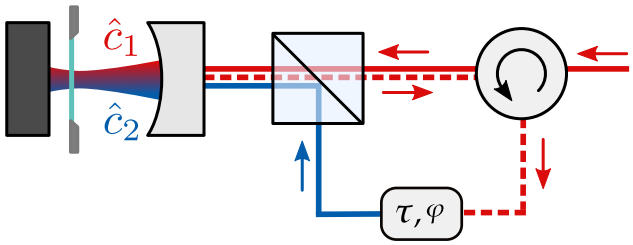

FIGURE 3: Sketch of optomechanical coherent feedback scheme implemented by two orthogonal cavity modes, where the second mode is driven by the output of the first one.

the delay τ, the loop phase φ controls the character of the feedback on the mechanical motion. This system allows us to perform experiments where we modify the mechanical susceptibility via the tunability of the feedback parameters. As a first application of our coherent feedback platform, we demonstrate cooling of the mechanical occupation to $\bar{n}_{\mathrm{m}} = 4.89 \pm 0.14$, which is below the limit set by dynamical backaction cooling in the unresolved sideband regime.

The presented all-optical coherent feedback scheme on orthogonal cavity modes is relatively simple to implement, yet very powerful in performance. Unlike many other proposals, it does not require an overall high detection efficiency, fast switching, or other quantum resources [103, 9, 42, 34]. This makes it optimally suited to be incorporated into various optomechanical systems with only small modifications to the optical path.

The main results of this thesis are published in [113]. In Ch. 1, we provide a summary of the optomechanics theory that is essential for the subsequent sections. In Ch. 2, we develop the theoretical description of a coherent feedback loop on an optomechanical system. We explore the limits for ground-state cooling and compare this approach to other cooling strategies. In Ch. 3, we provide a characterisation on the nanomechanical membrane oscillators used in our experiments. In Ch. 4, we present and characterize the cavity optomechanical setup built and developped in this thesis. In Ch. 5, we show the experimental implementation of the optical coherent feedback loop in a double-pass scheme on a single mechanical mode. We demonstrate the versatility and controllability of this type of feedback and show improved cooling performance, which combines dynamical backaction cooling and coherent cooling of the mechanical oscillator, to realize a phonon occupation number below the limit of dynamical backaction cooling in the unresolved sideband regime. In the outlook (Ch. 6), we discuss future perspectives in quantum control and further applications of the presented feedback scheme.

Chapter 1

Cavity Optomechanics

Given the vast interest in the quantum fluctuations of mesoscopic mechanical oscillators and their potential applications, significant effort has been invested into developing efficient coupling mechanisms to access the mechanical degrees of freedom, and the field of optomechanics has received ample attention [44, 45, 79].

Most optomechanical setups combine the mechanically oscillating element with an optical cavity resonator, which allows to detect the mechanical vibrations interferometrically, and manipulate the mechanical motion through its parametric coupling to the electromagnetic radiation [44, 79]. This relies on the principle that the light modifies the mechanical motion via radiation pressure and vice-versa the mechanical displacement alters the cavity resonance condition, leading to a dispersive coupling between the optical light and the mechanical position. Driving the cavity with a coherent light field enhances the optomechanical coupling strength by the average photon number in the cavity [44]. Furthermore, the cavity also serves as an ideal quantum-limited readout system for the mechanical motion [5]. This means that determining the position of a mechanical system through the phase of the light exiting the cavity leads to the ideal quantum-limited product between the measurement imprecision and the backaction generated by the light beam used for readout [5].

In this chapter, we introduce the canonical description of an optomechanical system with an optical cavity, by examining each element of the combined system - the mechanical oscillator and the optical cavity - separately, before we deriving the optomechanical Hamiltonian that forms the basis of our work. We explore the impact of the light field on the mechanical oscillator through the radiation pressure force, and describe the linear optomechanical coupling between the mechanical vibrations and the cavity fluctuations around a coherent cavity drive. Additionally, we examine the dynamical backaction effects that occur in the case of a detuned cavity. We derive the relationship between the outgoing field of the optical cavity and the mechanical displacement. Furthermore, we describe the typical detection scheme used for the optical phase quadrature namely homodyne detection, and the limitations associated with detection of the mechanical signal.

1.1 Mechanical Oscillators

Starting with the mechanical oscillator, its mechanical mode forms a harmonic oscillator with position and momentum operators $\hat{x}_\mathrm{m}$ and $\hat{p}_\mathrm{m}$ resulting in the Hamiltonian

$$\hat{H}_\mathrm{m} = \frac{\hat{p}_\mathrm{m}^2}{2m} + \frac{m\Omega_\mathrm{m}^2 \hat{x}_\mathrm{m}^2}{2}, \tag{1.1}$$

where Ω_m is the mechanical resonance frequency and m the effective mass of the mechanical mode [cf. Ch. 3]. The mechanical position and momentum operators can be expressed via the ladder operators $\hat{b}$ as

$$\hat{x}_\mathrm{m} = x_0(\hat{b} + \hat{b}^\dagger), \quad \hat{p}_\mathrm{m} = \mathrm{i}p_0(\hat{b}^\dagger - \hat{b}), \tag{1.2}$$

in terms of the zero-point fluctuation of the position $x_0 = \sqrt{\hbar/2m\Omega_\mathrm{m}}$ and momentum $p_0 = \hbar/2x_0$, fulfilling the commutation relations $[\hat{b}, \hat{b}^\dagger] = 1$ and hence $[\hat{x}_\mathrm{m}, \hat{p}_\mathrm{m}] = \mathrm{i}\hbar$. We define the dimensionless operators for the mechanical motion that are rescaled by the displacement caused by a single mechanical excitation

$$\hat{X}_\mathrm{m} = \frac{1}{\sqrt{2}}(\hat{b} + \hat{b}^\dagger), \quad \hat{P}_\mathrm{m} = \frac{\mathrm{i}}{\sqrt{2}}(\hat{b}^\dagger - \hat{b}), \tag{1.3}$$

such that $[\hat{X}_\mathrm{m}, \hat{P}_\mathrm{m}] = \mathrm{i}$. The Hamiltonian of the mechanical oscillator is then

$$\hat{H}_\mathrm{m} = \frac{\hbar\Omega_\mathrm{m}}{2}(\hat{X}_\mathrm{m}^2 + \hat{P}_\mathrm{m}^2) = \hbar\Omega_\mathrm{m}(\hat{b}^\dagger\hat{b} + \frac{1}{2}), \tag{1.4}$$

where the number of excitations in the mechanical mode is $\langle\hat{n}_\mathrm{m}\rangle = \langle\hat{b}^\dagger\hat{b}\rangle$. Given that the mechanical oscillator is coupled to a thermal environment with the mechanical energy damping rate γ_m, the equation of motion for the mechanical displacement is given by

$$\partial_t^2\hat{X}_\mathrm{m}(t) + \gamma_\mathrm{m}\partial_t\hat{X}_\mathrm{m}(t) + \Omega_\mathrm{m}^2\hat{X}_\mathrm{m}(t) = \sqrt{2}\Omega_\mathrm{m}\xi_\mathrm{th}(t). \tag{1.5}$$

$\hat{\xi}_\mathrm{th}$ is the thermal noise forming an unavoidable external drive to the mechanical displacement due to the coupling to a thermal environment [114]. The mechanical oscillator is coupled to the thermal bath with coupling strength $\sqrt{\gamma_\mathrm{m}}$ such that the thermal noise term $\hat{\xi}_\mathrm{th} = \sqrt{\gamma_\mathrm{m}}\hat{Y}_\mathrm{in}$[1] is completely defined by its correlator

$$\langle\hat{\xi}_\mathrm{th}(t)\hat{\xi}_\mathrm{th}(t')\rangle = \gamma_\mathrm{m}(\bar{n}_\mathrm{th} + \frac{1}{2})\delta(t - t'), \tag{1.7}$$

with $\bar{n}_\mathrm{th}$ the bath occupation number. If the occupation probability follows Bose-Einstein statistics, as is the case for phonons (bosons) populating a harmonic oscillator in thermal equilibrium, the mean occupancy of the oscillator turns out to be

$$\bar{n}_\mathrm{th}(\omega) = [\exp(\hbar\omega/k_\mathrm{B}T) - 1]^{-1} \tag{1.8}$$

at a temperature T. In the high temperature limit $k_\mathrm{B}T \gg \hbar\Omega_\mathrm{m}$, and for $\omega = \Omega_\mathrm{m}$ the average thermal occupation simplifies to $\bar{n}_\mathrm{th} = k_\mathrm{B}T/\hbar\Omega_\mathrm{m}$.

[1] The thermal force can be described by the so-called independent oscillator model where the coupling to the thermal environment is described by the spring-coupling of an ensemble of j independent bath oscillators to the mechanical oscillator of interest. This results in the stochastic force $\hat{F}_\mathrm{th}(t) = \sum_j k_j\hat{x}_j(t)$ with the position $\hat{x}_j$ and the spring constant $k_j = m_j\Omega_j^2$ of oscillator j which has a mass m_j and frequency Ω_j. The expectation value of this force is equal to zero. Furthermore we can define the dimensionless input fluctuations $\hat{b}_\mathrm{in}$ with

$$\hat{Y}_\mathrm{in} = \frac{\mathrm{i}}{\sqrt{2}}(\hat{b}_\mathrm{in}^\dagger - \hat{b}_\mathrm{in}) = \frac{x_0\hat{F}_\mathrm{th}}{\hbar\sqrt{\gamma_\mathrm{m}}} \tag{1.6}$$

Using a Fourier transformation[2] and following from Eq. (1.5), we obtain the mechanical displacement operator in the frequency domain

$$\hat{X}_{\mathrm{m}}(\omega) = \sqrt{2}\chi_{\mathrm{m},0}(\omega)\hat{\xi}_{\mathrm{th}}(\omega), \tag{1.10}$$

with the intrinsic mechanical susceptibility

$$\chi_{\mathrm{m},0}(\omega) = \frac{\Omega_{\mathrm{m}}}{\Omega_{\mathrm{m}}^2 - \omega^2 - \mathrm{i}\omega\gamma_{\mathrm{m}}} \tag{1.11}$$

that describes the response of the mechanical oscillator to the thermal drive.

1.2 Canonical Optomechanical Interaction

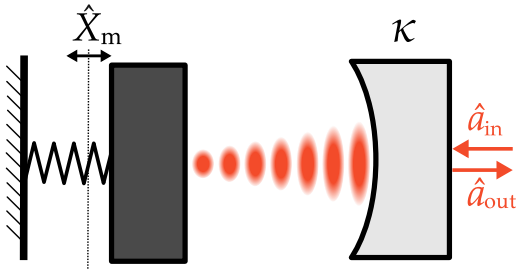

FIGURE 1.1: Sketch of the canonical optomechanical coupling scheme, where the variable position $\hat{X}_{\mathrm{m}}$ of one end-mirror of an optical cavity modifies the cavity length and thus its resonance frequency. For a cavity driven by a laser $\hat{a}_{\mathrm{in}}$ this results in a modulation of the outgoing light field $\hat{a}_{\mathrm{out}}$ proportional to the displacement $\hat{X}_{\mathrm{m}}$.

We now consider the interaction between a cavity light field and a mechanical oscillator, which can be envisioned as a mechanically compliant cavity mirror (see Fig. 1.1). The vibrations of the mirror modify the length of cavity, thereby affecting its resonance frequency. Conversely, the modulation of the cavity energy has implications on the mechanical motion and thus establishes the optomechanical interaction.

Here we consider a coherent incoming field $\hat{a}_{\mathrm{in}}$ entering the optical cavity of linewidth κ and driving a single cavity mode $\hat{c}$. Similar to the mechanical oscillator, the optical intracavity field is described by a harmonic mode, such that the Hamiltonian describing the cavity mode of interest is

$$\hat{H}_{\mathrm{c}} = \hbar\omega_{\mathrm{c}}(\hat{x}_{\mathrm{m}})\left(\hat{c}^\dagger\hat{c} + \frac{1}{2}\right), \tag{1.12}$$

where $\omega_{\mathrm{c}}(\hat{x}_{\mathrm{m}})$ is the cavity resonance frequency that is dispersively shifted by the mechanical displacement $\hat{x}_{\mathrm{m}}$. The cavity field annihilation operator $\hat{c}$ fulfills $[\hat{c}, \hat{c}^\dagger] = 1$, and the cavity photon number operator is given by $\hat{n}_{\mathrm{c}} = \hat{c}^\dagger\hat{c}$. The 1/2-term contribution from

[2] given by

$$\hat{O}(\omega) = \frac{1}{\sqrt{2\pi}}\int \hat{O}(t)\mathrm{e}^{\mathrm{i}\omega t}\mathrm{d}t \tag{1.9}$$

for an arbitrary operator $\hat{O}$, leading to $\partial_t \to -\mathrm{i}\omega$

the vacuum energy can be neglected in most cases, considering that the cavity is driven by a coherent field.

For small mechanical displacements, we can expand the cavity frequency around the mechanical equilibrium displacement $\langle \hat{x}_\mathrm{m} \rangle = 0$, which leads to

$$\omega_\mathrm{c}(\hat{x}_\mathrm{m}) \approx \omega_\mathrm{c} - G\,\hat{x}_\mathrm{m}, \tag{1.13}$$

where $G = -\partial\omega_\mathrm{c}/\partial x_\mathrm{m}$ represents the frequency shift per mechanical displacement. For a cavity end-mirror coupling, the cavity frequency pull parameter is directly given by $G = \omega_\mathrm{c}/L$ where L is the undisturbed cavity length [44], such that for a positive mechanical displacement, the cavity length increases, leading to a reduction of the cavity frequency.

Taking into account the mechanically-induced cavity frequency shift, the cavity Hamiltonian results in the sum of the unperturbed cavity energy and the optomechanical interaction Hamiltonian given by

$$\begin{aligned} \hat{H}_\mathrm{om} &= -\hbar G \hat{x}_\mathrm{m} \hat{c}^\dagger \hat{c} \\ &= -\hbar g_0 (\hat{b} + \hat{b}^\dagger) \hat{c}^\dagger \hat{c} = -\sqrt{2}\hbar g_0 \hat{X}_\mathrm{m} \hat{c}^\dagger \hat{c}, \end{aligned} \tag{1.14}$$

where we defined the single-phonon optomechanical coupling strength $g_0 = G\,x_0$, referencing the optomechanical coupling strength to the zero-point fluctuations of the mechanical oscillator. This Hamiltonian describes the coupling between the mechanical displacement and the intracavity photon number via the radiation pressure force

$$\hat{F}_\mathrm{rad} = -\frac{\mathrm{d}\hat{H}_\mathrm{om}}{\mathrm{d}\hat{x}_\mathrm{m}} = \hbar G \hat{n}_\mathrm{c}. \tag{1.15}$$

which will add an optical driving term to the mechanical equation of motion. Furthermore, the excursions from the cavity resonance generated by the mechanical displacement result in a detectable phase shift of the light reflected from the cavity by $\delta\hat{\phi}_\mathrm{c} = \sqrt{2}2g_0\hat{X}_\mathrm{m}/\kappa$, and provides us with a read-out mechanism for the mechanical motion. The optomechanical coupling strength g_0 effectively describes the coupling strength between a single photon and phonon, and thus the ratio g_0/κ indicates whether the cavity frequency fluctuations can resolve the shift generated by a single mechanical excitation. This represents a necessary requirement for nonlinear quantum optomechanics, enabling the observation of quantum jumps and an optomechanical photon blockade [44]. So far mainly in atomic systems, where their nature-given size intrinsically entails a strong impact of a single photon on their motional state, have values of g_0 been achieved that exceed the optical decay rate [57, 58]. Recently also strong vacuum coupling has been achieved for microwave mechanical circuits [115]. Since even the latest solid-state optomechanical experiments achieve $g_0/\kappa \sim 0.001$ [93, 116], the optomechanical coupling strength has remained in the regime where the approximation of a small dispersive shift is valid, and quantum effects can only be observed in the linearized regime.

1.3 Linearized Optomechanical Interaction

We can relate the intracavity light field $\hat{c}$ to the optical field outside the cavity, by treating the continuous external field incident onto the cavity $\hat{a}_\mathrm{in}$ as an optical bath. The

associated interaction Hamiltonian results in [117]:

$$\hat{H}_{\mathrm{int}} = \mathrm{i}\hbar\sqrt{\kappa}\int \frac{\mathrm{d}\omega}{\sqrt{2\pi}}\Big[\hat{a}^{\dagger}_{\mathrm{in}}(\omega)\hat{c} - \hat{c}^{\dagger}\hat{a}_{\mathrm{in}}(\omega)\Big], \tag{1.16}$$

where the coupling strength of the external field to the cavity is given by the cavity linewidth κ. Here we assume a single-sided cavity and only consider one input port. The incoming light field is described by its annihilation operator $\hat{a}_{\mathrm{in}}$ fulfilling the commutation relation $[\hat{a}_{\mathrm{in}}(\omega), \hat{a}^{\dagger}_{\mathrm{in}}(\omega')] = \delta(\omega - \omega')$. Defining $\alpha_{\mathrm{in}} = \langle \hat{a}_{\mathrm{in}} \rangle$, this leads to the ingoing photon flux $|\alpha_{\mathrm{in}}|^2$. From the interaction Hamiltonian we can derive the equation of motion for the cavity field

$$\partial_t \hat{c} = -\mathrm{i}\omega_{\mathrm{c}}\hat{c} - \frac{\kappa}{2}\hat{c} - \sqrt{\kappa}\hat{a}_{\mathrm{in}} \tag{1.17}$$

and consequently the well known input-output relation between the ingoing field $\hat{a}_{\mathrm{in}}$ and field leaving the cavity $\hat{a}_{\mathrm{out}}$ as [118]

$$\hat{a}_{\mathrm{out}} = \hat{a}_{\mathrm{in}} + \sqrt{\kappa}\hat{c}. \tag{1.18}$$

This relation will be used extensively in the following of this work.

The intracavity field is generated by a coherent ingoing drive field that is centred around a certain frequency ω_{L}. It is convenient to work in the rotating frame at the light frequency, such that the cavity Hamiltonian turns into

$$\hat{H}_{\mathrm{c}} = -\hbar\Delta\hat{c}^{\dagger}\hat{c}, \tag{1.19}$$

with the detuning $\Delta = \omega_{\mathrm{L}} - \omega_{\mathrm{c}}$ between the light field and the cavity resonance, where we replaced $\hat{c} \to \hat{c}\mathrm{e}^{-\mathrm{i}\omega_{\mathrm{L}}t}$. The equation of motion for the cavity field can then be written as

$$\partial_t \hat{c} = \mathrm{i}\Delta\hat{c} - \frac{\kappa}{2}\hat{c} - \sqrt{\kappa}\hat{a}_{\mathrm{in}} \tag{1.20}$$

such that steady state average displacement of the cavity field leads to

$$\alpha = \langle \hat{c} \rangle = -\frac{\sqrt{\kappa}}{\kappa/2 - \mathrm{i}\Delta}\alpha_{\mathrm{in}}, \tag{1.21}$$

such that the cavity field follows the ingoing drive adiabatically. We note that from the input-output relation, together with the expression for the steady state cavity displacement, on resonance, the outgoing light field obtains a π phase shift with respect to the ingoing field, due to the reflection off the cavity.

In order to get a better understanding of the dynamics of the optomechanical system, the cavity and mechanical oscillator modes can be split up into a coherent amplitude and a fluctuation part following

$$\begin{aligned} \hat{c} &\to \alpha + \hat{c}, \\ \hat{b} &\to \beta + \hat{b}, \end{aligned} \tag{1.22}$$

where α denotes the average cavity displacement as defined above, and $\beta = \langle b \rangle$ the mechanical steady-state displacement.

Static Interaction If we insert the expression for the cavity field as stated in Eq. (1.22) into the optomechanical Hamiltonian as given in Eq. (1.14), we get a first term describing the static optomechanical interaction $\hat{H}_{\text{static}} = -\hbar g_0 |\alpha|^2 (\hat{b} + \hat{b}^\dagger)$.
The radiation pressure force generated by the presence of a coherent optical field leads to a static shift of the mechanical equilibrium position given by $\bar{x}_{\text{m}} = \langle \hat{F}_{\text{rad}} \rangle / (m\Omega_{\text{m}}^2) = \hbar g_0 \bar{n}_{\text{c}} / (x_0 m \Omega_{\text{m}}^2)$, with the average cavity occupation number $\bar{n}_{\text{c}} = |\alpha|^2$.
Conversely, the modified equilibrium position of the mechanical oscillator leads to the average cavity displacement field that, taking into account the modified detuning $\delta\Delta = g_0 \bar{x}_{\text{m}} / x_0$, results in

$$\alpha = -\frac{\sqrt{\kappa}}{\kappa/2 - \mathrm{i}(\Delta + g_0 \bar{x}_{\text{m}}/x_0)} \alpha_{\text{in}}. \tag{1.23}$$

Notably, the cavity resonance photon occupation number is modified by the mechanical displacement in a straightforward manner given by [44]

$$\bar{n}_{\text{c}} = |\alpha|^2 = \frac{\bar{n}_0}{1 + \left[\frac{2}{\kappa}(\Delta + g_0 \bar{x}_{\text{m}}/x_0)\right]^2}, \tag{1.24}$$

with $\bar{n}_0 = (4/\kappa)|\alpha_{\text{in}}|^2$ the empty cavity resonant occupation number. We note that the intracavity photon number has a nonlinear dependence on the average mechanical position. In case that the change in the cavity detuning $g_0 \bar{x}_{\text{m}}/x_0$ becomes appreciable, it leads to a large modifications in both the mechanical displacement and the average cavity number, and multiple solutions for the intracavity field. This can potentially lead to an unstable behavior and is discussed in more detail in Sec. 5.5.1. Otherwise, the average displacements will not play a role in the dynamics of the system, such that we can account for them by redefining the mechanical equilibrium position with the offset $\hat{x}_{\text{m}} \to \hat{x}_{\text{m}} - \bar{x}_{\text{m}}$, and the cavity detuning with the additional shift

$$\Delta \to \Delta + \frac{2 g_0^2 |\alpha|^2}{\Omega_{\text{m}}}. \tag{1.25}$$

Dynamical Interaction For a strong coherent drive, we can resort to a linear description of the optomechanical interaction. This time, when replacing the cavity field with $\hat{c} \to \alpha + \hat{c}$ in the general optomechanical Hamiltonian [Eq. (1.14)] we only keep the terms that are linear in the average cavity field amplitude α, leading us to the linearized version of the optomechanical Hamiltonian between the mechanical and cavity fluctuations

$$\begin{aligned} \hat{H}_{\text{om}} &= -\hbar g (\hat{b} + \hat{b}^\dagger)(\hat{c}^\dagger + \hat{c}) \\ &= -2\hbar g \hat{X}_{\text{m}} \hat{X}_{\text{c}}, \end{aligned} \tag{1.26}$$

where the optomechanical coupling strength $g = |\alpha| g_0$ is enhanced by the coherent cavity amplitude and we defined the intracavity amplitude and phase quadratures

$$\hat{X}_{\text{c}} = \frac{1}{\sqrt{2}}(\hat{c} + \hat{c}^\dagger), \quad \hat{P}_{\text{c}} = \frac{\mathrm{i}}{\sqrt{2}}(\hat{c}^\dagger - \hat{c}). \tag{1.27}$$

This Hamiltonian describes different coupling regimes that are present in the dispersive optomechanical interaction [44], and that can be selected via the detuning of the optical cavity drive. The efficiency of the selection of either interaction depends on ratio between

the cavity linewidth and the mechanical frequency and profits from $\Omega_m \gg \kappa$, denoted the resolved sideband regime.

For a detuning of $\Delta = -\Omega_m$, the cavity mode realizes a harmonic oscillator with equal energy to the mechanical mode, enabling the exchange of excitations through the term $\propto \hat{b}\hat{c}^\dagger + \hat{b}^\dagger\hat{c}$, which corresponds to a beam-splitter interaction. It embodies the relevant process for coherent state swaps and cooling of the mechanical mode.

For a positive cavity detuning $\Delta = \Omega_m$, the resonant terms in the interaction are given by $\propto \hat{b}^\dagger\hat{c}^\dagger + \hat{b}\hat{c}$, corresponding to the pairwise creation (respectively annihilation) of excitations, describing a two-mode squeezing interaction that can be used for the generation of entanglement.

If both process are perfectly balanced as is the case for a resonantly driven cavity, the interaction is described by the full term $\propto \hat{X}_m\hat{X}_c$ and enables a quantum non-demolition (QND) detection, and thus ideal conditions for mechanical displacement read-out.

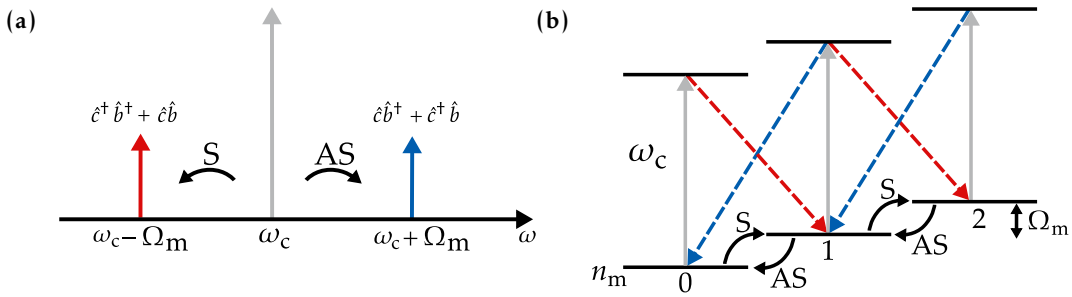

FIGURE 1.2: Sketch of **(a)** the sidebands and **(b)** the transitions involving a resonant cavity drive, illustrating the Stokes (S) and anti-Stokes(AS) scattering processes. During the Stokes transition, one carrier photon is scattered into a phonon and a red-detuned photon, thus contributing to the sideband at $-\Omega_m$. For the anti-Stokes process, the scattering of a carrier photon and mechanical phonon result in a blue-sideband photon at $+\Omega_m$. The peak at positive frequencies thus describes the emission of energy from the mechanics to the light, whereas the peak at negative frequencies accounts for the pumping of energy into the mechanical degree of freedom.

Scattering picture Furthermore, we can describe the optomechanical interaction in a Raman scattering picture through a conversion between photons and phonons, as illustrated on the transition scheme in Fig. 2.10. The optomechanical interaction terms can be understood as two scattering processes producing optical sidebands on the driving carrier field.

For a resonant cavity drive, on the one hand, one cavity photon can scatter into a phonon and a photon emitted in the red sideband at $-\Omega_m$, generating a transition of the phonon occupation number from $n_m \to n_m + 1$, corresponding to a Stokes scattering process. On the other hand, one carrier photon can combine with one phonon to form a photon scattered into the blue sideband at Ω_m, entailing the mechanical transition $n_m \to n_m - 1$, which corresponds to an anti-Stokes process. The scattering rate of the Stokes transition is given by $\Gamma_{n\to n-1} = nA_-$, and of the anti-Stokes $\Gamma_{n\to n+1} = (n+1)A_+$, where the rates $A_\pm$ are determined by Fermi's golden rule and the intracavity photon number fluctuation spectrum at $\pm\Omega_m$ [5]. When the frequency of the optical drive is exactly on resonance with the optical cavity, these two processes are exactly balanced and occur with the same probability. However, if the beam is red-detuned [as shown

in Fig. 2.10 (b)], the beam-splitter interaction generating state-swaps ($\propto \hat{c}\hat{b}^\dagger + \hat{c}^\dagger\hat{b}$) is favoured. This can be explained by the change in the final density of states of the scattering process, caused by the cavity detuning [5]. Conversely, a blue-detuned drive supports the pairwise generation and annihilation of excitations ($\propto \hat{c}^\dagger\hat{b}^\dagger + \hat{c}\hat{b}$). The interplay of these two scattering processes allows us to determine an effective temperature that can be associated to the optical bath and that can change sign depending on the detuning of the ingoing light field. This already hints at the potential of optical light to alter the mechanical occupation number, a phenomenon we will explore in greater detail in the subsequent discussion [5].

1.4 Dynamical Backaction

To deepen our understanding of the system dynamics governed by the linearized interaction Hamiltonian derived above, we revisit the equations of motion of the mechanical quadratures and obtain the linearized quantum Langevin equations

$$\begin{aligned}\partial_t \hat{X}_\mathrm{m} &= \Omega_\mathrm{m}\hat{P}_\mathrm{m},\\ \partial_t \hat{P}_\mathrm{m} &= -\Omega_\mathrm{m}\hat{X}_\mathrm{m} - \gamma_\mathrm{m}\hat{P}_\mathrm{m} - 2g\hat{X}_\mathrm{c} + \sqrt{2}\hat{\xi}_\mathrm{th},\end{aligned} \tag{1.28}$$

where the momentum quadrature now contains the optical drive, as well as thermal noise and damping term. The cavity evolution is governed by

$$\partial_t \hat{c} = -\Big[\frac{\kappa}{2} - \mathrm{i}\Delta\Big]\hat{c} - \mathrm{i}g(\hat{b} + \hat{b}^\dagger) - \sqrt{\kappa}\hat{a}_\mathrm{in}, \tag{1.29}$$

which in terms of the cavity quadratures reads

$$\begin{aligned}\partial_t \hat{X}_\mathrm{c} &= -\frac{\kappa}{2}\hat{X}_\mathrm{c} - \Delta\hat{P}_\mathrm{c} - \sqrt{\kappa}\hat{X}_\mathrm{in},\\ \partial_t \hat{P}_\mathrm{c} &= \Delta\hat{X}_\mathrm{c} - \frac{\kappa}{2}\hat{P}_\mathrm{c} - \sqrt{\kappa}\hat{P}_\mathrm{in} - 2g\hat{X}_\mathrm{m},\end{aligned} \tag{1.30}$$

with the incoming light quadratures defined as

$$\hat{X}_\mathrm{in} = \frac{1}{\sqrt{2}}(\hat{a}_\mathrm{in}^\dagger + \hat{a}_\mathrm{in}), \quad \hat{P}_\mathrm{in}(\omega) = \frac{\mathrm{i}}{\sqrt{2}}(\hat{a}_\mathrm{in}^\dagger - \hat{a}_\mathrm{in}). \tag{1.31}$$

We note that a non-zero detuning generates a mixing between the cavity quadratures. Transforming the equations of motion into the frequency domain, we can solve the system and obtain for the cavity field [114]

$$\hat{c}(\omega) = -\chi_\mathrm{c}(\omega)\Big[\sqrt{\kappa}\hat{a}_\mathrm{in}(\omega) + \mathrm{i}\sqrt{2}g\hat{X}_\mathrm{m}(\omega)\Big], \tag{1.32}$$

where we defined the bare cavity susceptibility $\chi_\mathrm{c}(\omega)^{-1} = \kappa/2 - \mathrm{i}(\Delta + \omega)$. The mechanical displacement can be written in terms of the cavity amplitude quadrature and the intrinsic mechanical susceptibility $\chi_{\mathrm{m},0}(\omega)$ such that

$$\hat{X}_\mathrm{m}(\omega) = \chi_{\mathrm{m},0}(\omega)\Big[\sqrt{2}\hat{\xi}_\mathrm{th} - 2g\hat{X}_\mathrm{c}\Big]. \tag{1.33}$$

The cavity quadratures are then related to the ingoing light quadratures following

$$\begin{pmatrix}\hat{X}_\mathrm{c}\\ \hat{P}_\mathrm{c}\end{pmatrix} = -\sqrt{\kappa}\chi_{\mathrm{c,eff}}\begin{pmatrix}\frac{\kappa}{2}-\mathrm{i}\omega & -\Delta\\ \Delta+\Gamma_\mathrm{meas}\kappa\chi_{\mathrm{m},0}(\omega) & \frac{\kappa}{2}-\mathrm{i}\omega\end{pmatrix}\begin{pmatrix}\hat{X}_\mathrm{in}\\ \hat{P}_\mathrm{in}-\sqrt{2\Gamma_\mathrm{meas}}\chi_{\mathrm{m},0}(\omega)\hat{\xi}_\mathrm{th}\end{pmatrix}, \tag{1.34}$$

where we defined the optomechanical measurement rate $\Gamma_\mathrm{meas} = 4g^2/\kappa$ describing the rate with which the mechanical signal is imprinted on the cavity field, and the effective cavity susceptibility that is modified by the coupling to the mechanical motion

$$\chi_{\mathrm{c,eff}}(\omega) = \Big[\chi_\mathrm{c}(\omega)^{-1} + \Gamma_\mathrm{meas}\kappa\chi_{\mathrm{m},0}(\omega)\Big]^{-1}. \tag{1.35}$$

We can define the expressions

$$\begin{aligned} C_+(\omega) &= \frac{1}{2}\Big[\chi_\mathrm{c}^*(-\omega)+\chi_\mathrm{c}(\omega)\Big] = \frac{\kappa/2-\mathrm{i}\omega}{(\kappa/2-\mathrm{i}\omega)^2+\Delta^2},\\ C_-(\omega) &= \frac{\mathrm{i}}{2}\Big[\chi_\mathrm{c}^*(-\omega)-\chi_\mathrm{c}(\omega)\Big] = \frac{\Delta}{(\kappa/2-\mathrm{i}\omega)^2+\Delta^2}, \end{aligned} \tag{1.36}$$

and regroup the driving terms such that the mechanical displacement is given by

$$\hat{X}_\mathrm{m}(\omega) = \sqrt{2}\chi_\mathrm{m}(\omega)\Big[\hat{\xi}_\mathrm{th}(\omega)+\hat{\xi}_\mathrm{L}(\omega)\Big], \tag{1.37}$$

with the effective mechanical susceptibility

$$\chi_\mathrm{m}(\omega) = \frac{\Omega_\mathrm{m}}{\Omega_\mathrm{m}^2-\omega^2-\mathrm{i}\gamma_\mathrm{m}\omega+4g^2\Omega_\mathrm{m}\Delta/[(\kappa/2-\mathrm{i}\omega)^2+\Delta^2]}, \tag{1.38}$$

and the optical drive

$$\hat{\xi}_\mathrm{L}(\omega) = \sqrt{\Gamma_\mathrm{meas}}\frac{\kappa}{\sqrt{2}}\Big[C_+(\omega)\hat{X}_\mathrm{in}(\omega)-C_-(\omega)\hat{P}_\mathrm{in}(\omega)\Big]. \tag{1.39}$$

We note that the optomechanical measurement rate Γ_meas also describes the rate at which the optical fluctuation quadratures $\hat{X}_\mathrm{in}$ and $\hat{P}_\mathrm{in}$ are affecting the mechanical displacement, which is known as the quantum backaction of the light on the mechanical motion. We can bring the effective susceptibility into the form of the intrinsic susceptibility such that

$$\chi_\mathrm{m}(\omega) = \frac{\Omega_\mathrm{m}}{\Omega_\mathrm{m}^2+2\omega\delta\Omega_\mathrm{m}-\omega^2-\mathrm{i}\omega(\Gamma_\mathrm{m}+\gamma_\mathrm{m})}. \tag{1.40}$$

Where the real part of the optically-induced term in the mechanical susceptibility can be associated to a shift of the mechanical frequency $\delta\Omega_\mathrm{m}$ and the imaginary part to an additional damping rate Γ_m, given by

$$\begin{aligned} \delta\Omega_\mathrm{m}(\omega) &= \mathrm{Re}\left[\frac{2g^2\Delta}{\Delta^2+(\kappa/2-\mathrm{i}\omega)^2}\right],\\ \Gamma_\mathrm{m}(\omega) &= -\frac{\Omega_\mathrm{m}}{\omega}\mathrm{Im}\left[\frac{4g^2\Delta}{\Delta^2+(\kappa/2-\mathrm{i}\omega)^2}\right]. \end{aligned} \tag{1.41}$$

Assuming that the response of the mechanical oscillator is strongly peaked around its resonance frequency ($\gamma_\mathrm{m} \ll \Omega_\mathrm{m}$), and that the broadening due to the optical field remains small ($\Gamma_\mathrm{m} \ll \Omega_\mathrm{m}$), we can evaluate these expressions at the mechanical frequency $\omega = \Omega_\mathrm{m}$

and obtain

$$\delta\Omega_\mathrm{m} = g^2\left[\frac{\Delta+\Omega_\mathrm{m}}{(\kappa/2)^2+(\Delta+\Omega_\mathrm{m})^2}+\frac{\Delta-\Omega_\mathrm{m}}{(\kappa/2)^2+(\Delta-\Omega_\mathrm{m})^2}\right],$$
$$\Gamma_\mathrm{m} = g^2\left[\frac{\kappa}{(\kappa/2)^2+(\Delta+\Omega_\mathrm{m})^2}-\frac{\kappa}{(\kappa/2)^2+(\Delta-\Omega_\mathrm{m})^2}\right]. \tag{1.42}$$

We observe that the damping is generated by the difference of the cavity susceptibility evaluated at plus and minus the mechanical frequency

$$\Gamma_\mathrm{m} = g^2\kappa\left[|\chi_\mathrm{c}(-\Omega_\mathrm{m})|^2-|\chi_\mathrm{c}(\Omega_\mathrm{m})|^2\right]. \tag{1.43}$$

If the cavity resides in the unresolved sideband regime $\kappa \gg \Omega_\mathrm{m}$, the modifications to the mechanical susceptibility simplify to

$$\delta\Omega_\mathrm{m} = \frac{2g^2\Delta}{(\kappa/2)^2+\Delta^2}, \qquad \Gamma_\mathrm{m} = -\frac{4g^2\Delta\kappa\Omega_\mathrm{m}}{[(\kappa/2)^2+\Delta^2]^2}. \tag{1.44}$$

The mechanical susceptibility describes the response of the mechanical oscillator to external forces. By driving the cavity with an optical beam that is detuned from the cavity resonance $\Delta \neq 0$, this susceptibility is modified by the dynamical backaction of the light. For a negative detuning $\Delta < 0$, corresponding to a red-detuned beam, the mechanical resonance frequency is lowered, and the damping is increased. Since the optical beam opens a dissipation channel to the optical bath, which at optical laser frequencies can safely be assumed to be in its ground state, the additional optical damping leads to a reduction of the mechanical mode occupation number [44]. The resulting cooling limits depend on the sideband resolution factor κ/Ω_m. As the difference between the cavity susceptibility evaluated at positive and negative mechanical frequencies determines the damping rate [cf. Eq. (1.43)], a narrow cavity is thus a necessary requirement for a large optically induced broadening Γ_m and hence for an efficient cooling process. In the resolved sideband regime, where the cavity linewidth is smaller than the mechanical frequency ($\Omega_\mathrm{m} \gg \kappa$) this can even lead to ground state cooling. In the unresolved sideband regime ($\kappa \gg \Omega_\mathrm{m}$), the optically induced damping is insufficient to suppress the accompanying quantum backaction due to the optical vacuum noise. The resulting cooling limits are discussed in Ch. 2.

For a positive detuning $\Delta > 0$ the mechanical frequency is increased, whereas the mechanical damping is reduced, leading to parametric amplification of the mechanical mode. If the total mechanical damping $\gamma_\mathrm{m}+\Gamma_\mathrm{m} < 0$, it leads to unstable behaviour related to an exponential growing of the mechanical motion amplitude [44]. For a resonant cavity drive $\Delta = 0$ the effective susceptibility reduces to the intrinsic one, determined by the coupling of the mechanical oscillator to the thermal bath with the damping rate γ_m. In our experiment, the optical cavity resides in the unresolved sideband regime and for most experiments the cavity is driven with a red-detuned beam, used to precool the mechanical mode and ensure stable measurement conditions.

Mechanical Displacement In the following, the relevant quantity used to study the mechanical state driven by the ingoing noises consists in the power spectral density [3] of its displacement as stated in Eq. (1.37), and can be written as

$$S_{X_\mathrm{m}X_\mathrm{m}}(\omega) = 2|\chi_\mathrm{m}(\omega)|^2\Big[S_\mathrm{th}(\omega) + S_\mathrm{qba}(\omega)\Big]. \tag{1.47}$$

We identify the contributions from both the thermal force $S_\mathrm{th}(\omega)$ and the light-induced backaction noise $S_\mathrm{qba}(\omega)$. The latter is generated by the contribution of optical drive $\hat{\xi}_\mathrm{L}$, defined in Eq. (1.39), to the mechanical power spectral density, and is given in terms of the ingoing light quadratures

$$S_\mathrm{qba}(\omega) = \Gamma_\mathrm{meas}\frac{\kappa^2}{2}\Big[|C_+(\omega)|^2 S^\mathrm{in}_{XX}(\omega) + |C_-(\omega)|^2 S^\mathrm{in}_{PP}(\omega)\Big], \tag{1.48}$$

where we neglect any correlations between these noise quadratures[4]. It describes the backaction force introduced by the light that interacts with the mechanical oscillator. In the case of shot-noise limited ingoing light ($\bar{S}^\mathrm{in}_{XX}(\omega) = \bar{S}^\mathrm{in}_{PP}(\omega) = 1/2$)[5] the resulting optical backaction power spectral density reads

$$\bar{S}_\mathrm{qba}(\omega) = \Gamma_\mathrm{meas}\frac{\kappa^2}{8}\left[\frac{1}{(\kappa/2)^2 + (\Delta+\omega)^2} + \frac{1}{(\kappa/2)^2 + (\Delta-\omega)^2}\right]. \tag{1.51}$$

The expression for the power spectral densities of the thermal force is obtained via te relation $\langle\hat{\xi}_\mathrm{th}(\omega')\hat{\xi}_\mathrm{th}(\omega)\rangle = \delta(\omega+\omega')S_\mathrm{th}(\omega)$, where the correlator is defined as stated in Eq. (1.7). The thermal force power spectral density distinguishes between the positive and negative frequencies following [119]

$$\begin{aligned} S_\mathrm{th}(\omega) &= \gamma_\mathrm{m}\frac{\omega}{\Omega_\mathrm{m}}(\bar{n}_\mathrm{th}+1), \\ S_\mathrm{th}(-\omega) &= \gamma_\mathrm{m}\frac{\omega}{\Omega_\mathrm{m}}\bar{n}_\mathrm{th}. \end{aligned} \tag{1.52}$$

[3] mathematically defined for an arbitrary operator $\hat{O}$ as

$$S_{AB}(\omega) = \int_{-\infty}^{\infty}\mathrm{d}t\mathrm{e}^{\mathrm{i}\omega\tau}\langle\hat{A}(t+\tau)\hat{B}(t)\rangle_{t=0}. \tag{1.45}$$

where we used the Wiener- Khinchin theorem and that the autocorrelation can be related to the ensemble average following

$$\langle\hat{A}(t)\hat{B}(t+\tau)\rangle = \lim_{T\to\infty}\int_{-T/2}^{T/2}\hat{A}(t)\hat{B}(t+\tau)\mathrm{d}t. \tag{1.46}$$

Furthermore this allows us to write $\langle\hat{A}(\omega)\hat{B}(\omega')\rangle = \delta(\omega+\omega')S_{AB}(\omega)$ [5].

[4] These cannot be neglected in case of a strong backaction $\Gamma_\mathrm{meas} \gg \gamma_\mathrm{m}$ leading to correlations and the resulting

$$S_\mathrm{qba}(\omega) = \Gamma_\mathrm{m}\frac{\kappa^2}{2}\Big(|C_+|^2 S^\mathrm{in}_{XX}(\omega) + |C_-|^2\bar{S}^\mathrm{in}_{PP}(\omega) + \mathrm{i}C_+C_-^* S^\mathrm{in}_{XP}(\omega) - \mathrm{i}C_-C_+^* S^\mathrm{in}_{PX}(\omega)\Big), \tag{1.49}$$

with the additional cross terms $S^\mathrm{in}_{XP}, S^\mathrm{in}_{PX}$.

[5] where we defined the symmetrized power spectral density

$$\bar{S}_{AB}(\omega) = \frac{S_{AB}(\omega) + S_{AB}(-\omega)}{2} \tag{1.50}$$

We can define the symmetrized thermal force power spectral density $\bar{S}_{\mathrm{th}}(\omega) = (S_{\mathrm{th}}(\omega) + S_{\mathrm{th}}(-\omega))/2$, which, for high quality mechanical oscillators, can be evaluated at $\omega \approx \Omega_{\mathrm{m}}$ and results in $\bar{S}_{\mathrm{th}} = \gamma_{\mathrm{m}}(\bar{n}_{\mathrm{th}} + 1/2)$. Hence the symmetrized spectral density of the mechanical displacement can be written as

$$\bar{S}_{XX}(\omega) = 2\gamma_{\mathrm{m}}|\chi_{\mathrm{m}}(\omega)|^2\Big(\bar{n}_{\mathrm{th}} + \frac{1}{2} + \frac{\Gamma_{\mathrm{eff}}(\omega)}{\gamma_{\mathrm{m}}}\Big), \tag{1.53}$$

where we defined the effective measurement rate as

$$\Gamma_{\mathrm{eff}}(\omega) = \Gamma_{\mathrm{meas}}\frac{\kappa^2}{8}\left[\frac{1}{(\kappa/2)^2 + (\Delta+\omega)^2} + \frac{1}{(\kappa/2)^2 + (\Delta-\omega)^2}\right]. \tag{1.54}$$

For a resonantly driven cavity the effective measurement rate simplifies to

$$\Gamma_{\mathrm{eff}}(\omega) = \frac{4g^2}{\kappa}\frac{1}{1 + (2\omega/\kappa)^2}, \tag{1.55}$$

meaning that solely the direct radiation pressure of the ingoing amplitude noise onto the mechanical oscillator needs to be considered. In this case the symmetrized mechanical displacement spectrum results in

$$\bar{S}_{X_{\mathrm{m}}X_{\mathrm{m}}}(\omega) = 2|\chi_{\mathrm{m}}(\omega)|^2\Big[\bar{S}_{\mathrm{th}}(\omega) + 2\Gamma_{\mathrm{eff}}(\omega)\bar{S}^{\mathrm{in}}_{XX}(\omega)\Big]. \tag{1.56}$$

The second term corresponds to the power spectral density of the optical bath, $\bar{S}^{\mathrm{in}}_{XX}(\omega) \geq 1/2$, such that, on resonance, the light field does not modify the mechanical susceptibility to the environment, but solely introduces an additional heating term [114].

1.5 Phonon Occupation Number

Here we describe two methods to determine the mechanical phonon occupation number from the power spectral densities discussed in the previous section. On the one hand, the power spectral density of the quantum noise allows us to determine the occupation number of the mechanical oscillator via its frequency asymmetry. On the other hand, the integral of the symmetrized power spectral density of the mechanical displacement provides a direct proportionality to the mechanical occupation number [44].

The optomechanical interaction can be described by the transitions appearing between mechanical and optical excitations, and are fully determined by the quantum noise spectrum of the radiation pressure force. For a harmonic oscillator, the noise in the applied forces at the mechanical frequency causes transitions between the oscillator's eigenstates. The contribution of the force noise spectrum at $-\Omega_{\mathrm{m}}$ leads to absorption of energy from the noise source to the mechanical mode, and thus increase of the phonon number, and the contribution from Ω_{m} leads to the emission of energy to the bath [5]. The strength of these transitions is determined by the quantum noise spectrum. That is why the mechanical position fluctuations are directly related to the force noise, and thus display the same asymmetry between positive and negative frequencies [44, 5]. In thermal equilibrium, there is detailed balance between the displacement power spectral density at positive and negative frequencies, corresponding to transitions to higher and

lower energies [114], such that

$$\bar{n}_{\mathrm{m}} = \frac{S_{X_{\mathrm{m}}X_{\mathrm{m}}}(-\Omega_{\mathrm{m}})}{S_{X_{\mathrm{m}}X_{\mathrm{m}}}(\Omega_{\mathrm{m}}) - S_{X_{\mathrm{m}}X_{\mathrm{m}}}(-\Omega_{\mathrm{m}})}. \tag{1.57}$$

This allows to infer the mechanical occupation number without prior knowledge of the environmental temperature.

Moreover, $\bar{S}_{X_{\mathrm{m}}X_{\mathrm{m}}}$ can be used to determine the average phonon occupation number. Indeed, the variance of the mechanical motion can be determined by the integral of the power spectral density[6], such that

$$\langle \hat{X}_{\mathrm{m}}^2(t) \rangle = 2 \int_0^\infty \bar{S}_{X_{\mathrm{m}}X_{\mathrm{m}}}(\omega) \frac{d\omega}{2\pi}. \tag{1.58}$$

For high quality mechanical oscillators, the power spectral density is strongly peaked around the mechanical frequency $\pm\Omega_{\mathrm{m}}$, which allows us to approximate the spectral density of the momentum as

$$\bar{S}_{P_{\mathrm{m}}P_{\mathrm{m}}}(\omega) = \frac{\omega^2}{\Omega_{\mathrm{m}}^2} \bar{S}_{X_{\mathrm{m}}X_{\mathrm{m}}}(\omega) \approx \bar{S}_{X_{\mathrm{m}}X_{\mathrm{m}}}(\omega). \tag{1.59}$$

The integral of $\bar{S}_{X_{\mathrm{m}}X_{\mathrm{m}}}(\omega)$[7] leads to the relation between the variance in the mechanical displacement and the mechanical occupation number $\bar{n}_{\mathrm{m}}$ given by

$$\bar{n}_{\mathrm{m}} + \frac{1}{2} = \frac{1}{2}\langle \hat{X}_{\mathrm{m}}^2 + \hat{P}_{\mathrm{m}}^2 \rangle = \langle \hat{X}_{\mathrm{m}}^2 \rangle = \frac{\gamma_{\mathrm{m}}}{\gamma_{\mathrm{m}} + \Gamma_{\mathrm{m}}} \Big[\bar{n}_{\mathrm{th}} + \frac{1}{2} + \frac{\Gamma_{\mathrm{eff}}(\omega)}{\gamma_{\mathrm{m}}} \Big]. \tag{1.60}$$

We observe that the mechanical occupation number contains contributions from the fluctuations of the zero-point, the thermal and the radiation pressure force. Furthermore, the mechanical occupation can be reduced by the optically induced mechanical broadening Γ_{m}. Indeed, in the limit of large damping $\Gamma_{\mathrm{m}} \gg \gamma_{\mathrm{m}}$, the modification of the mechanical susceptibility entails a drastic reduction of the thermal bath contribution to the mechanical occupation number $\bar{n}_{\mathrm{th}}\gamma_{\mathrm{m}}/\Gamma_{\mathrm{m}} \ll 1$. However, this does not hold true for the backaction term, to which we can assign the equivalent occupation number $\bar{n}_{\mathrm{qba}} \equiv \Gamma_{\mathrm{eff}}(\omega)/\gamma_{\mathrm{m}}$. Depending on the cavity parameters this term can hinder ground-state cooling, and its implications are discussed in greater detail within the context of cooling limits in Sec. 2.4.7.

Quantum Cooperativity Considering the ratio between the backaction rate versus the thermal decoherence provides us with the definition for the quantum cooperativity

$$C_{\mathrm{qu}} = \frac{\Gamma_{\mathrm{meas}}}{\gamma_{\mathrm{m,th}}}, \tag{1.61}$$

where the thermal decoherence rate is given by $\gamma_{\mathrm{m,th}} = \gamma_{\mathrm{m}}\bar{n}_{\mathrm{th}}$. A large cooperativity $C_{\mathrm{qu}} > 1$ entails that the quantum backaction noise dominates over thermal noise, which is a necessary requirement to address mechanical states other than thermal states, for quantum state control and entanglement experiments.

[6] where we employed Parseval's theorem relating the energy in the time domain to the energy in the frequency domain as $\lim_{\tau\to\infty} \int_{-\tau/2}^{\tau/2} \langle \hat{X}^\dagger(t)\hat{X}(t)\rangle \mathrm{d}t = \frac{1}{2\pi}\int_{-\infty}^{\infty} S_{X_{\mathrm{m}}X_{\mathrm{m}}}(\omega)\frac{\mathrm{d}\omega}{2\pi}$ [114]

[7] where we use the integral $\int_{-\infty}^{\infty} |\chi_{\mathrm{m}}(\omega)|^2 \mathrm{d}\omega/(2\pi) = 1/2(\gamma_{\mathrm{m}} + \Gamma_{\mathrm{m}})$

1.6 Optomechanical Read-out

In order to relate the mechanical motion to the detected field, we examine the mechanical transduction onto the outgoing light field, building the foundation of the mechanical displacement measurements using optical cavities.

1.6.1 Cavity Outcoupling

We recall the input-output relation between the intra- and extracavity fields as

$$\hat{a}_{\text{out}} = \hat{a}_{\text{in}} + \sqrt{\kappa}\hat{c}, \tag{1.62}$$

where we consider the outgoing field leaking out through the incoupling port, which corresponds to the reflection from the cavity. In general, the optical cavity losses, summarized in κ, contain contributions from both cavity ports, as well as internal loss mechanisms due to scattering or absorption. Here, we assume that the total cavity losses κ are entirely due to the two incoupling ports, i.e. $\kappa = \kappa_1 + \kappa_2$. Since we are dealing with an asymmetric cavity driven through the low reflectivity port, our main interest lies in the reflection amplitude $\mathcal{R}$ and we define the cavity incoupling efficiency as $\eta_c = \kappa_1/\kappa$. The amplitude reflectivity of the incoupling cavity mirror is then given by the ratio

$$\mathcal{R}(\Delta) = \frac{\langle \hat{a}_{\text{out}} \rangle}{\langle \hat{a}_{\text{in}} \rangle} = \frac{(\kappa_2 - \kappa_1)/2 - \mathrm{i}\Delta}{\kappa/2 - \mathrm{i}\Delta} = \frac{\kappa/2(1-2\eta_c) - \mathrm{i}\Delta}{\kappa/2 - \mathrm{i}\Delta}. \tag{1.63}$$

The amount of back-reflected power depends on both the detuning Δ and the incoupling coefficient η_c. On resonance ($\Delta = 0$), the reflection amplitude becomes $\mathcal{R}(\Delta = 0) = 1 - 2\eta_c$. The cavity coupling can be categorized into three distinct regimes: the undercoupled regime where $\eta_c < 0.5$, resulting in most of the light being lost through ports other than the incoupling one; the critically coupled regime where $\eta_c = 0.5$, resulting in no light being reflected on resonance; and the overcoupled regime where $\eta_c > 0.5$, which is the most desirable scenario for our experiments, as most of the light is back-reflected from the incoupling port. In fact, for maximal incoupling ($\eta_c = 1$), the back-reflected light is exactly the ingoing light field with a π phase shift. For finite detunings ($\Delta \neq 0$), the phase shift of the back-reflected light results in

$$\phi_c = \arg[\mathcal{R}(\Delta)] = \arctan\left[\frac{\eta_c \kappa \Delta}{(\kappa/2)^2(1-2\eta_c) + \Delta^2}\right], \tag{1.64}$$

which is at the origin of the rotation between the amplitude and phase light quadratures. Figure 1.3 illustrates the dependence of both the transmitted and the back-reflected powers on the detuning for various incoupling parameters, along with the phases ϕ_c.

Considering the finite cavity incoupling η_c, the effective ingoing field building up the cavity field can be written as

$$\hat{a}_{\text{in}} = \sqrt{\eta_c}\hat{a}'_{\text{in}} + \sqrt{1-\eta_c}\hat{v}_{\text{in}} \tag{1.65}$$

where $\hat{a}'_{\text{in}}$ represents the physical input field in front of the cavity, and $\hat{v}_{\text{in}}$ the vacuum noise field that couples in through the loss port. In the following, to simply the notation, we are going to omit the vacuum noise contribution $\hat{v}_{\text{in}}$. Analogous to the input-output

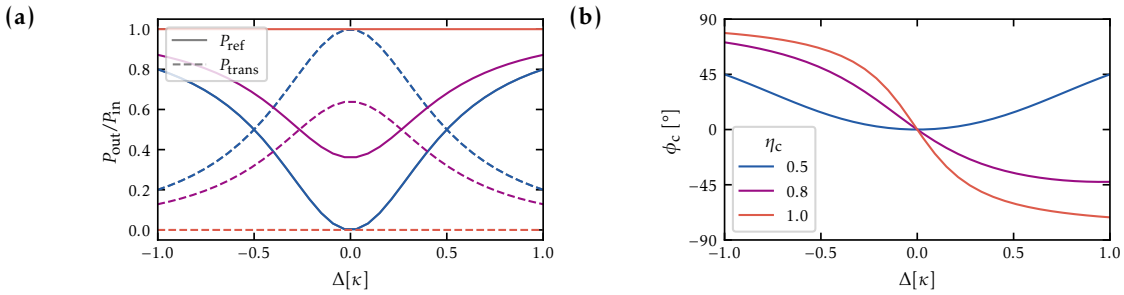

FIGURE 1.3: Power ratio of the transmitted and back-reflected light as a function of detuning from a cavity with linewidth κ for **(a)** different cavity incoupling parameters η_c and **(b)** the corresponding phases.

relation, recalled in Eq. (1.62), we can write the expression the for physical output field

$$\hat{a}'_{\mathrm{out}} = \hat{a}'_{\mathrm{in}} + \sqrt{\eta_c \kappa}\hat{c}, \tag{1.66}$$

in terms of the cavity field

$$\hat{c}(\omega) = -\chi_c(\omega)\Big[\sqrt{\eta_c \kappa}\hat{a}'_{\mathrm{in}}(\omega) + \mathrm{i}\sqrt{2}g\hat{X}_{\mathrm{m}}(\omega)\Big]. \tag{1.67}$$

Furthermore, we note that the definition of the optomechanical coupling strength also includes the cavity incoupling efficiency $g = g_0|\sqrt{\kappa}\chi_c(0)\alpha_{\mathrm{in}}| = g_0\sqrt{\eta_c}|\chi_c(0)\alpha'_{\mathrm{in}}|$. For the ease of notation, in the remainder of this chapter we will use $\hat{a}'_{\mathrm{out}} \to \hat{a}_{\mathrm{out}}$ and $\hat{a}'_{\mathrm{in}} \to \hat{a}_{\mathrm{in}}$ and $\alpha'_{\mathrm{in}} \to \alpha_{\mathrm{in}}$.

1.6.2 Outgoing Light Quadratures

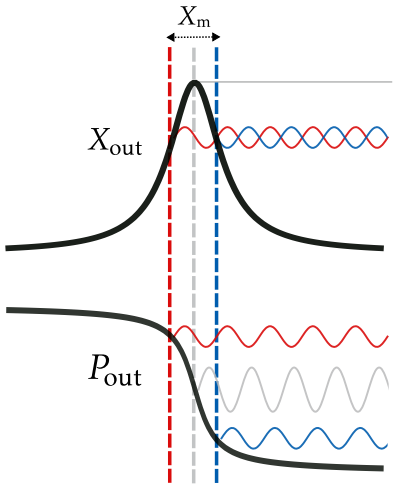

FIGURE 1.4: Transduction of the mechanical displacement onto the outgoing light field, depending on the detuning (red/blue) or resonant cavity drive.

The signal of the mechanical motion is imprinted as a modulation on the phase, and for a non-resonant cavity also the amplitude quadrature of the light leaking out of the

cavity, as illustrated in Fig. 1.4. From the input-output relations, together with the expression of the cavity field operator as stated Eq. (1.32) the outgoing field in frequency domain reads

$$\begin{aligned}\hat{a}_{\mathrm{out}}(\omega) &= \hat{a}_{\mathrm{in}}(\omega) + \sqrt{\eta_{\mathrm{c}}\kappa}\hat{c}(\omega) \\ &= \hat{a}_{\mathrm{in}}(\omega)\Big[1 - \eta_{\mathrm{c}}\kappa\chi_{\mathrm{c}}(\omega)\Big] - \mathrm{i}\sqrt{2\eta_{\mathrm{c}}\kappa}g\chi_{\mathrm{c}}(\omega)\hat{X}_{\mathrm{m}}(\omega),\end{aligned} \tag{1.68}$$

and allows to define the outgoing light quadratures

$$\hat{X}_{\mathrm{out}}(\omega) = \frac{1}{\sqrt{2}}\Big[\hat{a}^{\dagger}_{\mathrm{out}}(-\omega) + \hat{a}_{\mathrm{out}}(\omega)\Big], \tag{1.69}$$

$$\hat{P}_{\mathrm{out}}(\omega) = \frac{\mathrm{i}}{\sqrt{2}}\Big[\hat{a}^{\dagger}_{\mathrm{out}}(-\omega) - \hat{a}_{\mathrm{out}}(\omega)\Big]. \tag{1.70}$$

In terms of the mechanical displacement $\hat{X}_{\mathrm{m}}$, these are given by

$$\hat{X}_{\mathrm{out}}(\omega) = \Big[1 - \eta_{\mathrm{c}}\kappa C_{+}(\omega)\Big]\hat{X}_{\mathrm{in}}(\omega) + \eta_{\mathrm{c}}\kappa C_{-}(\omega)\hat{P}_{\mathrm{in}}(\omega) + 2\sqrt{\eta_{\mathrm{c}}\kappa}C_{-}(\omega)g\hat{X}_{\mathrm{m}}(\omega), \tag{1.71}$$

$$\hat{P}_{\mathrm{out}}(\omega) = -\eta_{\mathrm{c}}\kappa C_{-}(\omega)\hat{X}_{\mathrm{in}}(\omega) + \Big[1 - \eta_{\mathrm{c}}\kappa C_{+}(\omega)\Big]\hat{P}_{\mathrm{in}}(\omega) - 2\sqrt{\eta_{\mathrm{c}}\kappa}C_{+}(\omega)g\hat{X}_{\mathrm{m}}(\omega). \tag{1.72}$$

Inserting the expression for the mechanical quadrature [cf. Eq. (1.37)], we obtain the outgoing light quadratures in terms of the ingoing fluctuations, written in matrix notation as

$$\begin{aligned}\begin{pmatrix}\hat{X}_{\mathrm{out}}\\ \hat{P}_{\mathrm{out}}\end{pmatrix} &= \begin{pmatrix}1-\eta_{\mathrm{c}}\kappa C_{+} & \eta_{\mathrm{c}}\kappa C_{-}\\ -\eta_{\mathrm{c}}\kappa C_{-} & 1-\eta_{\mathrm{c}}\kappa C_{+}\end{pmatrix}\begin{pmatrix}\hat{X}_{\mathrm{in}}\\ \hat{P}_{\mathrm{in}}\end{pmatrix} \\ &+ \chi_{\mathrm{m}}(\omega)\eta_{\mathrm{c}}\Gamma_{\mathrm{meas}}\kappa^2\begin{pmatrix}C_{-}C_{+} & -C_{-}^2\\ -C_{+}^2 & C_{-}C_{+}\end{pmatrix}\begin{pmatrix}\hat{X}_{\mathrm{in}}\\ \hat{P}_{\mathrm{in}}\end{pmatrix} + \chi_{\mathrm{m}}(\omega)\sqrt{2\eta_{\mathrm{c}}\Gamma_{\mathrm{meas}}}\kappa\hat{\xi}_{\mathrm{th}}(\omega)\begin{pmatrix}C_{-}\\ -C_{+}\end{pmatrix}.\end{aligned} \tag{1.73}$$

Here we have taken into account the losses due to imperfect cavity incoupling $\eta_{\mathrm{c}} < 1$, but neglected the additional vacuum noise terms that couple through the loss ports[8].

If we consider the outgoing light phase-quadrature of a resonantly driven cavity, we obtain the simplified expression

$$\hat{P}_{\mathrm{out}}(\omega) = -\eta_{\mathrm{c}}g_0\alpha_{\mathrm{in}}\zeta_{\mathrm{c}}(\omega)\hat{X}_{\mathrm{m}}(\omega), \tag{1.74}$$

where $\zeta_{\mathrm{c}}(\omega)$ describes the cavity transduction factor and is given by

$$\zeta_{\mathrm{c}}(\omega) = \kappa\Big[\chi_{\mathrm{c}}(0)\chi_{\mathrm{c}}(\omega) + \chi^{*}_{\mathrm{c}}(0)\chi^{*}_{\mathrm{c}}(-\omega)\Big]. \tag{1.75}$$

For a cavity driven close resonance, and operating in the unresolved sideband regime $\Omega_{\mathrm{m}} \ll \kappa$, where the delay induced by cavity remains small, we can approximate the cavity susceptibility as $\chi_{\mathrm{c}}(\omega) \approx 2/\kappa$. Assuming a perfect incoupling $\eta_{\mathrm{c}} \approx 1$, and a weak optomechanical coupling $g \ll \kappa$, the relationship between the incoming light quadrature

[8] In case of significant backaction compared to thermal noise $\Gamma_{\mathrm{meas}} \gg \gamma_{\mathrm{m}}$, we expect the appearance of mechanically mediated correlations between the two quadratures of the ingoing light noise, which is referred to as ponderomotive squeezing. The effect will be enhanced close to the mechanical resonance due to the scaling with the mechanical susceptibility.

and the cavity quadratures simplifies to

$$\begin{aligned}\hat{X}_{\mathrm{c}}(\omega) &= -\frac{2}{\sqrt{\kappa}}\hat{X}_{\mathrm{in}}(\omega),\\ \hat{P}_{\mathrm{c}}(\omega) &= -\frac{2}{\sqrt{\kappa}}\hat{P}_{\mathrm{in}}(\omega) + \frac{4g}{\sqrt{\kappa}}\hat{X}_{\mathrm{m}}(\omega),\end{aligned} \tag{1.76}$$

where the cavity fields adiabatically follow the ingoing light fields. Thus we obtain the compact form of the outgoing light quadratures

$$\begin{aligned}\hat{X}_{\mathrm{out}}(\omega) &= -\hat{X}_{\mathrm{in}}(\omega),\\ \hat{P}_{\mathrm{out}}(\omega) &= -\hat{P}_{\mathrm{in}}(\omega) + 2\sqrt{\Gamma_{\mathrm{meas}}}\hat{X}_{\mathrm{m}}(\omega),\end{aligned} \tag{1.77}$$

where the phase quadrature contains, additionally to the incoming light noise, the mechanical displacement transduced with the measurement rate $2\sqrt{\Gamma_{\mathrm{meas}}}$.

1.7 Homodyne Detection

In order to extract the mechanical signal imprinted onto the light field, we want to have access to both the amplitude and phase quadrature of the outgoing light field. Whereas the amplitude quadrature can be accessed in a direct detection scheme, the approach to acquire the phase quadrature of the optical light uses an interferometric overlap with a phase-referencing beam, such as homodyne or heterodyne detection [114]. In the homodyne detection scheme one employs a reference beam at the same frequency as the probe beam, providing access to the symmetrized power spectral densities in the probe signal. The heterodyne detection requires a frequency-shifted reference, and provides access to both positive and negative frequency parts of the detected power spectral density. For a description of heterodyne detection we refer to App. A.

In this section we consider a balanced homodyne detection scheme, that can be implemented using an optical setup as sketched in Fig. 1.5. The light mode to be measured $\hat{a}$ is mixed with a strong local oscillator $\hat{a}_{\mathrm{LO}}$ in a Mach-Zehnder interferometer [114]. Starting with a single light mode $\hat{a}_{\mathrm{in}}$ entering on one port of a beamsplitter with amplitude transmission coefficient ϵ, the fields leaving the transmission and reflection output ports are given by

$$\begin{aligned}\hat{a} &= \epsilon\hat{a}_{\mathrm{in}} + \sqrt{1-\epsilon^2}\hat{v},\\ \hat{a}_{\mathrm{LO}} &= \sqrt{1-\epsilon^2}\hat{a}_{\mathrm{in}} - \epsilon\hat{v},\end{aligned} \tag{1.78}$$

where the open input port of the beamsplitter is filled with vacuum noise $\hat{v}$. However, since we mostly consider coherent ingoing fields, we can neglect the mixing with vacuum fields due to empty ports. After their independent propagation in the respective interferometer arms, where the probe beam had a chance to interact with the experiment, the probe beam $\hat{a}$ and the strong reference beam $\hat{a}_{\mathrm{LO}}$, denoted the local oscillator, are reunited on a balanced (50/50) beamsplitter cube. The fields at the output ports of the beamsplitter are given by

$$\hat{d}_{\pm} = \frac{1}{\sqrt{2}}(\hat{a}_{\mathrm{LO}}\mathrm{e}^{\mathrm{i}\theta} \pm \hat{a}). \tag{1.79}$$

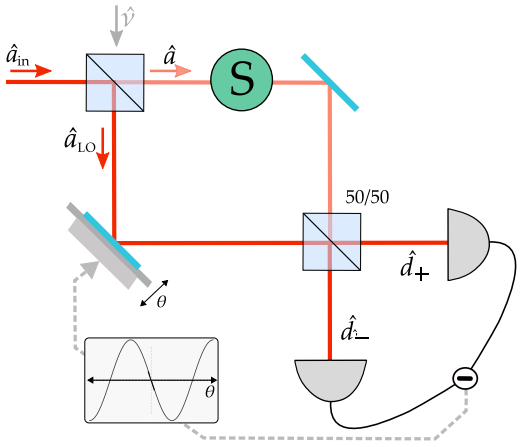

FIGURE 1.5: Sketch of the Mach-Zehnder interferometer used for a balanced homodyne detection of the light's phase quadrature after the interaction with a system S.

Using absorbing photodetectors, only the intensity of the light and hence the photon number can be measured. The photocurrent at the detectors, denoted with $D_\pm$, reads

$$\hat{D}_\pm = d_\pm^\dagger d_\pm = \frac{1}{2}(\hat{a}^\dagger\hat{a} + \hat{a}_{\text{LO}}^\dagger\hat{a}_{\text{LO}} \pm e^{i\theta}\hat{a}^\dagger\hat{a}_{\text{LO}} \pm e^{-i\theta}\hat{a}_{\text{LO}}^\dagger\hat{a}). \tag{1.80}$$

The signal provided by the balanced detector corresponds to the subtracted photocurrent between the two photodiodes following

$$\begin{aligned}\hat{D} &= d_+^\dagger d_+ - d_-^\dagger d_- \\ &= e^{i\theta}\hat{a}^\dagger\hat{a}_{\text{LO}} + e^{-i\theta}\hat{a}_{\text{LO}}^\dagger\hat{a} \\ &\approx \alpha_{\text{LO}}(e^{i\theta}\hat{a}^\dagger + e^{-i\theta}\hat{a}) \\ &\approx \sqrt{2}\alpha_{\text{LO}}\left[\hat{X}_a\cos(\theta) + \hat{P}_a\sin(\theta)\right],\end{aligned} \tag{1.81}$$

where $\alpha_{\text{LO}} = \langle\hat{a}_{\text{LO}}\rangle$ is the average displacement of the local oscillator. Here we assumed that the local oscillator has a constant phase and a large amplitude $|\alpha_{\text{LO}}| \gg |\alpha|$, such that we can directly relate the amplitude X_a and phase quadrature P_a of the light mode $\hat{a}$ to the detected homodyne photocurrent. The choice of the homodyne phase θ of the local oscillator determines which quadrature of $\hat{a}$ will be measured. The ideal setting for optimizing the phase quadrature acquisition requires a homodyne phase of $\theta = \frac{\pi}{2}$ [9].

Furthermore, if the amplitude of the local oscillator is substantially larger than the

[9] In general we can detect a linear combination of the outgoing amplitude and phase quadrature, such that $\hat{X}_\theta = \cos\theta\hat{X}_a(\omega) + \sin\theta\hat{P}_a(\omega) = \cos\theta\hat{X}_{\text{out}}(\omega) + \sin\theta\hat{P}_{\text{out}}(\omega)$ with the experimentally detected light quadratures $\hat{X}_{\text{out}}$ and $\hat{P}_{\text{out}}$, resulting in the corresponding power spectral density

$$\begin{aligned}S_{X_\theta X_\theta}(\omega) = \frac{1}{2} + 2\gamma_{\text{m}}\Gamma_{\text{meas}}\kappa^2 C_+(\omega)^2|\chi_{\text{m}}(\omega)|^2\left(\bar{n}_{\text{th}} + \frac{1}{2} + \frac{\kappa^2\Gamma_{\text{meas}}}{2\gamma_{\text{m}}}C_+(\omega)^2\right)\sin^2\theta \\ - \Gamma_{\text{meas}}\kappa^2 C_+(\omega)^2\chi_{\text{m}}(\omega)\Big(\kappa^2 C_+(\omega)^2\left[1 - \kappa C_+^*(-\omega)\right] \\ + \chi_{\text{m}}^*(-\omega)\kappa^2 C_+^*(-\omega)^2\left[1 - \kappa C_+(\omega)\right]\Big)\sin 2\theta.\end{aligned} \tag{1.82}$$

The first term describes the optical field shot noise, the second term represents the backaction heating, and the third term is generated by correlations and can be negative. The presence of strong correlations in the

one of the probing field ($|\alpha_{\mathrm{LO}}| \gg |\alpha|$), the response of the photocurrent amplitude to a known variation in the homodyne phase can be used directly to calibrate the cavity phase fluctuations [cf. Sec. 4.5.2].

In order to get a quantitative relation between the quadratures of the mechanical oscillator on the homodyne measurement signal, we need to examine the optomechanical transduction onto the light field, which is contained in the output field of the cavity as stated in Eq. (1.73).

The detector signal can be split into a static part D_0 and a fluctuation part $\delta\hat{D}(\omega)$ containing the modulation imprinted by the mechanical oscillator, such that $\hat{D}(\omega) = \hat{D}_0\sqrt{2\pi}\delta(\omega) + \delta\hat{D}(\omega)$. For the optimal optomechanical measurement configuration, where the probing beam is close to cavity resonance $\Delta \approx 0$, the detection signal solely contains the cavity phase quadrature P_{out} as given by

$$\hat{D} = \sqrt{2\eta_{\mathrm{det}}}\alpha_{\mathrm{LO}}\Big[-\cos\theta\hat{X}_{\mathrm{in}} + \sin\theta\Big(-\hat{P}_{\mathrm{in}} + \sqrt{\Gamma_{\mathrm{meas}}}\hat{X}_{\mathrm{m}}\Big)\Big]. \tag{1.83}$$

This results in the term encompassing the mechanical modulation

$$\delta\hat{D}(\omega) = \sqrt{2\eta_{\mathrm{det}}\Gamma_{\mathrm{meas}}}\alpha_{\mathrm{LO}}\hat{X}_{\mathrm{m}}(\omega)\sin\theta, \tag{1.84}$$

providing direct access to the mechanical displacement $\hat{X}_{\mathrm{m}}$, given that the measurement rate Γ_{meas} is known through an independent calibration.

When using an off-resonant probe beam $\Delta \neq 0$, the acquired light quadrature $\hat{P}_{\mathrm{out}}$ contains contributions from both the amplitude and phase quadrature of the cavity field [cf. Eq. (1.73)]. The detected modulation term, proportional to the mechanical oscillator displacement, is then given by

$$\delta\hat{D}(\omega) = \sqrt{2\eta_{\mathrm{det}}\Gamma_{\mathrm{meas}}}\alpha_{\mathrm{LO}}\kappa\Big[\cos\theta C_{-}(\omega) - \sin\theta C_{+}(\omega)\Big]\hat{X}_{\mathrm{m}}(\omega), \tag{1.85}$$

where the read-out mechanical displacement scales with the prefactors $C_{+}(\omega)$ and $C_{-}(\omega)$ that vary with the detuning.

1.8 Optomechanical Response

In general, it is valuable to be aware how the mechanical oscillator responds to specific modulations of the light field. Understanding the optomechanical response to external modulations not only enables us to calibrate the optomechanical coupling strength, but it also provides insights into the system's behaviour during coupling experiments.

To start with, we consider the transduction of a classical ingoing modulation onto the detected homodyne signal as defined in the previous section. For a general modulation $q(t) = \alpha_{\mathrm{L}}\beta_0\cos(\omega_0 t)$ on the ingoing field $\hat{a}_{\mathrm{in}}$ with photon flux $|\alpha_{\mathrm{L}}|^2$, modulation depth β_0, and modulation frequency ω_0, the detector signal containing the modulation can be expressed as

$$\delta D(\omega) = \sqrt{2\pi}\beta_0|\alpha_{\mathrm{L}}|^2\zeta(\omega)\Big[\delta(\omega-\omega_0) + \delta(\omega+\omega_0)\Big], \tag{1.86}$$

where $\zeta(\omega)$ is the modulation transduction function that includes the frequency response of the optomechanical system. We can again separate the outgoing light quadratures

outgoing field quadratures, resulting in $S_{X_\theta X_\theta}(\omega) < 1/2$, represents a signature of the backaction dominated regime.

into the frequency-independent terms included in D_0, and the modulated terms in δD. The latter can be accessed via demodulation of the detector signal at the modulation frequency using a lock-in amplifier.

First, we consider a coherent light field with an average amplitude α_L, with light quadratures given by

$$\begin{pmatrix} X_\mathrm{in} \\ P_\mathrm{in} \end{pmatrix} = \sqrt{2}\alpha_\mathrm{L} \begin{pmatrix} 1 \\ 0 \end{pmatrix}. \tag{1.87}$$

Inserting these ingoing fields into the expressions for the outgoing light quadratures, as stated in Eqs. (1.73), only considering the terms that are linear in the coherent field amplitude α_L, we obtain the modulation transfer function for a coherent input field, omitting the frequency dependence of C_+ and C_- for readability

$$\zeta_\mathrm{coh}(\omega) = \cos\theta\Big[\eta_\mathrm{c}\kappa^2 C_- C_+ \Gamma_\mathrm{meas}\chi_\mathrm{m}(\omega)\Big] - \sin\theta\Big[\eta_\mathrm{c}\kappa^2 C_+^2 \Gamma_\mathrm{meas}\chi_\mathrm{m}(\omega)\Big], \tag{1.88}$$

which on resonance simplifies to

$$\zeta_\mathrm{coh}(\omega) = -\sin\theta\Big[\frac{\eta_\mathrm{c}\kappa^2}{(\kappa/2 - \mathrm{i}\omega)^2}\Gamma_\mathrm{meas}\chi_\mathrm{m}(\omega)\Big]. \tag{1.89}$$

For an input amplitude modulation with frequency ω_0 and modulation depth β_0, the ingoing field can be written as

$$\begin{pmatrix} X_\mathrm{in} \\ P_\mathrm{in} \end{pmatrix} = \sqrt{2}\alpha_\mathrm{L} \begin{pmatrix} 1 + \beta_0 \cos(\omega_0 t) \\ 0 \end{pmatrix}. \tag{1.90}$$

Taking into account the imperfect coupling of the local oscillator, reflected from the cavity with the amplitude $\mathcal{R}$ defined in Eq. (1.63), we find the modulation transduction function

$$\begin{aligned} \zeta_\mathrm{ampl}(\omega) = &\cos\theta\Big[\mathcal{R} + 1 - \eta_\mathrm{c}\kappa C_+ + \eta_\mathrm{c}\kappa^2 C_- C_+ \Gamma_\mathrm{meas}\chi_\mathrm{m}(\omega)\Big] \\ &+ \sin\theta\Big[\eta_\mathrm{c}\kappa C_- - \eta_\mathrm{c}\kappa^2 C_+^2 \Gamma_\mathrm{meas}\chi_\mathrm{m}(\omega)\Big], \end{aligned} \tag{1.91}$$

which on resonance simplifies to

$$\zeta_\mathrm{ampl}(\omega) = \cos\theta\left[2(1-\eta_\mathrm{c}) - \frac{\eta_\mathrm{c}\kappa}{\kappa/2 - \mathrm{i}\omega}\right] - \sin\theta\left[\frac{\eta_\mathrm{c}\kappa^2}{(\kappa/2 - \mathrm{i}\omega)^2}\Gamma_\mathrm{meas}\chi_\mathrm{m}(\omega)\right]. \tag{1.92}$$

The response contains a linear combination of the in-phase response term $\propto \cos\theta$ that includes the interference of the input modulation present on the local oscillator, and the out-of-phase contribution $\propto \sin\theta$ that solely encompasses the mechanical response. The second term contains the measurement rate Γ_meas and the mechanical susceptibility $\chi_\mathrm{m}(\omega)$ and can be used for calibration measurement [see Sec. 4.4.3]. Similarly, for a phase modulation on the ingoing light field, the ingoing light field quadratures read

$$\begin{pmatrix} \hat{X}_\mathrm{in} \\ \hat{P}_\mathrm{in} \end{pmatrix} = \sqrt{2}\alpha_\mathrm{L} \begin{pmatrix} 1 \\ \beta_0 \cos(\omega_0 t) \end{pmatrix}, \tag{1.93}$$

which results in the transduction function for a phase modulated ingoing beam

$$\begin{aligned}\zeta_{\text{phase}}(\omega) = &\cos\theta\Big[\eta_c\kappa C_- - \eta_c\kappa^2 C_-^2\Gamma_{\text{meas}}\chi_m(\omega)\Big] \\ &+ \sin\theta\Big[1 - \eta_c\kappa C_+ + \eta_c\kappa^2 C_- C_+\Gamma_{\text{meas}}\chi_m(\omega)\Big],\end{aligned} \tag{1.94}$$

and on resonance simplifies to

$$\zeta_{\text{phase}}(\omega) = \sin\theta\Big(1 - \frac{\eta_c\kappa}{\kappa/2 - i\omega}\Big). \tag{1.95}$$

Since this expression is independent of the mechanical oscillator, in the resonant case we do not expect a mechanical response to an ingoing phase modulation. In Ch. 3 we develop on how this will change in the case of our coherent feedback scheme.

1.9 Detection Limit

Probing the mechanical motion with light not only leads to the modification of the outgoing light beam, that carries the signal of the mechanical displacement, but also induces backaction from the light on the mechanical motion. Due to this backaction, enhancing the intensity of the probe beam, which would typically be the strategy to reduce imprecision caused by shot noise in detection, does not allow for arbitrary improvement in detection accuracy. The interplay between measurement backaction and shot-noise imprecision gives rise to a limit in the uncertainty of the detection.

Assuming that we can neglect correlations between the ingoing light noise and the mechanical position quadrature, we can use Eq. (1.77) such that on resonance the phase-noise power spectral density of the outgoing light field reads

$$\begin{aligned}\bar{S}_{PP}^{\text{out}}(\omega) &= \bar{S}_{PP}^{\text{in}}(\omega) + 4\Gamma_{\text{eff}}(\omega)\bar{S}_{X_m X_m}(\omega) \\ &= \frac{1}{2} + 8\gamma_m\Gamma_{\text{eff}}(\omega)|\chi_m(\omega)|^2\left(\bar{n}_{\text{th}} + \frac{1}{2} + \frac{\Gamma_{\text{eff}}(\omega)}{\gamma_m}\right).\end{aligned} \tag{1.96}$$

The first term describes the white noise due to photon shot-noise $\bar{S}_{PP}^{\text{in}}(\omega) = 1/2$, while the second term represents the transduced mechanical displacement that is read out at a rate of $\Gamma_{\text{eff}}(\omega)$. Alternatively, we can express the outgoing phase quadrature as

$$\bar{S}_{PP}^{\text{out}}(\omega) = 4\Gamma_{\text{eff}}(\omega)\Big[\bar{S}_{\text{imp}}(\omega) + \bar{S}_{X_m X_m}(\omega)\Big], \tag{1.97}$$

given by the sum of the actual mechanical displacement and the associated equivalent mechanical motion corresponding to the shot-noise signal, referred to as imprecision noise $\bar{S}_{\text{imp}}(\omega) = \bar{S}_{PP}^{\text{in}}(\omega)/4\Gamma_{\text{eff}}(\omega)$. The inferred mechanical excursion on resonance, considering the contributions of the imprecision noise, light-induced backaction and thermal bath, is given by

$$\begin{aligned}\bar{S}_{X_m X_m}^{\text{tot}}(\omega) &= \bar{S}_{\text{imp}}(\omega) + \bar{S}_{X_m X_m}(\omega) \\ &= 2\gamma_m|\chi_m(\omega)|^2(\bar{n}_{\text{th}} + \frac{1}{2}) + \frac{1}{4\Gamma_{\text{eff}}(\omega)}\bar{S}_{PP}^{\text{in}}(\omega) + 4\Gamma_{\text{eff}}(\omega)|\chi_m(\omega)|^2\bar{S}_{XX}^{\text{in}}(\omega).\end{aligned} \tag{1.98}$$

The optical backaction force, which describes the heating due to the radiation pressure shot-noise, scales with the measurement rate following $\bar{S}_{\text{qba}} = 4\Gamma_{\text{eff}}\bar{S}_{XX}^{\text{in}}$. Thus we can derive the lower bound for the product of the imprecision and the backaction contributions

[114]

$$\bar{S}_{\mathrm{qba}}(\omega)\bar{S}_{\mathrm{imp}}(\omega) = \bar{S}^{\mathrm{in}}_{XX}(\omega)\bar{S}^{\mathrm{in}}_{PP}(\omega) \geq \left(\frac{1}{2}\right)^2. \tag{1.99}$$

The backaction noise introduces additional displacement fluctuations which blur the oscillator's displacement as seen by the detection and contribute to the overall uncertainty. The optimal measurement conditions minimizing the added fluctuations establish the standard quantum limit (SQL) for displacement and force measurement [47]. The SQL is expressed as the product between the amplitude and phase quadrature and represents the lower limit that is reached when the ingoing light fields are shot-noise limited. Finally the total acquired noise power spectral density is given by the sum of the intrinsic thermal fluctuations and the added heating term due to the detection process, which for quantum-limited input fields results in

$$\bar{S}_{\mathrm{det}}(\omega) = \frac{1}{4\Gamma_{\mathrm{eff}}(\omega)} + 4\Gamma_{\mathrm{eff}}(\omega)|\chi_{\mathrm{m}}(\omega)|^2. \tag{1.100}$$

This additional noise term contributes to the detection noise floor and can be minimized for the interaction strength that exactly balances measurement imprecision and backaction noises, given by $\Gamma_{\mathrm{optimal}} = 1/(2|\chi_{\mathrm{m}}(\omega)|)$. This setting realizes the optomechanical SQL with the optimal measurement precision lower bound given by $\bar{S}_{\mathrm{det}}(\omega) = |\chi_{\mathrm{m}}(\omega)|$. Reaching the SQL implies that the zero-point fluctuations of the mechanical oscillator can be resolved in the measurement time $\Gamma_{\mathrm{eff}}^{-1}$ [44]. The measurement rate can be adjusted to the optimal value through the incident probe power.

Furthermore, the detection limit can still be circumvented by more elaborated experimental schemes. For instance, non-continuous measurements of the output field, such as stroboscopic measurements [44, 120], implementing quantum non-demolition (QND) measurements and other backaction evasion schemes [121, 83], as well as coherent cancellation techniques [26, 122, 123], or the usage of non-classical input states [124, 103, 125] can be employed.

Measurement sensitivity Based on the preceding discussion, we observe that the detection sensitivity is constrained by $\bar{S}_{\mathrm{det}}$, representing the trade-off between the imprecision and the backaction contribution. So far this indicates the precision with which we can detect the thermal motion created by the thermal noise $\hat{\xi}_{\mathrm{th}}$. However, in experiments, our interest may extend to detecting external forces beyond the stochastic thermal force. In that case we may aim to distinguish the mechanical displacement caused by these external forces from the thermal motion of the mechanical oscillator, and the thermally driven motion has to be considered as an additional noise source contributing to the final noise floor [114]. The expression for the detected mechanical displacement is given by

$$\bar{S}^{\mathrm{det}}_{X_{\mathrm{m}}X_{\mathrm{m}}}(\omega) = \bar{S}^{\mathrm{th}}_{X_{\mathrm{m}}X_{\mathrm{m}}}(\omega) + \bar{S}_{\mathrm{det}}(\omega), \tag{1.101}$$

where $\bar{S}^{\mathrm{th}}_{X_{\mathrm{m}}X_{\mathrm{m}}}(\omega) = 2|\chi_{\mathrm{m}}(\omega)|^2\bar{S}_{\mathrm{th}}(\omega)$ is the mechanical displacement without the presence of optical light.

For a high-quality harmonic oscillator, the fluctuation-dissipation theorem allows us to establish the conversion from the displacement power spectral density to the force power spectral density. The power spectral density of the force sensitivity is then given

by [126]

$$\bar{S}_{FF}^{\mathrm{th}} = \frac{\hbar m \Omega_{\mathrm{m}}}{|\chi_{\mathrm{m}}(\omega)|^2} \bar{S}_{X_{\mathrm{m}} X_{\mathrm{m}}}^{\mathrm{th}}(\omega) = \hbar m \Omega_{\mathrm{m}} 2 \bar{S}_{\mathrm{th}}(\omega) = 2 m \gamma_{\mathrm{m}} k_{\mathrm{B}} T, \tag{1.102}$$

where we used the relation $k_{\mathrm{B}} T = \hbar \Omega_{\mathrm{m}} \bar{n}_{\mathrm{m}}$. It is worth noting that the thermomechanical noise can be minimized by reducing both the mechanical damping rate γ_{m} and the effective mass m of the mechanical oscillator. These are important design criteria for the mechanical oscillators described in Ch. 3.

1.10 Conclusion

In this chapter, we introduced the basic theoretical concepts related to optomechanical systems, specifically the interaction between a mechanical oscillator and an optical cavity field. For a resonant cavity drive, the mechanical motion is imprinted entirely on the phase quadrature of the outgoing light field and can be detected with a homodyne scheme, whereas the mechanical oscillator solely responds to modulations in the amplitude quadrature.

In case of finite detuning, there is a dynamical backaction effect of the light field on the mechanical oscillator that modifies its resonance frequency and damping rate. A red-detuned beam leads to a broadening of the mechanical linewidth and, consequently, to cooling.

Furthermore, we considered the detection limit encountered in such an optomechanical system, which can be reached for a probe beam power that exactly balances the imprecision of the cavity phase measurement and the measurement backaction generated by the probing light. Additionally, the sensitivity of the detection of the mechanical motion depends on both the mass and the damping rate of the employed mechanical oscillator and plays an essential role in the design considerations described in Ch. 3.

Having covered the basic optomechanical concepts, we are now well-prepared to consider such a system in a more involved optical scheme, namely embedded in a coherent feedback loop as described in Ch. 2.

Chapter 2

Optical Coherent Feedback

With our current understanding of quantum physics, it appears that we can enhance the performance of quantum feedback control by avoiding measurements. However, it is not immediately evident which applications profit from a feedback scheme that avoids measurement and classical processing, a scheme denoted coherent feedback, and which ones have an analogous measurement-based alternative [5, 21].

To develop our understanding of the potential advantages of coherent feedback, we present and analyze in this chapter an all optical coherent feedback loop on an optomechanical setup as a prototype. We derive the equations governing the dynamics of such a feedback platform that is implemented by a light field, collected after a first interaction with a mechanical oscillator inside an optical cavity and redirected to the cavity for a second interaction. As an application of this scheme, we focus on the specific task of cooling the mechanical oscillator and show that coherent feedback enables ground-state cooling, thus outperforming dynamical backaction cooling in the unresolved sideband regime. Moreover, we compare the performance of this scheme to that of measurement-based feedback techniques and find that their lower bounds for cooling are analogous and solely determined by their efficiency. Furthermore, we demonstrate that the coherent feedback scheme enables the reduction of quantum noise by backaction cancellation and the generation of non-classical states.

Parts of this chapter have been published in [113].

2.1 Introduction

Cold mechanical oscillators are a promising starting point for various experiments in quantum sensing, tests of fundamental quantum mechanics and quantum technology application like quantum transducers [79]. These mechanical oscillators possess outstanding features, such as convenient and versatile coupling mechanisms through strain, electro- and optomechanical forces, ultrahigh quality factors, and masses that can both be small enough for force sensitivity and large enough for testing fundamental physics like quantum gravity and macroscopic superpositions [45].

In this chapter, we will explore how coherent feedback can aid in preparing mechanical oscillators in interesting quantum states. Specifically, we will analyse the scenario for an optomechanical cavity where the cavity decay rate κ is larger than the mechanical frequency Ω_{m}, known as the unresolved sideband regime. This regime allows the mechanical oscillator to exchange information rapidly with external fields and thus with other systems, which is crucial for hybrid coupling experiments [102, 127, 34].

In fact, for optomechanical systems in the unresolved sideband regime, the cavity cannot spectrally distinguish between the processes that entail an emission or an absorption of a mechanical excitation. Thus, the broad cavity frequency response makes it

challenging to resonantly enhance exclusively either one or the other transition. However, this selectivity is required for many interesting tasks, like ground-state cooling, optomechanical state-swaps (via the beamsplitter interaction) and entangling tasks (via parametric amplification interaction).

One solution for the sideband selectivity issue relies on using coherent feedback by means of an additional passive optical element, like a cavity or a mirror, in combination with a time delay, which modifies the resulting optical force on the mechanical oscillator [110, 112, 42].

This feedback can be generated by collecting the outgoing mode of the optomechanical cavity and passing it through an auxiliary cavity or reflecting it off a mirror with a certain delay line before redirecting it for a second interaction to the same optomechanical cavity as sketched in Fig. 2.1 (b). The broad cavity containing the mechanical oscillator can then be adiabatically eliminated, and the mechanical mode is effectively coupled to the auxiliary cavity, resulting in a modified optical decay rate. By using a narrow auxiliary cavity ($\kappa_{\mathrm{aux}} \ll \Omega_{\mathrm{m}}$), the mechanical oscillator is effectively coupled to a cavity in the resolved sideband regime. However, this comes at the cost of a reduction of the optomechanical coupling strength g, which requires a reoptimization of the parameters for maximal quantum cooperativity [42]. As such, feedback with passive elements based on interference loops is predicted to be helpful for concrete applications like cooling, squeezing, entanglement and state transfer [112, 42].

In contrast to the previously mentioned optical feedback schemes, we have developed a scheme that generates feedback using one optomechanical cavity simultaneously driven in two different cavity modes [24, 27], see Fig. 2.1 (a). The feedback results from the optical force that already contains the mechanical signal from the first interaction and acts directly on the mechanical oscillator during the second interaction, potentially leading to interfering terms in the optomechanical interaction.

In the following chapter we introduce the concept of such a coherent feedback platform. First, we derive the equations describing both the feedback schemes of a one and a two-optical-mode feedback loop on a single system. We discuss the quantum control gained by a loop that feeds back via an orthogonal cavity mode and the predicted limitations for cooling, compare the limitations of our scheme to dynamical back-action cooling and measurement-based cooling. Furthermore we consider the potential of the coherent feedback loop for applications like backaction cancellation and mechanical squeezing, also in the context of a hybrid system.

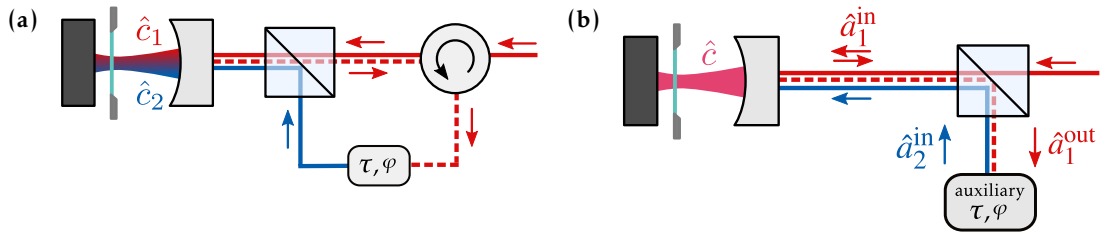

Figure 2.1: Sketch of two coherent feedback realizations, where the feedback loop is implemented **(a)** in two orthogonal cavity modes $\hat{c}_1$ and $\hat{c}_2$ and **(b)** in one single cavity mode $\hat{c}$ using an auxiliary optical element.

2.2 Coherent Feedback

To derive the equations of motion of our coherent feedback scheme, we begin with one mechanical mode $\hat{b}$ that is coupled with strength g_j to j cavity modes $\hat{c}_j$. The Hamiltonian describing the entire system is given by the sum of the mechanical, the cavity and the linearized optomechanical Hamiltonians as stated in Eqs. (1.4), (1.12) and (1.26),

$$\hat{H} = \hbar\Omega_{\mathrm{m}}\hat{b}^\dagger\hat{b} + \sum_j \hbar\omega_{\mathrm{c}}\hat{c}_j\hat{c}_j - \hbar g_j(\hat{c}_j^\dagger + \hat{c}_j)(\hat{b}^\dagger + \hat{b}). \tag{2.1}$$

To model the open dynamics of the optomechanical system we rely on the Langevin formalism [114]. The linearized Langevin equations for the cavity fields assuming a cavity linewidth κ_j for the mode j in the rotating frame at the laser frequency, read

$$\partial_t\hat{c}_j(t) = -\left[\frac{\kappa_j}{2} - \mathrm{i}\Delta\right]\hat{c}_j(t) - \mathrm{i}g_j[\hat{b}^\dagger(t) + \hat{b}(t)] - \sqrt{\kappa_j}\hat{a}_j^{\mathrm{in}}(t), \tag{2.2}$$

and for the mechanical oscillator

$$\partial_t\hat{b}(t) = -\left[\frac{\gamma_{\mathrm{m}}}{2} + \mathrm{i}\Omega_{\mathrm{m}}\right]\hat{b}(t) - \mathrm{i}\sum_j g_j[\hat{c}_j(t)^\dagger + \hat{c}_j(t)] - \mathrm{i}\sqrt{2\gamma_{\mathrm{m}}}\hat{b}_{\mathrm{in}}(t). \tag{2.3}$$

The coupling to the thermal bath is expressed by the intrinsic mechanical damping rate γ_{m} and the associated driving by the incoming fluctuations $\hat{b}_{\mathrm{in}}$ resulting in the thermal noise term $\hat{\xi}_{\mathrm{th}} = \sqrt{\gamma_{\mathrm{m}}}\frac{\mathrm{i}}{\sqrt{2}}(\hat{b}_{\mathrm{in}}^\dagger - \hat{b}_{\mathrm{in}})$ [cf. Eq. (1.6)].

Coherent feedback can now be implemented by using the light leaving the cavity after a certain interaction and cascading it for a next interaction. This can be described using the input-output relations

$$\hat{a}_j^{\mathrm{out}} = \hat{a}_j^{\mathrm{in}} + \sqrt{\kappa_j}\hat{c}_j \tag{2.4}$$

$$\hat{a}_j^{\mathrm{in}} = \sqrt{\eta_j}\mathrm{e}^{\mathrm{i}\varphi_j}\hat{a}_{j-1}^{\mathrm{out}}(t-\tau_j) + \sqrt{1-\eta_j}\hat{v}_j \qquad \text{for } j > 1 \tag{2.5}$$

with η_j the optical efficiency taking into account the propagation losses, $\hat{v}_j$ the noise coupling in through the loss-channel, τ_j the time delay, and φ_j the phase between the two interactions $j-1$ and j.

2.3 Coherent Feedback on a Single Cavity Mode

First we consider a coherent feedback scheme that relies on coupling one mechanical mode to one single cavity mode, $\hat{c} = \hat{c}_1 = \hat{c}_2$ generated from a field $\hat{a}_{\mathrm{in}}$ travelling in a loop, such that

$$\begin{aligned}\hat{a}_1^{\mathrm{out}} &= \hat{a}_{\mathrm{in}} + \sqrt{\kappa}\hat{c},\\ \hat{a}_2^{\mathrm{in}} &= \sqrt{\eta}\mathrm{e}^{\mathrm{i}\varphi}\hat{a}_1^{\mathrm{out}}(t-\tau)\end{aligned} \tag{2.6}$$

The resulting Langevin equation for the cavity mode then turns out to be

$$\begin{aligned}\partial_t \hat{c} =& \left[\mathrm{i}\Delta - \frac{\kappa}{2}\right]\hat{c}(t) - \mathrm{i}g[\hat{b}^\dagger(t) + \hat{b}(t)] - \sqrt{\eta}\kappa \mathrm{e}^{\mathrm{i}\varphi}\hat{c}(t-\tau) \\ & - \sqrt{\kappa}\hat{a}_{\mathrm{in}}(t) - \sqrt{\eta\kappa}\mathrm{e}^{\mathrm{i}\varphi}\hat{a}_{\mathrm{in}}(t-\tau).\end{aligned} \tag{2.7}$$

We can write the cavity field in the frequency domain as

$$\hat{c}(\omega) = -\chi_c(\omega)\left[\left(\sqrt{\kappa} + \sqrt{\eta\kappa}\mathrm{e}^{\mathrm{i}(\omega\tau+\varphi)}\right)\hat{a}_{\mathrm{in}}(\omega) + \mathrm{i}\sqrt{2}g\hat{X}_{\mathrm{m}}(\omega)\right], \tag{2.8}$$

with the modified cavity susceptibility

$$\chi_c(\omega) = \left[\frac{\kappa}{2} - \mathrm{i}\omega - \mathrm{i}\Delta + \sqrt{\eta}\kappa\mathrm{e}^{\mathrm{i}(\omega\tau+\varphi)}\right]^{-1}. \tag{2.9}$$

From the real and imaginary parts we can identify the effective cavity linewidth and detuning

$$\begin{aligned}\kappa_{\mathrm{eff}} &= \kappa\left(1 + 2\sqrt{\eta}\cos(\omega\tau+\varphi)\right), \\ \Delta_{\mathrm{eff}} &= \Delta - \sqrt{\eta}\kappa\sin(\omega\tau+\varphi).\end{aligned} \tag{2.10}$$

Recalling that the cavity field is composed of the average displacement and the fluctuation part $\alpha + \hat{c}$, the average cavity field is modified by the feedback and becomes

$$\alpha = -\frac{\sqrt{\kappa}(1+\sqrt{\eta}\mathrm{e}^{\mathrm{i}\varphi})}{\kappa_{\mathrm{eff}}/2 - \mathrm{i}\Delta_{\mathrm{eff}}}\alpha_{\mathrm{in}}, \tag{2.11}$$

which leads to the modification of the optomechanical coupling strength $g = |\alpha|g_0$. In general we note that the described feedback loop is very similar to the proposed scheme in [42] and mostly affects the parameters of the cavity, and thus can be used to modify the sideband resolution parameter $\Omega_{\mathrm{m}}/\kappa$ as well as the optomechanical coupling strength g.

The theoretical description as sketched above takes into account exactly two light-system interactions during the coherent feedback loop. Therefore, from an experimental perspective, combining two beams with identical polarization requires an advanced experimental setups to maintain the ability of a subsequent separation of the two beams after a first interaction. Specifically, we must rely on an optical switch to connect either the incoming light or light leaking out of the cavity after the first interaction and redirect it to an input port. If one wants to ensure that both beams are simultaneously in the cavity, the switching time must be shorter than the cavity lifetime, resulting in a required switching time of $1/\kappa \approx 3\,\mathrm{ns}$ in our case. Instead, in the following, we will consider a coherent feedback scheme that takes advantage of two orthogonal cavity modes, conveniently implemented via two orthogonal light polarizations.

2.4 Coherent Feedback on Orthogonal Cavity Modes

2.4.1 Overview

The coherent feedback scheme that we describe in this section consists in an all-optical feedback loop operating on two orthogonal cavity modes, as depicted in Fig. 2.2. Initially,

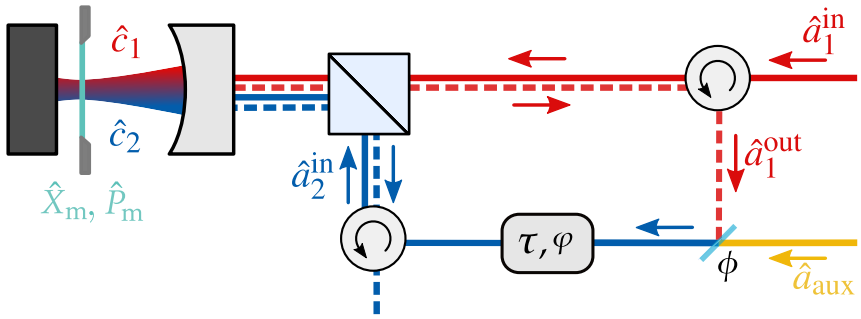

FIGURE 2.2: Optical path sketch of our double pass feedback scheme. An incoming light beam $\hat{a}_1^{in}$ drives a cavity field $\hat{c}_1$ that interacts via the radiation pressure force with a mechanical oscillator described by its quadratures $\hat{X}_m, \hat{P}_m$. The remaining beam is combined with an auxiliary local oscillator $\hat{a}_{aux}$, with a phase ϕ between $\hat{a}_1^{out}$ and $\hat{a}_{aux}$. thus generating a loop phase φ. The combined field $\hat{a}_2^{in}$ furthermore experiences a delay τ, before passing through the orthogonal port of the polarizing beamsplitter cube positioned in front of the cavity. This beam then drives the second cavity mode $\hat{c}_2$, which is orthogonal to $\hat{c}_1$. The outgoing light after the second interaction is discarded from the loop. The color coding of the light beams is used for visual guidance, and dashed lines differentiate between incoming and back-reflected beams.

an incoming light beam, denoted $\hat{a}_1^{in}$ (red), couples into an optomechanical cavity and drives the cavity field $\hat{c}_1$. The cavity field interacts with the mechanical oscillator through the radiation pressure force. The signal of the mechanical oscillator, represented by its displacement and momentum quadratures $\hat{X}_m, \hat{P}_m$ is imprinted as a modulation on the outgoing light field $\hat{a}_1^{out}$. The back-reflected beam $\hat{a}_1^{out}$ is combined with an auxiliary local oscillator field $\hat{a}_{aux}$ (yellow), resulting in a displacement in the optical phase space about the phase ϕ [see Fig. 2.6]. This combination effectively implements the loop phase, denoted as φ. The combined field of the local oscillator and the back-reflected beam (blue) propagates together, and is delayed by a time τ, before being used as an input $\hat{a}_2^{in}$ to drive a second cavity mode $\hat{c}_2$. The back-reflected beam after the second interaction exits the loop.

We note that the orthogonal polarization between the two cavity modes ensures that there is no disturbance from optical interference, allowing both light fields to interact peacefully with the mechanical oscillator. Furthermore, the second cavity field, already containing the mechanical signal from the first interaction, enables self-interactions of the mechanical oscillator that are controlled by the feedback parameters. The loop phase, on the one hand, makes sure that the mechanical signal is rotated in the desired optical quadrature to ensure the ideal optomechanical interaction. The delay τ between the two interaction, on the other hand, enables us to select how the mechanical quadratures of the oscillator are fed back to itself, thereby controlling the nature of the feedback force, which may involve an optical spring ($\propto \hat{X}_m$), a modification of the mechanical damping ($\propto \pm\hat{P}_m$), or a combination of both. The information flow generated by the coherent feedback loop is illustrated in the flow chart in Fig. 2.3.

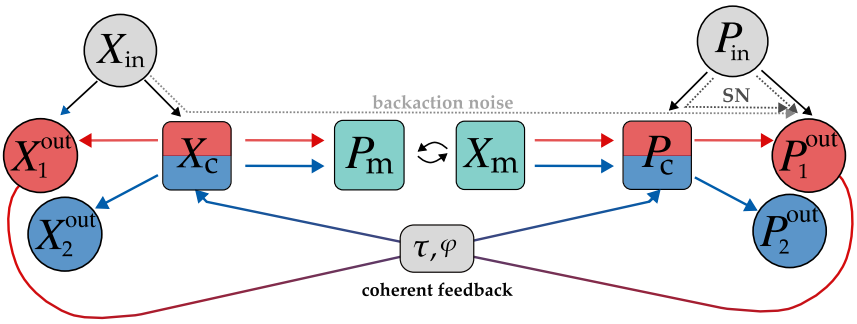

FIGURE 2.3: Flow chart of the coherent feedback scheme, relating the ingoing light field quadratures X_{in} and P_{in} to the outgoing quadratures X_2^{out} and P_2^{out}, illustrating the case for coherent feedback on two orthogonal modes with a resonant cavity, where the output of the cavity X_1^{out} and P_1^{out} after interaction with the mechanical quadratures X_{m} and P_{m} are fed back as an input to the cavity with a phase shift φ and a delay τ. The phase shift φ determines into which cavity quadratures the feedback is directed. The second cavity field (blue) populates an orthogonal cavity mode, and thus solely interacts with the mechanical oscillator, and can be separated from the first interaction at the output. The path of both the backaction noise, and the shot noise is drawn.

2.4.2 Langevin Equations

In our coherent feedback scheme we consider a double pass interaction of the light with an optomechanical cavity, coupling to two orthogonal polarization cavity modes. The complete optomechanical system is then described by the mechanical oscillator, and two cavity modes, where the second one depends on the first one via the cascade of interactions and the coupling of the mechanical oscillator.

In this scenario, the incoming travelling light field $\hat{a}_1^{\mathrm{in}}$ drives the cavity mode $\hat{c}_1$ of linewidth κ. The linearised Langevin equation for the first cavity field reads

$$\partial_t \hat{c}_1(t) = \left[\mathrm{i}\Delta - \frac{\kappa}{2}\right]\hat{c}_1(t) - \mathrm{i}g_1[\hat{b}^\dagger(t) + \hat{b}(t)] - \sqrt{\kappa}\hat{a}_1^{\mathrm{in}}(t), \tag{2.12}$$

with the optomechanical coupling strength of the first cavity mode g_1.

The mode leaking out of the cavity after the first interaction is given by the input-output relation [cf. Sec. 1.3]

$$\hat{a}_1^{\mathrm{out}} = \hat{a}_1^{\mathrm{in}} + \sqrt{\kappa}\hat{c}_1. \tag{2.13}$$

This outgoing field is transformed into the ingoing optical drive for the feedback mode after a delay τ, a phase shift φ, and the combination with an auxiliary local oscillator, such that

$$\begin{aligned}\hat{a}_2^{\mathrm{in}}(t) &= \sqrt{\eta}\mathrm{e}^{\mathrm{i}\varphi}\hat{a}_1^{\mathrm{out}}(t-\tau) + \sqrt{1-\eta}\hat{a}_{\mathrm{aux}}(t) \\ &= \sqrt{\eta}\mathrm{e}^{\mathrm{i}\varphi}\left[\hat{a}_1^{\mathrm{in}}(t-\tau) + \sqrt{\kappa}\hat{c}_1(t-\tau)\right] + \sqrt{(1-\eta)}\hat{a}_{\mathrm{aux}}(t).\end{aligned} \tag{2.14}$$

The loop efficiency η takes into account the unavoidable losses due to the beamsplitter required to combine the two fields $\hat{a}_1^{\mathrm{out}}$ and $\hat{a}_{\mathrm{aux}}$, and furthermore also encompasses all additional optical losses, which are discussed in greater detail in Sec. 2.4.3. The Langevin

equation for the second cavity field then turns out to be

$$\begin{aligned}\partial_t \hat{c}_2(t) &= \left[\mathrm{i}\Delta - \frac{\kappa}{2}\right]\hat{c}_2(t) - \mathrm{i}g_2[\hat{b}^\dagger(t) + \hat{b}(t)] - \sqrt{\kappa}\hat{a}_2^{\mathrm{in}}(t) \\ &= \left[\mathrm{i}\Delta - \frac{\kappa}{2}\right]\hat{c}_2(t) - \mathrm{i}g_2[\hat{b}^\dagger(t) + \hat{b}(t)] - \sqrt{(1-\eta)\kappa}\hat{a}_{\mathrm{aux}}(t) \\ &\quad - \sqrt{\eta\kappa}\mathrm{e}^{\mathrm{i}\varphi}\hat{c}_1(t-\tau) - \sqrt{\eta\kappa}\mathrm{e}^{\mathrm{i}\varphi}\hat{a}_1^{\mathrm{in}}(t-\tau),\end{aligned} \tag{2.15}$$

where we assumed for both cavity modes $\kappa = \kappa_1 = \kappa_2$. The expression for the cavity fields are split into a fluctuation and an average displacement part $\hat{c}_j \to \hat{c}_j + \alpha_j$. For the steady state, neglecting the optomechanical interaction, we obtain the average cavity field displacements

$$\begin{aligned}\alpha_1 &= -\frac{\sqrt{\kappa}}{\kappa/2 - \mathrm{i}\Delta}\alpha_1^{\mathrm{in}}, \\ \alpha_2 &= \frac{1}{\kappa/2 - \mathrm{i}\Delta}\left[\sqrt{\eta\kappa}\left(\frac{\kappa/2 + \mathrm{i}\Delta}{\kappa/2 - \mathrm{i}\Delta} - (1-\eta)\right)\alpha_1^{\mathrm{in}} - \sqrt{(1-\eta)\kappa}\mathrm{e}^{\mathrm{i}\phi}\alpha_{\mathrm{aux}}\right],\end{aligned} \tag{2.16}$$

where we introduced the average ingoing light field of the probe beam $\langle\hat{a}_1^{\mathrm{in}}\rangle = \alpha_1^{\mathrm{in}}$ and the auxiliary beam $\langle\hat{a}_{\mathrm{aux}}\rangle = \alpha_{\mathrm{aux}}$. As previously seen, the optomechanical coupling strengths are enhanced by these average cavity field displacements following $g_j = |\alpha_j|g_0$. Furthermore, the loop phase is determined by the angle between the two average displacement cavity fields $\varphi = \arg(\alpha_1/\alpha_2)$, which is controlled by the effective experimental phase $\phi = \arg(\alpha_{\mathrm{aux}}/\alpha_1^{\mathrm{out}})$, with $\alpha_1^{\mathrm{out}} = \langle\hat{a}_1^{\mathrm{out}}\rangle$, through an interference lock.

The loop phase φ includes the phase shift due to the reflection of a detuned cavity $\phi_c = \arctan(2\Delta/\kappa)$ in between the two interactions[1], and is plotted in Fig. 2.4 (a). We observe that even without adding an auxiliary local oscillator and with a resonant cavity drive, our definition of the loop phase results in $\varphi = \pi$. To convert from the experimentally set phase ϕ, between the outgoing light field and the auxiliary local oscillator to the loop phase, we thus have to manually take into account the phase shift ϕ_{c} induced by the cavity-detuning.

We furthermore note that, besides the obvious feedback parameters φ and τ, the coherent amplitude of the auxiliary local oscillator beam α_{aux} also plays a role in achieving the correct phase and can be seen as an additional control knob. In fact, the experimental phase ϕ between $\hat{a}_1^{\mathrm{out}}$ and $\hat{a}_{\mathrm{aux}}$ depends on the power ratio $P_{\mathrm{aux}}/P_{\mathrm{in}}$, defined as $P_{\mathrm{in}} = \hbar\omega_{\mathrm{L}}|\alpha_1^{\mathrm{in}}|^2$ and $P_{\mathrm{aux}} = \hbar\omega_{\mathrm{L}}|\alpha_{\mathrm{aux}}|^2$ respectively. The resulting phase relation between ϕ and the loop phase φ, is illustrated in Fig. 2.4 (b) for different power ratios. For a large auxiliary power, and a resonant cavity drive the phase relationship simplifies to $\varphi \approx \pi - \phi$.

The position and momentum quadratures of the mechanical oscillator, $\hat{X}_{\mathrm{m}}(t)$ and $\hat{P}_{\mathrm{m}}(t)$, are coupled to these light modes via the radiation pressure force, such that their quantum Langevin equations read

$$\begin{aligned}\partial_t \hat{X}_{\mathrm{m}}(t) &= \Omega_{\mathrm{m}}\hat{P}_{\mathrm{m}}(t), \\ \partial_t \hat{P}_{\mathrm{m}}(t) &= -\Omega_{\mathrm{m}}\hat{X}_{\mathrm{m}}(t) - \gamma_{\mathrm{m}}\hat{P}_{\mathrm{m}}(t) - 2\sum_{j=1}^{2} g_j\hat{X}_j(t) + \sqrt{2}\,\hat{\xi}_{\mathrm{th}}(t).\end{aligned} \tag{2.17}$$

[1] whereas any potential phase shifts between the ingoing beam and the first cavity mode are not included

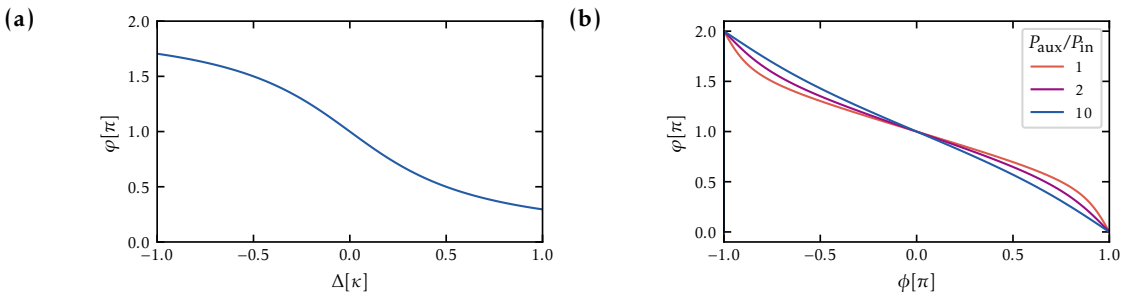

FIGURE 2.4: **(a)**: Contribution of a finite detuning of the optical cavity to the loop phase φ. **(b)**: Relation between the loop phase φ between the two intracavity average displacement fields α_1 and α_2, and the experimental phase ϕ between α_{aux} and α_1^{out}, plotted for different power ratios, at resonance.

where the amplitude and phase quadratures of the intracavity light field $\hat{X}_j$ and $\hat{P}_j$ are defined in Eq. (1.27). The incoming thermal noise $\hat{\xi}_{\mathrm{th}}$ and the decay term proportional to γ_{m} are added entirely to the momentum quadrature.

Frequency space To solve the equations for the mechanical oscillator, we can transform the cavity fields into the frequency domain using the Fourier transform as defined in Eq. (1.9) such that the mechanical oscillator quadratures in the frequency space yield

$$\begin{aligned} -\mathrm{i}\omega\hat{X}_{\mathrm{m}}(\omega) &= \Omega_{\mathrm{m}}\hat{P}_{\mathrm{m}}(\omega), \\ -\mathrm{i}\omega\hat{P}_{\mathrm{m}}(\omega) &= -\Omega_{\mathrm{m}}\hat{X}_{\mathrm{m}}(\omega) - \gamma_{\mathrm{m}}\hat{P}_{\mathrm{m}}(\omega) - 2\sum g_j\hat{X}_j(\omega) + \sqrt{2}\hat{\xi}_{\mathrm{th}}(\omega), \end{aligned} \tag{2.18}$$

where we can relate the momentum and the position operators

$$\hat{P}_{\mathrm{m}}(\omega) = -\frac{\mathrm{i}\omega}{\Omega_{\mathrm{m}}}\hat{X}_{\mathrm{m}}(\omega). \tag{2.19}$$

The cavity annihilation operators are then

$$\begin{aligned} \hat{c}_1(\omega) &= -\chi_{\mathrm{c}}(\omega)\Big(\sqrt{\kappa}\hat{a}_1^{\mathrm{in}}(\omega) + \mathrm{i}\sqrt{2}g_1X_{\mathrm{m}}(\omega)\Big), \\ \hat{c}_2(\omega) &= -\chi_{\mathrm{c}}(\omega)\Big(\sqrt{\eta\kappa}\mathrm{e}^{\mathrm{i}\varphi}\mathrm{e}^{\mathrm{i}\omega\tau}\Big[\sqrt{\kappa}\hat{c}_1(\omega) + \hat{a}_1^{\mathrm{in}}(\omega)\Big] + \sqrt{(1-\eta)\kappa}\hat{a}_{\mathrm{aux}}(\omega) + \mathrm{i}\sqrt{2}g_2\hat{X}_{\mathrm{m}}(\omega)\Big) \\ &= -\chi_{\mathrm{c}}(\omega)\Big(\sqrt{\eta\kappa}\mathrm{e}^{\mathrm{i}\varphi}\mathrm{e}^{\mathrm{i}\omega\tau}\hat{a}_1^{\mathrm{in}}(\omega)\Big(1-\kappa\chi_{\mathrm{c}}(\omega)\Big) + \sqrt{(1-\eta)\kappa}\hat{a}_{\mathrm{aux}}(\omega) \\ &\qquad + \mathrm{i}\sqrt{2}\hat{X}_{\mathrm{m}}(\omega)\Big[g_2 - \chi_{\mathrm{c}}(\omega)\sqrt{\eta}\kappa\mathrm{e}^{\mathrm{i}\varphi}\mathrm{e}^{\mathrm{i}\omega\tau}g_1\Big]\Big). \end{aligned} \tag{2.20}$$

Using the optical quadrature operators fulfilling the commutation relations

$$[\hat{X}_i(\omega), \hat{P}_j(\omega')] = \mathrm{i}\delta(\omega-\omega')\delta_{ij}, \qquad [\hat{X}_j, \hat{X}_j] = [\hat{P}_i, \hat{P}_i] = 0, \tag{2.21}$$

the ensemble of linear equation governing the optical quadratures is then given by

$$\begin{aligned}
-\mathrm{i}\omega\hat{X}_1 &= -\frac{\kappa}{2}\hat{X}_1 - \Delta\hat{P}_1 - \sqrt{\kappa}\hat{X}_1^{\mathrm{in}},\\
-\mathrm{i}\omega\hat{P}_1 &= \Delta\hat{X}_1 - \frac{\kappa}{2}\hat{P}_1 - \sqrt{\kappa}\hat{P}_1^{\mathrm{in}} - 2g_1\hat{X}_{\mathrm{m}},\\
-\mathrm{i}\omega\hat{X}_2 &= -\sqrt{\eta\kappa}\cos(\varphi)\mathrm{e}^{\mathrm{i}\omega\tau}(\sqrt{\kappa}\hat{X}_1 + \hat{X}_1^{\mathrm{in}}) + \sqrt{\eta\kappa}\sin(\varphi)\mathrm{e}^{\mathrm{i}\omega\tau}(\sqrt{\kappa}\hat{P}_1 + \hat{P}_1^{\mathrm{in}})\\
&\quad - \frac{\kappa}{2}\hat{X}_2 - \Delta\hat{P}_2 - \sqrt{1-\eta}\kappa\hat{X}_{\mathrm{aux}},\\
-\mathrm{i}\omega\hat{P}_2 &= -\sqrt{\eta\kappa}\sin(\varphi)\mathrm{e}^{\mathrm{i}\omega\tau}(\sqrt{\kappa}\hat{X}_1 + \hat{X}_1^{\mathrm{in}}) - \sqrt{\eta\kappa}\cos(\varphi)\mathrm{e}^{\mathrm{i}\omega\tau}(\sqrt{\kappa}\hat{P}_1 + \hat{P}_1^{\mathrm{in}})\\
&\quad + \Delta\hat{X}_2 - \frac{\kappa}{2}\hat{P}_2 - \sqrt{1-\eta}\kappa\hat{P}_{\mathrm{aux}} - 2g_2\hat{X}_{\mathrm{m}},
\end{aligned} \tag{2.22}$$

where we have omitted the dependencies on ω of all operators for readability. These equations illustrate how the mechanical signal is transduced into the optical quadratures and provide useful insights. If we consider the resonant case ($\Delta = 0$) for simplicity, we note that the mechanical displacement is directly imprinted onto $\hat{P}_1$ and $\hat{P}_2$. Additionally, there is a contribution from $\hat{P}_1$ to both $\hat{X}_2$ and $\hat{P}_2$, with a prefactor $\sim \sin(\varphi)\mathrm{e}^{\mathrm{i}\omega\tau}$ and $\sim \cos(\varphi)\mathrm{e}^{\mathrm{i}\omega\tau}$, respectively. This hints already at the possibility of establishing mechanical self-interactions.

Inserting the expressions for the cavity fields as stated in Eqs. (2.22) into the Langevin equations for the mechanical oscillator, given in Eq. (2.18), we can eliminate the cavity modes. Assuming a high quality oscillator ($\gamma_{\mathrm{m}} \ll \Omega_{\mathrm{m}}$) and that $\delta\Omega_{\mathrm{m}} \ll \Omega_{\mathrm{m}}$, we obtain

$$\begin{aligned}
-\omega^2\hat{X}_{\mathrm{m}}(\omega) = -\Big[(\Omega_{\mathrm{m}}^2 + 2\Omega_{\mathrm{m}}\delta\Omega_{\mathrm{m}}(\omega)\Big]\hat{X}_{\mathrm{m}}(\omega) + \mathrm{i}\omega[\Gamma_{\mathrm{m}}(\omega) + \gamma_{\mathrm{m}}]\hat{X}_{\mathrm{m}}(\omega)\\
+ \sqrt{2}\Omega_{\mathrm{m}}\hat{\xi}_{\mathrm{th}} + \sqrt{2}\Omega_{\mathrm{m}}\hat{\xi}_{\mathrm{fb}}(\omega),
\end{aligned} \tag{2.23}$$

where the real prefactors of $\hat{X}_{\mathrm{m}}$ are grouped into the frequency shift $\delta\Omega_{\mathrm{m}}$ and the imaginaries into the damping rate Γ_{m}. Similar to the optomechanical interaction derived in the previous chapter, this leads to two distinct effects of the optical interaction on the motion of the mechanical oscillator: First the optical field modifies the properties of the mechanical oscillator, namely the resonance frequency $\delta\Omega_{\mathrm{m}}$ through an optical spring effect as well as the damping rate Γ_{m} through a viscous force. Secondly there is the corresponding noise term $\hat{\xi}_{\mathrm{fb}}(\omega)$, caused by the fluctuations of the incoming light field, denoted as the backaction of the light. Explicitly the feedback noise term is given by

$$\begin{aligned}
\hat{\xi}_{\mathrm{fb}}(\omega)/\sqrt{2\kappa} = \hat{X}_1^{\mathrm{in}}(\omega)\Bigg\{ & g_1 C_+(\omega) + \sqrt{\eta}g_2\mathrm{e}^{\mathrm{i}\omega\tau}\Big[\cos(\varphi)\Big(C_+(\omega) - \kappa\Big[C_+(\omega)^2 - C_-(\omega)^2\Big]\Big)\\
& - \sin(\varphi)\Big(C_-(\omega) - 2\kappa C_+(\omega)C_-(\omega)\Big)\Big]\Bigg\}\\
+ \hat{P}_1^{\mathrm{in}}(\omega)\Bigg\{ & - g_1 C_-(\omega) - \sqrt{\eta}\mathrm{e}^{\mathrm{i}\omega\tau}g_2\Big[\cos(\varphi)\Big(C_-(\omega) - 2\kappa C_+(\omega)C_-(\omega)\Big)\\
& + \sin(\varphi)\Big(C_+(\omega) - \kappa[C_+(\omega)^2 - C_-(\omega)^2]\Big)\Big]\Bigg\}\\
+ \sqrt{1-\eta}g_2 & \Big(C_+(\omega)\hat{X}_{\mathrm{aux}} - C_-(\omega)\hat{P}_{\mathrm{aux}}\Big)\Bigg\},
\end{aligned} \tag{2.24}$$

with the factors $C_\pm$ as defined in Eq. (1.36). Without the coherent feedback ($\eta = 0$) this expression reduces to the optical force term of the standard optomechanical interaction $\hat{\xi}_\mathrm{L}$ as given in Eq. (1.39). In terms of the driving noise terms $\hat{\xi}_\mathrm{th}(\omega)$, $\hat{\xi}_\mathrm{fb}(\omega)$ the mechanical displacement can now be expressed as

$$\hat{X}_\mathrm{m}(\omega) = \sqrt{2}\chi_{\mathrm{m,eff}}(\omega)\Big[\hat{\xi}_\mathrm{th}(\omega) + \hat{\xi}_\mathrm{fb}(\omega)\Big] \tag{2.25}$$

with the modified susceptibility

$$\chi_{\mathrm{m,eff}}(\omega) = \frac{\Omega_\mathrm{m}}{\omega^2 + \Omega_\mathrm{m}(\Omega_\mathrm{m} + 2\delta\Omega_\mathrm{m}) - \mathrm{i}\omega(\Gamma_\mathrm{m} + \gamma_\mathrm{m})}. \tag{2.26}$$

The optical feedback $\hat{\xi}_\mathrm{fb}$ leads thus to a shift of the mechanical resonance frequency

$$\delta\Omega_\mathrm{m}(\omega) = \mathrm{Re}\Bigg\{\frac{2\Delta(g_1^2 + g_2^2)}{\Delta^2 + (\kappa/2 - \mathrm{i}\omega)^2} - 2\mathrm{e}^{\mathrm{i}\omega\tau} g_1 g_2 \sqrt{\eta}\kappa \frac{2\Delta(\kappa/2 - \mathrm{i}\omega)\cos(\varphi) - [\Delta^2 - (\kappa/2 - \mathrm{i}\omega)^2]\sin(\varphi)}{\Big[\Delta^2 + (\kappa/2 - \mathrm{i}\omega)^2\Big]^2}\Bigg\}, \tag{2.27}$$

and the additional damping rate

$$\Gamma_\mathrm{m}(\omega) = \frac{\Omega_\mathrm{m}}{\omega}\mathrm{Im}\Bigg\{-\frac{4\Delta(g_1^2 + g_2^2)}{\Delta^2 + (\kappa/2 - \mathrm{i}\omega)^2} + 4\mathrm{e}^{\mathrm{i}\omega\tau} g_1 g_2 \sqrt{\eta}\kappa \frac{2\Delta(\kappa/2 - \mathrm{i}\omega)\cos(\varphi) - [\Delta^2 - (\kappa/2 - \mathrm{i}\omega)^2]\sin(\varphi)}{\Big[\Delta^2 + (\kappa/2 - \mathrm{i}\omega)^2\Big]^2}\Bigg\}. \tag{2.28}$$

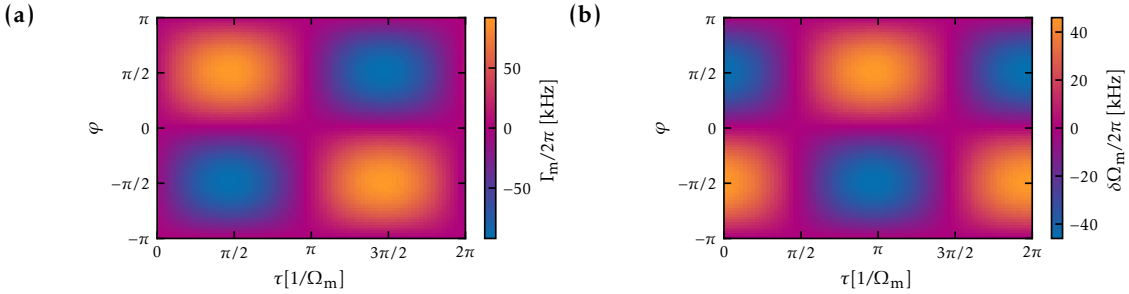

FIGURE 2.5: **(a)**: Expected damping rate Γ_m and **(b)** frequency shift $\delta\Omega_\mathrm{m}$ resulting from the coherent feedback loop for a resonant cavity drive $\Delta = 0$, scanning the feedback parameters φ and τ, for the standard experimental settings[2].

Considering a high quality mechanical oscillator we can replace $\delta\Omega_\mathrm{m}(\omega) \to \delta\Omega_\mathrm{m} = \delta\Omega_\mathrm{m}(\Omega_\mathrm{m})$ and $\Gamma_\mathrm{m}(\omega) \to \Gamma_\mathrm{m} = \Gamma_\mathrm{m}(\Omega_\mathrm{m})$. If additionally we are in the

unresolved sideband regime $\Omega_m \ll \kappa$, then Eqs. (2.27) and (2.28) simplify to

$$\begin{aligned}\delta\Omega_\mathrm{m} &= \frac{2\Delta(g_1^2+g_2^2)}{\Delta^2+(\kappa/2)^2} - 2\cos(\Omega_\mathrm{m}\tau)g_1g_2\sqrt{\eta}\kappa\frac{\Delta\kappa\cos(\varphi)-\left[\Delta^2-(\kappa/2)^2\right]\sin(\varphi)}{\left[\Delta^2+(\kappa/2)^2\right]^2},\\ \Gamma_\mathrm{m} &= 4\sin(\Omega_\mathrm{m}\tau)g_1g_2\sqrt{\eta}\kappa\frac{\Delta\kappa\cos(\varphi)-\left[\Delta^2-(\kappa/2)^2\right]\sin(\varphi)}{\left[\Delta^2+(\kappa/2)^2\right]^2}.\end{aligned} \tag{2.29}$$

It is worth noting that the damping generated by the coherent feedback is independent of the sideband resolution Ω_m/κ to first order as is discussed in more detail in section 2.4.7.

On resonance $|\Delta| \ll \kappa$, the equations for the light-induced frequency shift and broadening reduce further to

$$\begin{aligned}\delta\Omega_\mathrm{m} &= -8\sqrt{\eta}\frac{g_1g_2}{\kappa}\sin(\varphi)\cos(\Omega_\mathrm{m}\tau),\\ \Gamma_\mathrm{m} &= 16\sqrt{\eta}\frac{g_1g_2}{\kappa}\sin(\varphi)\sin(\Omega_\mathrm{m}\tau),\end{aligned} \tag{2.30}$$

and are plotted in Fig. 2.5, illustrating that both the largest damping and frequency shift occur for a loop phase $\varphi = \pm\pi/2$. The type of modifications induced by the coherent feedback, targeting either the frequency or the linewidth are determined by the delay τ.

Furthermore, these simplified expressions enable us to break down the coherent feedback scheme to understandable terms and develop an intuition for its working principles. The occurrence of the maximal values for the simplified expression at $\varphi = \pi/2$ can be explained using the sketch in Fig. 2.6 (a). For the feedback to be effective, the membrane signal imprinted onto the phase quadrature of the light during the first interaction must be rotated to the amplitude quadrature, so that it has an impact on the membrane motion during the second interaction through radiation pressure. This rotation of the optical quadratures can be controlled by the feedback loop phase φ. Given $\tau\gamma_\mathrm{m} \ll 1$, we can ignore the effect of the thermal noise on the mechanical oscillator during the time τ. This allows us to approximate the time evolution of the mechanical displacement operator by

$$\hat{X}_\mathrm{m}(t-\tau) \simeq \cos(\Omega_\mathrm{m}\tau)\hat{X}_\mathrm{m}(t) - \sin(\Omega_\mathrm{m}\tau)\hat{P}_\mathrm{m}(t). \tag{2.31}$$

This illustrates, that the delay has then the ability to determine which mechanical quadrature $\hat{X}_\mathrm{m}$ or $\hat{P}_\mathrm{m}$ (or a linear combination thereof) is fed back via the coherent loop, as illustrated in Fig. 2.6 (b). The delay τ can be chosen to match the feedback signal with the instantaneous membrane motion as illustrated in Fig. 2.7, and exert a force that is proportional to either the membrane position, generating an optical spring effect, or the momentum and thus the velocity of the mechanical motion, thereby generating a damping or a driving force depending on the sign.

In the case of a non-zero detuning $\Delta \neq 0$, the simple picture described above becomes more involved. The detuning leads to a rotation of the cavity quadratures with respect to the ingoing light quadratures, and consequently the mechanical signal is not solely

[2] For the entirety of the theory predictions, the standard experimental settings denote the ingoing powers $P_\mathrm{in} = 400\,\mu\mathrm{W}$ and $P_\mathrm{aux} = 1200\,\mu\mathrm{W}$, the environment temperature $T = 20\,\mathrm{K}$, and an overall loop efficiency $\eta = 0.22$

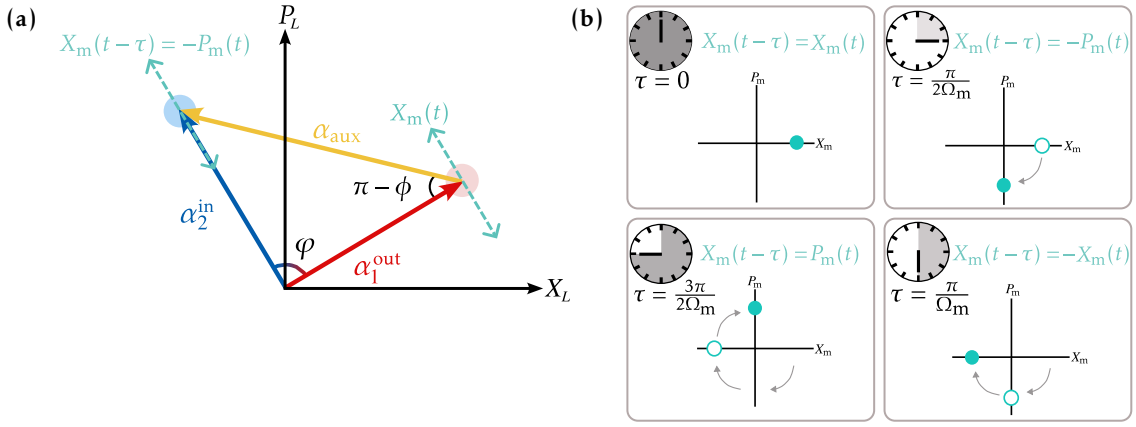

FIGURE 2.6: Sketch of the working principle of the coherent feedback scheme both of **(a)** the phase φ visualized in the phase-space of the amplitude and phase quadratures of the light outside the cavity and **(b)** the delay τ in the mechanical phase space. **(a)**: On resonance, the mechanical displacement $X_m(t)$ is imprinted onto the light phase quadrature through the optomechanical interaction. Combining an auxiliary local oscillator α_{aux} and the outgoing light α_1^{out} with the appropriate phase ϕ, we can adjust the loop phase φ, such that the incident light field for the second interaction α_2^{in} contains the mechanical displacement in the amplitude quadrature and thus couples to the mechanical motion via the interaction $\hat{X}_m\hat{X}_c$. **(b)**: The mechanical quadratures are rotating with the frequency Ω_m. Depending on the delay of the feedback τ we can feed back either $\pm X_m(t)$ or $\pm P_m(t)$ or in a linear combination and thus choose the type of force that the feedback is exerting. In fact, feeding back a signal $\propto X(t)$ generates an optical spring, whereas a signal $\propto \pm P(t)$ results in a viscous or driving force.

imprinted onto the phase quadrature of the outgoing beam. The more complex transduction of the mechanical signal onto the outgoing beam has to be considered in setting the correct loop phase for a proper second-pass interaction.

Furthermore as already mentioned above, the loop phase φ contains a detuning-dependent contribution, such that even without any auxiliary oscillator $\hat{a}_{aux} = 0$, the loop phase results in the expression $\varphi = \pi - 2\arctan(2\Delta/\kappa)$ that is entirely determined by Δ/κ. We note however, that if we insert this expression for φ in the absence of an auxiliary local oscillator into the expression for the feedback-induced damping Eq. (2.29) , the damping results in $\Gamma_m = 0$ if we only consider the zeroth order in Ω_m/κ. Hence, under these conditions, we do not expect the feedback loop to provide any cooling advantage with respect to the dynamical backaction, scaling in Ω_m/κ.

Quantum Cooperativity We recall that for the standard optomechanical interaction, the quantum cooperativity is defined as the ratio between quantum and thermal fluctuations, given by $C_{qu} = \Gamma_{meas}/\gamma_{m,th}$ with Γ_{meas} the measurement rate, and $\gamma_{m,th} = \gamma_m \bar{n}_{th}$ the thermal decoherence rate. For a resonant coupling the measurement rate is given by $\Gamma_{meas} = 4g^2/\kappa$.

For the double pass interaction we find that the overall cooperativity results in

$$C_{qu} = \frac{4g_1 g_2}{\kappa \gamma_{m,th}}. \tag{2.32}$$

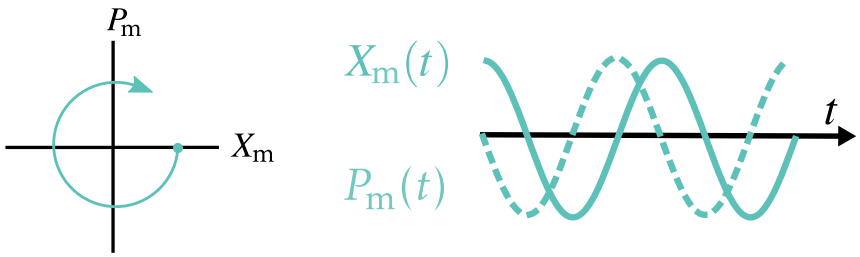

FIGURE 2.7: Sketch of the working principle of a mechanical oscillator

For the coherent feedback the cooperativity is proportional to the coupling constant $g = \sqrt{g_1 g_2}$, given by the product of the two interactions strengths g_1 and g_2 modified by the coherent feedback loop. In analogy, we can define the measurement rate of the coherent feedback loop as $\Gamma_{12} = 4g^2/\kappa = \sqrt{\Gamma_1 \Gamma_2}$ with $\Gamma_1 = 4g_1^2/\kappa$ and $\Gamma_2 = 4g_2^2/\kappa$.

We also observe that different coupling strengths are necessary, depending on the type of coupling regime we intend to establish. For example, strong coupling requires the light-mediated coupling to exceed the local damping, which can be quantified by the coupling rate greater than the average intrinsic damping rates $\gamma_{j,\mathrm{int}}$, i.e. $g > (\gamma_{1,\mathrm{int}} + \gamma_{2,\mathrm{int}})/2$. For quantum coherent coupling, the light-mediated coupling must exceeded the average total decoherence rate $\gamma_{j,\mathrm{tot}}$, i.e. $g > (\gamma_{1,\mathrm{tot}} + \gamma_{2,\mathrm{tot}})/2$ [27, 69].

2.4.3 Including Optical Losses

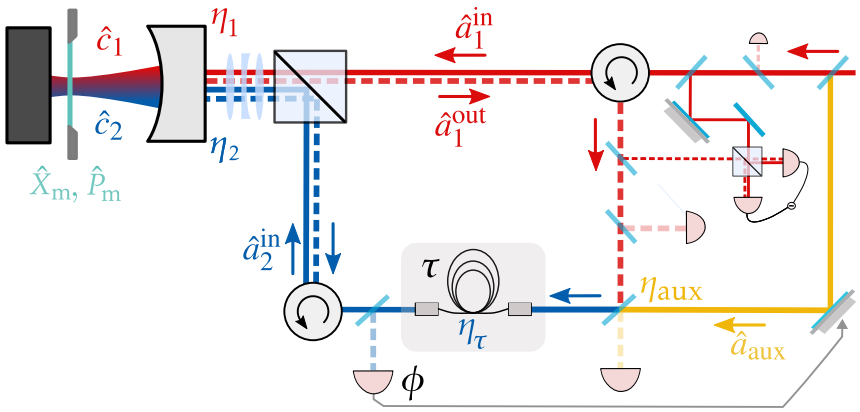

FIGURE 2.8: Optical path sketch of double pass feedback scheme including optical losses along the propagation path of the light

Optical losses along the path, as illustrated in Fig. 2.8, effectively result in a rescaling of the physical fields. For the first ingoing field, the imperfect cavity incoupling η_1 entails a rescaling of the physical mode $\hat{a}_1'^{\mathrm{in}}(t)$, the vacuum noise $\hat{v}_1(t)$ due to the loss channel:

$$\hat{a}_1^{\mathrm{in}}(t) = \sqrt{\eta_1}\hat{a}_1'^{\mathrm{in}}(t) + \sqrt{1-\eta_1}\,\hat{v}_1(t). \tag{2.33}$$

The effective outgoing mode after the first interaction can now be written

$$\hat{a}_1'^{\mathrm{out}}(t) = \hat{a}_1'^{\mathrm{in}}(t) + \sqrt{\eta_1 \kappa}\hat{c}_1(t). \tag{2.34}$$

For the second ingoing mode we have to consider the unavoidable losses at the beamsplitter that combines $\hat{a}_1^{\mathrm{out}}$ and $\hat{a}_{\mathrm{aux}}$, denoted η_{aux}, the losses that are common to the

propagation of the combined beams,among others in the fiber, η_τ and the coupling of the second mode into the cavity η_2. The second ingoing mode is then reexpressed as

$$\begin{aligned}\hat{a}_2^{\text{in}}(t) &= \sqrt{\eta_2\eta_\tau\eta_{\text{aux}}}\mathrm{e}^{\mathrm{i}\varphi}\hat{a}_1'^{\text{out}}(t-\tau) + \sqrt{\eta_2\eta_\tau(1-\eta_{\text{aux}})}\hat{a}'_{\text{aux}}(t-\tau) + \sqrt{1-\eta_2\eta_\tau}\hat{v}_2(t)\\ &= \sqrt{\eta_2\eta_\tau\eta_{\text{aux}}}\mathrm{e}^{\mathrm{i}\varphi}\hat{a}_1'^{\text{in}}(t-\tau) + \sqrt{\eta_1\eta_2\eta_\tau\eta_{\text{aux}}\kappa}\mathrm{e}^{\mathrm{i}\varphi}\hat{c}_1(t-\tau)\\ &\quad + \sqrt{\eta_2\eta_\tau(1-\eta_{\text{aux}})}\hat{a}'_{\text{aux}}(t-\tau) + \sqrt{1-\eta_2\eta_\tau}\hat{v}_2(t),\end{aligned} \tag{2.35}$$

where $\hat{v}_2(t)$ encompasses the noise term due to losses during the second pass. The second mode is effectively composed of a combination of the physical input field $\hat{a}_1'^{\text{in}}(t)$, which is a sum of differently scaled noise terms. For convenience, we can summarize the entire loop losses in

$$\eta = \eta_1\eta_2\eta_\tau\eta_{\text{aux}}. \tag{2.36}$$

This allows us to define an effective auxiliary mode

$$\begin{aligned}\hat{a}_{\text{aux}}(t) =& \sqrt{\frac{\eta_2\eta_\tau(1-\eta_{\text{aux}})}{1-\eta}}\hat{a}'_{\text{aux}}(t-\tau) + \sqrt{\frac{1-\eta_2\eta_\tau}{1-\eta}}\hat{v}_2(t)\\ &+ \sqrt{\frac{(1-\eta_1)\eta_2\eta_{\text{aux}}}{1-\eta}}\,e^{i\varphi}\left[\sqrt{1-\eta_1}\hat{a}_1'^{\text{in}}(t-\tau) - \sqrt{\eta_1}\hat{v}_1(t-\tau)\right],\end{aligned} \tag{2.37}$$

which encodes a fraction of the time-delayed ingoing field. We note that a finite cavity incoupling $\eta_1 \neq 1$ implies $\hat{a}_{\text{aux}}(t) \neq 0$ even without adding any explicit auxiliary field $\hat{a}'_{\text{aux}}(t-\tau) = 0$.

The rescaling established for the auxiliary mode allows us to bring the expression for the second ingoing mode into the compact form

$$\hat{a}_2^{\text{in}}(t) = \sqrt{\eta}\mathrm{e}^{\mathrm{i}\varphi}\left[\sqrt{\kappa}\hat{c}_1(t-\tau) + a_1^{\text{in}}(t-\tau)\right] + \sqrt{1-\eta}\hat{a}_{\text{aux}}(t), \tag{2.38}$$

and the average displacement of the auxiliary modes becomes

$$\alpha_{\text{aux}} = (1-\eta_1)\sqrt{\frac{\eta_2\eta_\tau\eta_{\text{aux}}}{1-\eta}}\alpha_1'^{\text{in}} + \sqrt{\frac{\eta_2\eta_\tau(1-\eta_{\text{aux}})}{1-\eta}}\alpha'_{\text{aux}}. \tag{2.39}$$

In the ideal scenario, where all potentially avoidable optical losses are zero ($\eta_1 = \eta_2 = \eta_\tau = 1$), rescaling of the auxiliary field only causes a time translation of the quantum field: $\hat{a}_{\text{aux}}(t) = \hat{a}'_{\text{aux}}(t-\tau)$. Consequently, for the average fields, we have $\alpha_{\text{aux}} = \alpha'_{\text{aux}}$, as expected.

2.4.4 Power Spectral Densities

In the previous sections we have dealt with the dynamics of the cavity fields and the mechanical quadratures. To obtain the steady-state phonon occupation number of the mechanical mode, it is useful to calculate the power spectral densities, as described in

Sec. 1.5. The power spectral density of the optical feedback term is defined by the relation

$$\delta(\omega+\omega')S_{\mathrm{fb}}(\omega) = \langle\hat{\xi}_{\mathrm{fb}}(\omega)\hat{\xi}_{\mathrm{fb}}(\omega')\rangle. \tag{2.40}$$

Using the definition for $\hat{\xi}_{\mathrm{fb}}(\omega)$ given in Eq. (2.24), we obtain

$$\begin{aligned} S_{\mathrm{fb}}(\omega) = \kappa&\frac{(g_1^2+g_2^2)}{(\kappa/2)^2+(\Delta+\omega)^2} \\ &+ 2g_1g_2\sqrt{\eta}\kappa\frac{[(\Delta+\omega)^2-(\kappa/2)^2]\cos(\varphi+\omega\tau)+\kappa(\Delta+\omega)\sin(\varphi+\omega\tau)]}{[(\kappa/2)^2+(\Delta+\omega)^2]^2}. \end{aligned} \tag{2.41}$$

The expression above describes the various noise contributions of the light in our feedback scheme and illustrates that the power spectral density of the optical force has two contributions: The first term describes the backaction of the optical force of both cavity fields separately, while the second term is associated with the interference generated by the coherent feedback. Since this interference term can have a positive or negative sign, it can increase or decrease the total optical backaction noise acting on the mechanical oscillator. In fact, the backaction term can be maximally reduced when $\varphi+\Omega_{\mathrm{m}}\tau = N2\pi$, with N an integer. This condition is fulfilled, for example for $\varphi=\tau=0$, or for any other value where $\Omega_{\mathrm{m}}\tau=-\varphi$.

The symmetric part of the force noise term $\bar{S}_{\mathrm{fb}}(\omega) = [S_{\mathrm{fb}}(\omega)+S_{\mathrm{fb}}(-\omega)]/2$ can be associated with the classical noise term responsible for the random perturbation force associated with backaction heating. On the other hand, the anti-symmetric part of the quantum noise $[S_{\mathrm{fb}}(\omega)-S_{\mathrm{fb}}(-\omega)]/2$ can be associated with the corresponding damping rate [5, 114]. The detailed balance between the positive and negative frequency terms can be used to extract an effective temperature, thanks to the fluctuation-dissipation theorem. In analogy to the thermal environment, the coupling to the optical field opens up a channel to an environment bath with that effective temperature. This point of view can be highly useful in understanding the opportunities for laser cooling of mechanical oscillators including coherent feedback. Furthermore, the Hamiltonian description in Sec. 2.7 provides a convenient framework for describing the possibilities for backaction cancellation provided by our platform.

Mechanical displacement PSD Considering a high quality mechanical oscillator, we can use the damping and frequency shift evaluated at the mechanical frequency and make the approximations $\Omega_{\mathrm{m}} \gg \delta\Omega_{\mathrm{m}}, \Gamma_{\mathrm{m}}$ and $\Omega_{\mathrm{m}}(\Omega_{\mathrm{m}}+\delta\Omega_{\mathrm{m}}) \approx (\Omega_{\mathrm{m}}+\delta\Omega_{\mathrm{m}})^2$, such that from Eq. (2.23) we obtain the equation for the damped harmonic oscillator

$$\begin{aligned} -\omega^2\hat{X}_{\mathrm{m}}(\omega) = &-(\Omega_{\mathrm{m}}+\delta\Omega_{\mathrm{m}})^2\hat{X}_{\mathrm{m}}(\omega)+\mathrm{i}\omega(\Gamma_{\mathrm{m}}+\gamma_{\mathrm{m}})\hat{X}_{\mathrm{m}}(\omega) \\ &+\Omega_{\mathrm{m}}\sqrt{2}\hat{\xi}_{\mathrm{th}}(\omega)+\Omega_{\mathrm{m}}\sqrt{2}\hat{\xi}_{\mathrm{fb}}(\omega), \end{aligned} \tag{2.42}$$

which can be directly related to the power spectral density

$$S_{X_{\mathrm{m}}X_{\mathrm{m}}}(\omega) = \frac{2\Omega_{\mathrm{m}}^2}{|N|^2}\Big[S_{\mathrm{th}}(\omega)+S_{\mathrm{fb}}(\omega)\Big] \tag{2.43}$$

with the denominator

$$N = (\Omega_{\mathrm{m}}+\delta\Omega_{\mathrm{m}})^2 - \mathrm{i}\omega(\gamma_{\mathrm{m}}+\Gamma_{\mathrm{m}}) - \omega^2. \tag{2.44}$$

The power spectral density is strongly peaked around the mechanical resonance frequency, which is why we can evaluate both the thermal and feedback spectral density at $\omega = \pm\Omega_\mathrm{m}$, yielding

$$S_{X_\mathrm{m}X_\mathrm{m}}(\omega) = \frac{1}{2}\frac{S_\mathrm{th}(\Omega_\mathrm{m}) + S_\mathrm{fb}(\Omega_\mathrm{m})}{(\Omega_\mathrm{m} + \delta\Omega_\mathrm{m} - \omega)^2 + [(\gamma_\mathrm{m} + \Gamma_\mathrm{m})/2]^2} + \frac{1}{2}\frac{S_\mathrm{th}(-\Omega_\mathrm{m}) + S_\mathrm{fb}(-\Omega_\mathrm{m})}{(\Omega_\mathrm{m} + \delta\Omega_\mathrm{m} + \omega)^2 + [(\gamma_\mathrm{m} + \Gamma_\mathrm{m})/2]^2}. \tag{2.45}$$

Inserting the frequency shift and damping rate $\delta\Omega_\mathrm{m}$, Γ_m for the unresolved sideband regime as stated in Eq. (2.29), the power spectral density then explicitly results in

$$\begin{aligned} S_{X_\mathrm{m}X_\mathrm{m}}(\omega) = \frac{1}{|N|^2}\Bigg\{ & \frac{\gamma_\mathrm{m}}{2}\left[(\bar{n}_\mathrm{th}+1)\left(\left(\frac{\gamma_\mathrm{m}}{2}\right)^2 + (\omega+\Omega_\mathrm{m})^2\right) + \bar{n}_\mathrm{th}\left(\left(\frac{\gamma_\mathrm{m}}{2}\right)^2 + (\omega-\Omega_\mathrm{m})^2\right)\right] \\ & + \frac{\kappa}{2}\frac{\Omega_\mathrm{m}^2(g_1^2+g_2^2)}{(\kappa/2)^2 + (\omega+\Delta)^2} \\ & + g_1 g_2 \sqrt{\eta}\kappa\Omega_\mathrm{m}^2 \frac{[(\omega+\Delta)^2 - (\kappa/2)^2]\cos(\varphi+\omega\tau) + \kappa(\omega+\Delta)\sin(\varphi+\omega\tau)}{[(\kappa/2)^2 + (\omega+\Delta)^2]^2}\Bigg\}. \end{aligned} \tag{2.46}$$

The whole expression is multiplied by the denominator that also contains the feedback contribution

$$\begin{aligned} N(\omega,\Delta,\tau,\varphi) = & \Omega_\mathrm{m}^2 + \left(\frac{\gamma_\mathrm{m}}{2} - \mathrm{i}\omega\right)^2 + \frac{\Delta\Omega_\mathrm{m}(g_1^2+g_2^2)}{\Delta^2 + (\kappa/2 - \mathrm{i}\omega)^2} \\ & - \mathrm{e}^{\mathrm{i}\omega\tau} g_1 g_2 \sqrt{\eta}\kappa\Omega_\mathrm{m} \frac{2\Delta(\kappa/2 - \mathrm{i}\omega)\cos(\varphi) - \left[\Delta^2 - (\kappa/2 - \mathrm{i}\omega)^2\right]\sin(\varphi)}{[\Delta^2 + (\kappa/2 - \mathrm{i}\omega)^2]^2}. \end{aligned} \tag{2.47}$$

2.4.5 Phonon Occupation Number

The phonon number of a specific mechanical mode is obtained via the integration over both the position and momentum power spectral densities [44]

$$2\bar{n}_\mathrm{m} + 1 = \int_{-\infty}^{\infty} [S_{X_\mathrm{m}X_\mathrm{m}}(\omega) + S_{P_\mathrm{m}P_\mathrm{m}}(\omega)]\frac{d\omega}{2\pi} \simeq 2\int_{-\infty}^{\infty} S_{X_\mathrm{m}X_\mathrm{m}}(\omega)\frac{d\omega}{2\pi}, \tag{2.48}$$

where we used the identity as stated in Eq. (1.59). Inserting the expression for the power spectral density of the mechanical displacement [cf. Eq. (2.45)] into the above expression yields

$$\bar{n}_\mathrm{m} = \frac{1}{2}\frac{1}{\gamma_\mathrm{m} + \Gamma_\mathrm{m}}\bar{S}_\mathrm{th}(\Omega_\mathrm{m}) + \frac{1}{2}\frac{1}{\gamma_\mathrm{m} + \Gamma_\mathrm{m}}\bar{S}_\mathrm{fb}(\Omega_\mathrm{m}) - \frac{1}{2}. \tag{2.49}$$

The complete explicit expression for the mechanical occupation number is given in App. 15. To meet the quantum limit of cooling, we require large quantum cooperativity, i.e. $C_\mathrm{qu} \gg 1$, which means that we have a large optical damping $\Gamma_\mathrm{m} \gg \gamma_\mathrm{m}$. In the unresolved sideband regime, the phonon occupation number then results in

$$\bar{n}_\mathrm{m} = \frac{\kappa}{\Gamma_\mathrm{m}}\frac{(g_1^2+g_2^2)}{(\kappa/2)^2 + \Delta^2} + \frac{1}{2}\frac{\cos(\Omega_\mathrm{m}\tau)}{\sin(\Omega_\mathrm{m}\tau)}\frac{\kappa\Delta\sin(\varphi) + [\Delta^2 - (\kappa/2)^2]\cos(\varphi)}{\kappa\Delta\cos(\varphi) - [\Delta^2 - (\kappa/2)^2]\sin(\varphi)} - \frac{1}{2}, \tag{2.50}$$

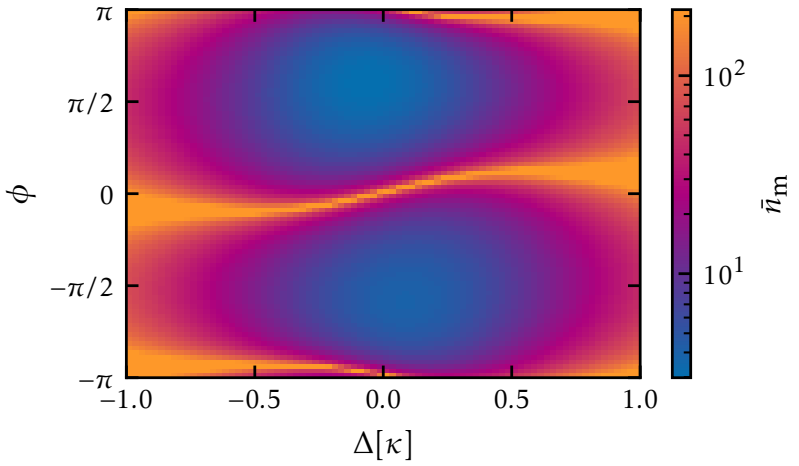

FIGURE 2.9: Expected membrane occupation number $\bar{n}_\mathrm{m}$ for different phases ϕ and detunings Δ of the coherent feedback loop, with the standard experimental settings.

which is plotted in Fig. 2.9. In the case of zero detuning $\Delta = 0$ the phonon limit becomes

$$\bar{n}_\mathrm{m} = \frac{4}{\kappa\Gamma_\mathrm{m}}\left[g_1^2 + g_2^2 - 2\sqrt{\eta}g_1 g_2 \cos(\Omega_\mathrm{m}\tau - \varphi)\right]. \tag{2.51}$$

To determine the optimal cooling parameter in this regime of strong cooling $\Gamma_\mathrm{m} \gg \gamma_\mathrm{m}$, we can maximize the damping rate Γ_m as given in Eq. (2.29) with respect to the feedback parameters φ and τ. The optimal delay is determined as $\tau = \pi/(2\Omega_\mathrm{m})$, and the phase $\varphi = \Omega_\mathrm{m}\tau$, such that the maximal damping turns out to be

$$\Gamma_\mathrm{m}^\mathrm{max} = \frac{\kappa g_1 g_2 \sqrt{\eta}}{(\kappa/2)^2 + \Delta^2}. \tag{2.52}$$

It is worth noting that a detuning $\Delta \neq 0$ is not advantageous for maximizing Γ_m. It is thus not surprising that we obtain the same parameters maximizing the damping considering solely the simplified expressions in Eq. (2.30) that include already the assumption $\Delta = 0$. Inserting the maximal damping and the corresponding optimal values $\varphi = \Omega_\mathrm{m}\tau = \pi/2$ into the expression for the phonon number in Eq. (2.51) we obtain

$$\bar{n}_\mathrm{m} = \frac{g_1^2 + g_2^2}{4\sqrt{\eta}g_1 g_2} - \frac{1}{2} = \frac{(g_1 - g_2)^2 + 2g_1 g_2(1 - \sqrt{\eta})}{4g_1 g_2\sqrt{\eta}} \geq \frac{1 - \sqrt{\eta}}{2\sqrt{\eta}} \quad (\text{for } C_\mathrm{qu} \gg 1). \tag{2.53}$$

The equality, and thus the minimal value, is achieved for $g_1 = g_2$. The expression shows that the coherent feedback loop enables ground state cooling, under the assumption of a large quantum cooperativity $C_\mathrm{qu} \gg 1$, and thus strong cooling. Taking optical losses into account, the scheme is quite robust, requiring a loop efficiency of only $\eta > 0.12$ for reaching $\bar{n}_\mathrm{m} = 1$.

Furthermore, we examine in more detail the consequences of the condition that $g_1 = g_2$ determined for optimal cooling above. This boils down to solving $|\alpha_1|^2 = |\alpha_2|^2$ for the average intracavity field displacements as written in Eq. (2.16). If we assume a high efficiency ($\eta \to 1$) the mentioned condition is fulfilled for $\sqrt{1-\eta}\alpha_\mathrm{aux} = 2\cos\phi\alpha_1^\mathrm{in}$. We

note that, in that case $g_1 = g_2$ is also fulfilled for $\alpha_{\text{aux}} = 0$. However, this requires $\varphi = \pi$, resulting in the damping $\Gamma_{\text{m}} = 0$, such that the coherent feedback does not provide any cooling advantage.

Furthermore, in principle we aim for a high loop efficiency $\eta \to 1$, which can be achieved for efficient cavity couplings η_1 and η_2 and low propagation losses η_τ. However, the loop efficiency η can never be truly unity due to the beamsplitter ratio $\eta_{\text{aux}} \neq 1$ required to combine the auxiliary local oscillator. As we can always choose a sufficiently high efficiency for this beamsplitter such that other loop losses dominate, it does not represent a limitation for our scheme, but might require large optical powers in the auxiliary local oscillator arm.

Taking into account losses, the relation between the coherent amplitudes of the ingoing and auxiliary field for a specific experimental phase ϕ is given by

$$\alpha_{\text{aux}} = \alpha_1^{\text{in}} \frac{\sqrt{\eta}\cos(\phi) \pm \sqrt{1-\eta\sin(\phi)^2}}{\sqrt{1-\eta}}, \tag{2.54}$$

and can be adjusted via the ingoing light powers P_{in} and P_{aux} .

2.4.6 Sideband Picture

To provide a more intuitive understanding of the working principle of the coherent feedback loop, we will resort to the sideband picture that already allowed us to describe the standard optomechanical interaction and the effect of a cavity detuning. Here we recall that it is the imbalance between the Stokes and anti-Stokes processes that generates either a cooling or an amplifying process. For a cavity optomechanical system this can be implemented via a finite cavity detuning, altering the final density of states for the scattering photons, and thus influencing their transition probabilities into the respective mechanical sidebands. Here we examine the influence of the coherent feedback loop on

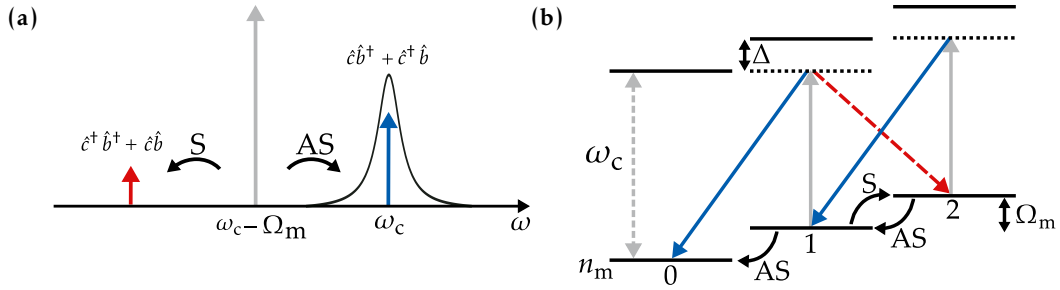

FIGURE 2.10: Sketch of the optomechanical sideband scattering with a red-detuned beam. **(a)**: Sketch illustrating the transitions for a red-detuned cavity drive, where the cavity is enhancing the AS transitions to the blue sideband, leading to a depletion of the mechanical excitations. **(b)**: The level scheme of a cavity driven with a red-detuned beam (gray) $\Delta < 0$, favouring the AS scattering (blue) over the S scattering(red), leading to cooling.

the cavity sidebands. For this, we start from the ingoing light fields of the feedback loop in frequency space, $\hat{a}_1^{\text{in}}(\omega)$ and

$$\hat{a}_2^{\text{in}}(\omega) = \sqrt{\eta}e^{i\omega\tau}e^{i\varphi}\left[\hat{a}_1^{\text{in}}(\omega) + \sqrt{\kappa}\hat{c}_1(\omega)\right] + \sqrt{1-\eta}\hat{a}_{\text{aux}}(\omega). \tag{2.55}$$

From the expression of the mechanical displacement operator, as stated in Eq. (2.18) we obtain

$$\begin{aligned}\frac{1}{\chi_{\mathrm{m}}(\omega)}\hat{X}_{\mathrm{m}}(\omega) = \text{thermal} + \text{auxiliary} \\ + \sqrt{2\kappa}\chi_{\mathrm{c}}(\omega)\hat{a}_1^{\mathrm{in}}(\omega)\Big(g_1 + g_2\sqrt{\eta}\mathrm{e}^{\mathrm{i}\omega\tau}\mathrm{e}^{\mathrm{i}\varphi}\Big[1-\kappa\chi_{\mathrm{c}}(\omega)\Big]\Big) \\ + \sqrt{2\kappa}\chi_{\mathrm{c}}^*(-\omega)\hat{a}_1^{\mathrm{in}}(-\omega)^\dagger\Big(g_1 + g_2\sqrt{\eta}\mathrm{e}^{\mathrm{i}\omega\tau}\mathrm{e}^{-\mathrm{i}\varphi}\Big[1-\kappa\chi_{\mathrm{c}}^*(-\omega)\Big]\Big),\end{aligned} \tag{2.56}$$

where for now we only consider the driving from the optical input field, and neglect the contributions from the thermal noise and the auxiliary field.

The situation of the standard cavity dynamical backaction, which can be achieved by setting $g_2 = 0$ such that $g = g_1$, $\hat{a}_{\mathrm{in}} = \hat{a}_1^{\mathrm{in}}$ and $\hat{c} = \hat{c}_1$, we obtain

$$\frac{1}{\chi_{\mathrm{m}}(\omega)}\hat{X}_{\mathrm{m}}(\omega) = \sqrt{2}\hat{\xi}_{\mathrm{th}}(\omega) + \sqrt{2\kappa}g\Big[\chi_{\mathrm{c}}(\omega)\hat{a}_{\mathrm{in}}(\omega) + \chi_{\mathrm{c}}^*(-\omega)\hat{a}_{\mathrm{in}}(-\omega)^\dagger\Big]. \tag{2.57}$$

For the coherent scheme, in the unresolved sideband regime, with $\chi_{\mathrm{c}}(\omega) \approx 2/\kappa$, $\chi_{\mathrm{c}}^*(-\omega) - \chi_{\mathrm{c}}(\omega) = 0$, and $g_2 = g_2^*$, we obtain the following expression

$$\begin{aligned}\frac{1}{\chi_{\mathrm{m}}(\omega)}\hat{X}_{\mathrm{m}}(\omega) = \text{thermal} + \text{auxiliary} \\ + \sqrt{2}\hat{a}_1^{\mathrm{in}}(\omega)\Big(\sqrt{\Gamma_1} - \sqrt{\Gamma_2}\mathrm{e}^{\mathrm{i}\omega\tau}\mathrm{e}^{\mathrm{i}\varphi}\Big) + \sqrt{2}\hat{a}_1^{\mathrm{in}}(-\omega)^\dagger\Big(\sqrt{\Gamma_1} - \sqrt{\Gamma_2}\mathrm{e}^{\mathrm{i}\omega\tau}\mathrm{e}^{-\mathrm{i}\varphi}\Big),\end{aligned} \tag{2.58}$$

with the measurement rates $\Gamma_1 = 4g_1^2/\kappa$ and $\Gamma_2 = 4\eta g_2^2/\kappa$. The comparison between the

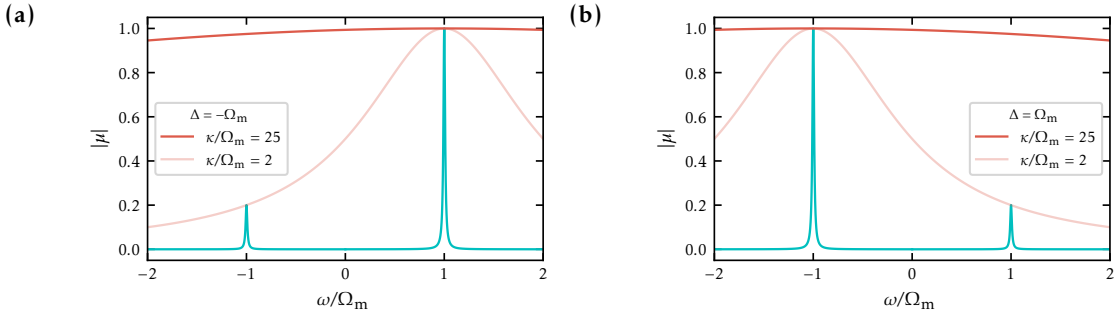

FIGURE 2.11: The sideband amplitudes on the light, in the case of dynamical backaction cooling by the cavity for different sideband resolution factors and **(a)** negative detuning and **(b)** positive detuning.

equation of motion resulting from coherent feedback and dynamical backaction cooling can thus be done via general prefactors of the equation written under the form

$$\frac{1}{\chi_{\mathrm{m}}(\omega)}\hat{X}_{\mathrm{m}}(\omega) = \text{thermal} + \sqrt{2\Gamma}\Big[\mu\hat{a}_{\mathrm{in}}(\omega) + \nu\hat{a}_{\mathrm{in}}(-\omega)^\dagger\Big]. \tag{2.59}$$

For dynamical backaction cooling we can identify

$$\Gamma = \frac{g^2}{\kappa}, \quad \mu = \kappa\chi_c(\omega), \quad \nu = \kappa\chi_c^*(-\omega). \tag{2.60}$$

For feedback cooling, we find the parameters

$$\Gamma = \Gamma_1, \quad \mu = 1 - \frac{\sqrt{\Gamma_2}}{\sqrt{\Gamma_1}} e^{i\omega\tau} e^{i\varphi}, \quad \nu = 1 - \frac{\sqrt{\Gamma_2}}{\sqrt{\Gamma_1}} e^{i\omega\tau} e^{-i\varphi}. \tag{2.61}$$

The sideband scattering rates for the coherent feedback scheme then become [44]

$$A_\pm = \Gamma\,|\mu(\mp\Omega_m)|^2 = 2\left(\sqrt{\Gamma_1\Gamma_2}\Big[\cos(\varphi)\cos(\Omega_m\tau) \pm \sin(\varphi)\sin(\Omega_m\tau)\Big] - \Gamma_1\right), \tag{2.62}$$

Here, the rate A_+ describes the Stokes process where the mechanical oscillator undergoes an amplification process from n to $n+1$, resulting in a red-shifted photon at $-\Omega_m$. In turn, A_- describes the anti-Stokes process associated with cooling, where the phonon state changes from n to $n-1$, and results in the emission of a blue detuned photon at $+\Omega_m$, as sketched in Fig. 2.10. The expected damping and frequency shift are

$$\begin{aligned} \Gamma_m &= 2\Gamma\,\mathrm{Re}[\mu - \nu] = \Gamma_- - \Gamma_+, \\ \delta\Omega_m &= \Gamma\,\mathrm{Im}[\mu - \nu], \end{aligned} \tag{2.63}$$

where we used the identities $|\mu|^2 = 2\mathrm{Re}[\mu]$, and

$$\mu - \nu = 2\sqrt{\Gamma_2}/\sqrt{\Gamma_1}\sin\varphi\Big[i\cos(\omega\tau) - \sin(\omega\tau)\Big]. \tag{2.64}$$

The effective damping rate is given by the difference between the cooling and the heating rates. Also the expressions obtained for the damping and frequency shift generated by our coherent feedback coincide with the expressions derived from the Langevin equations in Eq. (2.30). The sideband amplitudes $|\mu(\omega)|$ are plotted for standard dynamical backaction in Fig. 2.11 and our coherent feedback scheme in Fig. 2.12 and help to visualize the relation between the sideband scattering rates.

In terms of the scattering rates, the phonon occupation evolves as [44]

$$\partial_t \bar{n}_m = (\bar{n}_m + 1)(\Gamma_+ + \bar{n}_{th}\gamma_m) - \bar{n}_m\Big[\Gamma_- + (\bar{n}_{th} + 1)\gamma_m\Big], \tag{2.65}$$

with the thermal occupation $\bar{n}_{th}$, and leads to the phonon number of the mechanical oscillator

$$\bar{n}_m = \frac{\bar{n}_{th}\gamma_m + A_+}{\gamma_m + A_- - A_+}. \tag{2.66}$$

For negligible coupling to the thermal bath $\gamma_m \to 0$, or for a low environment temperature $T \to 0$, this leads to a minimal achievable occupation number

$$\bar{n}_m = \frac{A_+}{A_- - A_+} \geq \frac{1 - \sqrt{\eta}}{2\sqrt{\eta}}. \tag{2.67}$$

The last equality illustrates how the mechanical occupation number is determined by the suppression of the Stokes heating process A_+ by the damping rate $A_- - A_+$. The sideband

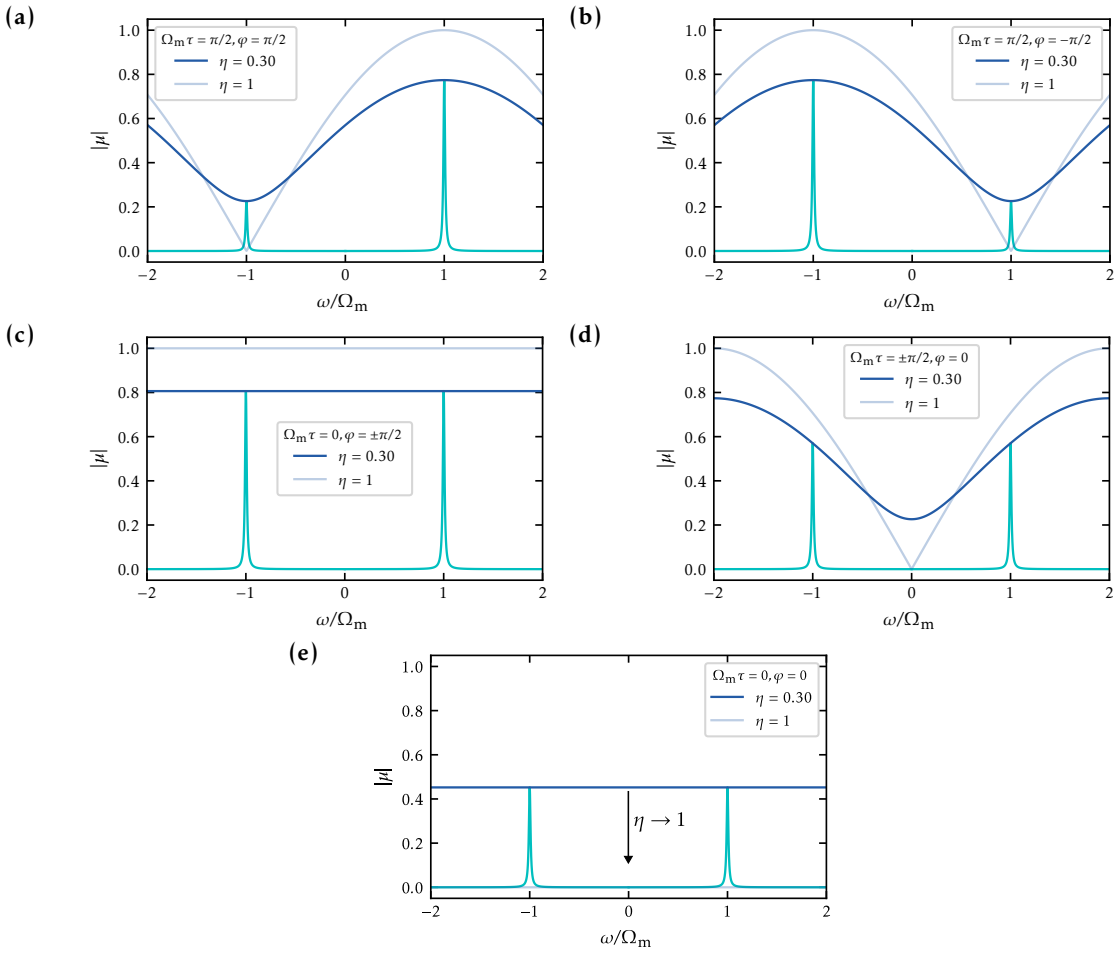

FIGURE 2.12: The sideband amplitudes on the light, realized in the case of coherent feedback for $\Delta = 0$ and feedback parameters that generate a sideband asymmetry **(a)** and **(b)**, that leave a symmetric sideband spectrum **(c)** and **(d)**, and that generate a backaction cancellation where both sideband amplitudes go to zero for a perfect efficiency **(e)**.

picture yields the same lower bound for the mechanical occupation number as previously determined by the integration of the power spectral densities in Eq. (2.53). Moreover, we observe that in the regime of large quantum cooperativity $C_{qu} \gg 1$ and ideal settings for cooling $\Omega_m\tau = \varphi = \pi/2$, $g_1 = g_2$ the feedback scheme is only limited by the achievable loop efficiency η.

Alternatively, the mechanical damping rate can be directly determined from the optical force noise power spectral density of the fluctuating radiation-pressure force [5, 44]. In fact, the scattering rates can be calculated from the quantum noise spectrum $A^{\pm} = S_{fb}(\mp\Omega_m)$. The spectral density of the feedback noise as stated in Eq. (2.41) simplifies for a resonant cavity in the unresolved sideband regime to

$$S_{fb}(\omega) = \frac{8}{\kappa}\left[\frac{g_1^2 + g_2^2}{2} - \sqrt{\eta}g_1 g_2 \cos(\varphi + \omega\tau)\right]. \tag{2.68}$$

The force spectrum can be asymmetric for the sidebands at $\pm\Omega_m$. It is exactly this asymmetry that describes an unbalance between the Stokes and the anti-Stokes processes

($A_- < A_+$) and thus a damping effect. For dynamical backaction cooling, the suppression of either one of the sidebands can be generated by driving the optical cavity with detuned light [44, 5].

For the coherent feedback it is the interference of the optical force between the first and the second interaction that leads to a frequency dependent modulation of optical noise force $S_{\mathrm{fb}}(\omega)$, which can lead to a modification of both its symmetric part linked to backaction heating, or its antisymmetric part related to damping.

Figures 2.11 and 2.12 illustrate the sideband spectra for dynamical backaction and coherent feedback with different loop parameters. Regarding dynamical backaction, the difference in sideband amplitudes is determined by the detuning and linewidth of the cavity relative to the mechanical frequency. A low sideband resolution factor results in weak suppression of the Stokes process, hinting already at the limitations for ground-state cooling further demonstrated in the next section. For coherent feedback, we confirm that the previously obtained ideal parameters for cooling $\Omega_{\mathrm{m}}\tau = \pi/2 = \varphi$ effectively suppress the heating sideband. Conversely, when the phase φ has the opposite sign compared to the delay τ, it implements amplification. The achieved sideband imbalance is solely limited by the loop efficiency. When the delay and phase differ by $\pi/2$, both sidebands are equally affected by the feedback and no particular process is favoured.

In case where the delay and loop phase are both integer multiples of 2π, both sidebands are suppressed up to the loop efficency, resulting in backaction cancellation. We note that the ideal loop phase for cooling thus differs from the parameters that maximize the backaction cancellation. Hence backaction cancellation cannot directly support the cooling effect.

2.4.7 Dynamical Backaction Cooling

With no external coherent feedback $\eta = 0$, the optomechanical interaction results in the well-known dynamical backaction. This can be interpreted as a type of coherent feedback scheme, where the cavity acts as the feedback controller [44]. The detuning parameter serves as the control knob for regulating the phase relationship between intracavity field quadratures, actuating the dynamical backaction feedback on the mechanical displacement. In the unresolved sideband regime $\Omega_{\mathrm{m}} \ll \kappa$, Eqs. (2.29) reduce to the well known results for dynamical backaction in the presence of a finite cavity-light detuning $\Delta \neq 0$, and result in a modifications of the mechanical susceptibility as

$$\delta\Omega_{\mathrm{m}} = \frac{2\Delta(g_1^2 + g_2^2)}{\Delta^2 + (\kappa/2)^2}, \qquad \Gamma_{\mathrm{m}} = -4\frac{\Delta\kappa\Omega_{\mathrm{m}}(g_1^2 + g_2^2)}{\left[\Delta^2 + (\kappa/2)^2\right]^2}. \tag{2.69}$$

We observe that both the frequency shift $\delta\Omega_{\mathrm{m}}$ and damping rate Γ_{m} disappear for $\Delta = 0$, which is illustrated and compared to the coherent feedback case in Fig. 2.13. Furthermore the damping is maximal for a detuning $\Delta \approx -\kappa/(2\sqrt{3})$.

For a large optical damping $\Gamma_{\mathrm{m}} \gg \gamma_{\mathrm{m}}$, where the cooling quantum limit can be reached, the phonon occupation as stated in Eq. (2.50) becomes independent of the ingoing light power, and yields

$$\bar{n}_{\mathrm{m}} = \frac{\Delta^2 + (\kappa/2)^2}{4|\Delta|\Omega_{\mathrm{m}}} - \frac{1}{2}. \tag{2.70}$$

where we assumed a negative detuning for cooling $\Delta < 0$. In the sideband unresolved regime, the minimal achievable phonon number is obtained for $\Delta = -\kappa/2$ and results in

$$\bar{n}_{\mathrm{min}} = \frac{\kappa}{4\Omega_{\mathrm{m}}} \gg 1, \tag{2.71}$$

where we neglected the factor 1/2 as it is negligible for $\bar{n}_{\mathrm{min}} \gg 1$. This expression clearly shows that dynamical backaction cooling alone does not allow to produce ground-state cooling $\bar{n}_{\mathrm{m}} < 1$.

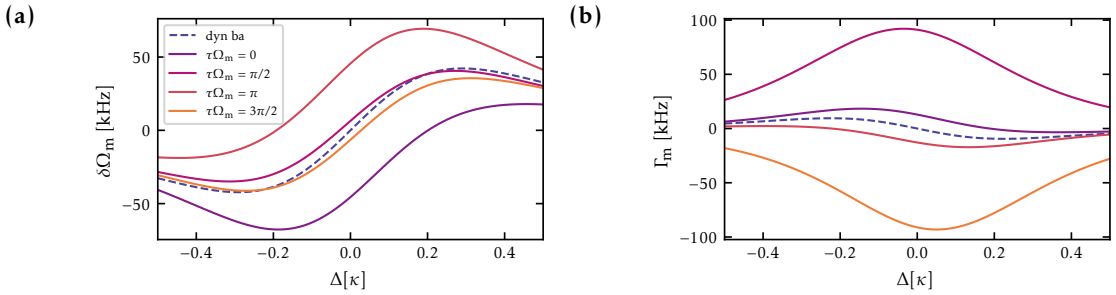

FIGURE 2.13: Comparing **(a)** the expected frequency shift $\delta\Omega_{\mathrm{m}}$ and **(b)** the damping rate Γ_{m} between dynamical backaction and coherent feedback with phase $\varphi = \pi/2$ and various delays τ, scanning the cavity detuning Δ for standard experimental settings.

For comparison, in the resolved sideband regime with $\Omega_{\mathrm{m}} \gg \kappa$, for a negative detuning $\Delta < 0$, the phonon occupation results in [44]

$$\bar{n}_{\mathrm{m}} = \frac{(\kappa/2)^2 + (\Delta + \Omega_{\mathrm{m}})^2}{4|\Delta|\Omega_{\mathrm{m}}}, \tag{2.72}$$

which results in the minimal occupation number achievable for $\Delta = -\Omega_{\mathrm{m}}$

$$\bar{n}_{\mathrm{min}} = \left(\frac{\kappa}{4\Omega_{\mathrm{m}}}\right)^2 < 1, \tag{2.73}$$

and thus enables ground state cooling.

Figure 2.14 compares the cooling processes generated by both the dynamical backaction, which requires a non-zero detuning, to the coherent feedback scheme, for which zero detuning is actually maximizing the cooling effect. This can be intuitively understood considering that the light measures the mechanical position most sensitively on resonance, and thus, the feedback based on the mechanical signal imprinted onto the light is also strongest in that situation. In contrast, dynamical backaction requires a certain cavity detuning to generate the correct delay and thus feed back the desired mechanical oscillator quadrature to itself.

Additionally, we can compare the cooling effect generated by either the coherent feedback and the dynamical cavity cooling, depending on the sideband resolution factor of the optomechanical cavity $\kappa/\Omega_{\mathrm{m}}$, as illustrated in Fig. 2.14. However, to make a fair comparison, we have to consider different detunings Δ, as they not only influence dynamical backaction cooling, but also the coherent feedback through the loop phase φ, thereby affecting the cooling performances.

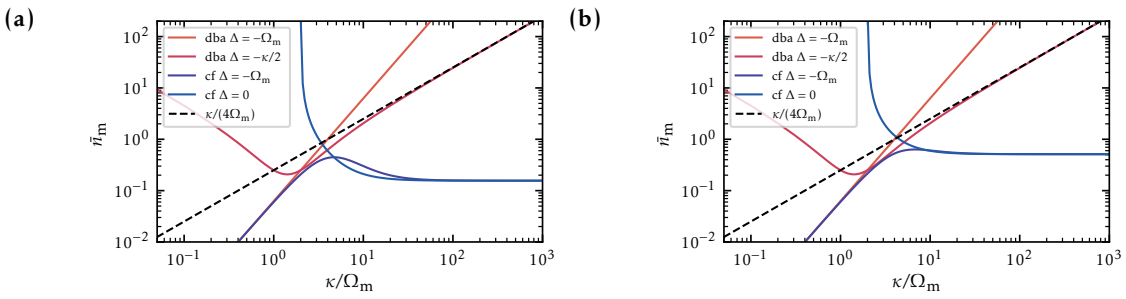

FIGURE 2.14: **(a)**: The mechanical occupation number, for both dynamical backaction cooling (dba) and coherent feedback (cf), for different sideband resolution ratios $\kappa/\Omega_{\mathrm{m}}$, plotted for different detunings, in the limit of large cooperativity and neglecting losses. **(b)**: Taking into account significant losses ($\eta_\tau = 0.5$), the cf cooling proves to be quite resistant to losses.

In the resolved sideband regime ($\kappa < \Omega_{\mathrm{m}}$), the best cooling performance for coherent feedback is achieved at a detuning of $\Delta = -\Omega_{\mathrm{m}}$. However, in this regime, dynamical backaction cooling provides an equally strong cooling effect, for the same detuning ($\Delta = -\Omega_{\mathrm{m}}$), where the cavity most efficiently selects the anti-Stokes process.

In the unresolved sideband regime, the best performance for dynamical backaction cooling is achieved at a detuning of $\Delta = -\kappa/2$. Coherent feedback largely outperforms this cooling technique and is the preferable cooling strategy. There is a certain range of resolution factors where coherent feedback is preferably used on resonance. For larger resolution ratios ($\kappa \gg \Omega_{\mathrm{m}}$), the detuning becomes less important. In fact, if the cavity is much faster than the dynamics of the mechanical oscillator, the effect of the cavity delay becomes insignificant, and the feedback can be described as acting directly on the mechanical oscillator.

2.5 Measurement-Based Cooling

To provide context for the coherent feedback technique in relation to previously employed feedback schemes for cooling a mechanical oscillator, we consider measurement-based feedback schemes, that have been used for ground state-cooling [105, 9, 107]. In fact, the high read-out sensitivity built into optomechanical cavities promotes the idea that active feedback based on the result of the measurement of a mechanical oscillator can be used for cooling, known as cold damping [44].

The feedback force is based on an estimation of the mechanical displacement, which electronic processing then transforms into a signal proportional to the derivative of the estimated displacement. For the optomechanical interaction, the feedback force can be implemented via actuation on the amplitude quadrature of the ingoing light beam.

In comparison to our feedback scheme, the all-optical loop is now replaced by an optoelectronic loop, and our feedback interaction with the second cavity mode in the equation of motion of the mechanical momentum quadrature [cf. Eq. (2.18)] can now be replaced by the feedback force $F_{\mathrm{mf}} = (h * p_1^{\mathrm{est}})$, determined by the convolution of the estimated mechanical displacement detected via the phase quadrature of the light p_1^{est} and the feedback filter function h. We note that estimation of p_1^{est} is based on the measurement of p_1^{out} and thus depends on the quantum efficiency of the detector η_{det}. To use the quadrature estimation for cold damping, a standard derivative high-pass spectral filter

function must be applied

$$h(\omega) = -\mathrm{i}\frac{g_{\mathrm{mf}}\,\omega}{1-\mathrm{i}\omega/\omega_{\mathrm{mf}}}, \tag{2.74}$$

with the bandwidth ω_{mf} and feedback gain g_{mf} [128]. For a large bandwidth $\omega_{\mathrm{mf}} \gg \omega \approx \Omega_{\mathrm{m}}$ the argument of the filter function approaches $-\pi/2$, such that the feedback force becomes proportional to the momentum and provides a viscous force that dampens the mechanical motion. In the ideal scenario, where the value of $\omega_{\mathrm{mf}}^{-1}$, representing the delay in the feedback loop, tends towards zero, the feedback realizes an ideal derivative.

Similar to the coherent feedback scheme, the measurement-based feedback introduces a modification of the effective mechanical susceptibility, introducing an additional damping and frequency shift. In the limit that $\omega_{\mathrm{mf}}, \kappa \gg \Omega_{\mathrm{m}}$, where the delay of the feedback loop and the cavity response are negligible, the resulting noise power spectral density of the modified mechanical motion leads the final mechanical occupation number

$$\bar{n}_{\mathrm{m}} = \frac{1-\sqrt{\eta}}{2\sqrt{\eta}}, \tag{2.75}$$

and is completely determined by the total efficiency η of the feedback loop. When comparing this limit to the coherent feedback limit found in Eq. (2.75), we observe that both ratios are analogous. The only distinction resides in that fact that here the efficiency η now depends not only on the losses during the propagation of the beam in the experiment, but also on the detector efficiency η_{det}, ultimately limiting the performance of this cooling scheme.

2.6 Outgoing Light Fields

In order to determine the outgoing fields at the end of the double pass experiment, we first recall the outgoing light field after the first interaction

$$\hat{a}_1^{\mathrm{out}}(\omega) = \hat{a}_1^{\mathrm{in}}(\omega) + \sqrt{\kappa}\hat{c}_1(\omega), \tag{2.76}$$

which leads to the ingoing field of the second pass

$$\hat{a}_2^{\mathrm{in}}(\omega) = \sqrt{\eta}\mathrm{e}^{\mathrm{i}\varphi}\mathrm{e}^{\mathrm{i}\omega\tau}\hat{a}_1^{\mathrm{out}}(\omega) + \sqrt{1-\eta}\hat{a}_{\mathrm{aux}}(\omega). \tag{2.77}$$

The outgoing light mode after the double pass interaction can analogously be written as

$$\hat{a}_2^{\mathrm{out}}(\omega) = \hat{a}_2^{\mathrm{in}}(\omega) + \sqrt{\kappa}\hat{c}_2(\omega). \tag{2.78}$$

For a coherent feedback scheme on resonance ($C_- = 0$), and in the broad cavity limit ($C_+ \approx 2/\kappa$) the outgoing light field can be expressed as

$$\hat{a}_2^{\mathrm{out}}(\omega) = \eta\mathrm{e}^{\mathrm{i}\omega\tau}\mathrm{e}^{\mathrm{i}\varphi}\hat{a}_1^{\mathrm{in}}(\omega) - \sqrt{1-\eta}\hat{a}_{\mathrm{aux}}(\omega) - \mathrm{i}\sqrt{2}\Big[\sqrt{\Gamma_2} - \sqrt{\eta\Gamma_1}\mathrm{e}^{\mathrm{i}\omega\tau}\mathrm{e}^{\mathrm{i}\varphi}\Big]\hat{X}_{\mathrm{m}}(\omega), \tag{2.79}$$

leading to the corresponding outgoing light quadratures

$$\begin{aligned}\hat{X}_2^{\mathrm{out}}(\omega) = \sqrt{\eta}\Big[&\cos(\omega\tau+\varphi)\hat{X}_{\mathrm{in}}(\omega) - \sin(\omega\tau+\varphi)\hat{P}_{\mathrm{in}}(\omega)\Big] \\ &- 2\sqrt{\eta\Gamma_1}\sin(\omega\tau+\varphi)\hat{X}_{\mathrm{m}}(\omega) \\ &- \sqrt{1-\eta}\hat{X}_{\mathrm{aux}}, \end{aligned} \tag{2.80}$$

$$\begin{aligned}\hat{P}_2^{\mathrm{out}}(\omega) = \sqrt{\eta}\Big[&\sin(\omega\tau+\varphi)\hat{X}_{\mathrm{in}}(\omega) + \cos(\omega\tau+\varphi)\hat{P}_{\mathrm{in}}(\omega)\Big] \\ &- 2\Big[\sqrt{\Gamma_2} - \sqrt{\eta\Gamma_1}\cos(\omega\tau+\varphi)\Big]\hat{X}_{\mathrm{m}}(\omega) \\ &- \sqrt{1-\eta}\hat{P}_{\mathrm{aux}}. \end{aligned} \tag{2.81}$$

From these last expressions we note that for the delay and phase fulfilling $\sin(\omega\tau+\varphi) = 0$ and $\cos(\omega\tau+\varphi) = 1$, the mechanical signal is eliminated from the outgoing light quadratures up to the balancing of both interaction (for $\Gamma_1 = \Gamma_2$) and the optical losses ($\eta \approx 1$). This requirement is for instance fulfilled for $\varphi = \tau = 0$ for all frequencies, or, considering the signals at the mechanical frequency, by $\Omega_{\mathrm{m}}\tau = -\varphi$. In this scenario, the coherent feedback loop is closed and establishes a coherent interaction between the two passes without any mechanical signal dissipated to the environment. Then, the simplified expression for the mechanical displacement reads

$$\begin{aligned}\hat{X}_{\mathrm{m}}(\omega) = \sqrt{2}\chi_{\mathrm{m}}(\omega)\Bigg\{&\hat{\xi}_{\mathrm{th}} + \sqrt{2(1-\eta)\Gamma_2}\hat{X}_{\mathrm{aux}}(\omega) \\ &+ \hat{X}_{\mathrm{in}}(\omega)\Big[\sqrt{2\Gamma_1} - \sqrt{2\eta\Gamma_2}\cos(\omega\tau+\varphi)\Big] + \hat{P}_{\mathrm{in}}(\omega)\sqrt{2\eta\Gamma_2}\sin(\omega\tau+\varphi)\Bigg\}, \end{aligned} \tag{2.82}$$

and illustrates that for the same feedback parameters, the optical backaction is eliminated from the mechanical displacement. This is due to the a destructive interference in the feedback loop of the quantum noise introduced by the light field and does not only lead to an undoing of the optomechanical interaction, but also to a complete decoupling of the mechanical oscillation from the light field after the second interaction. The backaction cancellation as well as the prevention of information leaking to the outside can for instance become a useful tool in the case where an additional element interacting with the optical beam is inserted in the feedback loop. In the context of a hybrid coupling scheme this is realized by optically interacting with an additional physical system in between the two optomechanical interactions [27].

2.7 Hamiltonian Description

In addition to the Langevin equations that describe the dynamic behaviour of the coherent feedback scheme, the description of our feedback scheme using an effective Hamiltonian can provide further insights. Starting with the standard optomechanical Hamiltonian

$$\hat{H}_{\mathrm{om}} = -2\hbar g\hat{X}_{\mathrm{m}}\hat{X}_{\mathrm{c}}, \tag{2.83}$$

where in the broad cavity limit the first cavity field turns into

$$\hat{c}_1(\omega) = -\frac{2}{\sqrt{\kappa}}\hat{a}_1^{\mathrm{in}}(\omega) - 2\sqrt{2}\frac{g_1}{\kappa}\hat{X}_{\mathrm{m}}(\omega), \tag{2.84}$$

the cavity amplitude quadrature is given by $\hat{X}_c = (-2/\sqrt{\kappa})\hat{X}^{in}$. The optomechanical Hamiltonian describing a direct coupling to the external light field results in

$$\hat{H}_{om} = 2\hbar\sqrt{\Gamma_{meas}}\hat{X}_m\hat{X}_{in}, \tag{2.85}$$

with the measurement rate $\Gamma_{meas} = 4g^2/\kappa$. For a resonant double pass interaction, where the measurement rates of the first pass is denoted by Γ_1, the optomechanical interaction transforms the ingoing beam $\hat{a}_1^{in}(t)$ into

$$\hat{a}_1^{out}(t) = -\hat{a}_1^{in}(t) - i\sqrt{2\Gamma_1}\hat{X}_m(t), \tag{2.86}$$

which, after the propagation through the feedback loop enters the cavity as

$$\hat{a}_2^{in}(t) = -\sqrt{\eta}e^{i\varphi}\hat{a}_1^{in}(t-\tau) + \sqrt{1-\eta}\hat{a}_{aux}(t) - i\sqrt{2\eta\Gamma_1}e^{i\varphi}\hat{X}_m(t-\tau), \tag{2.87}$$

with the delay τ and the loop phase φ between the two interaction, and the measurement rate of the second interaction $\Gamma_2 = 4g_2^2/\kappa$ [3].

The ingoing light field quadratures for the second interaction are given in terms of the ingoing light $\hat{X}_1^{in}$ and $\hat{P}_1^{in}$ by

$$\begin{aligned}\hat{X}_2^{in}(t) = \sqrt{\eta}\Big[&\sin(\Omega_m\tau+\varphi)\hat{P}_1^{in}(t) - \cos(\Omega_m\tau+\varphi)\hat{X}_1^{in}(t)\Big] \\ &+ 2\sqrt{\eta\Gamma_1}\sin(\varphi)\hat{X}_m(t-\tau) + \sqrt{(1-\eta)\Gamma_2}\hat{X}_{aux}(t),\end{aligned} \tag{2.88}$$

where we assumed in the rotating wave approximation for the travelling field fulfils $\hat{a}_1^{in}(t-\tau) \approx e^{i\Omega_m\tau}\hat{a}_1^{in}(t)$. The total optomechanical Hamiltonian then results in

$$\begin{aligned}\hat{H}_{om} &= 2\hbar\hat{X}_m\Big[\sqrt{\Gamma_1}\hat{X}_1^{in} + \sqrt{\Gamma_2}\hat{X}_2^{in}\Big] \\ &= 2\hbar\hat{X}_m(t)\Bigg(\sqrt{\Gamma_1}\hat{X}_1^{in}(t) + \sqrt{\eta\Gamma_2}\Big[\sin(\Omega_m\tau+\varphi)\hat{P}_1^{in}(t) - \cos(\Omega_m\tau+\varphi)\hat{X}_1^{in}(t)\Big] \\ &\qquad + 2\sqrt{\eta\Gamma_1\Gamma_2}\sin(\varphi)\hat{X}_m(t-\tau) + \sqrt{1-\eta}\Gamma_2\hat{X}_{aux}(t)\Bigg).\end{aligned} \tag{2.89}$$

Eliminating the light fields and assuming only small delays $\Omega_m\tau \ll 1$ within the Markov approximation, we can identify the effective Hamiltonian

$$\hat{H}_{eff} = 4\hbar\sqrt{\eta\Gamma_1\Gamma_2}\sin(\varphi)\hat{X}_m^2. \tag{2.90}$$

In the general framework of cascaded interaction [27], the same effective Hamiltonian can be derived, by considering the interaction operators $\hat{B}_1 = \hat{X}_m$ and $\hat{B}_2 = -e^{i\varphi}\hat{X}_m$ [4], leading to the general operator A, which for a cascaded interaction on one single systems turns into $A = \sqrt{\Gamma_1\Gamma_2}B_2^\dagger(t)B_1(t-\tau) + \Gamma_1 B_1^\dagger(t)B_1(t) + \Gamma_2 B_2^\dagger(t)B_2(t)$. The effective Hamiltonian is then described by the difference $A - A^\dagger$, whereas the dissipative term is given by the sum $A + A^\dagger$, such that

$$\hat{\Lambda}_{eff} = 4\Big[\Gamma_1 + \Gamma_2 - 2\sqrt{\eta\Gamma_1\Gamma_2}\cos(\varphi)\Big]\hat{X}_m^2. \tag{2.91}$$

[3] We note that the value of g_2 also depends on the feedback phase and efficiency.

[4] where the sign takes into account the additional π phase shift due to the reflection off the resonant cavity

Since the effective Hamiltonian has taken the form of a squeezing Hamiltonian $\sim \hat{X}_{\mathrm{m}}^2$, we can identify the squeezing rate

$$\Gamma_{\mathrm{sq}} = 2\sqrt{\eta\Gamma_1\Gamma_2}\sin(\varphi). \tag{2.92}$$

From the prefactor of the dissipative term we obtain the backaction rate

$$\Gamma_{\mathrm{ba}} = 2(\Gamma_1+\Gamma_2) - 4\sqrt{\eta\Gamma_1\Gamma_2}\cos(\varphi). \tag{2.93}$$

For a loop phase $\varphi = \pm\pi/2$, the squeezing rate reaches its extrema, but we are also facing a non-vanishing backaction term. When $\varphi = N\pi$, N being an integer, the effective Hamiltonian disappears such that there are no feedback-mediated self-interactions. For $\varphi = \pi$, the coupling becomes purely dissipative, leading to a maximal backaction rate. For $\varphi = 0$, not only do the self-interactions vanish, but backaction cancellation can be achieved by balancing the two interactions $\Gamma_1 \sim \Gamma_2$ and assuming negligible losses $\eta \sim 1$. This scenario corresponds to a Hamiltonian coupling regime, where the optomechanical interaction is completely decoupled from the light field and does not transfer excitations to the environment. At the same time this entails a cancellation of the backaction that we have already observed for the expression of the mechanical displacement as stated in Eq. (2.82), and results in a closed system. This becomes mainly interesting once there are additional operations that occur during the optical loop, such as an interactions with additional physical systems or nonlinear elements [27].

Here we want to highlight that our schemes allows for a cancellation of the backaction that takes place during the first interaction due to the implementation of its time-reversal during the second interaction, generated by a destructive interference of the quantum noise in the feedback loop [26, 27]. Thus we note a subtle difference compared to the backaction evasion measurements that are commonly encountered in the literature, which circumvent the backaction on a certain target quadrature that is to be acquired by using an additional inverted harmonic oscillator in the negative mass regime, a two-tone drive, or a pulsed scheme for instance [121, 44, 129, 130, 131, 132, 133, 134].

Considering also non-negligible delays in the loop, the effective Hamiltonian interaction turns into

$$\hat{H}_{\mathrm{eff}} = 4\hbar\sqrt{\eta\Gamma_1\Gamma_2}\sin(\varphi)\hat{X}_{\mathrm{m}}(t)\hat{X}_{\mathrm{m}}(t-\tau), \tag{2.94}$$

and the corresponding dissipation term

$$\hat{\Lambda}_{\mathrm{eff}} = 4(\Gamma_1+\Gamma_2)\hat{X}_{\mathrm{m}}(t)^2 - 8\sqrt{\eta\Gamma_1\Gamma_2}\cos(\varphi)\hat{X}_{\mathrm{m}}(t)\hat{X}_{\mathrm{m}}(t-\tau). \tag{2.95}$$

Depending on the delay τ, the mechanical displacement has evolved according to Eq. (2.31) and can be described by a linear combination of $\hat{X}_{\mathrm{m}}$ and $\hat{P}_{\mathrm{m}}$, defining the type of self-interaction that the feedback is implementing. In case of a mixture of the position and phase quadrature in the self-interactions, the definitions of the squeezing efficiency and the backaction rate have to be redefined according to the more complex relationships.

2.7.1 Mechanical Squeezing

As a potential application of the coherent feedback loop, we analyze its ability to generate mechanical squeezing. The effective Hamiltonian of the double pass optomechanical interactions as derived above [cf. Eq. (2.90)], assuming small delays and $\Gamma_1 = \Gamma_2 = \Gamma$

for simplicity, can be expressed with the mechanical operator in the interaction picture $\hat{b} \rightarrow \hat{b}e^{-i\Omega_m t}$ following

$$\begin{aligned}\hat{H}_{\text{eff}} &= 4\hbar\sqrt{\eta}\Gamma \sin(\varphi)\hat{X}_m(t)^2 \\ &= 2\hbar\sqrt{\eta}\Gamma \sin(\varphi)\Big[\hat{b}^\dagger\hat{b} + \hat{b}\hat{b}^\dagger + e^{-2i\Omega_m t}\hat{b}^2 + e^{2i\Omega_m t}(\hat{b}^\dagger)^2\Big].\end{aligned} \tag{2.96}$$

We observe that the Hamiltonian terms responsible for squeezing are precisely those corresponding to the parametric gain $\hat{b}^2$ and $(\hat{b}^\dagger)^2$, which rotate at a frequency of $2\Omega_m$. These terms can be selected by implementing a parametric modulation of the loop phase $\varphi(t) = \varphi_0 + \varphi_{\text{mod}}\cos(2\Omega_m t)$, resulting in $\sin[\varphi(t)] \approx -\varphi_{\text{mod}}\cos(2\Omega_m t)$. The resulting effective Hamiltonian corresponding to a one-axis squeezing Hamiltonian reads

$$\hat{H}_{\text{eff}} = \hbar\sqrt{\eta}\Gamma\varphi_{\text{mod}}\Big[\hat{b}^2 + (\hat{b}^\dagger)^2\Big], \tag{2.97}$$

with the effective coupling strength $\Gamma_{\text{sq}} = \sqrt{\eta}\Gamma\varphi_{\text{mod}}/2$. It is advantageous to choose an offset phase of $\varphi_0 = 0$ leading to a reduction of the backaction rate given by $\Gamma_{\text{ba}} = 2\Gamma[1 - \sqrt{\eta}\cos(\varphi(t)] \approx 2\Gamma[1 - \sqrt{\eta}(1 - \varphi_{\text{mod}}^2/4)]$ which in turn reduces the dissipative term that competes against the coherent evolution in the squeezing factor

$$\zeta_{\text{sq}} = \frac{\Gamma_{\text{ba}}}{\Gamma_{\text{sq}}} \approx \frac{4\Big[1 - \sqrt{\eta}(1 - \varphi_{\text{mod}}^2/4)\Big]}{\sqrt{\eta}\varphi_{\text{mod}}}. \tag{2.98}$$

For $\eta \approx 1$, the squeezing rate solely depends on the modulation depth $\zeta_{\text{sq}} = \varphi_{\text{mod}}$.

2.8 Further Applications

2.8.1 Hybrid Coupling Scheme

The coherent feedback scheme presented thus far involves an optical loop in which the light interacts twice with one mechanical mode. A similar protocol can be implemented with disparate systems located at a distance from each other, as is sketched in Fig 2.15. The combination of coherent feedback with a hybrid system allows us to use the established quantum control techniques available on one system to manipulate the other without the disturbance introduced by a measurement.

In the context of hybrid setups, a coherent optical feedback loop has been used to realize a strong bidirectional light-mediated coupling between the mechanical mode of a mechanical oscillator and the collective spin of a cold atomic ensemble [127]. The remote coupling is implemented by a travelling light field, that first passes the atoms, propagates to the mechanical oscillator, before being redirected to the atomic cloud.

The hybrid system which is sketched in Fig. 2.16 and discussed in more detail in [34, 135], consists in a cavity optomechanics setup analogous to the one used in this work, and an ensemble of ultracold ^{87}Rb atoms forming a collective pseudospin whose excursions can be approximated as a harmonic oscillator with position and phase quadratures $\hat{X}_s$ and $\hat{P}_s$. The atomic spin interacts with the light through the off-resonant Faraday interaction [136], where the circular component of the light field polarization interacts with the spin position quadrature $\hat{X}_s$, resulting in a tilt. At the same time, the tilted spin modifies the light polarization and generates a rotation of the incoming linear polarization by the Faraday angle $\propto \hat{X}_s$. The interaction between the mechanical and spin signals is realized using a polarimeter, which transforms fluctuations in the polarization of the light into an

amplitude modulation, that interacts with the mechanical system through the radiation pressure force. Moreover, the phase modulation imprinted by the mechanical oscillator on the light leaking out of the cavity is transformed into a modulation in the polarization using a polarization interferometer, such that the mechanical signal couples back to the atoms.

The looped interactions mediated by the light beam result in an effective bidirectional interaction between the spin and the mechanical mode. This interaction is further influenced by the feedback delay, which is determined by the propagation time of the travelling light field, and the loop phase accumulated between the two interactions. If we assume that the delay remains small for a broad cavity on the optomechanical side and a light travelling distance of approximately 2 meters, the loop phase can significantly change the nature of the interactions. Specifically, a π phase shift of the loop phase allows to switch from purely Hamiltonian to dissipative coupling. Furthermore, the time-reversed atom-light interaction in the second pass leads to the destructive interference of the quantum backaction noise and the spin signal. This approach allowed to implement a strong light-mediated interaction between the two systems [127].

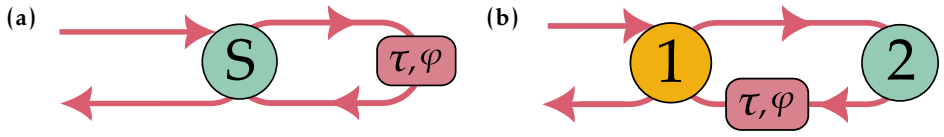

Figure 2.15: Sketch of coherent feedback loop **(a)** on a single system S and **(b)** between two separate systems 1 and 2.

Once a strong coupling between the two systems is established, one of the most obvious applications of the hybrid systems consists in sympathetic cooling, where the control over one of the hybrid system elements is utilized to cool the other. Recently, we demonstrated that the implementation of a coherent feedback scheme, realizing cooling via state swaps, improves the sympathetic cooling performance. In this case, tuning the dissipation in the atomic system used as a coolant, enables to increase the cooling efficiency for the mechanical oscillator [34]. However, the efficiency of the process is constrained by the swapping rate, which dependends on the strength of interaction between the systems. As a result, achieving effective cooling for systems that are distant and disparate presents significant challenges.

Up until now, the coupling strength that has been achieved between the two systems amounts to $2g = 2\pi \times 6.8\,\mathrm{kHz}$ and is larger than the average dissipation rates in the individual systems, realizing strong coupling. However, for quantum coherent coupling, g must exceed all thermal and quantum backaction decoherence rates [127]. This condition is necessary to produce non-classical state swaps and entanglement between the two systems.

In case of a looped interaction between two systems 1 and 2 in a coupling geometry 1-2-1, with an overall coupling rate of $g = g_1 g_2$ and backaction cancellation on system 1 (i.e., $\Gamma_1 \approx 0$ for a high efficiency), it is beneficial to follow a hierarchy of single system cooperativities C_1 and C_2 with $C_1 \gg C_2 \approx 1$. This ensures that the backaction rate on system 2 remains small in comparison to the coupling rate [27]. However, the upper bound on the cooperativity of system 2, and thus on the cooperativity of the cascaded system ($\propto C_1 C_2$), can be removed by utilizing the geometry 1-2-1-2, which enables backaction cancellation on both systems.

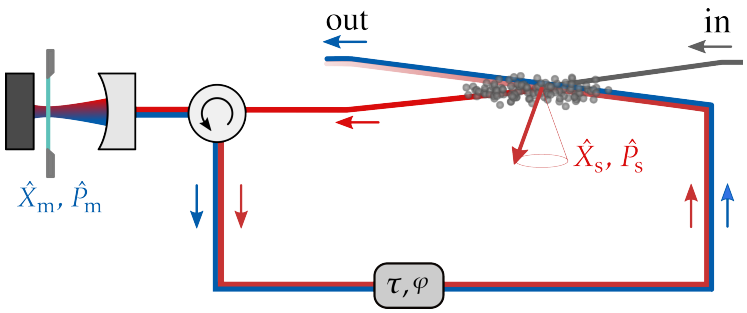

FIGURE 2.16: Sketch of the hybrid coupling experiment, combing a pseudo spin of a Rb^{87} atomic cloud with an optomechanical system comprising a membrane-in-the-middle cavity. The travelling light field first interacts with the spin, then interacts with the membrane, and is redirected for a second pass through the atomic cloud. The propagation of light between the atom-membrane interaction causes a delay of τ and a loop phase φ. The colors of the light fields encode the signal carried by the light field. (Figure adapted from [34])

Therefore, an additional double-pass interaction on the mechanical oscillator would constitute an upgrade for the hybrid setup. It could not only drastically reduce the mechanical occupation number, but also enable a reduction of the backaction rate on the mechanical oscillator, as demonstrated in this chapter. In the previous hybrid experiments, the mechanical thermal decoherence rate has been a limiting factor for remote coupling. The proposed coherent feedback loop on the mechanical oscillator could provide a crucial ingredient to enable the realization of quantum coherent coupling [127].

2.8.2 Optical Squeezing

So far, our discussion has centred on the quantum backaction of light, which acts as a heating mechanism on the mechanical mode. In fact, in the backaction dominated regime, the light meter induces a significant perturbation compared to the thermal fluctuations on the conjugate quadrature [5]. Other than a noisy drive for the mechanical motion, a strong backaction generates correlations between the mechanical displacement and the optical quantum noise. Hence, this can be used to squeeze one quadrature of the outgoing light below the shot noise level, and provides a source of entanglement [137, 138, 128]. The double pass interaction has the potential to increase light squeezing. In the output amplitude spectrum, negative correlation terms can reduce noise below the vacuum level for a large measurement rate compared to the thermal decoherence rate [137]. The necessary requirement for the outgoing amplitude quadrature $\hat{X}_2^{\text{out}}$ of the second pass is that its power spectral density reduces to $\bar{S}_{X_2^{\text{out}} X_2^{\text{out}}} < 1/2$, taking into account the correlation terms.

2.8.3 Photon-Phonon Entanglement

Once the precision of the state control of mechanical oscillators reaches the single phonon level, entanglement between phonons and photons can be generated and verified, and has already been achieved in the pulsed regime [72, 91, 139, 93]. The entanglement arises by transduction of information from the mechanical object to the measurement field during the optomechanical interaction. From the optomechanical Hamiltonian as derived in Eq. (1.26), entanglement can efficiently be generated by driving the Stokes

scattering process responsible for the generation of a photon-phonon pair, namely parametric down-conversion $\sim \hat{b}^\dagger \hat{c}^\dagger + \hat{b}\hat{c}$. The anti-Stokes process, corresponding to the beamsplitter interaction $\sim \hat{b}^\dagger \hat{c} + \hat{b}\hat{c}^\dagger$ can then be used for readout and verification [139]. In the resolved sideband regime, the cavity, which has a linewidth that is smaller than the mechanical frequency, can efficiently enhance one scattering process while suppressing the other. The entangling process is favoured for a blue-detuned drive, whereas the red-detuned beam generates state swaps.

In the unresolved sideband regime, the broad cavity realizes the entanglement creation and readout simultaneously and at the same rate, making it very difficult to generate and verify entanglement, even though there are proposals to perform the entanglement verification with stationary probing on resonance [140, 141]. Coherent feedback has been proposed to enhance entanglement generation [42] by employing various auxiliary cavities with different linewidths and fast switching between them in order to reduce the effective optomechanical cavity linewidth and improve its sideband selection capability that most conditional and unconditional entangling schemes require.

As we have discussed in the sideband cooling picture in Fig. 2.12, our coherent feedback protocol is capable of selecting one of the sideband processes through the interference of the optical force, with a much higher efficiency than the optical cavity in the unresolved sideband regime.

For a resonantly driven cavity, we can select the anti-Stokes process, as explained for the discussion about cooling, for the feedback parameters $\Omega_\mathrm{m}\tau = \pi/2 = \varphi$, while the entanglement operation is realized for $\Omega_\mathrm{m}\tau = \pi/2 = -\varphi$. In this manner we can use the loop phase to switch between writing in or reading out the entanglement.

2.8.4 Mechanical Entanglement

Even more challenging to realize, mechanical entanglement between macroscopic elements poses a highly interesting goal for fundamental research. Such entanglement is expected to be extremely fragile and will decrease to zero for any mechanical occupation larger than unity [138]. However, recent advances in various systems have enabled entanglement between distant mechanical modes, as has been shown for trapped ions, micromechanical oscillators, microwave circuits, and also hybrid spin-membrane systems [142, 87, 88, 90, 143].

In our case, it only makes sense to consider mechanical entanglement once we address two different mechanical modes or two entirely different oscillators. There are protocols to generate entanglement between two mechanical modes of different frequencies in the resolved sideband regime, mostly involving the transfer of entanglement via optical entanglement and a two tone drive [80, 110].

Without any major changes in our optomechanical system, we can envision two-mode squeezing operations on two different mechanical modes. This requires one of the oscillators to be inverted, meaning in the negative frequency configuration that can be accomplished with a two-tone drive where one of the beams is blue detuned [144, 131]. Additionally, the coherent coupling strength must exceed the sum of noise terms $g > \gamma_{1,\mathrm{tot}} + \gamma_{2,\mathrm{tot}}$ to generate significant two mode squeezing and thus entanglement. We note that this requirement is even more stringent than that for large quantum cooperativity $\mathcal{C}_\mathrm{qu} > 1$ [27].

Verification of entanglement can for instance be implemented with an additional auxiliary probe beam at a different longitudinal cavity mode, or a fast switch that allows for a temporal separation between entanglement generation and read-out process [42].

2.9 Conclusion

We have developed a theoretical framework for optical coherent feedback on a mechanical oscillator, that provides the possibility to ground-state cool the mechanical oscillator in the unresolved sideband regime without requiring any further resources nor the necessity to perform a measurement. In the regime of a large cooperativity, the final occupation number for the coherent feedback cooling process is limited not by the sideband resolution of the optical cavity, but by the optical losses. We find that the phonon occupation number has a lower bound than the one predicted for dynamical backaction cooling in the unresolved sideband regime. Additionally we have drawn an analogy between our approach and measurement-based feedback applied for cooling, where essentially the detection efficiency replaces the optical loop efficiency in the achievable cooling performance.

In addition to its cooling capabilities, coherent feedback techniques also show great promise as a platform for mechanical squeezing and photon-phonon entanglement. We have shown its ability for backaction cancellation which is particularly important for achieving quantum coherent coupling in hybrid systems. The versatility of the coherent feedback protocol has the potential to advance optomechanical systems and enhance their appeal for use in quantum technologies.

Chapter 3

Membrane Oscillators

This chapter covers the fundamental concepts of nanomechanical membranes, which are essentially thin sheets of suspended silicon nitride. We provide an overview of various dissipation mechanisms and explain how to overcome them through a refined nanomechanical design. In this work we consider two distinct membrane designs, namely square membranes with a silicon phononic shield and soft-clamped membranes with a mechanical mode localized in a defect embedded in a patterned phononic SiN structure. Finally, we present the characterization measurements of the primary figures of merit of membrane oscillators, which include their spectrum, quality factor and mode pattern.

3.1 Introduction

Designing a nanomechanical oscillator that can be used for quantum technologies is a challenging task. For optomechanical applications, mechanical oscillators with long coherence times, and efficient coupling to the light are desired [79]. As discussed in Ch. 2, the optomechanical interaction is realized through the radiation pressure force, which relies on the momentum kick of the photons reflected from the mechanical resonator. Therefore, the reflectivity, which defines the ratio of reflected photons, and the effective mass of the mechanical mode addressed, which defines the magnitude of the impact of the photon's momentum kick, play a key role in designing the mechanical oscillator.

Apart from coupling to light, the mechanical oscillator, being a nanomechanical device, is also directly connected to the environment through its support and linked to the environmental thermal bath. By default, it is susceptible to exchanging thermal phonons. In order to perform quantum experiments we require a weak environmental influence and dissipation, and thus a device exhibiting long coherence times. The figure of merit quantifying this is given by the Qf product, with Q the quality factor and f the mechanical resonance frequency. The quality factor quantifies the ratio between the energy stored in and lost during the mechanical motion. High quality factors have dominated the design criteria over the last few decades, and there has been enormous progress in engineering stress, strain and mode shapes towards this goal [63, 64, 145].

Several design platforms fulfill the aforementioned characteristics and have achieved remarkably high Qf products, thus being promising platforms for quantum experiments [79]. Among these we find optomechanical crystals in Silicon that hold the record of $Qf \sim 10^{19}$ Hz at cryogenic temperatures [146]. Additionally, SiN nanobeams with strain-engineered phononic crystals at room temperature ($Qf \sim 10^{15}$ Hz) [65] as well as nanomechanical membranes ($Qf \sim 10^{14}$ Hz) [63, 64, 145] have demonstrated extraordinary high mechanical coherence times. Furthermore, systems with different coupling mechanisms, like multilayer graphene drums capacitively coupled to microwave cavities [147], parallel-plate aluminium capacitors coupled to LC circuits [89], phononic

aluminium beams with piezoelectric coupling to a superconducting qubit [90], and double-clamped single-wall carbon nanotubes with extremely small masses, coupled via electron transport [148], have also demonstrated notable mechanical properties.

Here we focus on membrane resonators, which are suspended mechanical elements with high area-to-thickness ratio. Silicon nitride (SiN) is the material of choice for membranes due to the fabrication method on silicon (Si) wafers that allows for high in-plane stress, increasing the quality factors thanks to the principle of dissipation dilution [149, 55]. For optical wavelengths in the near infra-red $\lambda = 780\,\mathrm{nm}$, SiN has very low optical absorption (< 10 ppm), relatively high optical amplitude reflection $r_\mathrm{m} = 0.6$ for a thickness of $d = 100\,\mathrm{nm}$, both of which are essential prerequisites for optomechanical experiments [55]. Furthermore, quasi-two-dimensional membranes provide very low effective oscillator masses, leading to a high force sensitivity as discussed in Sec. 1.9 [64].

In this work we use the two membrane designs depicted in Fig. 3.1. The design on the left displays a SiN square membrane that is embedded in a phononic patterned Si chip, commercially fabricated[1]. The phononic pattern is selected to shield the membrane mode of interest from environmental noise and prevent acoustic waves from travelling across the membrane boundary. The unit cell size is chosen to provide a bandgap around the primary mode frequency of interest. At a target frequency of $f = 2\,\mathrm{MHz}$, our mechanical oscillator has a quality factor of $Q > 1 \times 10^6$. On the right, we display a soft-clamped membrane, in which a patterned SiN structure isolates the mechanical mode more effectively in a defect while decreasing bending losses [63]. Such membranes were fabricated in the Groeblacher group at TU Delft and made available to us through a collaboration.

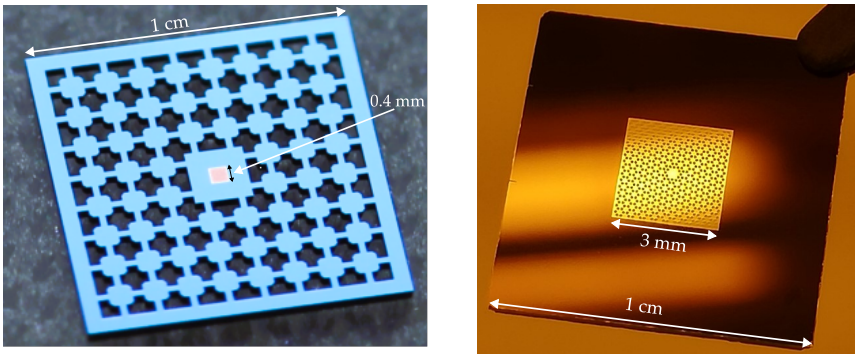

Figure 3.1: Photographs of the nanomechanical membrane oscillators used in this work. On the left a phononic bandgap mechanical oscillator with a membrane of side length of 400 µm (Norcada). On the right a soft-clamped membrane (SCM) with a patterned SiN membrane side length of 3.2 mm, fabricated by the members of Simon Gröblacher's group at TU Delft. Both silicon chips have a side length of 1 cm.

3.2 Square Membrane Oscillator

In this section, we introduce the basic concepts of the flexural modes of square membrane oscillators. These drum modes show displacements that are orthogonal to the plane and can be described as harmonic oscillators. For an isotropically tensioned thin sheet plate, the out-of-plane displacement $v(x, y, t)$ that we are interested in is described

[1] Norcada Inc.

by the fourth-order differential equation , which is given by the two-dimensional Euler-Bernoulli equation [150, 151, 152]

$$\frac{Ed^2}{12(1-\nu^2)}\nabla^4 v(x,y,t) - \sigma\nabla^2 v(x,y,t) + \rho\frac{\partial^2}{\partial t^2}v(x,y,t) = 0, \tag{3.1}$$

with the tensile stress σ, Poisson ratio ν, thickness d, Young modulus E and flexural rigidity of the plate $D = Ed^3/12(1-\nu^2)$. The rigidity describes the resistance of the material to bending, and thus the energy cost associated to higher-order modes containing more curvature. Since we are considering a membrane, which is a very thin sheet, the fourth-order term can be neglected for the motion away from the clamping points. This simplification allows us to describe the mechanical motion of the membrane using the standard wave equation for a two-dimensional oscillator

$$\nabla^2 v(x,y,t) = -\frac{1}{c^2}\frac{\partial^2}{\partial t^2}v(x,y,t), \tag{3.2}$$

with the propagation velocity $c = \sqrt{\sigma/\rho}$, depending on the tension σ and the material density ρ. We use a separation of variables into a part describing the spatial distribution $u(x,y)$ and the time evolution $q(t)$, such that

$$v(x,y,t) = u(x,y)q(t). \tag{3.3}$$

From the boundary conditions for a rectangular membrane which impose the displacement at its boundaries to vanish

$$u(l_x,y) = 0,\ u(0,y) = 0,\ u(x,l_y) = 0,\ u(x,0) = 0, \tag{3.4}$$

$$\partial_y u(l_x,y) = \partial_y u(0,y) = \partial_x u(x,l_y) = \partial_x u(x,0) = 0, \tag{3.5}$$

the longitudinal out-of-plane modes can be determined as

$$u_{ij}(x,y) = \sin(ik_x x)\sin(jk_y y),\ \ i,j = 1,2,\ldots \tag{3.6}$$

with i,j the square mode indices. The wavevectors $k_x = \pi/l_x$ and $k_y = \pi/l_y$ correspond to the length l_x and width l_y of the rectangular membrane. The fundamental drum mode of a square membrane oscillator is illustrated in Fig. 3.2.

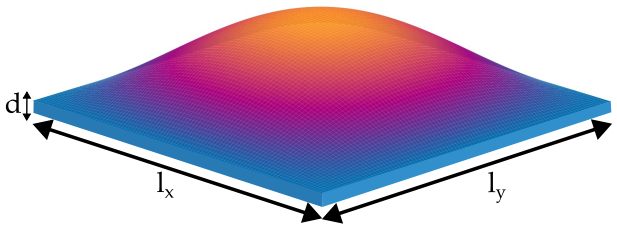

FIGURE 3.2: Fundamental flexural mode ($i = j = 1$) of a square membrane oscillator of side lengths l_x, l_y and thickness d.

The time evolution of the system is described by $q(t) = q_0\cos(\Omega_{ij}t)$, where the angular mode frequency Ω_{ij} depends on the size of the membrane and its fixation to the support. For a rectangular membrane with fixed edges, the mode frequencies are

$\Omega_{ij} = \pi c\sqrt{i^2/l_x^2 + j^2/l_y^2}$. For a square membrane with $l = l_x \approx l_y$ the mode frequencies simplify to $\Omega_{ij} = \Omega_{11}\sqrt{(i^2+j^2)/2}$ with the fundamental frequency given by $\Omega_{11} = \sqrt{2}\pi c/l$.

To simplify the analysis, we consider a single-mode description where the displacement amplitude $q(t)$ of a damped harmonic oscillator is driven by a force $F(t)$. The equation of motion for this system can be written as [44, 45]

$$m\partial_t^2 q(t) + m\gamma_\mathrm{m}\partial_t q(t) + m\Omega_\mathrm{m}^2 q(t) = F(t), \tag{3.7}$$

with the energy damping rate γ_m that we assume to be frequency independent, resonance frequency Ω_m, and the effective mass m of a given mechanical mode. For such a one-dimensional mechanical oscillator, the potential energy of a displacement $q(t)$ is given by $U(t) = \frac{1}{2}m\Omega_\mathrm{m}^2 q(t)^2$. Integrating the potential energy over the vibrational mode

$$U(t) = \frac{1}{2}\Omega_\mathrm{m}^2 \int v(x,y,t)^2 \mathrm{d}V = \frac{1}{2}\frac{\rho l^2 d}{4}\Omega_\mathrm{m}^2 q(t)^2, \tag{3.8}$$

allows to identify the effective mass $m = \rho l^2 d/4 = m_\mathrm{phys}/4$, given in our case by one quarter of the physical membrane mass m_phys, regardless of the mechanical mode. This simple relationship holds only for specific geometrical structures like the square membrane that we are discussing here. When considering significant mechanical excitations while disregarding thermal motion, the equation's general solution is

$$q(t) = q_0 \mathrm{e}^{-\gamma_\mathrm{m} t/2}\cos(\Omega_\mathrm{m} t + \phi_0), \tag{3.9}$$

where the amplitude q_0 and the phase ϕ_0 are determined by the initial conditions. This expression can be used to determine the mechanical linewidth by measuring the decay rate when driven to a large number of excitations.

Transforming Eq. (3.7) into the frequency domain, we observe that the mechanical response to a driving force is determined by its mechanical susceptibility

$$\chi(\omega) = \frac{q(\omega)}{F(\omega)} = \frac{1}{m(\Omega_\mathrm{m}^2 - \omega^2 - \mathrm{i}\omega\gamma_\mathrm{m})}. \tag{3.10}$$

For a weakly damped oscillator, the quality factor is defined as

$$Q = 2\pi\frac{U}{\Delta U} = \frac{2\pi}{1-\mathrm{e}^{\gamma_\mathrm{m}\mathcal{T}}} \approx \frac{\Omega_\mathrm{m}}{\gamma_\mathrm{m}}, \tag{3.11}$$

with the stored energy U and the lost energy ΔU during one oscillation period $\mathcal{T} = 2\pi/\Omega_\mathrm{m}$. In quantum mechanical experiments, we are interested in the coherence time of a mechanical oscillator, which is given by the time for which is can oscillate before its motion is disturbed by a thermal phonon leaking in from the environment. Hence, the condition for a quantum-coherent mechanical experiment requires $\Omega_\mathrm{m} > \gamma_\mathrm{m,th}$, where the thermal decoherence rate $\gamma_\mathrm{m,th} = \gamma_\mathrm{m}(\bar{n}_\mathrm{th} + 1/2)$ is given by the coupling rate to the thermal reservoir and the mean occupation of the latter. The coherence can thus be quantified by the number of coherent oscillations determined by the ratio

$$\frac{\Omega_\mathrm{m}}{\gamma_\mathrm{m,th}} \approx \frac{h}{k_\mathrm{B}T}Qf, \tag{3.12}$$

which scales directly with the product Qf, where $f = \Omega_\mathrm{m}/2\pi$, and inversely with the

environmental temperature T [44]. Therefore, both the Q factor and the mechanical frequency f are crucial parameters in designing a mechanical oscillator. For the nanomechanical membranes used in this work, we achieve $Qf > 10^{12}$ Hz at room temperature.

3.3 Dissipation Mechanisms

The number of coherent oscillations performed by a mechanical oscillator and its decoherence rate are determined by the dissipation processes occurring during its oscillations. Therefore, reducing dissipation is crucial in any kind of quantum experiment where quantum coherence is involved [79]. One advantage of nanomechanical oscillators is the design flexibility available to minimize these processes once the limiting factors are identified. In the case of membrane oscillators, we can identify two main categories of dissipation mechanisms:

$$Q^{-1} = Q_{\text{int}}^{-1} + Q_{\text{ext}}^{-1}, \tag{3.13}$$

with the internal loss mechanisms in Q_{int} and the external loss mechanisms united in Q_{ext}, which includes contributions from both damping due to collisions with environmental gas (Q_{gas}), and radiative losses due to the clamping of the membrane at the edge to a support structure (Q_{clamping}).

Starting with the external dissipation mechanisms, the losses generated by clamping to the surrounding can be modelled as phonon tunnelling through the edges of the membrane [61, 45] and can be mitigated with a phononic shielded membrane design. The expression for the Q factor limited by ballistic gas collisions for a mechanical mode is given by [153]

$$Q_{\text{gas}} = \frac{\rho d \Omega_{\text{m}}}{p} \sqrt{\frac{\pi R T}{32 m_{\text{mol}}}}, \tag{3.14}$$

with m_{mol} the molar mass of the surrounding gas, T the environmental temperature, R the gas constant and p the gas pressure. Using the molar mass value for dry air of $m_{\text{mol}} = 29\,\text{g}\,\text{mol}^{-1}$ [154], the value for Q_{gas} is limited to ~ 3 at room temperature and at ambient pressure. However at the standard pressures achieved in vacuum chambers $p \ll 10^{-6}$mbar, $Q_{\text{gas}} > 10^9$ and is not a limiting process anymore, further improved at cryogenic temperatures.

The intrinsic material damping in stoichiometric SiN can be modelled using a Zener loss model that takes into account inelastic motion through a complex Young's modulus $E = E_1 + \text{i}E_2$ [45]. The resulting Q factor can be expressed as $Q_{\text{int}} = E_1/E_2$ [155]. In fact, the material damping can be interpreted as the loss of inelastic energy due to the out-of phase oscillations of strain ϵ and stress σ, which are related via $\sigma = E\epsilon$ [149]. The intrinsic material losses which transform elastic mechanical motion into heat, result from various processes such as thermoeleastic effects, phonon-phonon interactions (Akhiezer damping), and imperfections in the surface and bulk materials.

Thermoelastic losses are caused by heat transport associated with thermal gradients that are due to periodic squeezing and stretching related to the flexural motion. For SiN membranes they have been estimated to limit the achievable Q factor to $Q_{\text{TED}} \approx 10^{11}$ [156], and can in principle be mitigated by choosing structures with small strain gradients, such as extensional modes [157]. A more fundamental dissipation process based on phonon-phonon interactions is given by Akhiezer damping, which is a quantum scattering effect. It occurs when the oscillation-induced distortions disturb the equilibrium

phonon distribution, leading to inelastic redistribution processes, and thus energy dissipation. For SiN, the theoretical upper limit of the achievable Q factor due to Akhiezer damping is estimated to be around $Q_{\text{Akhiezer}} \approx 10^9$ for frequencies in the range of $\sim$ MHz [157].

Further scattering losses, which occur primarily at surface defects, can be explained on a microscopic level by the coupling of phonons to defects modelled as two-level systems (TLS) [158]. It is suggested that they can be excited by a scattering process involving both a phonon of the mechanical mode and a thermally-excited high energy bulk phonon. Since the resonator phonons are not re-emitted into the mechanical mode, this process irreversibly leads to a loss of energy. These losses account for the empirically observed dependence of the Q factor on the membrane thickness and environmental temperature. For thin membranes with a thickness below 100 nm, surface effects dominate the intrinsic quality factor, which is expected to depend directly on the thickness given by $Q_{\text{int}} = Q_{\text{vol}}^{-1} + Q_{\text{surf}}^{-1} = (\beta d)^{-1}$ where β is the slope of the surface losses [159].

3.4 Highly Stressed SiN Membranes

Having discussed the relevant dissipation processes, we can adapt the design of the mechanical oscillator in order to mitigate them. A first strategy to increase the achievable Q factor of SiN membranes consists in maximizing the elastic motion with respect to the inelastic part. The intrinsic losses can be diluted by generating a large tensile prestress on the mechanical oscillator. The convenience with which SiN is grown in a stressed manner on Si wafers makes it a highly attractive material for optomechanical experiments, as it allows for a drastic increase of the achievable Q factors [159]. In fact, mechanical energy is stored in both the elongation and bending motion. Applying a structural prestress increases the elongation energy that thus largely exceeds the bending energy. Furthermore, the dissipated energy proportional to the square of the strain ϵ^2, can be attributed mostly to local bending-related damping mechanisms, related to the curvature of the mode [155, 152, 149].

To compute the Q factor, we need to compare the energy lost during one full oscillation cycle ΔU to the total stored energy U [155, 152]. In this case, we consider the stored energy of a one-dimensional oscillator with the mode shape $u(x)$, as it already captures the main insights. The stored energy contains both contributions $U = U_{\text{tension}} + U_{\text{bending}}$ while the term describing the losses can be simplified as $\Delta U = \Delta U_{\text{tension}} + \Delta U_{\text{bending}} \approx \Delta U_{\text{bending}}$ such that we obtain

$$Q = 2\pi \frac{U}{\Delta U} \approx 2\pi \frac{U_{\text{tension}} + U_{\text{bending}}}{\Delta U_{\text{bending}}}. \tag{3.15}$$

Following the derivations in [152], the stored energy that can be attributed to the tension, scales directly with the applied stress σ as

$$U_{\text{tension}} = \frac{1}{2}\sigma \Omega d \int_0^a \left(\frac{\partial u(x)}{\partial x} \right)^2 \mathrm{d}x, \tag{3.16}$$

in contrast to the energy stored in the bending

$$U_{\text{bending}} = \frac{1}{24} E_1 \Omega d^3 \int_0^a \left(\frac{\partial^2 u(x)}{\partial x^2} \right)^2 \mathrm{d}x, \tag{3.17}$$

and the corresponding losses appearing due to bending

$$\Delta U_{\text{bending}} = \frac{\pi}{12} E_2 \Omega d^3 \int_0^a \left(\frac{\partial^2 u(x)}{\partial x^2} \right)^2 \mathrm{d}x. \tag{3.18}$$

The loss term is obtained by integrating the squared curvature over the entire mechanical oscillator. As a result, it contains a term from the local flexural bending at the clamping site, as well as the curvature at the antinodes due to the modal motion itself [155, 149, 160]. Finally, applying a tensile stress increases U while leaving ΔU unchanged (up to a static strain component [145]), leads to the quality factor increased through dissipation dilution:

$$Q_\sigma = Q_{\text{int}} [2\lambda + (i^2 + j^2)\pi^2 \lambda^2]^{-1}, \tag{3.19}$$

where Q_{int} is the intrinsic material quality factor of the unstressed SiN membrane, and $\lambda = \sqrt{E_1/(12\sigma)}d/l$ is the dilution factor due to the prestress σ. The first term in the expression, which is independent of the mechanical mode number, only depends on the clamping at the edges. The mode-dependent term takes into account the modal bending at the antinodes during the mechanical oscillations. The expression indicates that the Q factor increases with decreasing thickness d and increasing membrane size l, as the bending becomes less important for the mechanical mode [159]. Furthermore, the diluted quality factor Q_σ can still be improved by eliminating the term responsible for the bending at the edge [149], which will be considered in Sec. 3.6.1.

3.5 Phononic Bandgap Membranes

3.5.1 Design Considerations

For the tensioned stoichiometric SiN membranes in ultra-high vacuum chambers, the most important dissipation process are clamping losses, which comprise radiative losses due to the coupling to frame modes, broadening of the mechanical linewidth due to hybridization with frame modes, and bending losses due to the rigidity at the border. Radiative losses can be formally described through phonon tunnelling and a weak coupling between the resonator modes and the support [61]. The strength of the coupling between the membrane and the support modes depends on the mismatch of their phase velocities, the mode number and the membrane aspect ratio of its size to thickness. The symmetry of the mechanical oscillations and the corresponding mode shape, as well as the exact phase between the material's strain and stresses during oscillations, can cause destructive interference of the modes radiating into in the substrate [161].

To shield the mechanical oscillator from environmental noise and prevent acoustic waves from radiatively leaking into the frame modes, the membrane is embedded into a phononic patterned Silicon (Si) chip. The periodic pattern leads to a modulated wave velocity that opens up a bandgap in the acoustic spectrum and thus reduces the density of states as seen by the mechanical mode. The phononic pattern is chosen to provide

a bandgap around the main modes of interest, with the unit cell size selected to match half of the acoustic wavelength in silicon, which is approximately $\lambda/2 = v/(2f) \approx 1\,\mathrm{mm}$ for a target frequency $f = 1\,\mathrm{MHz}$ and given the propagation velocity v in silicon [149]. A sketch of the unit cell is shown in Fig. 3.4. The bandgap is considered as the spectral region in which the mechanical signal drops to the shot noise background except for the mechanical peaks. Finite element simulations predict the opening of a complete bandgap for an infinite periodic structure. The center of the bandgap is defined by the size of the unit cell pad a, and the width of the bandgap is determined by the ratio between the wave velocities in the pads versus the bridges [64], such that for a given unit cell size a, the width of the produced bandgap is inversely proportional to the bridge width b. Thus, thin bridges in combination with large pads are preferred for a wide bandgap and large Q factors. However, the overall size of the mechanical oscillator should not be too large to avoid floppy low-frequency modes of the entire structure.

3.5.2 Experimental Sample

The square membrane used in this work has a side length of 400 µm, leading to a fundamental frequency of 0.96 MHz. The membrane is fabricated out of SiN, which has a density of $\rho = 2.8 \times 10^3\,\mathrm{kg/m^3}$ and a tensile stress of about 1.2 GPa. The thickness of the SiN film is $d = 100\,\mathrm{nm}$ and results in an amplitude reflectivity $r_\mathrm{m} = 0.6$ at a wavelength of 780 nm. The membrane is embedded in a patterned Silicon (Si) chip with a thickness of 200 µm and a side length of 10 mm. The expected phononic bandgap is 500 kHz wide for 100 µm bridges and up to 1 MHz for 50 µm-wide bridges. As the bandgap center frequency depends on the pattern's unit cell size a, the smaller pad of 1 mm centers the bandgap at the (2,2) mode around 2 MHz whereas the larger pad of 1.5 mm at the (1,1) mode around 1 MHz. Keeping the overall chip size constant, the lower target frequency and corresponding larger unit cell size reduces the number of cells that fit in the pattern from 9 to 7, and thus reduces the shielding.

However, obtaining the desired smaller bridge widths presents a challenge due to the structure's fragility and the increased risk of breaking when handling them. Additionally, we have to consider that extremely thin bridges result in a worse thermal connection between the SiN and the frame, which is detrimental in cryogenic experiments.

Figure 3.3 shows a thermal displacement spectrum of a typical square membrane, where we can associate almost all the visible peaks to specific mechanical modes. Slight asymmetries in the length of the square membrane lift the frequency degeneracy between modes with inverted indices (i, j) and (j, i). As a result, the modes (i, j) where $i \neq j = 1$ have lower Q factors due to reduced destructive interference with the frame modes [61]. These asymmetries are also visible in the raster scan presented in Sec. 3.8.2, particularly for the (1,2) and (2,1) modes. The displacement detected with a reflective interferometric measurement is in good agreement with the expected mean square thermal displacement of the (2,2) mode, given by $\sqrt{\langle x^2 \rangle} = k_B T / m\Omega_\mathrm{m}^2 \approx 10\,\mathrm{pm}$ at room temperature.

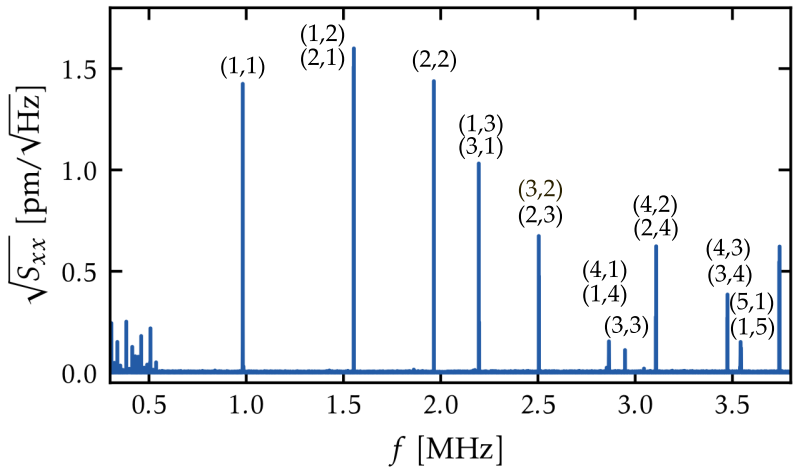

FIGURE 3.3: Thermal displacement power spectral density of the drum modes (i, j) of a square membrane. The corresponding mode shapes are illustrated in Figure 3.14.

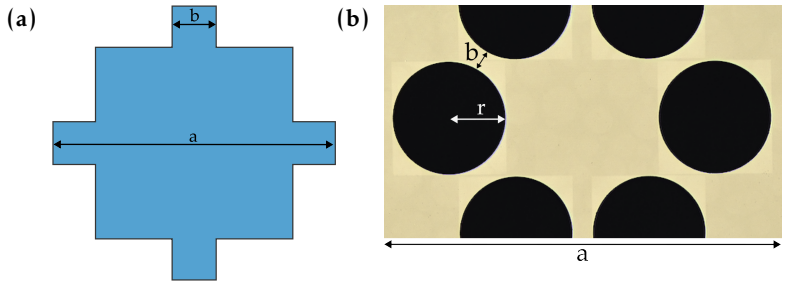

FIGURE 3.4: Phononic shield unit cell design parameters illustrating **(a)** the bridge width b and the unit cell size a for a square membrane surrounded by a phononic shield and **(b)** the hexagonal soft-clamped design, with overall cell size a, the hole radius r and the bridge width b.

3.6 Soft-Clamped Membranes

3.6.1 Design Consideration

To further improve the quality factors of the membrane mechanical oscillators that are already shielded by a phononic bandgap against radiative losses, it is necessary to re-evaluate the limiting dissipation processes. It turns out that phononically shielded membranes are well protected against external dissipation, and are now mainly constrained by their internal dissipation, where the bending losses at the borders form the most important contribution. Membrane designs have been developed to address these limiting factors through advances in phononic geometries [63, 64, 145], but also through engineering of the geometric strain. This is closely related to the mode curvature and thus bending losses [65, 145]. In this work we follow the concept of soft-clamped membranes (SCM) that, additionally to the reduction of radiation losses to the substrate using a phononic pattern, eliminate the bending losses at the strongly clamped edge region of the membrane, created by the transition from suspended SiN to the Si frame, thanks to a localization of the mechanical mode at a defect in the center of a patterned membrane

[63]. The phononic pattern is created inside the square SiN film itself with a central defect at its core, and as a result, the mechanical mode is confined far from the membrane border. The entire phononic crystal structure is depicted in Fig. 3.8. The size of the defect is determined by the size of the unit cell of the phononic shield a.

For the soft-clamped design, the boundary conditions, stated for the square membrane in (3.5), are modified. Instead of the membrane mode amplitude strictly decaying to zero at the boundary, we consider a defect amplitude that needs to match the modes in the pattern. In this way, the defect mode can evanescently couple into the pattern structure and avoid the strong bending at the edge. As a result, soft clamping eliminates the first dissipation term related to bending at the edges in Eq. (3.19), and the residual bending loss is now solely determined by the sinusoidal bending at the mode center, which scales with the defect area $\propto 1/a^2$. It is worth noting that for thin membrane oscillators, surface effects dominate the intrinsic dissipation mechanisms, and the intrinsic quality factor scales following $Q_{\text{int}} \approx \beta d^{-1}$. Therefore, we expect an overall quality factor dependence given by $Q \propto a^2/d$ [63] illustrated in Fig. 3.5.

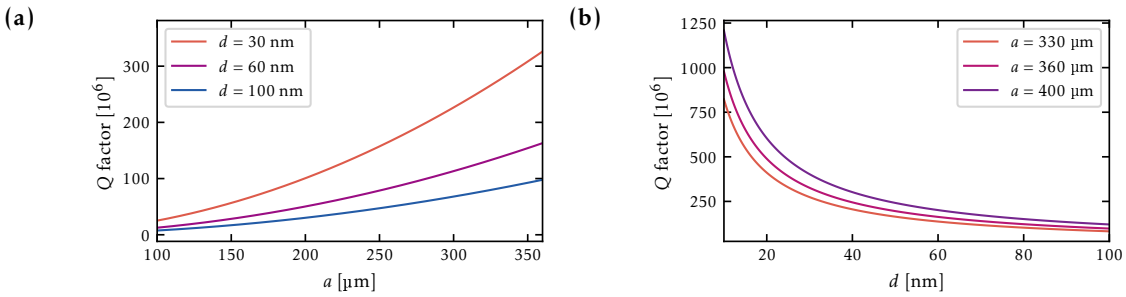

Figure 3.5: Theory predictions for the quality factor Q depending **(a)** on the defect size a and **(b)** on the membrane thickness d.

Similar to bandgap of the previously mentioned square membranes, the width of the bandgap is defined by the contrast between pads versus the tether sizes [64]. However, due to the extreme ratio between thickness and unit cell size $d/a \approx 1 \times 10^{-4}$, the bandgap opened by the phononic pattern is not expected to be complete but rather a quasi-bandgap according to simulations performed with the finite element method[2] [162]. The bandgap is first simulated via the stationary stress distribution, shown in Fig. 3.6 (a), through a parametric sweep of a unit cell for an unconstrained structure [64]. This is followed by an eigenfrequency estimation, which can be visualized by a band diagram, as shown in Fig. 3.6 (b) and (c). The material parameters used for the simulations are SiN density $\rho = 2700\,\text{kg/m}^3$, applied film stress 1 GPa, Poisson ratio $\nu = 0.27$, and Young's module $E = 270\,\text{GPa}$. Even with an incomplete bandgap we expect more than a 40 dB suppression of the mechanical amplitude in the phononic pattern.

For the design of the phononic pattern, determining the mass contrast between tethers and pad, we are thus facing a trade-off between strong localization and thus protection from the radiative losses for a high mass contrast, at the cost of an increase in the mode bending at the clamping point and the associated internal dissipation mechanism for a low mass contrast. The optimal compromise has to be evaluated for the application.

[2] COMSOL multiphysics simulations

At room temperature, soft clamping that is counteracting an internal dissipation mechanisms is of paramount importance, whereas for cryogenic applications, the reduced internal damping rates might allow for a reduction in soft-clamping and thus a stronger localization [64].

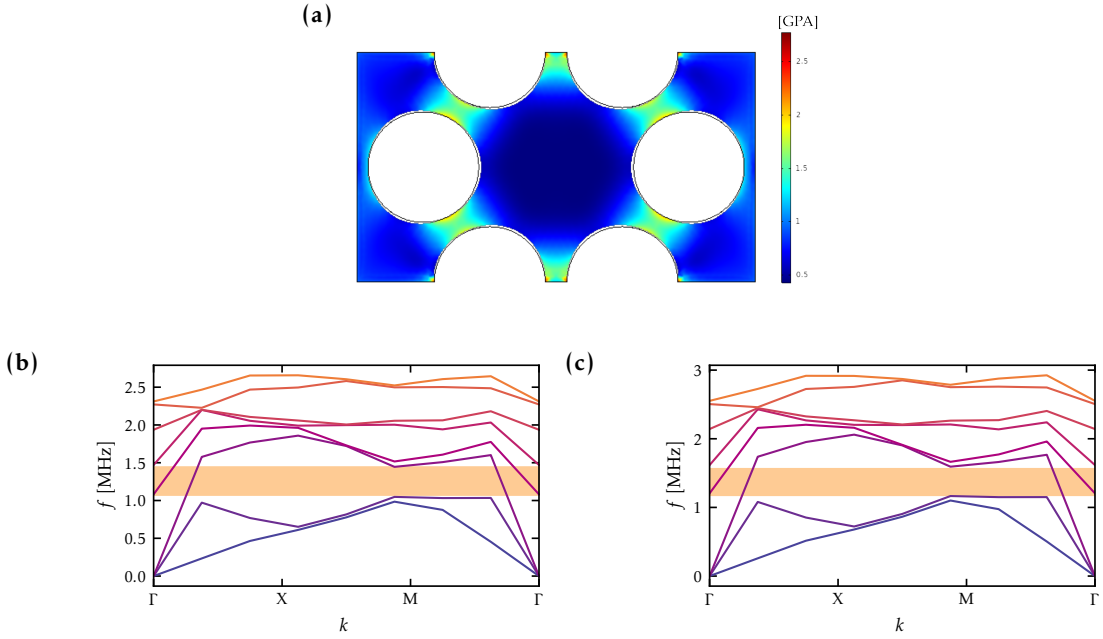

FIGURE 3.6: **(a)**: Simulations of the Von Mise stress of the phononic pattern unit cell in GPa. Resulting band diagram with respect to the wave vector k depending on the pattern geometry with a radius in **(b)** $r = 50\,\mu m$ and in **(c)** $r = 45\,\mu m$, assuming a stress of 1.2 GPa, and a bridge width $b = 20\,\mu m$ resulting in $a = 360\,\mu m$ respectively $a = 330\,\mu m$.

Our design follows the low-mass-contrast approach, and the phononic pattern is aiming for a mechanical resonance frequency above 1 MHz, in order to avoid technical noises from lasers and electronics, with a phononic bandgap around this central frequency. This involves design rules that are very similar to those discussed for the Si phononic shield membranes.

The central frequency is mostly determined by the size of the central defect a in the structure and the applied stress. The fundamental frequency reduces with increasing defect size a, which should not exceed $400\,\mu m$ to prevent the frequency from dropping below 1 MHz for an applied stress of around 1.2 GPa. The bandgap width depends on the mass ratio between pads and tethers, which is determined by the hole diameter in the pattern, $2r$, and the bridge width b. The dimension of the bridge width is limited by the fabrication yield of the tethers, as shown in the stress simulations that peak at the tethers, see Fig. 3.8. For $r = 50\,\mu m$ and $b = 20\,\mu m$ we obtain a lattice constant of $a = 6r + 3b = 360\,\mu m$, resulting in a bandgap width of 370 kHz around the frequency band of 1.2 to 1.5 MHz. A smaller a can shift the bandgap up in frequency, as shown in Fig. 3.6 (c) for $r = 45\,\mu m$, resulting in a lattice constant of $a = 330\,\mu m$ and a bandgap ranging from 1.3 to 1.7 MHz. For comparison, a design with $r = 50\,\mu m$ and $b = 10\,\mu m$ is simulated to open a bandgap of 450 kHz around a very similar central frequency.

There are a few design details allowing to improve the properties of the SCM even further. For instance the quality factors profit from designs that terminate the phononic

pattern with half holes, in order to prevent low quality modes from existing at the edge of the structure. These modes are undesirable as they can act as gateways for exterior acoustic noise and may have mechanical frequencies that lie within the bandgap [145]. Furthermore, the force sensitivity can be boosted by introducing additional holes in the pattern at the circumference of the central defect, leading to a reduction of the effective mass of the defect mode [145].

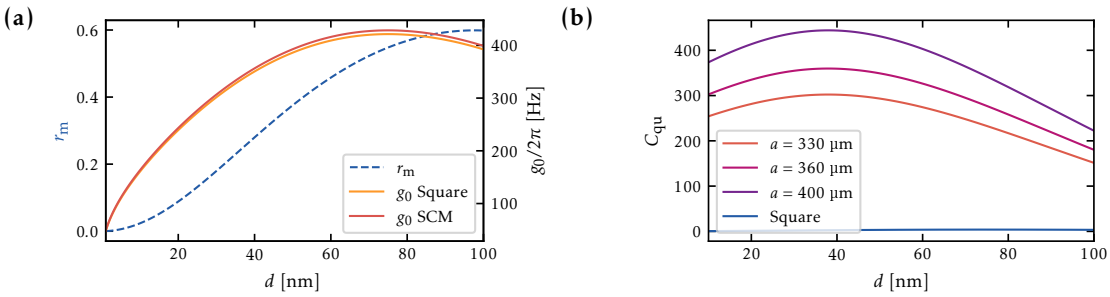

FIGURE 3.7: **(a)**: Theory predictions for optomechanical coupling depending on the membrane thickness compared to the membrane reflectivity (blue) on the left axis for both the square (orange) and the SCM (red). **(b)**: Resulting cooperativity for an environmental temperature $T = 10\,\mathrm{K}$ for various defect sizes a.

3.6.2 Optomechanical Coupling

During the design process of a mechanical oscillator for optomechanical experiments, it is crucial to consider the membrane thickness, which affects both the reflectivity and the effective mass, ultimately influencing the optomechanical coupling strength g_0. Additionally, the thickness also impacts the quality factor, creating a trade-off that is best evaluated using the quantum cooperativity [see Eq. (1.61)], which is given by the ratio between the measurement rate $\Gamma_{\mathrm{meas}} \propto g_0^2 \propto r_m^2/m$, and the thermal decoherence rate $\gamma_{m,\mathrm{th}} \propto Q^{-1}$. A quantum cooperativity $C_{qu} > 1$ benchmarks the entry into the quantum backaction dominated regime [cf. Ch. 1], and thus into quantum experiments [44]. Here, we will only consider the influence of the membrane design criteria on this value for the optical cavity used in the experiment.

Figure 3.7 illustrates that the square and the SCM are expected to have comparable vacuum coupling strengths, peaking at a thickness of approximately $d = 70\,\mathrm{nm}$. This thickness is slightly lower than the optimal value for reflectivity, which would be at $\lambda/4 \approx 100\,\mathrm{nm}$, due to the impact of the the effective mass on g_0. However, when considering the cooperativity at moderate cryogenic temperatures ($T = 10\,\mathrm{K}$), the soft clamped membranes are predicted to have significantly higher cooperativities $C_{qu} \gg 1$ owing to their higher quality factors, which vary linearly with the membrane thickness d. On the other hand, the square membrane is expected to have a much lower quality factor, with a cooperativity barely exceeding $C_{qu} > 1$. Note that we did not consider any modification of the quality factor with thickness for the square membrane, as losses are primarily dominated by bending at the edges.

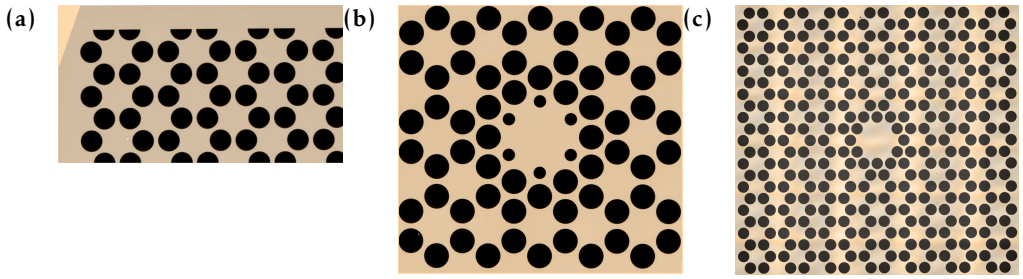

FIGURE 3.8: Microscope images showing details of different SCM designs. **(a)**: Half hole termination at the upper edge. **(b)**: Additional holes in the pattern at the center defect. **(c)**: Whole structure.

3.6.3 Experimental Samples

We will now consider three variations of SCM designs with holes of sizes $r = 45\,\mu\text{m}$ (Design 1), $r = 50\,\mu\text{m}$ (Design 2), and Design 3, featuring $r = 50\,\mu\text{m}$ and an additional ring of small holes at the center of the defect and half-hole terminations on two of the four membrane edges. The characteristics of these membrane designs are listed in Tab. 3.1. The thermal displacement spectra of membrane SCM-22-S1 is displayed in Fig. 3.9. We can identify a bandgap in the spectral region around the fundamental defect mode at $f = 1.34\,\text{MHz}$. In general we observe that the spectrum is more densely populated than for the square membranes. This is on the one hand due to the incompleteness of the generated bandgap, and on the other hand due to the numerous modes that are supported in the patterned structure. However as long as the spectral region around the main peak of interested remains mostly depleted of spurious noise peaks, the mechanical mode of interest can be expected to be addressed without further disturbance.

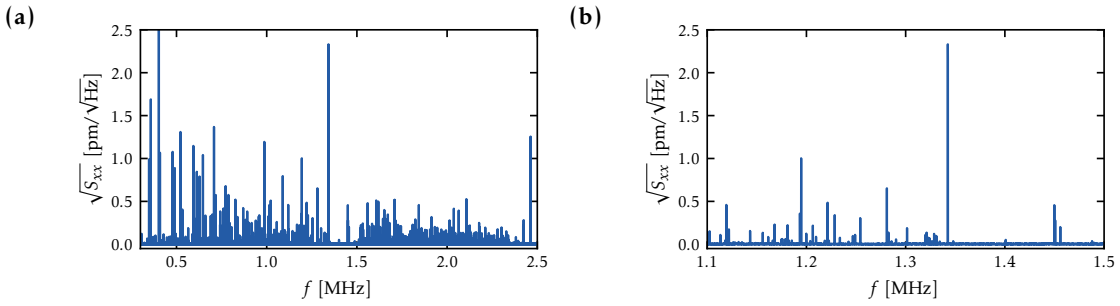

FIGURE 3.9: **(a)** : Thermal displacement spectrum of the membrane SCM-22-S1 at room temperature. **(b)**: Zoom into the bandgap region.

3.7 Optical Readout

Since the control of the mechanical motion in our optomechanical experiments is mediated by a light beam, the theoretically predicted optical readout efficiency, influenced by the geometrical dimensions of mechanical mode and the optical light beam, is considered as an important design parameter. The strength of the optomechanical coupling depends on the combination of the light field distribution coinciding with the mechanical mode shape under consideration. In fact, the light field performs a weighted average over the mechanical displacement amplitude distribution according to its intensity profile [163].

The optical mode used for probing is the fundamental TEM_{00}, which has a transverse intensity profile in the x, y plane given by

$$\phi_{\mathrm{opt}}(x,y) \propto \mathrm{e}^{-2\frac{x^2+y^2}{w_0^2}}, \tag{3.20}$$

where w_0 is the cavity mode waist. The overlap between the mechanical and the optical mode is expressed by the efficiency coefficient [55]

$$\eta_{ij} = \left| \int_0^{l_x} \int_0^{l_y} u_{ij}(x,y)\phi_{\mathrm{opt}}(x,y)\mathrm{d}x\mathrm{d}y \right|, \tag{3.21}$$

and the effective optomechanical coupling strength then results in $g_0 \to \eta_{ij} g_0$. For a good

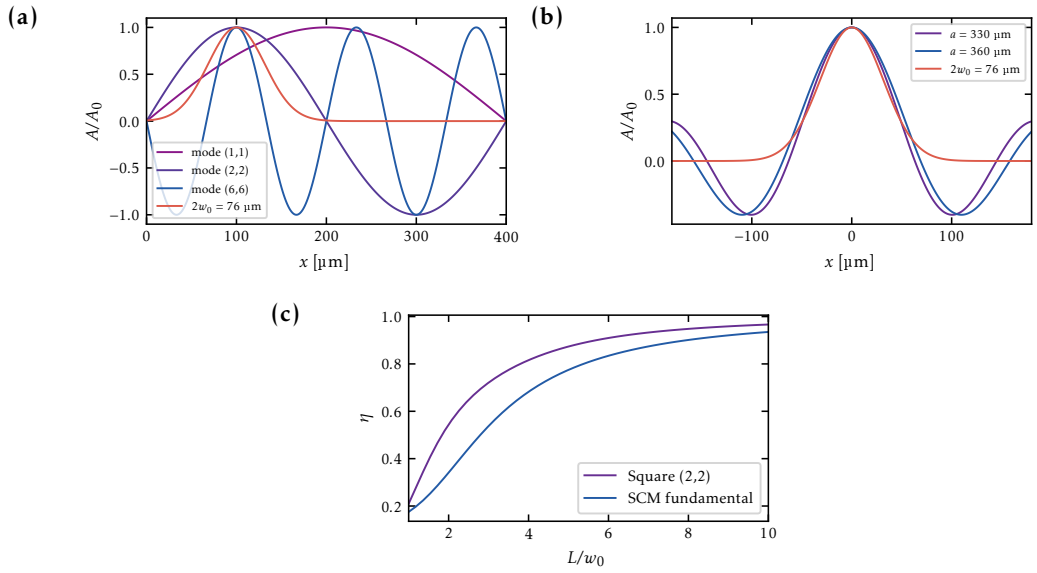

FIGURE 3.10: Expected amplitude of the mechanical and optical modes, each normalized to their maximal amplitude A_0, illustrating the optical overlap between the cavity light beam and the mechanical modes of **(a)** the square membrane and **(b)** the SCM modes. **(c)**: Computed overlap efficiency coefficient η for the experimentally relevant mechanical modes based on the ratio between the beam waist w_0 and the characteristic length of the membrane L, either the side length l for the square membrane, or the defect diameter a for the SCM.

overlap, it is essential to position the optical beam at an anti-node of the mechanical mode, and the optical waist should be much smaller than the mechanical wavelength $\lambda_{ij} = 2l/\sqrt{i^2+j^2}$. For the square membrane of side length $l = 400\,\mu\mathrm{m}$, which has $\lambda_{11} = 560\,\mu\mathrm{m}$ and the flexural mode shape as stated in (3.6), together with a standard cavity waist of $38\,\mu\mathrm{m}$ used in our experiments, this is satisfied for the lower mechanical modes. In fact, we find that for a cavity beam aligned in the center of the membrane, $\eta_{11} = 0.97$. In the optomechanical experiments, we aim to couple to the (2,2) mode, which is why the beam is placed in one of the four quadrants, resulting in an ideal overlap $\eta_{22} = 0.88$. In that case, we expect a reduction of the coupling to the (1,1) mode to $\eta_{11} = 0.68$. For a higher order mode, such as the (6,6) for instance, the overlap coefficient is already drastically reduced, and we expect $\eta_{66} = 0.33$.

For the nearly circular mode shapes of the SCM, the theoretical prediction is plotted in Fig. 3.10 for two different defect sizes, resulting in $\eta_0 = 0.72$ for $a = 330\,\mu\text{m}$ and $\eta_0 = 0.75$ for $a = 360\,\mu\text{m}$. We can deduce as a rule of thumb that the cavity waist should not be larger than one quarter of the defect size.

3.8 Characterization Measurements

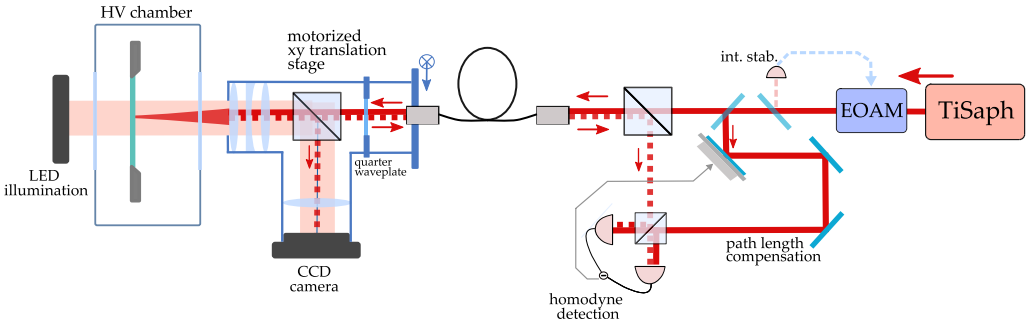

FIGURE 3.11: Optical setup for membrane characterization, starting from the laser light that is split into a local oscillator and a probe beam that is fiber coupled, with the fiber out-coupler and an objective to focus the light beam on the membrane center on a motorized translation stage. The back-reflected light is both imaged on a camera and overlapped with the local oscillator for detection in a homodyne setup.

We can characterize the nanomechanical membranes by determining the displacement spectrum, quality factors and spatial mode shapes of individual mechanical modes. Therefore, we place the membranes inside of a high-vacuum chamber at room temperature, embedded in an optical setup that is presented in Fig. 3.11. We address the membrane with a laser beam at a wavelength of $\lambda = 780\,\text{nm}$, passing through a polarizing beamsplitter cube and a quarter waveplate, such that the light reflected back from the membrane is separated from the ingoing beam and is combined with a local oscillator for a homodyne detection. The homodyne phase is controlled by a piezo-actuated mirror in the path of the local oscillator. Fixing the phase between the signal and the local oscillator to a constant value around zero, allows us to detect the phase quadrature of the backreflected light carrying the phase modulation created by the mechanical vibrations. The path length of the local oscillator is deliberately increased to make it more similar to the signal path length and improve the balanced detection. Figures 3.3 and 3.9 display the thermal displacement spectra for a square membrane and a SCM respectively. Additionally, the optical setup allows to illuminate the membranes with red LEDs and split off a small amount of light with a 90:10 beamsplitter cube to focus it on a CCD camera, obtaining the images shown in Fig. 3.12. Furthermore, the same optical setup allows to measure the quality factor of the membranes via ringdown measurements and image the mechanical mode shape using a piezo-actuated raster scan.

3.8.1 Quality Factor

The quality factor can be determined from the decay time of the mechanical oscillator, while it rings down to its steady-state thermal occupation. Therefore, we excite a specific mechanical mode by applying a drive at its resonance frequency using a piezo actuator

Name	r (μm)	b (μm)	Design #	f (MHz)	Q (10^6)
SCM-20-S1	45	20	1	1.27	57
SCM-20-S3	50	20	2	1.21	8
				1.31	52
SCM-22-S1	50	20	2	1.34	74
SCM-22-S2	50	20	3	1.21	63
SCM-22-S6	50	20	3	1.19	8.3

Table 3.1: Characteristic parameters of various SCM designs.

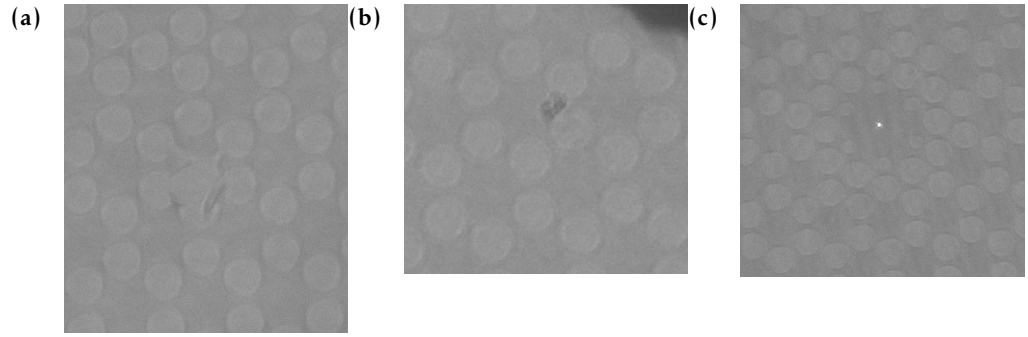

Figure 3.12: Three camera images of SCMs. **(a)**: Tether that yielded spontaneously while mounted inside vacuum chamber without external intervention. **(b)**: Dust particle on the phononic shield. **(c)**: Focused laser beam in optical test setup on the defect of a SCM.

mounted below the membrane holder inside of the vacuum chamber. Alternatively, we can apply an amplitude modulation to the ingoing light using an electro-optical amplitude modulator (EOAM)[3] as shown on the optical setup sketch in Fig. 3.11. Both methods allow to populate the targeted mechanical mode with a high number of excitations. After switching off the drive, we extract the rate at which the excitations decay, which determines the damping of the mechanical oscillations as stated in Eq. (3.9). The evolution of the excitations follows $\bar{n}(t) = \bar{n}(0)\mathrm{e}^{-\gamma_\mathrm{m} t}$, and allows us to infer the mechanical damping rate, and consequently, the quality factor using the expression $Q = \Omega_\mathrm{m}/\gamma_\mathrm{m}$. Figure 3.13 shows two exemplary ringdowns, illustrating the ringdown of a square membrane, resulting in a quality factor of $Q = 1.5 \times 10^6$ for the (2,2) mode at $f = 1.93\,\mathrm{MHz}$. In comparison, we obtain $Q = 75 \times 10^6$ for a SCM defect mode at $f = 1.34\,\mathrm{MHz}$, resulting in $Qf \approx 10^{14}\,\mathrm{Hz}$ for that particular mode.

3.8.2 Mode Imaging

To image the mechanical mode shape, we use a raster scan measurement setup shown in Fig. 3.11, which was built by Bachelor student Gabriel Gysin. For this purpose, the laser light is fiber-coupled, and both the out-coupler, together with the objective lens[4], used to focus the laser to a beam waist of $4\,\mu\mathrm{m}$, are mounted on a piezo-actuated[5] two-dimensional translation stage[6]. The piezo step size amounts to $0.047\,\mu\mathrm{m}$. The motorized piezo-actuators allow us move the incident light beam in the plane parallel to the

[3] Thorlabs EO-AM-NR-C1

[4] Thorlabs 1-inch Achromatic Doublet $f = 50\,\mathrm{mm}$ in a Thorlabs zoom precision mount

[5] Newport Closed Loop Picomotor Actuators 8311, New Focus Picomotor Controller 8743-CL

[6] New Focus Model 9066-XYZ-M

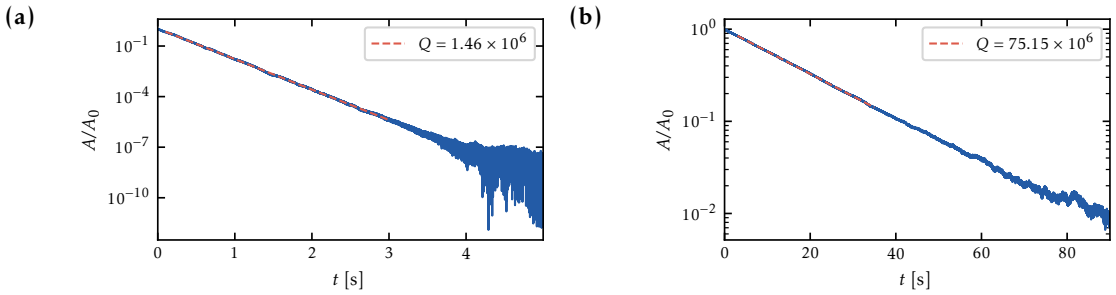

FIGURE 3.13: Ringdown measurement at room temperature **(a)** of the (2,2) mode of the square membrane 1-50-226/1 with $f = 1.9\,\mathrm{MHz}$ and **(b)** the fundamental defect mode of the SCM-22-S1 membrane with $f = 1.3\,\mathrm{MHz}$.

membrane surface, which can thus be scanned in two dimensions. At each step a spectrum of the mechanical displacement is acquired using the backreflected light from the membrane, coupled back into the fiber and sent onto the homodyne detection scheme as described previously. To increase the processing speed, we perform 275 piezo steps between consecutive acquisitions, resulting in a spatial resolution of $\sim 7\,\mu\mathrm{m}$. More details regarding the mode imaging setup can be found in [164].

A two-dimensional plot illustrating the spatial mode distribution of a certain mechanical mode is obtained by integrating each spectrum (acquired with a resolution bandwidth of 25 Hz) in a spectral window around the chosen mode frequency. Figure 3.14 illustrates the mode shapes recorded for each mechanical mode that shows a visible peak in the displacement spectrum in Fig. 3.3 for the square membrane. Also for the SCMs the mechanical displacement peaks visible in the spectrum in Fig. 3.9 can be associated to the mode shapes shown in Fig. 3.15 and 3.16.

In particular, raster scans allow us to shed light on the mechanical mode shape for SCM and associate the measured quality factors to well-defined defect modes. For the SCM-20-S1 and SCM-20-S3 devices, we measure high quality factor ($Q > 50 \times 10^6$) for modes that do not coincide with the fundamental defect modes reported for similar structures in the literature [63, 64]. Additionally, in the spectra, we observe a splitting of the fundamental mode into three distinct frequencies, which could be explained by a hybridization of the defect mode with modes in the structure in the three directions of symmetry. For the newer generation of devices, SCM-22-S1 and SCM-22-S2, the quality factors $Q > 70 \times 10^6$ appear for the fundamental defect mode, which meet the requirements for a sufficiently high optomechanical coupling strength in an optical cavity.

To gain insights into the lack of high quality factors for some samples, we analyze the mode localization at the center defect. Therefore, we plot the mode amplitude averaged over the central line, as shown in Fig. 3.17, for the points within the black lines. For example, when comparing SCM-22-S1, SCM-22-S2 and SCM-22-S6, displayed in Fig. 3.17, we observe $Q > 50{\times}10^6$ for S1 and S2, while for SCM-22-S6, the same mode only achieves $Q \approx 8{\times}10^6$. We plot the exponential decays following $\sim \mathrm{e}^{-\gamma_j(X-X_0)}$ and $\sim \mathrm{e}^{-\gamma_j(Y-Y_0)}$ in both X and Y direction across the sample (orange), where γ_j is the decay parameter of membrane sample SCM-22-Sj. Indeed the devices with higher Q factors have a larger decay parameter $\gamma_1 = \gamma_2 = 2\gamma_6$. This suggests to draw a link between a strong localization at the center defect, and thus a stronger spatial amplitude decay away from the central defect and the appearance of high quality factors ($Q > 50 \times 10^6$).

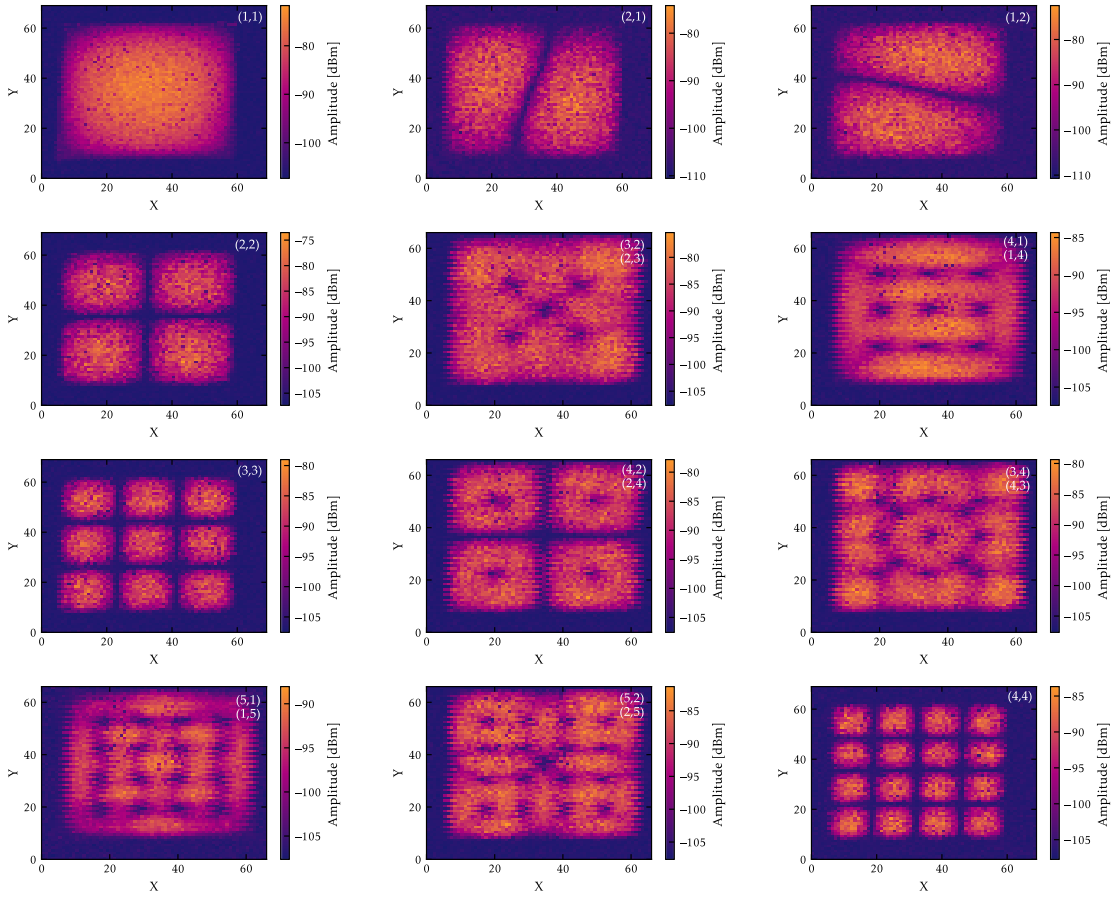

FIGURE 3.14: Raster scan of the square membrane 1-50-226/1, showing the lowest frequency drum modes, in sequential order as marked in the spectrum in Figure 3.3

3.9 Conclusion

In this chapter, we discussed the theoretical framework for describing the vibrations of membrane mechanical oscillators. We considered the various dissipation mechanisms present in these oscillators and described two design strategies that lead to the reduction of dissipation for certain mechanical frequencies: a phononic shielded square membrane mitigating radiative losses, and a SCM that additionally reduces the bending losses. We not only considered the design criteria for a high quality factor, but also for a strong coupling to a beam of light, which will be useful for our optomechanical experiments. Furthermore, we described an optical setup to characterize the mechanical displacement amplitude, quality factors, and mode shapes and presented the resulting measurements for both phononic shielded square membranes, and SCMs. For the square membranes we measured quality factors of $Q = 1.5 \times 10^6$ for the (2,2) mode at a frequency of $f = 1.93\,\mathrm{MHz}$ at room temperature, whereas for the SCM we found $Q = 75 \times 10^6$ at $f = 1.34\,\mathrm{MHz}$.

Furthermore, the mode shape imaging that we implemented using a motorized two-dimensional raster scan is especially interesting for the SCM, where the correspondence between resonance frequencies and mode shapes is not trivial, and illustrates a correlation between a strong localization of the modes at the center and a high quality factor.

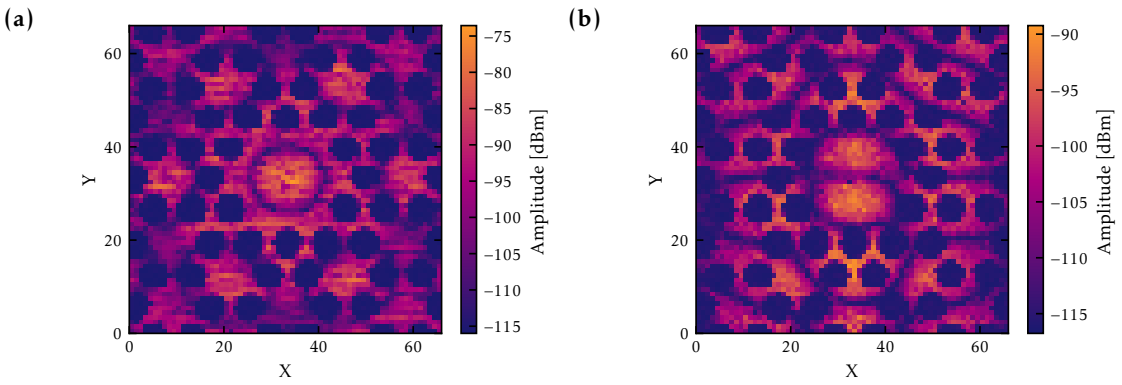

FIGURE 3.15: Raster scan of the membrane SCM-22-S1, showing the two lowest frequency spatial distributions in the spectral bandgap, at **(a)** $f = 1.34\,\mathrm{MHz}$ and at **(b)** $f = 1.45\,\mathrm{MHz}$.

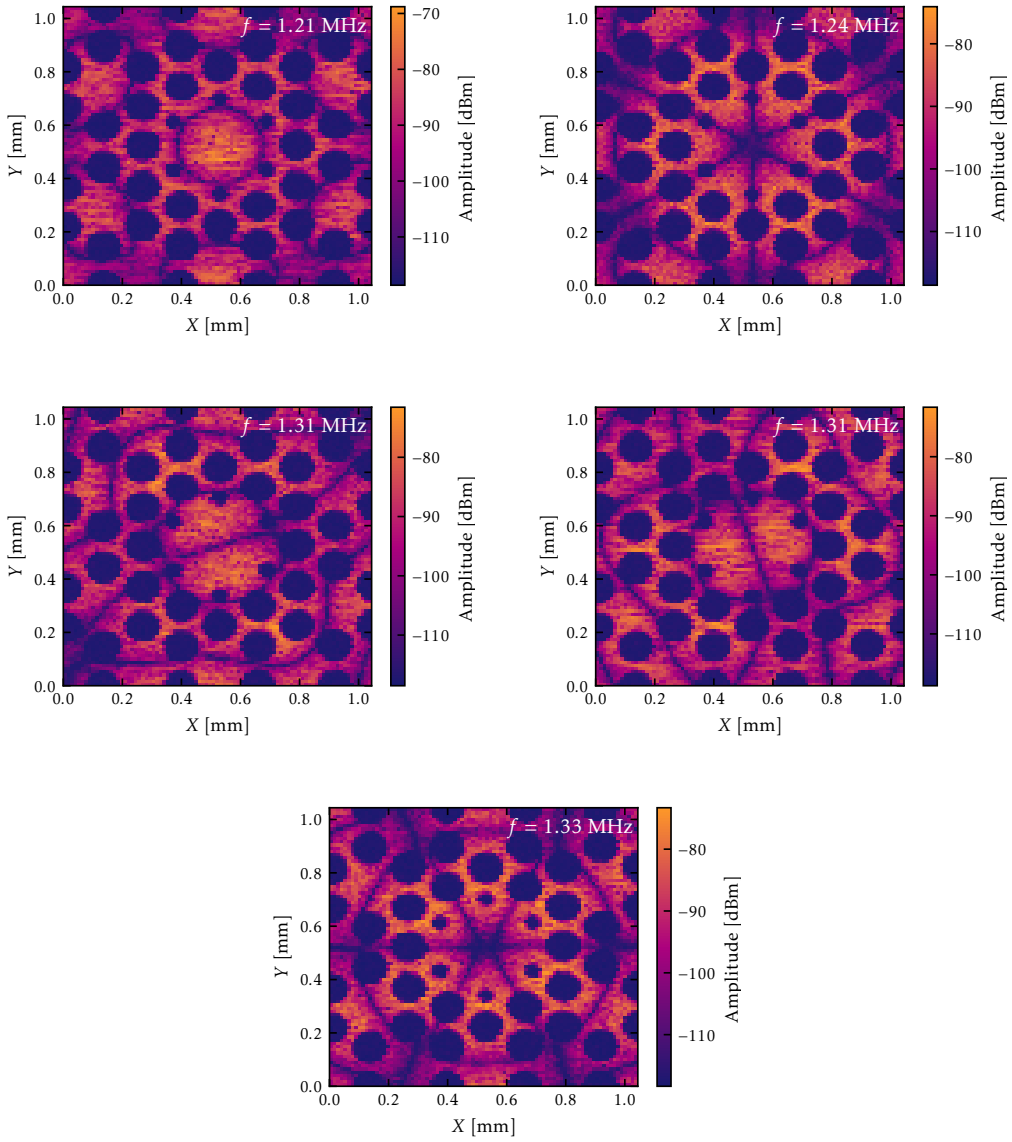

FIGURE 3.16: Raster scans of the membrane SCM-22-S2, showing zooms onto the defect for the lowest defect mode frequencies between $f = 1.21\,\mathrm{MHz}$ and $f = 1.33\,\mathrm{MHz}$.

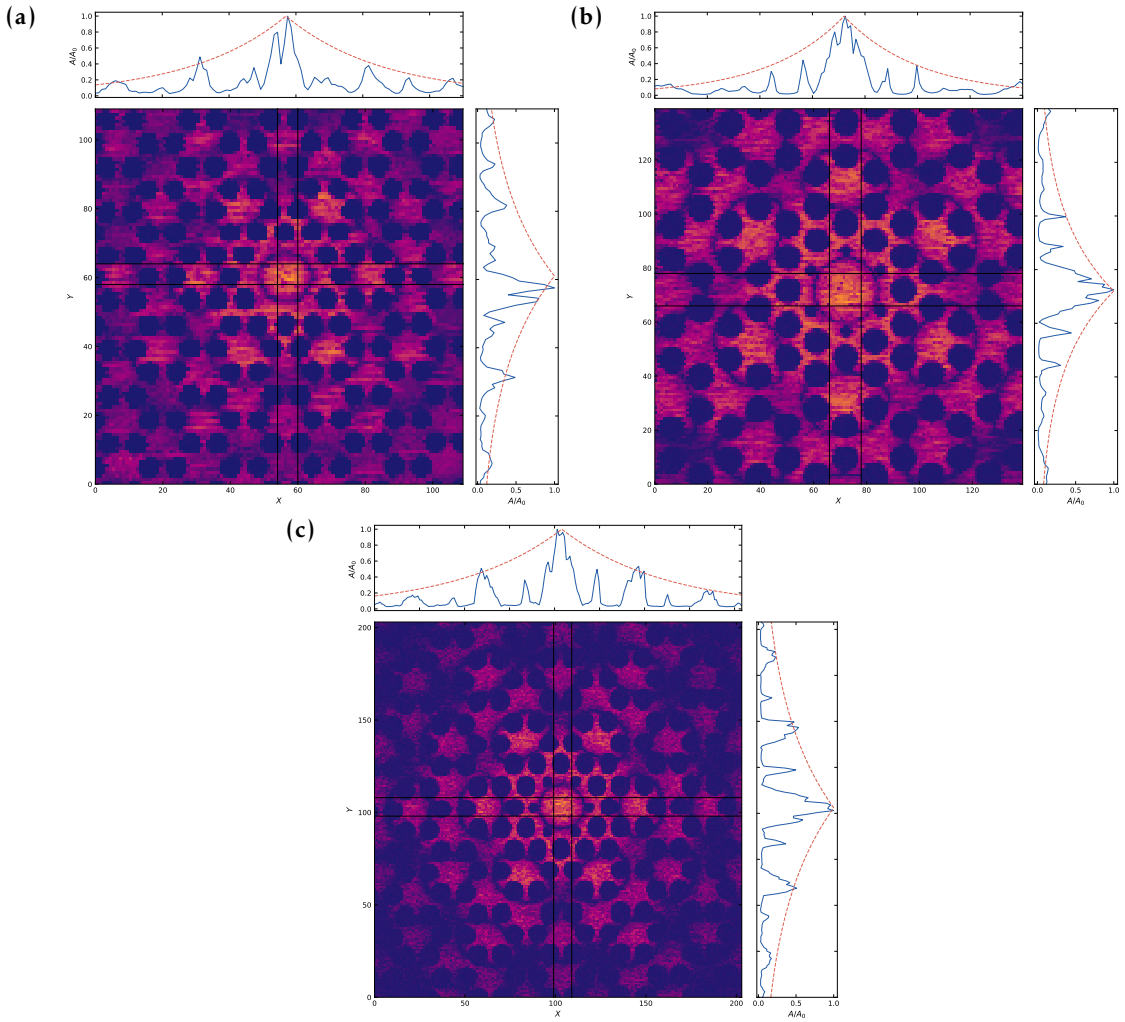

FIGURE 3.17: Raster scans of the membranes **(a)** SCM-22-S1, **(b)** SCM-22-S2, and **(c)** SCM-22-S6 for the fundamental defect mode. The sideplots show the normalized amplitude averaged over the points within the black lines. The exponential decay lines (red dashed) are plotted for visual guidance.

Chapter 4

Optomechanical Setup

The nanomechanical membranes described in the previous chapter, with their high quality factors and low masses, respresent one of the leading systems for optomechanical experiments. We construct our optomechanical setup using these SiN membrane oscillators and a free-space Farby-Perot cavity, as pioneered in [55]. This combination is especially advantageous because it allows for the independent optimisation of the constituting elements.

The membranes used in this work are thin sheets with a film thickness that typically lies between 30 and 100 nm. Thus, their thickness is small compared to the optical wavelength of 780 nm at which we operate, allowing for the resolution of the standing wave pattern of the light inside the cavity. Due to the refractive index of SiN, the vibrations of the mechanical oscillator inside the cavity standing wave produces a modulation of the cavity resonance frequency, which is measurable as a phase modulation on the outgoing light beam [55, 165]. The large area and the low effective mass of the mechanical mode promote the extent to which the radiation pressure of the optical field modifies the motion of the mechanical oscillator, given by the optomechanical coupling strength g_0.

For the optomechanical experiments presented in this work the requirements on the optical cavity consist in an efficient interface of the mechanical motion with light and a fast response. That is why we aim for a strongly asymmetric cavity, where the losses through the port that is not used for interfacing are minimized. The cavity mirrors are chosen to reduce losses through the transmissive port while obtaining the desired cavity bandwidth and spot size depending on the mechanical mode we plan to address. The cavity mirror reflectivities are chosen such that most of the light ($> 99\%$) is leaving the cavity again through the incoupling port. Furthermore, with the frequency of the mechanical mode of interest $\Omega_\mathrm{m}/(2\pi) = 2\,\mathrm{MHz}$ and the cavity linewidth $\kappa/(2\pi) = 55\,\mathrm{MHz}$, our membrane-cavity resides deeply in the unresolved sideband regime, providing a fast cavity response. The mechanical signal effectively couples directly to the travelling field outside of the cavity, with only a small delay ($\sim 6\,\mathrm{ns}$) generated by the cavity.

In this chapter, we characterize the optomechanical interaction that occurs between the optical cavity field and the inserted membrane. This membrane-cavity realizes a linear optomechanical coupling equivalent to the canonical formalism discussed in Ch. 1. We present our experimental setup that includes the membrane-cavity, optimized for usage at cryogenic temperatures, as well as the optical and electronic components used to address and detect the mechanical motion. We also discuss the associated characterization measurements determining the optomechanical coupling strength and the mechanical occupation number. These measurements are necessary to calibrate the experimental results presented in Ch. 5.

4.1 Membrane-in-the-Middle

In the following we will present the theoretical description of a membrane-in-the-middle system as depicted in Fig. 4.1.

Transfer matrix picture We begin by describing the so-called transfer matrix formalism, which was elaborated in the pioneering works of [165, 55, 166] for a stack of optical elements. This formalism establishes the relationship between the incident and transmitted electromagnetic field when encountering different optical elements in a concise notation. We will consider the matrices that arise for the most commonly encountered optical elements [167] (section6.2). For instance, the transmission through a dielectic element can be described in terms of the transfer matrix determined by its reflectivity r and transmission t [167]

$$M_{\mathrm{d}}(r,t) = -\frac{1}{t}\begin{pmatrix} t/t^* & -r^* \\ r & -1 \end{pmatrix}. \tag{4.1}$$

The matrix at an interface between two media with different refractive index n_1 and n_2 results in

$$M_{\mathrm{int}}(n_1,n_2) = -\frac{1}{2n_1}\begin{pmatrix} n_1+n_2 & n_1-n_2 \\ n_1-n_2 & n_1+n_2 \end{pmatrix}. \tag{4.2}$$

The propagation of the electromagnetic field with wavevector $k = 2\pi/\lambda$ and wavelength λ in a medium with refractive index n over a distance L is described by

$$M_{\mathrm{p}}(L) = \begin{pmatrix} \mathrm{e}^{\mathrm{i}knL} & 0 \\ 0 & \mathrm{e}^{-\mathrm{i}knL} \end{pmatrix}. \tag{4.3}$$

The propagation through a thin dielectric membrane with a refractive index n and a thickness d can thus be described by the transfer matrix
$M_{\mathrm{m}} = M_{\mathrm{int}}(1,n)M_{\mathrm{p}}(d)M_{\mathrm{int}}(n,1)$ see section 7.1 of [167] . By associating the composed matrix M_{m} with the expression in Eq. (4.1), we can determine the complex reflection and transmission coefficients $t_{\mathrm{m}} = 1/M_{\mathrm{m}}^{(2,2)}$ and $r_{\mathrm{m}} = M_{\mathrm{m}}^{(1,2)}/M_{\mathrm{m}}^{(2,2)}$, such that

$$\begin{aligned} t_{\mathrm{m}} &= \frac{2n}{(1+n^2)\mathrm{i}\sin(nkd) + 2n\cos(nkd)}, \\ r_{\mathrm{m}} &= \frac{(1-n^2)\mathrm{i}\sin(nkd)}{(1+n^2)\mathrm{i}\sin(nkd) + 2n\cos(nkd)}. \end{aligned} \tag{4.4}$$

We proceed by considering the situation where the membrane is placed between two highly reflective mirrors with reflection and transmission coefficients r_1, r_2 and t_1, t_2 respectively. The origin of the membrane displacement x_{m}, is chosen at the position of the second mirror. The transfer matrix that describes the propagation through the membrane-cavity can be expressed as a sequence of matrices corresponding to the beam passing through the two mirrors, the membrane in the center, and the free propagation between the optical elements

$$M_{\mathrm{MIM}} = M_{\mathrm{d}}(r_2,t_2)M_{\mathrm{p}}(x_{\mathrm{m}})M_{\mathrm{d}}(r_{\mathrm{m}},t_{\mathrm{m}})M_{\mathrm{p}}(L-x_{\mathrm{m}})M_{\mathrm{d}}(r_1,t_1). \tag{4.5}$$

The complete transmission of light through the membrane-cavity, as illustrated in Fig. 4.1 results in

$$\begin{pmatrix} A_{\text{out}} \\ 0 \end{pmatrix} = M_{\text{MIM}} \begin{pmatrix} A_{\text{in}} \\ A_{\text{refl}} \end{pmatrix}. \tag{4.6}$$

In the following, we make the assumption that the reflection and transmission coefficients denoted as r_i and t_i respectively, have zero imaginary parts, such that $t_i = \sqrt{1 - r_i^2}$. This assumption holds when losses are negligible, and results in the expression of the overall transmission and reflection

$$\begin{aligned} t_{\text{MIM}} &= \frac{t_1 t_2 t_{\text{m}} \mathrm{e}^{\mathrm{i}kL}}{r_1 r_2 \mathrm{e}^{2\mathrm{i}kL} + r_1 r_{\text{m}} \mathrm{e}^{2\mathrm{i}k(L-x_{\text{m}})} + r_2 r_{\text{m}} \mathrm{e}^{2\mathrm{i}kx_{\text{m}}} - 1}, \\ r_{\text{MIM}} &= -\frac{1}{r_2}\left(1 - \frac{(1+r_2^2)\left(r_1 r_{\text{m}} \mathrm{e}^{\mathrm{i}k(L-x_{\text{m}})} - 1\right)}{r_1 r_2 \mathrm{e}^{2\mathrm{i}kL} + r_1 r_{\text{m}} \mathrm{e}^{2\mathrm{i}k(L-x_{\text{m}})} + r_2 r_{\text{m}} \mathrm{e}^{2\mathrm{i}kx_{\text{m}}} - 1}\right). \end{aligned} \tag{4.7}$$

The resonance condition of the modified cavity frequency $\omega_{\text{c}} = ck$ with the propagation speed of light in free space c, can be determined by finding the maxima of the transmission coefficient numerically. This can be done by solving for the length of the cavity L that satisfies $|\mathrm{d}t_{\text{MIM}}(L)/\mathrm{d}L|^2 = 0$, which is equivalent to determining the parameters that maximize the intracavity power. The resulting equation for the general case, is plotted in Fig. 4.2. For a high finesse cavity, the effect of different reflectivities of both mirrors on the resonance frequency shift can be neglected [168].

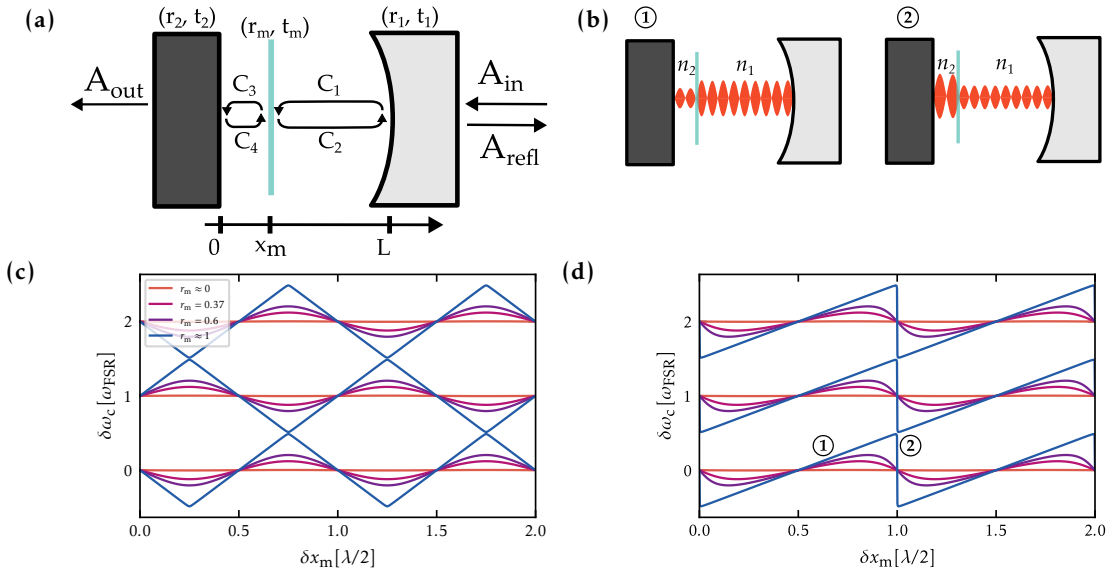

FIGURE 4.1: **(a)**: Sketch of the in- and outgoing light fields of the optomechanical setup, along with the circulating fields in both subcavities formed by the membrane. **(b)**: Two subcavities formed by the mechanical oscillator with ①: the low-reflective incoupling mirror, and ②: with the highly-reflective end mirror. **(c,d)**: Modification of the optical cavity frequency depending on the membrane displacement and reflectivity, for relevant membrane thicknesses, in the case of a SCM ($d = 35\,\text{nm}$), a square membrane ($d = 100\,\text{nm}$) and a highly reflective membrane, with the coarse membrane position **(c)** $\bar{x}_{\text{m}} = L/2$ as described in Eq. (4.8) and **(d)** $\bar{x}_{\text{m}} = 0$ from Eq. (4.9)

The mechanical position can be expressed as $x_\mathrm{m} = \bar{x}_\mathrm{m} + \delta x_\mathrm{m}$ where $\bar{x}_\mathrm{m}$ is the average position and δx_m the small displacement excursions. For certain membrane positions, such as at the center or the end of the cavity ($\bar{x}_\mathrm{m} = L/2$ or $\bar{x}_\mathrm{m} = 0$), and assuming a small modification of the resonance frequency ($\omega_\mathrm{c} = \omega_N + \delta\omega_\mathrm{c}$) compared to the Nth order mode frequency ($\omega_N = N\pi/cL$), we obtain a simplified resonance equation for the cavity length. The membrane excursions δx_m around the equilibrium position $\bar{x}_\mathrm{m} = L/2$ result in a modification of the cavity resonance frequency

$$\delta\omega_\mathrm{c} = 2\omega_\mathrm{FSR}\left(N - \frac{(-1)^N}{2\pi}\arccos\left[|r_\mathrm{m}|\cos\left(2\frac{\omega_N}{c}\delta x_\mathrm{m}\right)\right]\right), \tag{4.8}$$

with $\omega_{FSR} = 2\pi c/(2L)$ the free spectral range. For a membrane placed at the end of a cavity ($\bar{x}_\mathrm{m} = 0$), the resonance condition is instead modified to

$$\delta\omega_\mathrm{c} = \omega_\mathrm{FSR}\left(N - \frac{(-1)^N}{2\pi}\arccos\left[\frac{-1 + |r_\mathrm{m}|\cos\left(2\frac{\omega_N}{c}\delta x_\mathrm{m}\right)}{1 + r_\mathrm{m}}\right]\right). \tag{4.9}$$

Both equations are plotted in Figure 4.1, where we additionally compare the modulation of the cavity resonance frequency depending on the reflectivity r_m of the inserted mechanical element. We note that at the maximal slope of the modulation of the cavity resonance, $\delta\omega_\mathrm{c}$ is linearly modified by the mechanical displacement δx_m and thus can easily be described by the canonical coupling formalism that we have previously derived.

Furthermore, the resulting cavity resonance condition can be interpreted as two subcavities, with lengths $\bar{x}_\mathrm{m}$ and $L - \bar{x}_\mathrm{m}$, that have been split up more or less strongly depending on the membrane reflectivity. Furthermore, the change in cavity resonance frequency is directly related to the optomechanical coupling parameter, as previously noted: $g_0 = -x_0\partial\omega_c/\partial x_\mathrm{m}$, where we only consider the linear coupling term, that occurs where the slope of the resonance frequency modulation is maximal. This corresponds to the situation where exactly one of the two subcavities is resonant with the light and the other one is anti-resonant. This generates the largest imbalance in radiation pressure between both sides of the membrane, leading to a strong optomechanical coupling, as will be explained in more detail in the following section.

Subcavity picture As an alternative to the transfer matrix formalism, we can treat the optomechanical cavity as being formed by two subcavities that are coupled via the weakly reflective membrane element as illustrated in Fig. 4.1. For a very low membrane reflectivity ($r_\mathrm{m} \approx 0$), the cavity behaves as a single cavity, while for a very high reflectivity, it behaves as two independent cavities. However, for intermediate reflectivites ($r_\mathrm{m} \ll r_1, r_2$) as expected for SiN membranes at a near infra-red optical frequency and with a thickness between 30 nm and 100 nm, there is a strong coupling between both subcavities, leading to avoided crossings and a modulation of the overall cavity resonance frequency. This is due to the mechanical motion effectively changing the lengths of the two subcavities, and thus their individual resonance frequencies.

We can derive an analytical expression for the optomechanical coupling strength using an intuitive approach, considering the radiation pressure force generated by the imbalance of photon momentum kicks from both sides of the mechanical oscillator, as described in [137].

The strength of the coupling depends on the distribution of the light field inside the cavity at the exact position of the membrane, given by the imbalance of light from

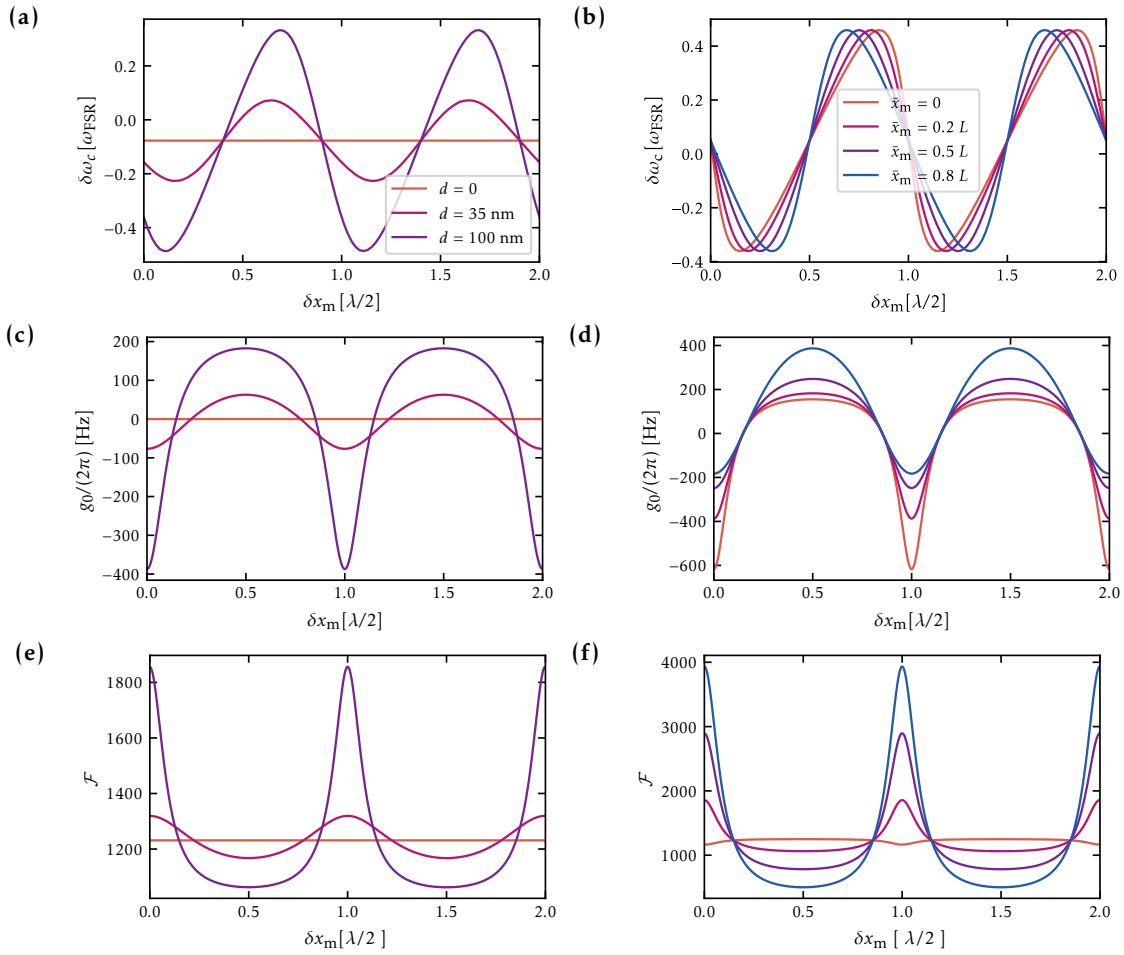

FIGURE 4.2: Theory predictions for optomechanical coupling and cavity parameters depending on the membrane position δx_{m} in the cavity standing wave for various membrane thicknesses d (left) and different coarse placements inside the cavity $\bar{x}_{\mathrm{m}}$ (right).

either side of the membrane, which itself is determined by its position. As the membrane thickness is only a fraction of a wavelength, the membrane is capable of resolving the nodes and antinodes of the cavity standing wave.

The photon lifetime in each subcavity is given as $\tau_1 = 2(L - x_{\mathrm{m}})/c$ and $\tau_2 = 2x_{\mathrm{m}}/c$. The population distribution for each of the subcavities then results in

$$\begin{aligned} n_1 &= \tau_1(|C_1|^2 + |C_2|^2), \\ n_2 &= \tau_2(|C_3|^2 + |C_4|^2). \end{aligned} \tag{4.10}$$

The cavity fields C_j are defined according to the sketch shown in Fig. 4.1, and are given by

$$\begin{aligned} C_1 &= -C_2 e^{2ik(L-x_{\mathrm{m}})}, \quad & C_3 &= t_{\mathrm{m}} C_1 + r_{\mathrm{m}} C_4, \\ C_4 &= -C_3 e^{2ikx_{\mathrm{m}}}, & C_2 &= r_{\mathrm{m}} C_1 + t_{\mathrm{m}} C_4. \end{aligned} \tag{4.11}$$

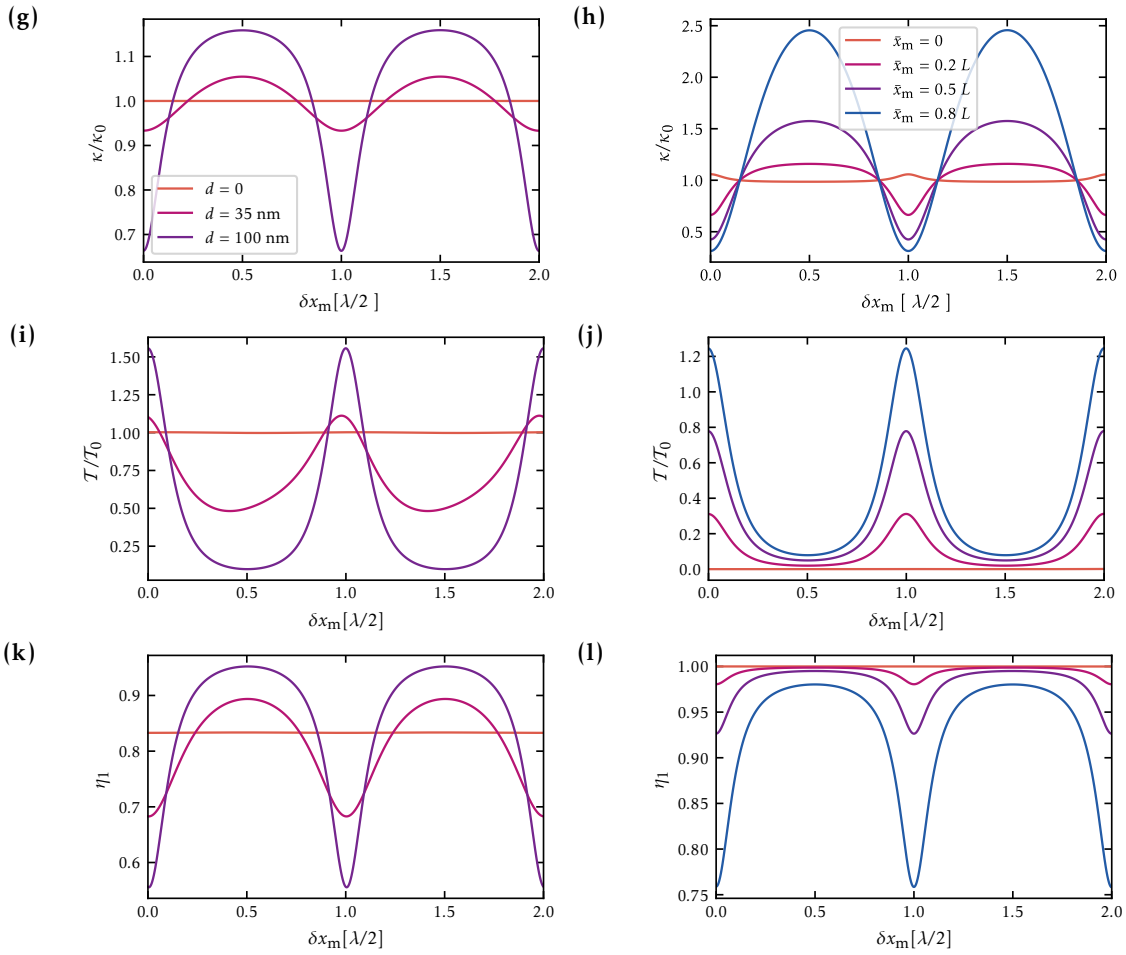

FIGURE 4.2: Theory predictions for optomechanical coupling and cavity parameters depending on the membrane position δx_m in the cavity standing wave for various mechanical thickness d (left) and different coarse placements inside the cavity $\bar{x}_m$ (right).

The effective radiation pressure force acting on the mechanical oscillator is given by the difference between photon impacts from both sides, which can be expressed as

$$F_{rad} = 2\hbar k\left(\frac{n_1}{\tau_1} - \frac{n_2}{\tau_2}\right). \tag{4.12}$$

We recall that for the canonical case of a cavity with a movable end-mirror, the radiation pressure results in $F_{rad} = \hbar g_0 \bar{n}_c / x_0$ in terms of the total cavity population number $\bar{n}_c = n_1 + n_2$.

By equating the two expressions for the radiation force, we can infer the optomechanical coupling rate as:

$$g_0 = x_0 \frac{2k}{n_1 + n_2}\left(\frac{n_1}{\tau_1} - \frac{n_2}{\tau_2}\right). \tag{4.13}$$

Solving the system of equations given in Eqs. (4.11), we obtain the analytical expression for the coupling strength

$$g_0 = x_0 \frac{\omega_{\mathrm{FSR}}}{\lambda} \frac{4|r_{\mathrm{m}}|L[|r_{\mathrm{m}}| - \cos(2kx_{\mathrm{m}})]}{L(1+|r_{\mathrm{m}}|^2) - 2|r_{\mathrm{m}}|^2 x_{\mathrm{m}} - 2|r_{\mathrm{m}}|(L-x_{\mathrm{m}})\cos(2kx_{\mathrm{m}})}. \tag{4.14}$$

Figure 4.2 illustrates the optomechanical coupling parameter for different membrane positions and thicknesses, while Fig. 4.1 shows that when the subcavity lengths are asymmetric, the maximal slope of the frequency modulation increases significantly for the shorter cavity, resulting in a greater optomechanical coupling. Indeed for the optimal placement of the mechanical oscillator, the maximally achievable optomechanical coupling strength can be approximated for a small membrane reflectivity ($|r_{\mathrm{m}}| \ll 1$) by

$$g_0^{\max} \approx 2x_0\omega_{\mathrm{L}} \frac{|r_{\mathrm{m}}|}{L}. \tag{4.15}$$

Furthermore, the modulation of the population number leads to a modification in the finesse. The overall finesse of the cavity results from the combination of losses through both mirrors, such that a higher fraction of photons in the higher reflective cavity results in an increased overall finesse. The energy stored in the cavity is given by

$$E = \hbar\omega_{\mathrm{L}}(n_1 + n_2), \tag{4.16}$$

with the ingoing light frequency ω_{L}, and the decay described as

$$\partial_t E = -\kappa E = -\hbar\omega_{\mathrm{L}}\Big(|t_1|^2 \frac{n_1}{\tau_1} - |t_1|^2 \frac{n_2}{\tau_2}\Big), \tag{4.17}$$

which leads to the expression for the steady state cavity decay rate

$$\kappa = \frac{|t_1|^2 n_1/\tau_1 + |t_1|^2 n_2/\tau_2}{n_1 + n_2}. \tag{4.18}$$

Without the membrane, we find the linewidth for the empty cavity $\kappa_0 = (|t_1|^2 + |t_2|^2)/\tau$ and for the subcavities $\kappa_j = |t_j|^2/\tau_j$. Hence the finesse in comparison to the bare cavity finesse $\mathcal{F} = 2\pi/(|t_1|^2 + |t_2|^2)$ turns out to be

$$\mathcal{F} = 2\pi \frac{\omega_{\mathrm{FSR}}}{\kappa} = \omega_{\mathrm{FSR}} \frac{n_1 + n_2}{|t_1|^2 n_1/\tau_1 + |t_1|^2 n_2/\tau_2}. \tag{4.19}$$

In the case of a strongly asymmetric cavity, where port 1 is used as the cavity in- and outcoupling port, the cavity incoupling efficiency η_{c} is completely defined through that port. In fact, it is given by the ratio between the light leaving the cavity through the output port and the amount leaving the cavity in total, following

$$\eta_{\mathrm{c}} = \frac{\kappa_1}{\kappa} = \frac{|t_1|^2|A_2|^2}{|t_1|^2|A_2|^2 + |t_2|^2|A_3|^2}. \tag{4.20}$$

For our experiments, where we use the same cavity port for incoupling and for detection, we are aiming the largest possible incoupling efficency, ultimately limited by imperfect mode matching. We note that if the reflectivities of the two subcavities end-mirrors differ, a variation in the resonance conditions for either the first or the second subcavity thus leads to a modification of the cavity linewidth and cavity incoupling.

The overall cavity transmission $\mathcal{T} = |t_{\mathrm{MIM}}|^2$ can be inferred directly from the photon occupation number of the second cavity n_2 and the transmission of the second mirror t_2. As shown in Fig. 4.2, the normalized transmission $\mathcal{T}_{\mathrm{MIM}}/\mathcal{T}_0$ where $\mathcal{T}_0$ is the transmission of the empty cavity, provides a strong indication of the position of the membrane in the cavity standing wave δx_{m}. When the membrane is placed close to one end of an asymmetric cavity ($\bar{x}_{\mathrm{m}} \ll L/2$), an increase in transmission and cavity finesse coincides with the maximal coupling position. In the experiment, the intensity of the light leaking out through the transmissive port can be directly measured, providing a convenient tool for estimating the cavity linewidth and the corresponding membrane position and optomechanical coupling strength.

Our main interest lies in the reflection amplitude $\mathcal{R}$ for a given cavity incoupling $\eta_{\mathrm{c}} = \kappa_1/\kappa$, where the total cavity losses κ are entirely due to the two incoupling ports, i.e. $\kappa = \kappa_1 + \kappa_2$, such that reflection is given by $\mathcal{R} = 1 - \mathcal{T}$, and corresponds to the signal that is mostly used for detection of the mechanical displacement.

In summary, we have derived all the necessary parameters required to perform a full characterization of the optomechanical cavity, namely the optomechanical coupling strength related to the variation in the cavity frequency, the cavity finesse and linewidth, the transmission allowing for direct deduction of the membrane position, and the incoupling efficiency, which is an important experimental parameter.

4.2 Optomechanical Setup

We now turn to the description of the optomechanical setup that is used for the experimental results shown in this work. At the heart of our experimental setup stands a free-space optical cavity that has been specifically designed for coupling the cavity light field to the membrane oscillator and is suitable for use at cryogenic temperatures. In the following sections, we will describe the composition of the membrane-cavity as well as the optical setup in which it is embedded, used to characterize its properties.

4.2.1 Cryogenic Cavity Design

We consider an optical cavity consisting of two free-space mirrors arranged in a plano-concave configuration. The curved mirror has a curvature radius $R = 30\,\mathrm{mm}$ and the cavity length is $L = 1\,\mathrm{mm}$, resulting in a beam waist of $w_0 = 40\,\mu\mathrm{m}$ at the position of the membrane, at approximately $0.2\,\mathrm{mm}$ from the flat mirror, and a Rayleigh range of $z_R = 6\,\mathrm{mm}$. Consequently, the beam size does not vary strongly over the length of the cavity, and does not change significantly depending on the exact placement of the membrane.

We drive the optical cavity with a light beam of wavelength $\lambda = 780\,\mathrm{nm}$. At this wavelength, the cavity mirrors have reflection coefficients of $R_1 = 0.995$ and $R_2 = 0.9999$, respectively. The finesse of the cavity without the membrane is $\mathcal{F} = 1200$, with a free spectral range of $\omega_{\mathrm{FSR}}/(2\pi) = c/(2L) = 150\,\mathrm{GHz}$, resulting in an overall cavity linewidth of $\kappa/(2\pi) = \omega_{\mathrm{FSR}}/(2\pi\mathcal{F}) = 100\,\mathrm{MHz}$. As shown in Fig. 4.2, the motion of the membrane modifies the properties of the cavity. Specifically, for the coarse placement of the membrane ($\bar{x}_{\mathrm{m}} = 0.2L$) used in the experiment, we expect the cavity linewidth to vary by approximately 25% depending on the fine-tuned position of the mechanical oscillator within the cavity standing wave. The experimentally chosen membrane placement resulting in the maximal optomechanical coupling strength entails a cavity linewidth of $\kappa = 2\pi \times 55\,\mathrm{MHz}$.

The cavity design is tailored to meet the specific requirements for cryogenic operation, closely following the previous design described in [169]. The main support material consists in titanium, owing to its stiffness, light weight and small thermal expansion. However, its low thermal conductivity is a disadvantage as it hinders fast membrane thermalization to the environment. The mirrors are glued in three distinct points using vacuum and croygenic compatible epoxy[1]. To ensure stability, the mirror mounts are clamped together with the piezo actuators under pretension. The piezo actuators[2] can move the mirrors and adjust the membrane position with respect to the cavity standing wave. The membrane is clamped to the mount and is not movable itself. A side view of cavity assembly is shown in Fig. 4.3.

As acoustic resonances in the cavity pieces are a concern [48], the resonances of the cavity mirrors have been simulated using finite element methods[3], taking into account two mirror designs with diameters of 12.7 mm (half-inch) and 8 mm. The analysis of the expected eigenmodes reveals that both mirrors exhibit eigenfrequencies that are low enough, i.e. less than 10 kHz, to be accounted for by the cavity lock. In fact, during a spectral response measurement, where one of the piezos is excited at a certain frequency and its response in the cavity lock signal is acquired, the empty cavity shows no significant resonances up to 100 kHz except for a very small resonance at 2.5 kHz.

4.2.2 Clamping Optimization

Experimental evidence proves that the precise anchoring mechanisms are crucial for fixing the square membranes to the support without introducing acoustic resonances or coupling to noisy support modes [170]. Acoustic resonances occur due to constructive interference between the normal modes of the piezo actuators and the mounting structure, leading to instabilities in the locking mechanisms.

Additionally, the stringent requirement of alignment maintenance during cryogenic cooling further requires a careful selection of clamping materials. In previous experiments, a massive titanium piece used as a clamp was found to be insufficient, and has been replaced with a stack of a 125 µm thick kapton sheet directly in contact with the membrane, combined with a sheet of brass ($CuBe_2$) with a thickness of 200 µm as a reinforcement. The kapton sheet is intended to serve as a soft clamping material for the square membranes. Experiments with viton, although soft and capable of damping some cavity resonance, exhibited low frequency resonances. Various combinations of clamping materials were tested with a membrane in the optical cavity using the frequency response measurement, as described previously for the empty cavity, with driving frequencies ranging from 1 to 20 kHz. It was found that resonances that are not present in an empty cavity configuration can be modified with the correct clamping combination, with the goal to minimize resonances for frequencies below 12 kHz. The clamping materials and the final configuration used in the subsequent optomechanical experiments are illustrated in Fig. 4.3.

[1] Stycast 2850 FT, catalyst 9
[2] Piezomechanik HPCh 150/15-8/3
[3] COMSOL multiphysics

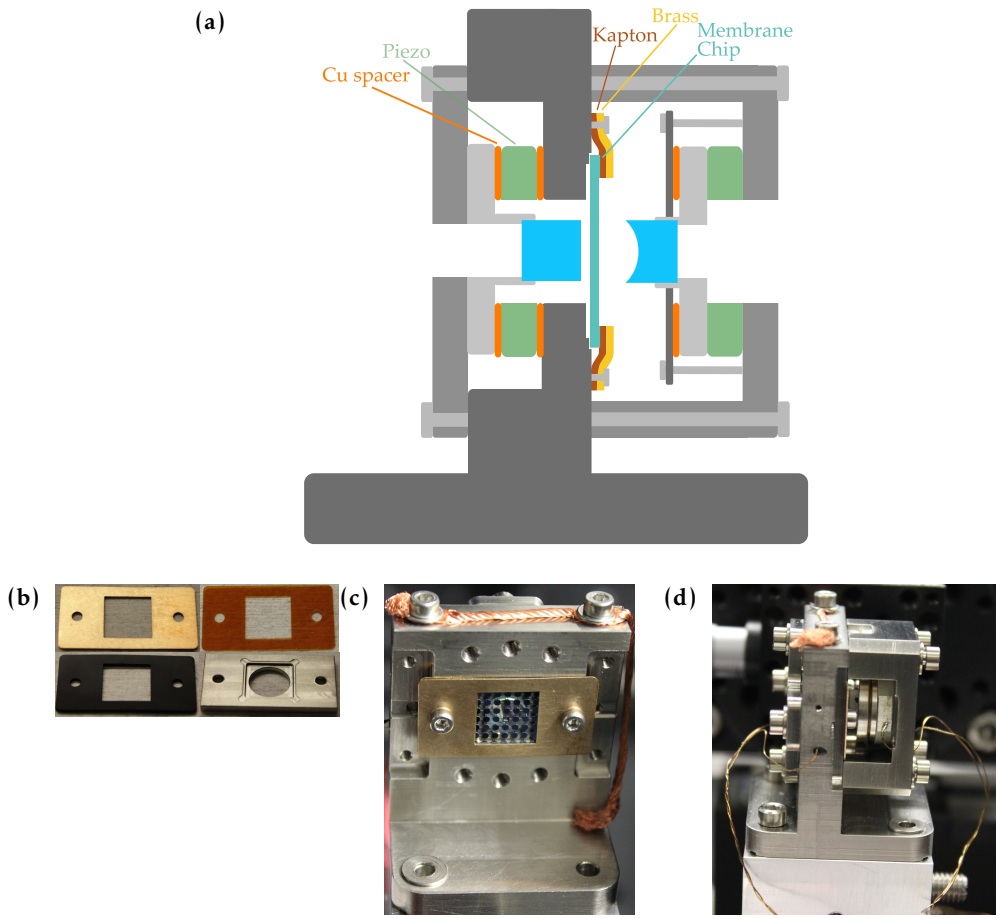

FIGURE 4.3: **(a)** Sideview sketch illustrating the arrangement of the cavity mirrors and their corresponding piezo actuators, around the membrane that is in direct contact with the main mount. Pictures of **(b)** different clamping materials, brass, kapton, viton and titanium, **(c)** the final clamping configuration with a stack of kapton and brass and **(d)** the assembled cavity side view.

4.2.3 Temperature Control

The environmental temperature of the membrane-cavity is controlled using a flow cryostat[4] that is operated with liquid-helium at 4.2 K. The cryostat installation has been described in [169], the main difference being a larger cryostat base diameter which facilitates mounting of the cavity. The temperature is controlled based on a temperature sensor attached to the cold plate of the cryostat, and is regulated using a PI loop on a magnetic flow-control valve of the heated exhaust gas that leaves the cryostat and enters the recovery network of the physics department. With this PI loop, we are able to maintain the cryostat temperature constant with fluctuations limited to 0.1 K. Furthermore, there is a voltage-controlled proportional valve for pressure control of the dewar, maintaining a pressure of 3 psi during cryogenic operation.

To investigate the thermalization of the cavity with respect to the cold plate temperature indicated by the integrated temperature sensor, we perform a scan of the cavity

[4]Cryovac GmbH, KONTI Mikro, UHV compatible, with DN160CF flange

piezos over multiple resonances of the cavity. The temperature-dependent piezo capacitance leads to a variation in the stroke range for an identical applied voltage, allowing us to estimate the temperature based on the required voltage difference needed to scan the cavity over the resonances.

Figure 4.4 illustrates the transmitted signal corresponding to the cavity resonance, when scanning the position of both cavity mirrors for two different environment temperatures, once at room temperature and once at a cryostat set temperature of $T_{\mathrm{set}} = 10\,\mathrm{K}$. The modulation in the cavity resonance is due to the changing position of the membrane in the cavity field when both cavity mirrors are moved. Assuming that the cavity length is not modified by the change in temperature, we observe that the piezo stroke is roughly reduced by a factor 2. In addition, we can directly measure the piezo capacitances to ob-

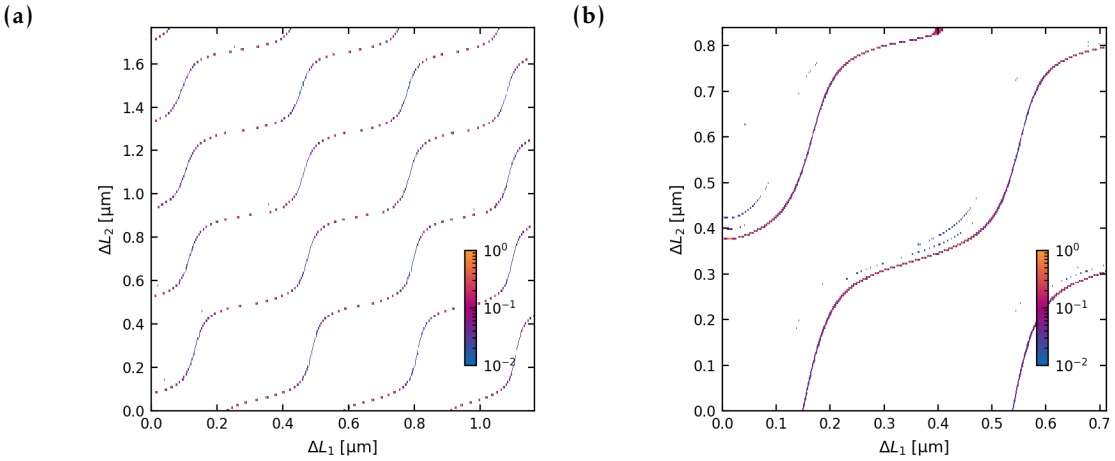

FIGURE 4.4: **(a)**: Two-dimensional cavity mirror piezo scan at room temperature $T = 300\,\mathrm{K}$ and **(b)** at the set cryostat temperature $T_{\mathrm{set}} = 10\,\mathrm{K}$ normalised to the maximal transmission. The modulation of the cavity resonance is due to the variation in the position of the membrane with respect to the cavity field.

tain an indication of their temperature. At room temperature, the capacitances amount to 820 nF and 780 nF, while they reduce to 175 nF and 156 nF at the set cryostat temperature $T_{\mathrm{set}} = 10\,\mathrm{K}$. Furthermore, we can utilize the correspondence between temperature and the area of the thermal displacement power spectral density, as described in Sec. 4.5.1, to verify the agreement between the temperature indicated by the cryostat sensor and the temperature that the mechanical mode is effectively thermalized to.

The average Helium consumption for the continuous operation at different temperatures ranges from $0.2\,\mathrm{L\,h^{-1}}$ at a base temperature of $T_{\mathrm{set}} = 120\,\mathrm{K}$, to $3\,\mathrm{L\,h^{-1}}$ at $T_{\mathrm{set}} = 4\,\mathrm{K}$.

4.2.4 Mechanical Temperature Dependence

The environmental temperature has an influence on the material properties of SiN, especially on the internal loss mechanisms, which are slowed down at cryogenic temperatures and thus modify the Q factor. Since only the cavity setup is equipped with a cryostat, we perform cavity ringdowns at different temperatures to determine the temperature dependence of the quality factors. These are performed with low optical powers and a coarse

membrane position that minimizes the optomechanical coupling and thus the dynamical backaction effects. We measure an increase of the quality factor from $Q = 1.9 \times 10^6$ at room temperature to $Q = 3 \times 10^6$ for the set cryostat temperature $T_{\text{set}} = 60\,\text{K}$ and $Q = 3.2 \times 10^6$ at $T_{\text{set}} = 10\,\text{K}$, which is in good agreement with previous reports [63, 171], where additionally we would expect a drastic increase in the quality factor if the environmental temperature reduces below 1 K. Furthermore, the change in environmental temperature entails a shift of the mechanical resonance frequency of 40 kHz between room temperature and $T_{\text{set}} = 20\,\text{K}$.

4.2.5 Optical Setup

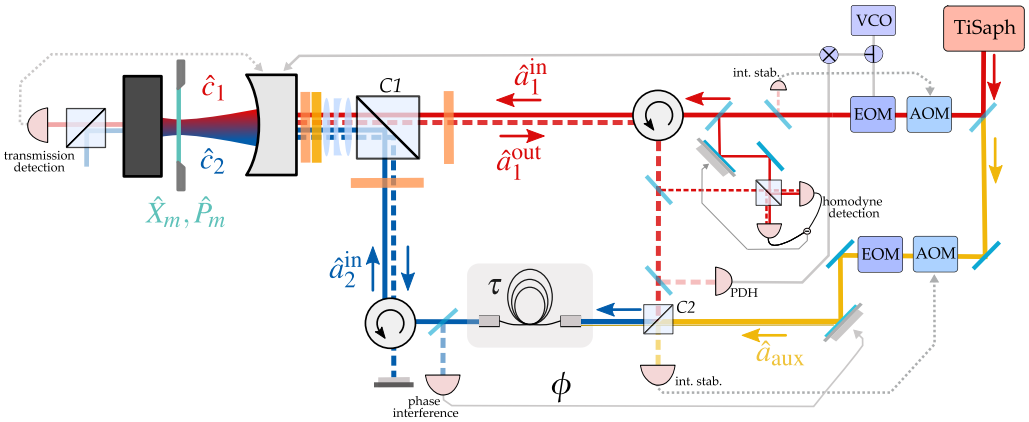

FIGURE 4.5: Sketch of the optical setup used for the coherent feedback double pass experiment. One laser beam emitted by the TiSaph laser is split into the probe beam $\hat{a}_1^{\text{in}}$ (red) and the auxiliary local oscillator $\hat{a}_{\text{aux}}$ (yellow). Another portion of the probing beam is split off as a local oscillator for in-loop homodyne detection. The first beam is transmitted through polarizing cube (C1) and passes an optical telescope and stack of $\lambda/2$ and $\lambda/4$ waveplates to compensate the cavity birefringence before the incoupling into the cavity, where it forms the cavity field $\hat{c}_1$. The backreflected beam $\hat{a}_1^{\text{out}}$ passes C1 through the incoming port and is split from the ingoing beam by an optical isolator. A small portion is directed towards a homodyne detection setup, and a fast photodiode for the cavity lock. The remaining part of $\hat{a}_1^{\text{out}}$ is combined on a non-polarizing beamsplitter cube (C2) with the auxiliary local oscillator. The combined beam $\hat{a}_2^{\text{in}}$ (blue) propagates together in the optical fiber before a small fraction is detected to produce the error signal for the loop phase lock. The polarization of $\hat{a}_2^{\text{in}}$ is rotated such that it passes C2 through the reflective port, ensuring a polarization of the cavity field $\hat{c}_2$ orthogonal to $\hat{c}_1$. The backreflected beam retraces its ingoing path and is separated from the ingoing beam by an optical isolator, after which it is discarded out of the loop.

The optical setup sketched in Fig. 4.5 has been built up completely during the course of this thesis, and consists mostly of free-space optical components that guide the laser beams to the optomechanical cavity and the detection.

A single light beam emitted from the TiSaph laser[5] is split into two separate beams, each of which passes through a free space acousto-optical modulator (AOM) and fiber-coupled electro-optical modulator (EOM). The main optomechanics beam (depicted in

[5] MSquared (Sols TiS)

red) is intensity stabilized through a feedback loop on the AOM before being split into a local oscillator (LO) used for homodyne detection, and the probing beam. This probing beam passes an optical isolator in the forward direction, followed by a $\lambda/2$ waveplate and a thin film beam polarizer cube (C1), which is used for the combination and splitting of the two passes, in the coherent feedback experiment. Furthermore, all beams coupled into the cavity share the same path through a periscope, a telescope and a stack of $\lambda/4$ and $\lambda/2$ waveplates to correct for the cavity mirror birefringence before coupling into the cavity. The transmission through the highly reflective mirror of the cavity is detected both on a photodiode and on a CCD camera, as shown in Fig. 4.12.

The beam that leaks back out of the low reflectivity mirror passes back through the same optics and the identical port of the first beam-splitter cube, until it reaches the optical isolator where it separated from incoupling beam. A small portion of the back-reflected beam (approximately 10%) is sent on a homodyne detection and overlapped with the local oscillator to provide the phase detection of the outgoing light beam. Furthermore, along the beam path, a small portion of the light is detected on a fast photodiode for the cavity lock [cf Sec. 4.2.6].

In double pass experiments, the majority of the backreflected light is combined on a non-polarizing cube with an efficiency η_{aux} (C2) with an additional local oscillator ($\mathrm{LO}_{\mathrm{aux}}$, depicted in yellow), before both beams are coupled into a fiber. The intensity of the auxiliary local oscillator can be stabilized based on the light leaking through the uncoupled port of the combining cube (C2), and by actuating on an AOM. The combined beam (depicted in blue), consisting of the $\mathrm{LO}_{\mathrm{aux}}$ and $\hat{a}_1^{\mathrm{out}}$, travels through the non-polarization-maintaining optical fiber[6]. The polarization after the fiber can be adjusted using fiber paddles. After the fiber, a small portion of the combined beam is split off using a polarizing beamsplitter cube and is detected on a photodiode. This fraction of the combined beam provides the interference locking signal between the two beams, ultimately defining the loop phase φ. The phase lock is implemented by a piezo-actuated mirror in the beam path of $\mathrm{LO}_{\mathrm{aux}}$ [cf Sec. 4.2.7].

Moreover, the combined beam continues its path to the cavity, passing through an optical isolator and a $\lambda/2$ waveplate before meeting the combining beamsplitter cube (C1) for a second time and being combined with the first incoming beam. The optical losses accumulated during the combined propagation are summarized in η_τ.

Upon entering the polarizing cube C1, the two beams are in orthogonal polarizations. The orthogonality of their polarizations can be used to separate the corresponding beams backreflected from the cavity with high precision, in order to avoid spurious interference effects. Therefore, polarization optics with high extinction ratios are required, especially for the cube C1 and the waveplates directly in front of the cavity.

In fact, we observe that the cavity mirror birefringence becomes noticeable for cryogenic temperatures below 100 K. In this case we have to add a stack of $\lambda/4$ and $\lambda/2$ waveplates in front of the cavity for compensation of the birefringence. This can be explained by temperature-dependent stress on the mirrors and the support structures.

Furthermore, analogous to the first beam, the backreflection of the second pass retraces its steps until it reaches the optical isolator, where it is split off from the forward-travelling beam and is discarded out of the loop, potentially available for detection.

The efficiencies through the optical setup are $\eta_1 = 0.91$ for the cavity incoupling of the first beam, the efficiency of the combination of the local oscillator with the outgoing light

[6] Thorlabs 780 HP, between 1 m and 71 m long

$\eta_{aux} = 0.87$, the common propagation loss $\eta_\tau = 0.3$, and the second pass cavity incoupling efficiency $\eta_2 = 0.9$, resulting in an overall double pass efficiency of $\eta = 0.22$.

The signal detection is performed on a homodyne detection set, using a balanced detector[7]. The photodiode signal is sent onto a fully a digital lock-in amplifier[8] (LIA), that provides us with the demodulation at the desired mechanical frequency and results in a spectrum with a rather narrow bandwidth < 500 kHz,

4.2.6 Cavity Lock

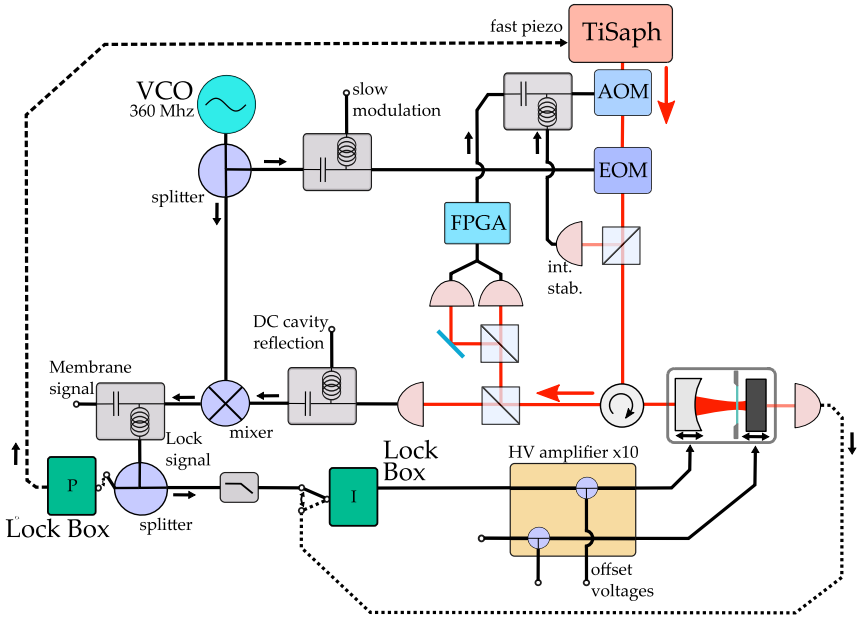

FIGURE 4.6: Sketch of the electronic setup used for the optomechanical cavity lock, and measurement-based feedback. The signal of the VCO is sent to an EOM which produces a phase modulation on the ingoing light field. The backreflected light from the cavity is detected in a homodyne scheme. The detected mechanical displacement signal can be processed using an FPGA and is subsequently fed back to the ingoing light beam, thus enabling feedback cooling. Furthermore the backreflected light is also detected on a fast photodiode, and demodulated at the EOM modulation frequency. The high frequency signal of this demodulation contains the membrane signal directly. The low frequency part can be used to implement the cavity lock. We have both access to a fast proportional lock on a fast piezo in the TiSaph laser, and integral gain lock on the cavity mirror piezo.

In our optomechanics experiments, one of the cavity mirror piezos is used to lock the cavity length to the laser frequency, in order to stabilize the cavity resonance frequency as sketched in Fig. 4.5. Mostly, the lock is executed on the piezo actuator mounted on the curved cavity mirror, which is further away from the membrane and has less influence on the optomechanical coupling strength than the flat mirror. The piezo actuator has a capacitance of 800 nF at room temperature, which, in combination with our HV amplifier

[7] Electronic Workshop University of Basel, Balanced Photo-Detector SP1023, with a 50 MHz BW and gain 10^4 V/A

[8] Zurich Instruments HF2LI 50 MHz

limits the bandwidth of the feedback to 4 kHz. In comparison, at cryogenic temperatures of 20 K, where the piezo capacitance reduces to 170 nF, the bandwidth increases to 18 kHz.

The error signal for the cavity lock is generated using a Pound-Drever-Hall (PDH) scheme [172, 173], with a phase-modulation at a frequency $f_{\mathrm{PDH}} = 360\,\mathrm{MHz}$, larger than the cavity linewidth $\kappa/(2\pi) = 55\,\mathrm{MHz}$. The signal detection and processing paths for the locking scheme are illustrated in Fig. 4.7. The incoming light field is phase-modulated by an EOM with an RF signal provided by a voltage-controlled oscillator (VCO[9]). As the modulation frequency exceeds the cavity linewidth, the modulation sidebands are mostly reflected by the cavity incoupling mirror, providing a phase reference with respect to the light leaking out of the cavity. The back-reflected beam is detected with a fast photodiode[10]. The detected signal is mixed down with the RF modulation signal, resulting in a low-frequency part, providing the error signals for the cavity lock, and a high-frequency part containing the cavity resonance fluctuations and thus the mechanical oscillator signal. Both the modulation demodulation are realized by an assembly of RF components[11]. Furthermore, the error signal is split once more, where one part is low-pass filtered and processed with an analog lock box, applying an integral gain (I-gain) before passing through a high-voltage (HV) amplifier[12] that both amplifies the input signal and is capable of adding an adjustable offset voltage to its output. The static offset voltage can be used to set the coarse position of the cavity mirror, in order to determine the membrane position relative to the cavity field. The combined voltage consisting of the static offset and the amplified feedback term, is applied to the piezo controlling the curved mirror. The other part of the lock signal is used to provide a feedback signal applied to the fast cavity piezo of the TiSaph laser (with a bandwidth of $\approx 100\,\mathrm{kHz}$) with a proportional gain (P-gain) set in a separate lock box[13] in order to provide additional stability to the cavity lock.

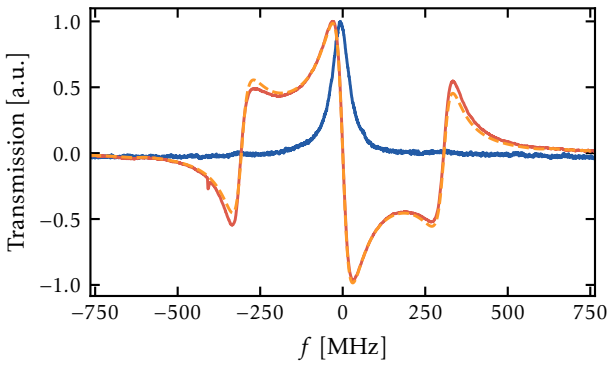

Figure 4.7: Scan over the cavity resonance, the transmitted signal (blue) and the backreflected beam (orange) that can be fitted to the expected signal shape (yellow).

[9] Minicircuits VCO ZX95-400-S+

[10] Menlo systems FPD610-FC-VIS High Sensitivity Fast Photodetector

[11] Minicircuits Splitter ZFSC-2-2-S+, Mixer ZFM-2-S+, Diplexer ZBPLX-2150-S+, Bias Tee ZFBT-282-1.5A+

[12] Piezomechanik SVR150/x

[13] SRS SIM960 Analog PID controller

Furthermore, the phase modulation used for the cavity lock, at a well known frequency can also be used to determine the cavity linewidth κ. By scanning the cavity mirror position across the cavity resonance and detecting the backreflected signal and the cavity transmission as shown in Fig. 4.7, the modulation sidebands contained in these signal can be used as a frequency reference to calibrate the cavity linewdith.

As an alternative to the PDH lock, when a cavity lock at larger detuning is desired, we can lock the cavity length on the fringe of the transmitted peak. By detecting the light transmitted through the cavity using a photodiode, we can use the transmission as the locking error signal directly. This approach allows us to lock the cavity in a detuning range from $\Delta \lesssim -1.5\kappa$ to $\Delta \approx -0.22\kappa$.

4.2.7 Loop Phase Lock

To stabilize the loop phase ϕ of the coherent feedback experiment, we acquire the interference between the auxiliary local oscillator $\hat{a}_{\text{aux}}$ and the back-reflected beam after the first interaction $\hat{a}_1^{\text{out}}$. The phase ϕ is directly related to the effective loop phase φ between the two orthogonal cavity fields, as described in more detail in Ch. 1.

Throughout the coherent feedback experiments, we have undergone multiple evolutions of phase locks, as it has proven to be critical to determine the optimal location for probing the phase between the two beams and feeding back the resulting error signal in the optical setup. The locking scheme employed in the described experiments is shown in Fig. 4.8. The interference signal is acquired after the combination of both beams and their common journey through the fiber. The feedback signal is then sent to a piezo-actuated mirror in the path of the auxiliary local oscillator.

To reduce low-frequency noise and gain the ability to scan the entire phase space, the phase lock error signal is generated through a 310 kHz phase or amplitude modulation of the ingoing light field. The signal detected at the photodiode is then demodulated, resulting in an error signal that can be used for locking. For amplitude modulation, we employ an AOM in the auxiliary beam path. For phase modulation, we rely on a fiber EOM in the probing beam path. For the latter, we combine the slow modulation of the phase lock with the fast PDH modulation and send both to the EOM. The generation of the modulation signal, the demodulation, as well as amplification, are performed with a lock-in amplifier[14] (LIA). The error signal is then sent to an FPGA[15] that provides the PI control, before being amplified by an x10 HV amplifier[16] and applied to the piezo-mirror.

The advantage of this locking scheme lies in the convenience that the loop phase can be locked before actually sending the second beam towards the cavity. The main downside consist in the optical losses generated by splitting off a small portion of the combined beam, resulting in a few percent loss of coherent feedback signal.

The stability of the phase lock can be evaluated through the cavity transmission, which consists of the two transmitted orthogonal cavity fields. In the case of a successful phase lock, this interference signal remains constant. In this manner, in our current scheme, we estimate a remaining a phase variation of $\delta\phi \approx 1°$. The bandwidth of the phase lock is ultimately limited by the capacitance of the piezo actuator, which forms a low-pass filter and results in a bandwidth of approximately 6 kHz. The possibility of implementing a faster phase lock, feeding back on the frequency of the light beam via

[14] Zurich Instruments HF2LI 50 MHz
[15] Red Pitaya STEM-lab 125-14
[16] Electronic Workshop University of Basel, SP908

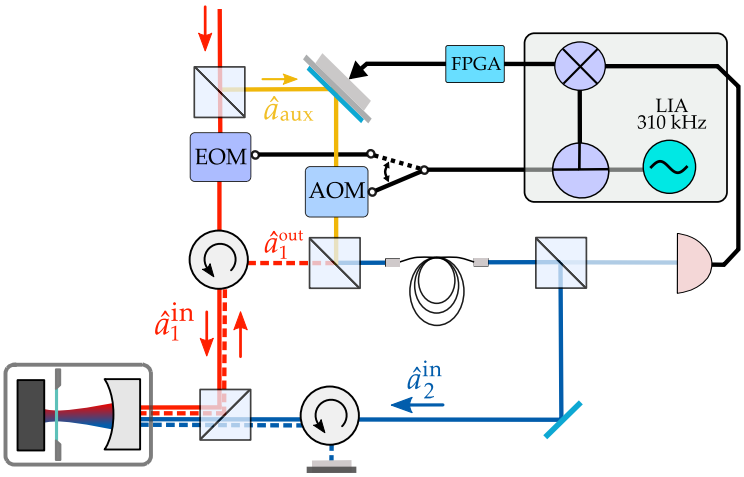

FIGURE 4.8: Sketch of the electronic setup used for locking the loop phase in double pass experiments. The lock-in amplifier (LIA) generates a modulation signal that is either send to an AOM for amplitude modulation or an EOM for phase modulation. The light leaking out of the cavity $\hat{a}_1^{\mathrm{out}}$ is mixed with an auxiliary local oscillator $\hat{a}_{\mathrm{aux}}$. A fraction of the combined beam is split off after propagation through the fibre, before the second incoupling into the cavity, and demodulated with the LIA to generate a phase error signal that is fed back on a piezo-actuated mirror standing in the local oscillator's beam path.

the AOM has been explored, but did not lead to an observable improvement in the phase stability with the additional lock.

4.3 Noise processes

The optomechanical system faces many different sources of noise that can elevate the mechanical bath temperature and limit the minimally achievable mechanical occupation number. The impact of quasi-unavoidable noises, such as the imprecision noise and the quantum backaction noise, on the cooling performance of mechanical oscillators has been extensively studied in the literature [5].

Classical noises of concern include laser noise, which comprises both amplitude and frequency noise, and cavity mirror frequency noise due to the thermal motion of the cavity length caused by the longitudinal motion of the mirrors. The influence of classical laser noise on the optomechanical interaction has been the target of many studies [174, 175, 176], and can be significantly reduced using shot-noise-limited lasers as we will in the following. The frequency noise due to the cavity mirror thermal motion is generated by the cavity length modifications due to the mirror substrate thermal mechanical modes and appears as discrete noise peaks in the displacement spectrum [177]. These narrow noise peaks do not affect the membrane signal as long as they are spectrally distant from the mechanical mode of interest. Also phononic structures on the mirror substrate have been investigated to mitigate this noise source [178].

In our experiment we also encounter mechanical noise of the oscillator itself, arising from nonlinearities in the optomechanical coupling that has to be actively counteracted to prevent heating of the mechanical mode. In the case of a double-pass coherent feedback scheme, certain noise processes, such as phase noise and cavity photon number

instabilities, become more significant and are considered as potential processes limiting the cooling performance in Sec. 5.5.

4.3.1 Mechanical Noise

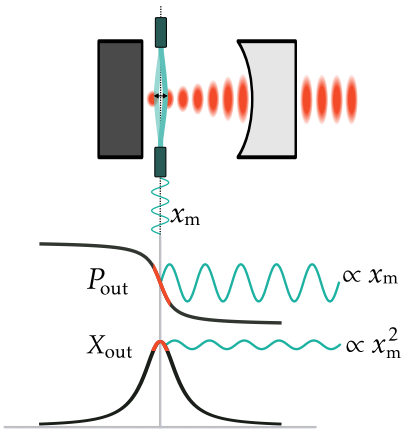

FIGURE 4.9: Coupling between the displacement of the mechanical oscillator x_m and the optical cavity field, illustrating the linear coupling resulting in a modulation of the phase of the outgoing light field proportional to x_m, and the quadratic coupling, realizing a modulation of the light amplitude proportional to x_m^2.

In Ch. 2 we have derived the optomechanical interaction considering the linear modification of the cavity resonance with the mechanical displacement. Figure 4.9 illustrates, that, besides the linear modulation of the phase quadrature, there is a modulation in the amplitude quadrature depending on the quadratic mechanical displacement. The nonlinear terms included in the transduction between the cavity frequency fluctuations onto the light field can be modelled by expanding the cavity susceptibility around small fluctuations in the detuning [160] . We start by considering the operation of the cavity close to resonance ($\Delta \approx 0$) with small detuning fluctuations ($\delta\Delta$) modified by the mechanical motion $\delta\Delta = gX_m(t)$. We recall that in fact, the optomechanical coupling strength is defined as the mechanically-induced cavity frequency fluctuations $g_0 = -x_0 \partial\omega_c/\partial x_m$. The steady-state cavity field as given by Eq. (1.21), can be expanded around $\Delta + \delta\Delta$ such that

$$\hat{c}(t) = \frac{1}{\kappa/2 - i\Delta(t)}\sqrt{\kappa}\hat{a}_1^{in} = \frac{2}{\sqrt{\kappa}}\left(1 + ig\hat{X}_m(t) - (g^2 + ig^{(2)})\hat{X}_m(t)^2\right)\hat{a}_1^{in}. \tag{4.21}$$

where $\Delta \approx 0$ and $g^{(2)} = \partial^2\omega_c/\partial x_m^2$ is the second-order coupling term that can be neglected in following. For first-order nonlinear effects, the relevant quantity lies in the quadratic spectrum of the mechanical displacement $S_{XX}^{(2)}$, which leads to a spectrum involving frequency mixing of different mechanical modes. These additional noise peaks will appear in the orthogonal light quadrature, as can be seen from Eq. (4.21). The quadratic effect can be more or less pronounced depending on the detuning and the cavity linewidth and emerges as a broadband noise effect that can limit the sensitivity of the measurement to linear quantum correlations [160].

In the experiment we encounter the presence of spurious peaks from higher harmonics of lower-frequency mechanical modes, originating from nonlinear processes, when acquiring the displacement of a specific mechanical mode. To mitigate these noise peaks,

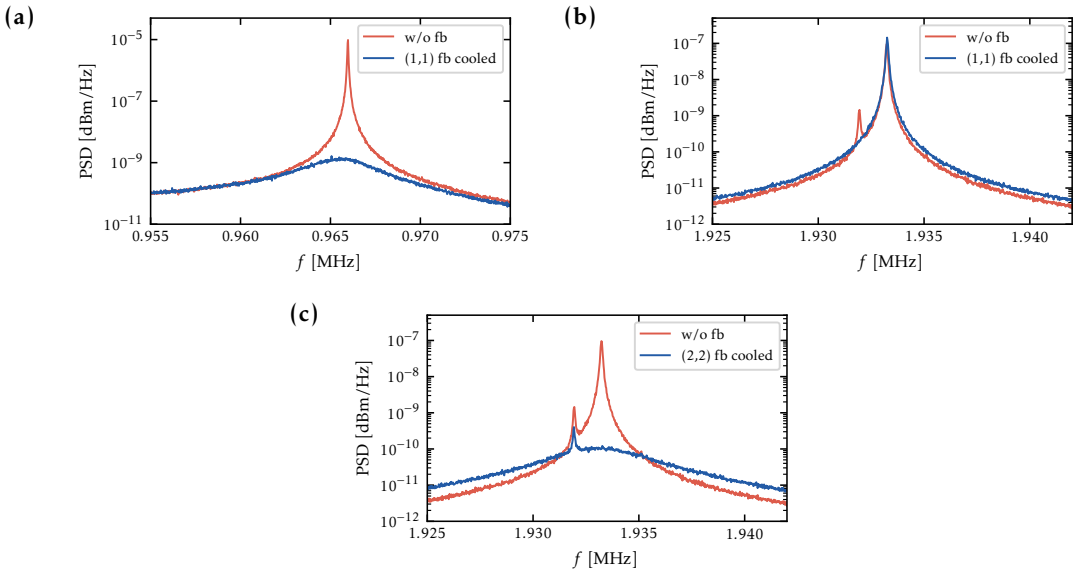

FIGURE 4.10: Mechanical displacement power spectral densities **(a)** with and without feedback cooling the (1,1) mode **(b)** the (2,2) mode with the feedback cooling addressing the (1,1) mode and **(c)** the (2,2) mode with feedback cooling addressing the (2,2) mode directly

we use measurement-based feedback cooling [cf Sec. 2.5] to dampen the mechanical mode responsible for the noise and minimize its impact on the mechanical spectrum at our target frequency. The experimental setup used to implement the measurement-based feedback cooling is included on the sketch in Fig. 4.7. The displacement of the mode to be eliminated is detected using a homodyne detection scheme. Based on this measurement, an amplitude modulation is applied to the incoming light, generating a feedback loop to suppress it. The delay and phase of the feedback are chosen such that a damping force is created to counteract the mechanical motion. The feedback is implemented using a digital IQ module [179] on a programmable FPGA[17]. This allows for adjustment of the gain, delay, and filter bandwidth of the feedback, providing flexibility in tuning the feedback parameters to maximize the damping effect.

The examples of cold damping illustrated in Fig. 4.10, show that this technique is effective in reducing the amplitude of the (1,1) mode and eliminating its spurious appearance at twice its frequency in the spectral vicinity of the (2,2) mode. The observed suppression of up to 40 dB for the (1,1)-mode indicates the effectiveness of the feedback control in damping the mechanical motion.

4.3.2 Laser Noise

The laser beams used in our optomechanical experiments are derived from a TiSaph laser that is quantum-noise-limited in amplitude for frequencies above the relaxation frequency of 1 MHz. The amplitude noise peak associated with the relaxation process of the laser depends on the power of the pumping laser[18]. During the experiment, a reduction of the pump power to 7 W was necessary in order to avoid excess amplitude

[17] Red Pitaya STEMlab 125-14
[18] Lighthouse Photonics 532 nm Nd:YAG 1064 nm Sprout laser.

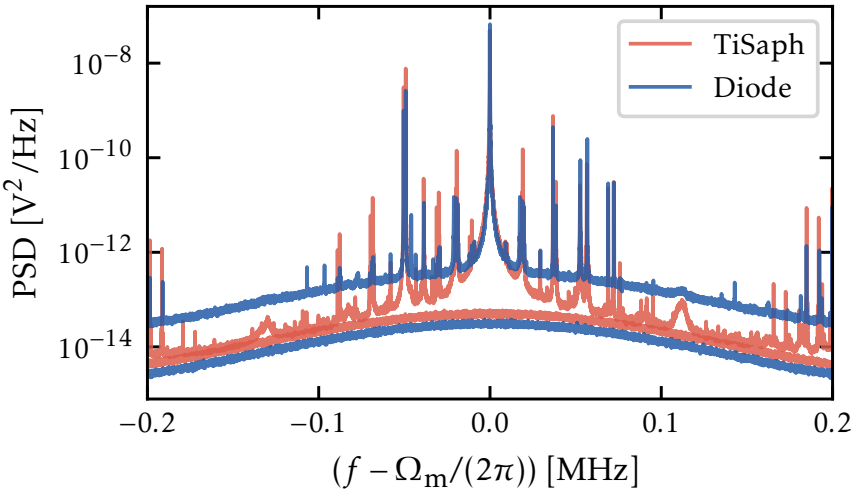

FIGURE 4.11: Membrane displacement power spectral density around the mechanical resonance frequency $\Omega_m/(2\pi) = 2\,\mathrm{MHz}$, where the cavity field is driven using a TiSaph or an external cavity diode laser. The flat lines correspond to the respective shot noise levels.

noise. In Fig. 4.11, we compare the membrane displacement spectrum detected by comparable powers of a low-noise external cavity diode laser[19] and the TiSaph laser. We observe that next to the mechanical peak, both light beams show several noise peaks that can be attributed to electronic and mirror noise. Furthermore, for the diode laser, the wings of the mechanical signal do not reach the shot noise limit due to excess amplitude and phase noise, leading to a broadband background noise noticeable as a general offset. However, for the TiSaph laser, the mechanical signal reaches the shot noise level, and we do not observe excess noise processes using the TiSaph with increasing optical powers for dynamical backaction cooling, as seen in Sec. 4.4.2.

4.4 Optomechanical Coupling Calibration

In order to calibrate the optomechanical coupling strength, we employ various calibration techniques, each dependent on a different set of parameters. These complementary calibration techniques allow us to obtain a parameter-independent mean value for g_0. We will restrict our study to the optomechanical coupling strength of the mechanical mode of interest in our experiments, namely the (2,2) mode. The position of the cavity beam on the square membrane is shown in Fig. 4.12 and is chosen to maximize the overlap between the cavity beam and the (2,2) mode, as discussed in Ch. 3. Consequently, the maximal optomechanical coupling g_0 occurs with the (2,2) mode, while the coupling to the (1,1) and other higher order modes is relatively weak.

4.4.1 Phase Modulation Tone

One method to calibrate the optomechanical coupling strength consists in using a phase modulation tone calibration as described in [180]. Among all the membrane parameters,

[19] self-made with long reference cavity for enhanced stability and low noise performance.

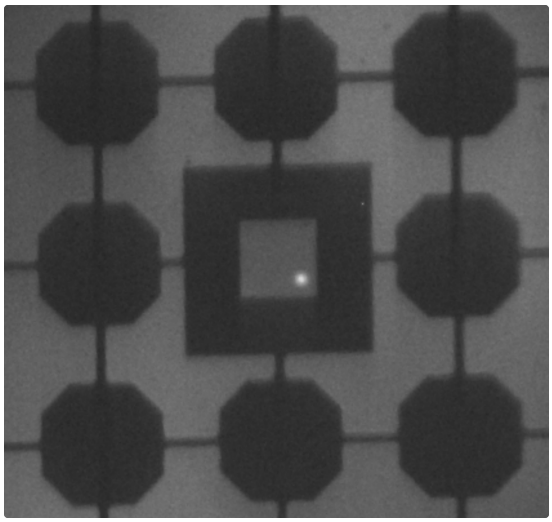

FIGURE 4.12: Camera image of the laser beam positioning on the square membrane, for maximal coupling to the (2,2) mode.

it relies solely on the knowledge of the mechanical mode occupation $\bar{n}_{\mathrm{th}} = k_{\mathrm{B}}T/\hbar\Omega_{\mathrm{m}}$. The phase quadrature of the outgoing light contains the modulation of the cavity resonance frequency at the membrane frequency and includes the symmetrized double-sided spectrum of the mechanical oscillator driven by thermal noise with a proportionality factor containing g_0^2. To implement this calibration, we use an EOM to phase-modulate the incoming light beam at a frequency ω_0, which differs by a few kHz from the mechanical resonance frequency. The modulation depth β_0 can be independently determined by heterodyning this beam with an unmodulated reference beam. To extract g_0, we detect the phase quadrature of the outgoing light using homodyne detection. Although the modulation due to the ingoing phase modulation and the membrane motion are dynamically very different, they are both transduced with the same function $\zeta_{\mathrm{det}}(\omega)$ in the spectral densities of the outgoing light quadrature. Therefore, on the detector, we have $S_{DD}(\omega) = (\zeta_{\mathrm{det}}(\omega)/\omega^2)g_0^2 S_{X_{\mathrm{m}}X_{\mathrm{m}}}(\omega)$ for the mechanical signal, and $S_{DD}(\omega) = \zeta_{\mathrm{det}}(\omega)S_{\mathrm{mod}}(\omega)$ for the calibration peak, where the ingoing phase modulation can be expressed as $S_{\mathrm{mod}}(\omega) = 2\pi(\beta_0^2/4)\Big[\delta(\omega-\omega_0)+\delta(\omega+\omega_0)\Big]$.

The function $\zeta_{\mathrm{det}}(\omega)$ comprises the various prefactors encountered due to losses and amplification in the detection chain, and includes the coherent ingoing light amplitude, cavity losses, optical propagation losses, the detection chain filter function, which is assumed to be flat over the spectral range $\Omega_{\mathrm{m}} \pm \omega_0$ and the homodyne amplification. The frequency-dependent part of the detection transfer function is given by $\zeta_{\mathrm{det}}(\omega) = \omega^2(4\eta_{\mathrm{c}}a_{\mathrm{det}}/\kappa)^2$, where the detection amplification $a_{\mathrm{det}} = D_{\mathrm{amp}}\sin\theta$ is given by the homodyne voltage contrast D_{amp} and the set phase θ.

We recall that the mechanical occupation number is directly related to the integral of the displacement power spectral density following $\int S_{X_{\mathrm{m}}X_{\mathrm{m}}}(\omega)\mathrm{d}\omega/(2\pi) = k_{\mathrm{B}}T/\hbar\Omega_{\mathrm{m}} = \bar{n}_{\mathrm{m}}$. The integrated detected peak area $A = \langle D(\omega)^2\rangle = \int S_{\mathrm{DD}}(\omega)\mathrm{d}\omega/(2\pi)$ then results in

$$A_{\mathrm{th}} = 2\bar{n}_{\mathrm{m}}\zeta_{\mathrm{det}}g_0^2 = 2\bar{n}_{\mathrm{m}}\Big(\eta_{\mathrm{c}}\frac{4a_{\mathrm{det}}}{\kappa}\Big)^2 g_0^2. \tag{4.22}$$

Furthermore the area of the calibration peak is independent of the optomechanical coupling, assuming the high quality mechanical oscillator to be strongly peaked at its mechanical resonance frequency, with no mechanical response from the modulation at the frequency ω_0 far away from the resonance [$\chi_m(\omega_0) = 0$]. The area under the calibration peak scales with the transfer function $\zeta_{det}(\omega)$

$$A_{calib} = \frac{1}{2}\beta_0^2\zeta_{det}(\omega_0) = \frac{1}{2}\beta_0^2\omega_0^2\left(\eta_c\frac{4a_{det}}{\kappa}\right)^2, \tag{4.23}$$

where we note that the calibration peak area depends on the cavity coupling η_c and the cavity linewidth κ. Finally the expression for the optomechanical coupling strength yields

$$g_0^2 = \frac{\omega_0^2\beta_0^2}{4\bar{n}_m}\frac{A_{th}}{A_{calib}}, \tag{4.24}$$

which turns out to be independent of the detection chain a_{det} and the cavity factors.

Moreover, the coupling strength depends on the position of the mechanical oscillator in the cavity standing wave, as shown in Fig. 4.2. In order to map out the variation in the coupling strength, we modify the membrane position δx_m relative to the cavity field and determine the coupling strength at each position. This is achieved by scanning the voltage applied to one of the cavity piezos, while using the other one to keep the total cavity length locked. For each data point, we compare the integrated spectrum of the mechanical peak to the corresponding calibration peak. During the measurement, we use a second cooling beam that is detuned by $\Delta = -0.3\kappa$ from the probing beam to generate dynamical backaction cooling. This allows us to keep the probing beam close to resonance without introducing instabilities. We take into account the modification of the dynamical backaction to the mechanical peak area by scaling the measured areas with the appropriate cooling factor $\sqrt{\epsilon_c}$. This factor ϵ_c is determined from the ratio between the fitted width of the corresponding measurement divided by the intrinsic mechanical linewidth obtained independently from a ringdown measurement. Figure 4.13 presents the values obtained for a g_0 calibration when scanning the voltage applied to the cavity mirror piezo 2 and using piezo 1 to keep the cavity length locked. The calibrated values vary between $g_0/(2\pi) = 170\,\text{Hz}$ at the maximal and $g_0/(2\pi) = 20\,\text{Hz}$ at the minimal coupling depending on the membrane position in the cavity standing wave.

4.4.2 Dynamical Backaction Cooling

Another method to calibrate the optomechanical coupling strength is based on dynamical backaction cooling. By monitoring the effect of a detuned light beam on the mechanical susceptibility for different optical powers, we can determine the optomechanical coupling strength.

This method is best implemented using two light beams. One beam is used for locking the cavity close to resonance and detecting the membrane signal, while the second beam is dedicated to cooling and is detuned with respect to the cavity by $\Delta = -\kappa/(2\sqrt{3}) = -2\pi \times 16\,\text{MHz}$. By varying the power of the cooling beam P_{cool}, we can modify the mechanical susceptibility and calibrate the coupling strength g_0. The impact of the cooling beam is determined by detecting the variation in the mechanical linewidth and resonance frequency depending on the ingoing cooling laser power P_{cool}, as predicted from the Eqs. (2.69). We can determine a value for g_0 using both the frequency shift $\delta\Omega_m$, which results

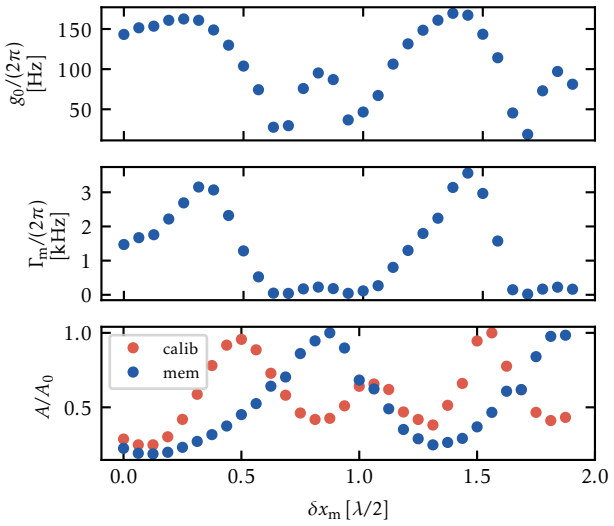

FIGURE 4.13: Calibration measurement of the optomechanical coupling strength g_0, scanning the membrane position δx_m with respect to the cavity standing wave. At each position we fit a Lorentzian to the mechanical peak and thus determine the mechanical linewidth γ_m. The lowest panel illustrates the comparison between the normalized area A/A_0 of the membrane and the calibration peak.

in $g_0/(2\pi) = 169\,\mathrm{Hz}$, and the broadening $\gamma_m + \Gamma_m \approx \Gamma_m$, which results in $g_0/(2\pi) = 161\,\mathrm{Hz}$. The slight discrepancy most likely comes from a small underestimation of the detuning ($< 10\%$), which affects the damping stronger than the frequency shift. Furthermore, even for high incoming light powers ($P_{\mathrm{cool}} > 1\,\mathrm{mW}$), the phonon occupation number decreases continuously. This indicates that classical laser noise does not generate a heating effect that counteracts the cooling process, and we are still in a regime where the dominant process is cooling.

4.4.3 Optomechanical Response

A third method to calibrate the optomechanical coupling strength involves detecting the optomechanical response to a known amplitude modulation of the light. By utilizing the previously derived expressions for the optomechanical response [see Sec. (1.8)], we can directly relate the optomechanical measurement rate to the response function without prior knowledge of other system parameters. The calibration can be achieved by amplitude modulating the incoming light field and detecting the response of the mechanical oscillator on the homodyne signal. We can detect different linear combinations of the light's amplitude and phase quadratures, by scanning the homodyne phase of the detection θ, as stated in Eq. (1.81).

From the amplitude modulation transfer function given in Eq. (1.91), in the unresolved sideband regime and for frequencies close to the mechanical resonance frequency ($\omega \approx \Omega_m \ll \kappa$), we can simplify $C_+(\omega) \approx 2/\kappa e^{i\omega\tau_c}$ with τ_c is the cavity delay, such that we obtain

$$\zeta_{\mathrm{amp}}(\omega) = \sqrt{\eta_{\mathrm{det}}}\beta_0\Big(\cos(\theta)\Big[2 - \eta_c(3 + e^{2i\omega\tau_c})\Big] - \sin(\theta)\Big[4\Gamma_{\mathrm{meas}}\chi_m(\omega)e^{2i\omega\tau_c}\Big]\Big). \tag{4.25}$$

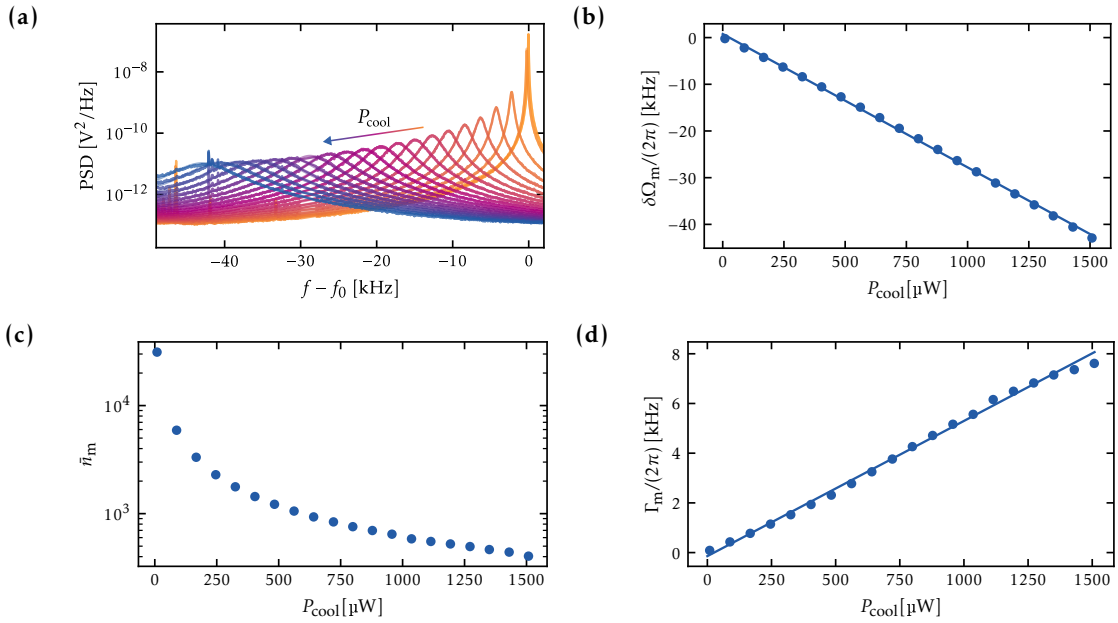

FIGURE 4.14: **(a)**: Mechanical displacement power spectral density for dynamical backaction cooling with varying incoming power of the cooling beam P from 0 to 1.5 mW, referenced to the mechanical frequency without a cooling beam f_0 and a detuning of $\Delta = 2\pi \times 15.8\,\mathrm{MHz}$, at an environmental temperature of $T = 300\,\mathrm{K}$. **(c)**: The inferred mechanical occupation number. The frequency shift $\delta\Omega_{\mathrm{m}}$ in **(b)** and broadening $\gamma_{\mathrm{m}} + \Gamma_{\mathrm{m}} \approx \Gamma_{\mathrm{m}}$ in **(d)** are obtained from fitting a Lorentzian to the mechanical power spectral densities.

We note that the terms resulting from modulation in both the amplitude and phase quadratures exhibit the same scaling with the detection efficiency and the modulation depth $\sqrt{\eta_{\mathrm{det}}}\beta_0$. Therefore, acquiring the signal for various homodyne phases θ, and consequently different combinations of quadratures, enables the elimination of these dependencies from the calibration process. The modulation depth β_0, homodyne phase θ, and the cavity delay τ_{c} can be fitted to the modulation transfer function. The first term, which is proportional to the cosine factor, solely contains the amplitude light quadrature, encompassing contributions from both the direct back-reflection off the cavity and the intracavity field. The second term, which is proportional to the sine factor, arises from the phase quadrature term and includes dependencies related to the effective mechanical susceptibility, as well as the measurement rate. As a result, this optomechanical response to an amplitude modulation exhibits interference between the optical drive and the mechanical response. By varying the phase between the local oscillator and the signal for the homodyne detection, we can alter the acquired quadrature between the phase quadrature ($\theta = 0$) and the amplitude quadrature ($\theta = 90°$). This calibration method resulted in measurement rates of $\Gamma_{\mathrm{meas}}/(2\pi) = 4\,\mathrm{kHz}$ for an ingoing power of $300\,\mu\mathrm{W}$, together with a fitted delay of $\tau = 4.9\,\mathrm{ns}$ and an inferred $\kappa_{\mathrm{fit}}/(2\pi) = 80\,\mathrm{MHz}$, at a temperature $T = 30\,\mathrm{K}$. The deduced optomechanical coupling strength is then $g_0/(2\pi) = 126\,\mathrm{Hz}$, which is lower than the usual values that we obtain at room temperature, which typically lie around $g_0/(2\pi) = 160\,\mathrm{Hz}$. Together with the cavity coupling κ, this indicates that the mechanical position might not have been adjusted to the ideal point for a maximal optomechanical coupling strength. For the given measurement rate the single-pass

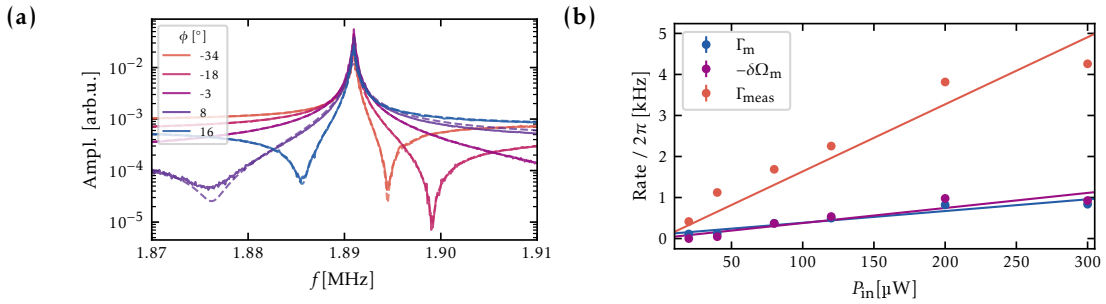

FIGURE 4.15: **(a)**: Optomechanical response measurement at cryostat temperature $T = 30\,\mathrm{K}$, with an incoming light power of $P_{\mathrm{in}} = 40\,\mu\mathrm{W}$ and a scan of the homodyne phase between $\theta = 50°$ and $\theta = 130°$ for ingoing power $P_{\mathrm{in}} = 40\,\mu\mathrm{W}$. The dashed line indicates the numerical fit. **(b)**: Inferred measurement rate Γ_{meas}, frequency shift $\delta\Omega_{\mathrm{m}}$ and mechanical linewidth $\gamma_{\mathrm{m}} + \Gamma_{\mathrm{m}} \approx \Gamma_{\mathrm{m}}$ for varying ingoing powers.

quantum cooperativity amounts to $C_{\mathrm{qu}} = 0.02$.

4.5 Mechanical Mode Occupation Calibrations

In order to estimate the thermal occupation number of a specific mechanical oscillator mode, we employ several methods depending on different pre-assumptions. This allows us to verify the associated temperature by comparing independently calibrated values.

4.5.1 Power Spectral Density Area Calibration

Starting from the expressions for the mechanical displacement power spectral density as stated in Eqs. (1.58) and (1.60), neglecting the factor 1/2, we obtain a direct proportionality between the mechanical occupation number and the integrated power spectral density of the mechanical motion.

Furthermore, as long as the occupation number remains well above the limit set by the fluctuations of the radiation pressure and the zero-point motion, the mechanical occupation number follows the direct classical relation

$$\bar{n}_{\mathrm{m}} = \bar{n}_{\mathrm{th}}(T)\frac{\gamma_{\mathrm{m}}}{\gamma_{\mathrm{m}} + \Gamma_{\mathrm{m}}}. \tag{4.26}$$

Given the knowledge of the intrinsic mechanical linewidth γ_{m}, the environmental temperature T, and thus the thermal occupation number $\bar{n}_{\mathrm{th}}(T)$, a measurement of the optically modified linewidth provides an additional way to determine the phonon occupation number, assuming that we remain in the regime dominated by thermal noise.

Once approaching the ground-state, we can reference the detected integrated areas at unknown mechanical temperatures to calibration measurements performed at higher temperatures using Eq. (4.26), in order to extract the phonon occupation number. Indeed, we can use the area of a given spectrum, A_{calib}, and associate it to an occupation $\bar{n}_{\mathrm{calib}}$, using the measured linewidth of that same detected spectrum. When additional cooling is present, the ratio between the new area A_{DD} and the calibration area A_{calib},

together with the known occupation number $\bar{n}_{\mathrm{calib}}$ provide a way to determine the occupation number $\bar{n}_{\mathrm{m}}$. The phonon number is then given by the ratio of areas

$$\bar{n}_{\mathrm{m}} = \frac{\bar{n}_{\mathrm{calib}}}{A_{\mathrm{calib}}} A_{DD}. \tag{4.27}$$

This allows us to verify the effect of additional cooling mechanisms, like the coherent feedback cooling described in Ch. 5. An essential requirement for the accuracy of the phonon number occupation estimation is to know the environmental temperature T to which the mechanical mode is thermalized. Therefore, a calibration area measurement is required at each cryostat temperature. Furthermore, the reliability of the calibration areas can be increased by performing standard dynamical backaction cooling experiments as described in Sec. 4.4.2, for each cryostat temperature, as illustrated in Fig. 4.16. As expected, increasing the power of a red-detuned beam leads to broadening of the mechanical linewidth and cooling of the mechanical oscillator, which can be detected with a resonant probe beam in a homodyne scheme. By referencing to a well-know temperature, such as room temperature, the ratio of the respective cooling curves allows to infer the corresponding environmental temperature. We note that for low cryogenic set temperatures, these calibrated environmental temperatures result in higher values, namely in the case of the cryostat set temperature of 4 K, the environmental temperature of the mechanical mode turns out to be 20 K. This could be due to a poor thermal contact of the mechanical oscillator with its support, and a bad thermal conductivity of the titanium mounts that form the membrane-cavity. The thermal contact could be improved using thermo-conductive grease, or copper thermalization clamps.

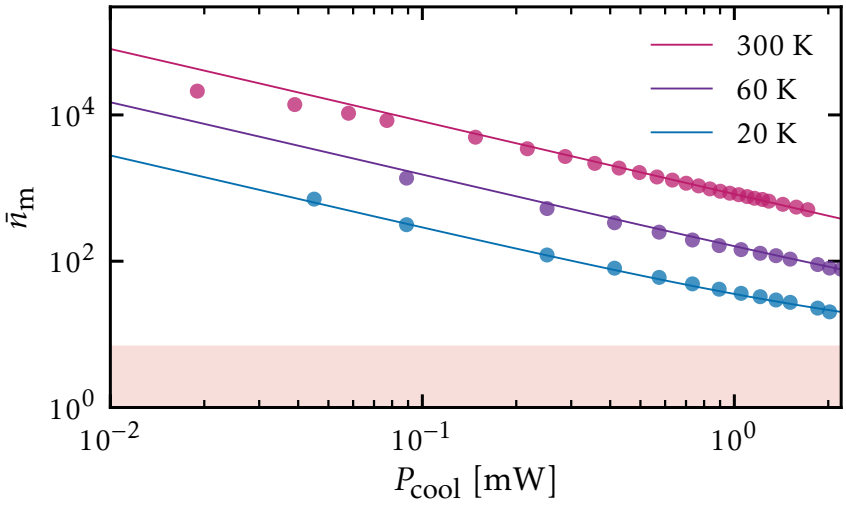

Figure 4.16: Dynamical backaction cooling performed at different cryostat temperatures.

4.5.2 Homodyne Voltage Calibration

The fluctuations in the voltage of the homodyne signal of the optical beam, can be directly used to calibrate the occupation number of a mechanical mode. In fact, the back-reflected beam leaking out of the cavity contains the mechanical signal as described in Eq. (1.81). Using homodyne detection, as described in Sec. 1.7, we overlap the output beam with a strong local oscillator of power $P_{\mathrm{LO}} = \hbar\omega_L|\alpha_{\mathrm{LO}}|^2 \gg P_1 = \hbar\omega_L|\alpha_1^{\mathrm{in}}|^2$. By means

of a movable mirror in the local oscillator arm, we can scan the homodyne angle θ, and the dc signal of the interference is given by $D(\omega = 0) = 2\alpha_{\mathrm{LO}}\alpha_1^{\mathrm{in}} \cos\theta$, such that scanning the phase over the full amplitude $D_0 = 2\alpha_{\mathrm{LO}}\alpha_1^{\mathrm{in}}$ describes a π phase shift of the light quadratures.

Locking the interferometer at $\theta = \pi/2$, we are detecting the phase quadrature $\hat{P}_1^{\mathrm{out}}$, as stated in Eq. (1.74) containing the membrane signal $\hat{X}_{\mathrm{m}}$ following

$$\hat{D}_{\theta=\frac{\pi}{2}}(\omega) = \sqrt{2}\alpha_{\mathrm{LO}}\alpha_1^{\mathrm{in}}\eta_{\mathrm{c}}g_0\zeta_{\mathrm{c}}(\omega)\hat{X}_{\mathrm{m}}(\omega), \tag{4.28}$$

with the cavity transduction function as defined in Eq. (1.75). From this signal $\hat{D}_{\theta=\frac{\pi}{2}}(\omega)$, we can compute the corresponding detected power spectral density (PSD)

$$S_{DD}(\omega) = \frac{1}{2}\left[\eta_{\mathrm{c}}g_0 D_0 |\zeta_{\mathrm{c}}(\omega)|\right]^2 S_{XX}(\omega), \tag{4.29}$$

with the membrane displacement power spectral density $S_{XX}(\omega)$. On the other hand, the average number of phonons is related to the integral of the membrane displacement [cf Eq. (1.60)] . Therefore, the phonon number can be directly obtained from the recorded power spectral density following

$$\bar{n}_{\mathrm{m}} = \frac{4}{\left[\eta g_0 D_0 |\zeta_{\mathrm{c}}(\omega)|\right]^2}\int_0^\infty \bar{S}_{DD}(\omega)\frac{d\omega}{2\pi} - \frac{1}{2}. \tag{4.30}$$

This method does not depend on the knowledge of the environmental temperature and only requires, other than the mechanical PSD, the measurement of the homodyne contrast.

4.6 Conclusion

In this chapter, we have established the theoretical and experimental characterization of a cavity optomechanical system in a crogenic setup, consisting of a membrane-in-the-middle in a free space Fabry-Perot cavity. The parameters of the cavity result in a linewidth of $\kappa/(2\pi) = 55\,\mathrm{MHz}$, and incoupling efficencies $\eta_1 = 0.91$ and $\eta_2 = 0.9$. We have discussed the main noise processes encountered in the optomechanical interaction and described how to use measurement-based cooling to cancel spurious mechanical noise peaks. Furthermore, we showed three independent characterization measurements for the vacuum optomechanical coupling strength, using dynamical backaction cooling, a phase modulation tone, as well as optomechanical response measurements, that agree on a value of $g_0 = 2\pi \times 160\,\mathrm{Hz}$. We have established two independent methods to determine the mechanical occupation number, namely from the fluctuations in the homodyne current directly, or the integrated mechanical displacement power spectral densities. Furthermore we explained how to use dynamical backaction cooling to determine the environmental temperature, and found that even at a cryostat set temperature of 4 K, the membrane thermalizes to 20 K.

Chapter 5

Optical Coherent Feedback Control of a Mechanical Oscillator

Feedback is a powerful and ubiquitous technique both in classical and quantum system control. Its standard implementation relies on measuring the state of a system, processing the classical signal, and feeding it back to the system. In quantum physics, however, measurements not only read out the state of the system but also modify it irreversibly. Coherent feedback is a different kind of feedback that coherently processes and feeds back quantum signals without actually measuring the system. Here, we report on the experimental realization and the theoretical analysis of an optical coherent feedback platform to control the motional state of a nanomechanical membrane in an optical cavity. The coherent feedback loop consists of a light field interacting twice with the same mechanical mode through different cavity modes, without performing any measurement. Tuning the optical phase and delay of the feedback loop allows us to control the motional state of the mechanical oscillator, its resonance frequency and also its damping rate, which we use to cool the membrane close to the quantum ground state. Our theoretical analysis provides the optimal cooling conditions, showing that this new technique enables ground-state cooling. Experimentally, we show that we can cool the membrane to a state with $\bar{n}_{\mathrm{m}} = 4.89 \pm 0.14$ phonons (480 μK) in a 20 K environment. This lies below the theoretical limit of cavity dynamical backaction cooling in the unresolved sideband regime and is achieved with only 1% of the optical power required for cavity cooling.

Parts of this Chapter have been published in [113].

5.1 Introduction

Quantum feedback is a powerful technique for cooling and controlling quantum systems [6]. The conventional strategy relies on quantum-limited measurements followed by classical processing and feedback actuation onto the system. However, quantum mechanics also allows for *coherent* feedback of *quantum* signals [20, 22], without destroying coherence in the process. This kind of feedback may exploit the information stored in non-commuting observables while circumventing the decoherence and back-action noise associated with a measurement [20, 23, 6]. Coherent feedback has thus the potential to improve quantum control and provide new capabilities across a broad range of physical systems [21, 25]. Coherent feedback strategies have so far been adopted to assist in a variety of different tasks [6], e.g. for noise cancellation [181, 26], pure-state preparation [25], optical squeezing [182, 30], stabilization and enhancement of entanglement [35, 31], sympathetic cooling [32, 33, 34], swaps of arbitrary states [183], qubit state control [36], and generating large optical nonlinearities at the single-photon level [38, 184].

Optomechanical systems are very well suited for coherent feedback control, as they offer a clean and tailored interface between highly coherent mechanical and electromagnetic field modes [44]. Indeed, various coherent feedback protocols have been theoretically proposed to enhance the cooling of optomechanical systems [111, 42, 43], to reduce the added noise in the low phonon-number regime of optomechanical precision measurements [24], to enable or enhance entanglement generation, verification, as well as state transfer [110, 185, 112, 42]. Coherent feedback can thus facilitate and extend the capabilities of quantum transducers between optics and mechanics [79].

Despite this wide range of possibilities, there have been surprisingly few experiments investigating coherent feedback in optomechanics [34, 186]. An optical coherent feedback loop acting directly onto a mechanical oscillator has not yet been realized. Moreover, while measurement-based feedback has been studied in some depth from a theory point of view [105, 9, 106, 107, 108], essential questions regarding the performance and limitations of coherent feedback in actual optomechanics experiments remain open.

In this work, we present an experimental realization of a simple, all-optical coherent feedback platform to control a single vibrational mode of a mechanical oscillator. We use a double-pass scheme where an optical signal interacts twice with the same mechanical mode through two different cavity modes of orthogonal polarization. The entire control of the phase and delay of the feedback signal is implemented purely via the optical field, without introducing measurements and subsequent electronic processing. Our approach is thus able to generate a variety of different interactions, ranging from Hamiltonian couplings to dissipative and non-reciprocal dynamics [27, 187, 188].

As a first application of the extended control offered by the coherent feedback loop, we investigate the cooling of the mechanical mode close to its quantum ground state, which is a prerequisite for many applications in quantum science and technology [44, 189, 190, 79]. Experimentally, we demonstrate the advantage of the coherent feedback loop by cooling below the theoretical limit of cavity dynamical backaction cooling in our system. This is particularly interesting for optomechanical systems with cavities of large bandwidth, which induce only a small delay and are frequently encountered in optomechanical displacement sensing, quantum interfaces and hybrid setups [102].

The remainder of this Chapter is structured as follows: We first provide an overview of the working principle of our coherent feedback platform for controlling a mechanical oscillator in an optical cavity. Next, we describe our experimental results on motional state control of one mechanical mode using the feedback parameters of delay and phase. Furthermore, we optimize the feedback parameters for reducing the mechanical occupation number. Finally we discuss some of the potential processes that might limit the achievable cooling.

5.2 Overview

Here we recall the working principle of our coherent feedback scheme, sketched in Fig. 5.1 and described in detail in Ch. 2. The goal is to control the motional state of a mechanical oscillator by designing an optical feedback loop that preserves the quantum coherent properties of the light field, which acts as the controller. To this end, the mechanical oscillator is radiation-pressure coupled to *two* cavity modes in a cascaded double-pass interaction. The first interaction takes place between the mechanical oscillator and the cavity mode $\hat{c}_1$, which is driven by a strong local oscillator, realizing the standard cavity optomechanical interaction [44]. Due to the optomechanical coupling,

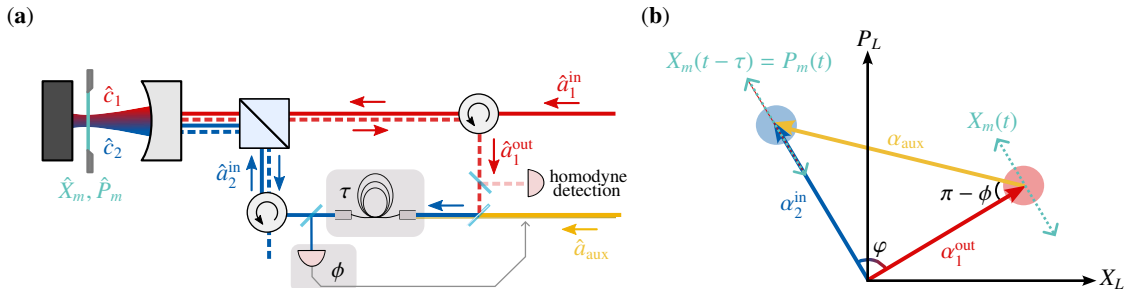

FIGURE 5.1: Sketch of the experimental setup and optical coherent feedback loop. **(a):** An incoming light beam $\hat{a}_1^{\text{in}}$ is injected into an optomechanical cavity, where it drives the cavity field $\hat{c}_1$ that interacts with a mechanical oscillator with quadratures $\hat{X}_{\text{m}}, \hat{P}_{\text{m}}$. The back-reflected beam $\hat{a}_1^{\text{out}}$ is combined with an auxiliary local oscillator mode $\hat{a}_{\text{aux}}$ to control the phase of the feedback loop φ. The combined field is delayed by τ with the help of an optical fibre, before being sent back as input $\hat{a}_2^{\text{in}}$ for a second interaction with the mechanical oscillator in an orthogonal polarization cavity mode $\hat{c}_2$. The outgoing light after the second interaction leaves the loop. A small fraction of $\hat{a}_1^{\text{out}}$ is picked up for detection and phase locking of the loop. The color coding of the light beams is used for visual guidance. Dashed lines are used for visual distinction between the incoming and back-reflected beams. **(b):** Phase-space visualisation of the feedback loop. The sketch represents the amplitude (X_{L}) and phase (P_{L}) quadratures of the light outside the cavity in an arbitrary frame. On resonance, the coherent cavity output field after the first interaction α_1^{out} is phase-modulated (dashed line) with the membrane displacement signal $X_{\text{m}}(t)$. This is converted into an amplitude modulation of α_2^{in} by mixing the coherent field with an auxiliary local oscillator α_{aux} with the appropriate relative phase ϕ, to achieve the desired value of φ between α_1 and α_2. After a delay $\Omega_{\text{m}}\tau = \pi/2$, the amplitude modulation becomes proportional to the momentum of the membrane P_{m} at time t (dashed line in α_2^{in}) and exerts a force on the mechanical oscillator.

information about the mechanical position $\hat{X}_{\text{m}}$ is imprinted onto the phase quadrature of $\hat{c}_1$. This mode is then cascaded into the second cavity mode $\hat{c}_2$ via an all-optical feedback loop. Specifically, the output light of the first mode, with mean amplitude α_1^{out}, is mixed with a second local oscillator and fed back as the input of the second cavity mode, with amplitude α_2^{in}, as shown in Fig. 5.1. The resulting optical feedback loop is characterized by two parameters, the relative phase φ and the in-loop delay time τ. The phase φ is controlled by the second local oscillator α_{aux}, which implements a displacement in the optical phase space of the modes traveling within the loop, see Fig. 5.1 (b).

Both feedback parameters are crucial for controlling the mechanical oscillator. The phase φ is adjusted so that the phase quadrature of the outgoing mode, which contains information on the mechanical position, is turned into the amplitude quadrature of the incoming mode, such that it exerts a feedback force by radiation pressure on the mechanical oscillator. As sketched in Fig. 5.1 (b), this occurs for $\varphi = \pi/2$. Adjusting the delay τ allows to either feed back the instantaneous position [when $\hat{X}_{\text{m}}(t-\tau) \simeq \hat{X}_{\text{m}}(t)$], momentum [when $\hat{X}_{\text{m}}(t-\tau) \simeq \hat{P}_{\text{m}}(t)$, as represented in Fig. 5.1 (b)], or a superposition thereof. While feeding back the position enables control of the mechanical oscillator frequency, feeding back the momentum allows control of its damping, which can be exploited for ground-state cooling.

Previous theoretical proposals for coherent feedback cooling of mechanical oscillators [111, 112, 42, 43] rely on coherently enhancing the interaction of the cavity light with the mechanics, mostly by modifying the effective cavity linewidth [112, 42], and on loops that impart only a delay (plus unavoidable coupling losses). In contrast, our scheme applies the coherent feedback directly to the mechanical oscillator, such that the feedback can be generated with a single cavity driven in two independent modes. Moreover, it allows tuning of the loop phase φ, which strongly influences the effect of the feedback.

Our scheme requires no additional optical devices such as cavities and only minor modifications of the optical path, resulting in a modular scheme that is optimally suited for incorporation into various types of optomechanical systems.

Furthermore, our double-pass scheme does not require non-classical input light states [103, 104, 190], additional interactions with other physical systems [32, 109, 34], nor the overall very high detector efficiency of measurement-based feedback schemes [105, 9, 106, 107, 108], which is now replaced by the requirement of small optical losses in the loop. The relaxation of the requirements on measurement efficiency renders our scheme valuable for systems working in wavelength ranges where efficient photodetectors are not available, e.g. in integrated circuit platforms [191].

5.3 Experimental Setup

Our experimental setup consists of a mechanical oscillator inside a cavity in a cryogenic environment provided by a low-noise liquid-Helium flow cryostat. The mechanical oscillator is the (2,2) square drum mode of a silicon nitride membrane [54] with a vibrational frequency $\Omega_\mathrm{m} = 2\pi \times 1.9\,\mathrm{MHz}$. The membrane is surrounded by a silicon phononic bandgap structure which shields this mode, leading to intrinsic quality factors that range from $Q = \Omega_\mathrm{m}/\gamma_\mathrm{m} = 1.9 \times 10^6$ at room temperature to $Q = 3.2 \times 10^6$ at 20 K. The membrane is placed inside a single-sided optical cavity of free spectral range 150 GHz, finesse $\mathcal{F} = 1200$ and linewidth $\kappa = 2\pi \times 55\,\mathrm{MHz}$, such that the optomechanical system operates in the unresolved sideband regime $\kappa \gg \Omega_\mathrm{m}$. The bare optomechanical coupling strength is $g_0 = 2\pi \times 160\,\mathrm{Hz}$.

The overall efficiency of the feedback loop is determined by a combination of different losses that accumulate along the optical path. Following the optical path illustrated in Fig. 5.1 (a), for the first beam we have to consider the finite cavity incoupling efficiency $\eta_1 = 0.91$. For the second pass, it includes the unavoidable loss at the beamsplitter that combines the auxiliary local oscillator $\hat{a}_\mathrm{aux}$ and the back reflection of the first beam $\hat{a}_1^\mathrm{out}$, which has a splitting ratio $\eta_\mathrm{aux} = 0.87$ in our experiment. Note that this loss can be made arbitrarily small in principle by using a strongly unbalanced beam splitter and higher incoming optical power for $\hat{a}_\mathrm{aux}$. Additionally, there is a cumulative loss due to the propagation in the optical fiber and other optical elements, leading to a transmission efficiency $\eta_T \simeq 0.3$ together with the cavity incoupling efficiency of the second beam in orthogonal polarization $\eta_2 = 0.9$. As discussed in Sec. 2.4.3, these losses can be fully taken into account by the overall efficiency of the feedback loop $\eta = 0.22$ and by an appropriate rescaling of the average displacements. Since the powers are measured in front of the cavity, P_1 is measured directly but the measured auxiliary power is given by $\tilde{P}_\mathrm{aux} = (1-\eta_\mathrm{aux})\eta_T P_\mathrm{aux}$. In the following experiments, we use the delay and the phase of the coherent feedback loop as the tuning knobs that allow us to control the mechanical state of the membrane, as described by Eq. (2.30). This shows up in the recorded mechanical

power spectral densities as a change of both the mechanical linewidth and the oscillation frequency, which we extract from Lorentzian fits to our data.

5.4 Results

5.4.1 Control via the Loop Delay

In a first set of experiments, we study the effect of delay alone without an auxiliary local oscillator in the feedback loop. We generate different delays between the two interactions with the mechanical oscillator by sending the light after the first pass through optical fibers of different lengths. Interesting situations arise once the delay is significant, i.e. of order $\Omega_m \tau \sim \pi$. We investigate the effect generated by different delays starting from a fiber length of 2 m going up to 80 m, which corresponds to $\Omega_m \tau = 0.07\pi$ up to $\Omega_m \tau = 1.55\pi$.

At zero detuning, the motion of the membrane is imprinted purely as a phase modulation onto the output light such that in the absence of the auxiliary local oscillator this results in $\varphi = \pi$ (due to the back reflection from the cavity) and we expect no effect from the coherent feedback loop [cf. Eqs. (2.30)]. With a finite detuning however, a phase shift $\varphi \neq \pi$ is introduced even without any auxiliary local oscillator [cf. Eqs. (2.16)]. Therefore, in that case, the motion is imprinted onto both the amplitude and phase quadratures and the effect of different delays due to feedback becomes apparent. Additionally, the standard cavity dynamical backaction effects that are not captured by Eqs. (2.30) modify the frequency shift and damping rate, see Ch. 1 for details.

Figure 5.2 shows experimental data where we study the effect of different feedback delays while scanning the detuning for an input power $P_1 = 60\,\mu\text{W}$. The coherent feedback onto the mechanical oscillator results in both in a shift of the mechanical frequency [Fig. 5.2(a)] and in a broadening or narrowing of the mechanical linewidth [Fig. 5.2(b)], leading to damping or driving, respectively. This is consistent with a picture in which the membrane motion couples via the light to a delayed version of itself, leading to feedback forces $F_{\text{fb}} \propto \pm P_m(t)$ for certain delays as shown in Eq. (2.23) and in Fig. 5.2(c).

Indeed, we observe that for a delay close to $\Omega_m \tau \sim \pi/2$ (i.e. a quarter of the oscillation period) the coupling is mostly proportional to $+P_m$ and we observe driving (narrowing of the linewidth) even with a red detuned beam. Half a period later, for $\Omega_m \tau \sim 3\pi/2$, the feedback force is mostly proportional to $-P_m$ and the motional damping is amplified by more than a factor 3 as compared to a single interaction, leading to additional cooling of the mechanical oscillator. Finally, we see that for the smaller delays $\Omega_m \tau \sim 0$, the effect of the second interaction on the broadening is small $\Gamma_m \simeq 0$, since the feedback force, in this case, is mostly $\propto X_m$.

The agreement with the theoretical predictions in Eqs. (2.27) and (2.28) (solid lines in Fig. 5.2) is excellent. The theory lines for the feedback interaction contain no free parameters. The detuning axis is calibrated from the recorded linewidths in the single-pass interaction under the effect of the standard cavity dynamical backaction [44] and can be extracted with an uncertainty of ±5%.

5.4.2 Control via the Loop Phase

Control over the feedback phase is a handy knob in a feedback platform, allowing to modify the effect of the feedback on the system under control. Here, we investigate how the loop phase modifies the membrane motion at a fixed delay and cavity detuning. As

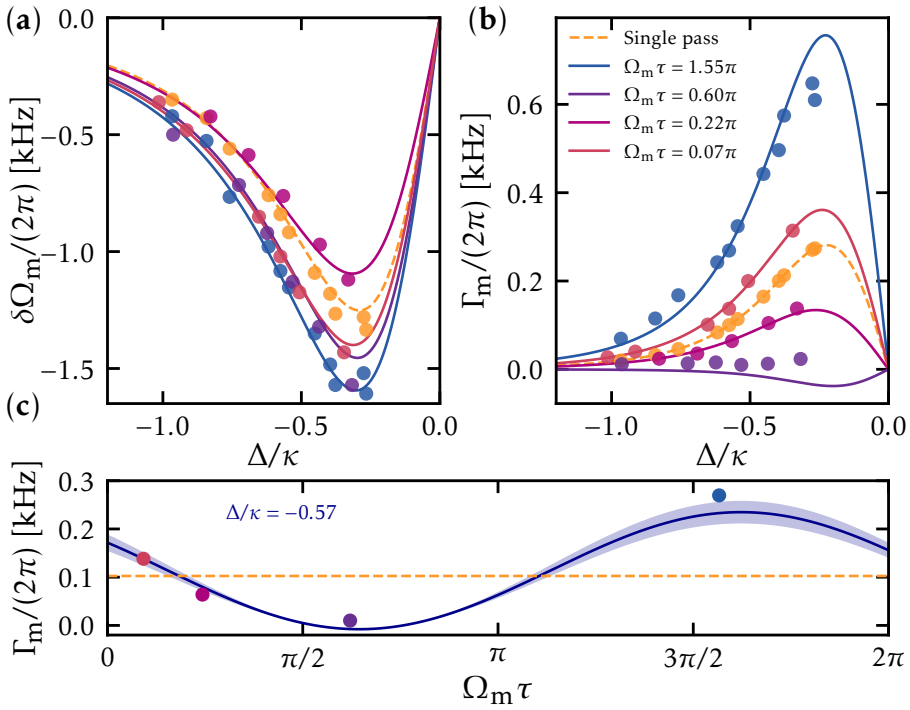

FIGURE 5.2: Mechanical frequency shift **(a)** and damping rate **(b)** as a function of the cavity detuning for different feedback delays, with $\hat{a}_{\mathrm{aux}} = 0$. The data points correspond to the results of Lorentzian fits to the mechanical power spectral density. The solid lines correspond to the theoretical predictions in Eqs. (2.30) evaluated at $\omega = \Omega_m$ with no free parameters. The detuning axis is calibrated from the measured linewidth in the single-pass interaction (dashed yellow line). **(c)**: The mechanical linewidth at a detuning of Δ/κ = -0.57 for the different fibres and respective delays.

previously discussed, this phase allows us to control the amount of motional information that is transferred onto the amplitude quadrature of the second interaction beam, thereby maximizing or minimizing the feedback force on the membrane, as well as the overall sign of the interaction. Experimentally, we vary the loop phase φ by adjusting the phase of the auxiliary local oscillator $\phi = \arg(\alpha_{\mathrm{aux}}/\alpha_1^{\mathrm{out}})$, which is selected and stabilized by locking at a specific angle of the interferometric signal between a small leak of α_1^{out} and α_{aux} [see Fig. 5.1].

The measured frequency shifts and linewidths are shown in Fig. 5.3. In this measurement, the delay is held constant at $\Omega_m\tau \sim 0.07\pi$ and the detuning at $\Delta/\kappa = -0.2$, the input powers were set to $P_1 = 20\,\mu\mathrm{W}$ and $\tilde{P}_{\mathrm{aux}} = 3\,\mu\mathrm{W}$. This detuning is experimentally chosen such that the amount of standard cavity dynamical backaction cooling is strong. This allows us to show the coherent feedback effect by scanning the full range 2π of the loop phase without running into instabilities when approaching negative effective linewidths. In practice, when we reach this unstable regime [blue dashed lines in Fig. 5.3 (b)], the system is driven and the measured linewidth is close to zero.

Scanning the phase, we observe that both the resonance frequency and the linewidth can be modified to either higher or lower values compared to the optical spring and broadening that occur even without the coherent feedback. We exploit this aspect in the next section to optimally feedback cool the mechanical oscillator. Here again, we find an excellent agreement between the experimental data points and the theoretical prediction

in Eq. (2.30) with no free parameters.

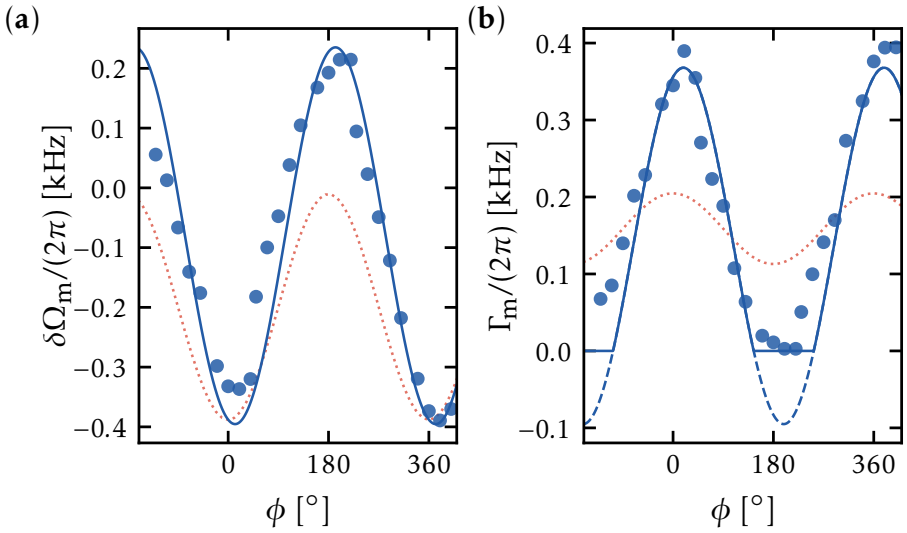

FIGURE 5.3: Mechanical frequency shift **(a)** and damping rate **(b)** as a function of the phase of the auxiliary local oscillator. The red dotted lines correspond to the broadening expected in the absence of feedback, but with an equivalent power in a single beam. The solid lines correspond to Eqs. (2.30) evaluated at $\omega = \Omega_m$ with no free parameters. The solid line in the plot of the damping rate is set to zero for negative values (dashed line), where the mechanical oscillator is driven by the feedback.

5.4.3 Coherent Feedback Cooling Below the Dynamical Backaction Limit

For cavity optomechanical systems within the so-called resolved sideband regime, it has been established theoretically and demonstrated in multiple platforms that a red-detuned drive allows cooling the mechanical oscillator close to its motional ground state [44]. Outside this regime, cavity dynamical backaction cooling to the ground state is no longer attainable and the most widely used cooling technique is measurement-based feedback [105, 128], where the optical signal is measured and converted into a classical electronic signal that drives the feedback actuator.

Here, we exploit the control provided by the coherent feedback loop demonstrated in the previous section to cool the membrane close to the ground state in the unresolved sideband regime. The available tuning knobs are the loop phase φ and delay τ as well as the detuning Δ and the powers of the first and auxiliary local oscillators P_1 and P_{aux}. In standard cavity cooling, the minimal number of phonons achievable in the unresolved sideband regime is bounded by $\kappa/(4\Omega_m)$ (cf. Eq. (2.70)), which in our case corresponds to about 7 phonons. In order to reach this dynamical backaction limit with our mechanical quality factor, we would need a laser power on the order of 100 mW [see Fig. 5.4]. The coherent feedback loop dramatically relaxes this power constraint and we are able to cool the motion of the membrane below the dynamical backaction limit, approaching the ground state.

In Fig. 5.4 (a) we show experiments where we reach our lowest membrane phonon occupation by scanning the experimental feedback loop phase. We present measurements at different cryostat temperatures, where the delay is set to $\Omega_m\tau \sim \pi/4$ and the detuning is kept fixed at $\Delta/\kappa = -0.35$. The powers for the first and auxiliary local oscillators are

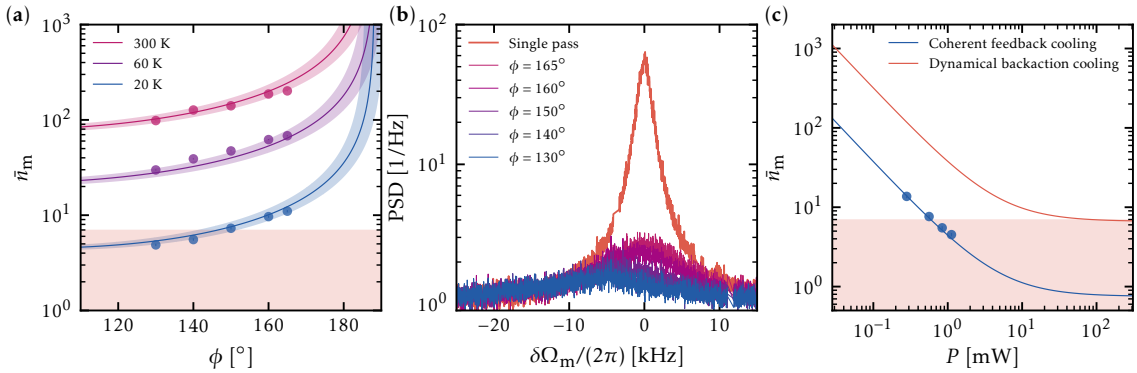

FIGURE 5.4: Coherent feedback cooling below the dynamical backaction limit. **(a)**: Phonon occupation plotted as a function of the phase of the auxiliary local oscillator at different cryostat temperatures for input powers $P_1 = 0.4\,\mathrm{mW}$ and $\tilde{P}_{\mathrm{aux}} = 1.2\,\mathrm{mW}$ and detuning $\Delta/\kappa = -0.35$. The red shaded area indicates the limit of cavity dynamical backaction cooling. The shaded areas around the theory lines correspond to a ±5% uncertainty in the inferred detuning. The error bars take into account both the numerical uncertainty from the fit of the raw data and the propagation of uncertainties from the calibrated quantities and are small compared to the point size. **(b)**: Shot-noise normalized mechanical power spectral densities corresponding to the data points at $T = 20\,\mathrm{K}$ in the phonon occupation plot, the frequency origin is centered so that the $\delta\Omega = 0$ corresponds to the single-pass mechanical resonance frequency. **(c)**: Coherent feedback cooling compared to standard cavity dynamical backaction cooling. Blue line and data points: Phonon occupation at a constant phase $\phi = 130°$, scanning the total input power resulting from the double-pass interaction $P = P_1(1+\eta_T\eta_{\mathrm{aux}}) + \tilde{P}_{\mathrm{aux}} + 2(\eta_{\mathrm{aux}}\eta_2 P_1 \tilde{P}_{\mathrm{aux}})^{1/2}\cos(\phi)$ while keeping the ratio $\tilde{P}_{\mathrm{aux}}/P_1 = 3$ fixed, at a detuning $\Delta/\kappa = -0.35$. Red line: cooling by standard cavity dynamical backaction given the same total input power P at the optimal detuning $\Delta/\kappa = -0.5$ for dynamical backaction.

set to 400 µW and 1.2 mW, respectively. With these experimental parameters, the feedback loop drives the mechanical oscillator towards a state with phonon occupation of $\bar{n}_m = 4.89 \pm 0.14$ phonons for a cryostat temperature of 20 K, reaching a phonon number below the theoretical limit of cavity dynamical backaction cooling for our membrane-cavity assembly. The coherent feedback cooling rate is $\Gamma_m > 10\,\Gamma_{\mathrm{dyn}}$, where Γ_{dyn} is the cooling rate of dynamical backaction cooling at the same power. The double pass quantum cooperativity for the settings that achieved maximal cooling results in $C_{\mathrm{qu}} = 0.3$.

In these experiments, the membrane phonon occupation is determined from the area of the mechanical power spectral density, recorded via phase-sensitive homodyne detection. We extract $\bar{n}_m$ by determining the reduction in area with respect to a single interaction [see Fig. 5.4 (b) and Sec. 4.5].

5.5 Potential Limitations

We note that higher powers, smaller detunings, and slightly smaller phases should further reduce the final number of phonons, but these parameter regimes were not accessible due to technical instabilities related to the cavity lock. Moreover, the optimal delay $\Omega_m\tau \sim \pi/2$ could not be implemented. That is why we consider here a series of potential

candidates to explain the encountered limitations, such as instability effects in the cavity photon number and phase noise in optical fibers .

5.5.1 Mechanically Induced Instabilities

A potential process that could prevent us from reaching the experimental operation of the cavity necessary for ground-state cooling in terms of optical power could be caused by unstable photon numbers in the optical cavity. Apart from the dispersive shift of the cavity resonance frequency due to the presence of the mechanical oscillator, the light field also induces an instantaneous static displacement of the equilibrium position of the mechanical oscillator denoted as $\bar{x}_\mathrm{m}$ and described in Sec. 1.3. By inserting the modified equilibrium equation in the expression for the cavity steady state, we obtain a third-order polynomial expression for the average intracavity field occupation number

$$\bar{n}_\mathrm{c}\Big(4g_0^4\bar{n}_\mathrm{c}^2 + 4\Delta\Omega_\mathrm{m}g_0^2\bar{n}_\mathrm{c} + \Omega_\mathrm{m}^2[\Delta^2 + (\kappa/2)^2]\Big) = \Omega_\mathrm{m}^2(\kappa/2)^2\bar{n}_0, \tag{5.1}$$

such that for certain ingoing powers, there are multiple values of the average cavity population that satisfy the equation. For a given ingoing light power, there exists a certain detuning beyond which multiple roots occur, leading to a multistable behavior of the average cavity population number, in turn affecting the mechanical equilibrium position $\bar{x}_\mathrm{m}$. In fact, the optical field can be seen as an additional potential that alters the shape of the effective mechanical potential, allowing for the existence of multiple minima [44]. This condition is achieved when the slope of the Lorentzian cavity response exceeds the linear radiation pressure force, resulting in the emergence of multiple solutions. This

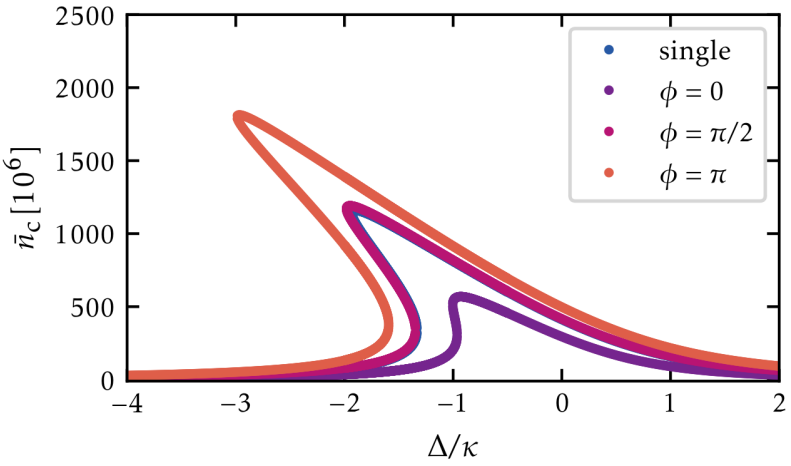

FIGURE 5.5: Average cavity photon occupation number, with the ingoing power for one single interaction $P_1 = 25\,\mathrm{mW}$ compared to the double pass experiment, with the ingoing power of the first beam $P_1 = 12.5\,\mathrm{mW}$ and the local oscillator $P_\mathrm{aux} = 12.5\,\mathrm{mW}$, for a mechanical frequency of $\Omega_\mathrm{m}/(2\pi) = 2\,\mathrm{MHz}$ and a second pass efficiency of $\eta = 0.3$.

bistable behavior is depicted in Fig. 5.5 as we scan the detuning. In the experiment, bistability appears as a hysteresis when scanning over the cavity resonance and an unstable behavior of cavity locks. For our standard experimental settings, the critical intracavity photon occupation number is given by $P_\mathrm{crit} = \Omega_\mathrm{m}\kappa/(6\sqrt{3}g_0^2)$ [44]. At this critical

intracavity power, the bistability appears for detunings smaller than the onset detuning $\Delta = -\sqrt{3}\kappa/2$. The higher the optical power, the closer the onset detuning moves towards resonance. At a detuning of $\Delta = -0.22\kappa$, this corresponds to an ingoing power of about $P_{\mathrm{crit}}^{\mathrm{in}} \approx 10\,\mathrm{mW}$. The presence of bistability limits the amount of power that can be sent in stable conditions to the cavity at negative detuning, ultimately imposing a limitation on achievable dynamical backaction cooling.

In the double pass scheme, where we have two incoming light fields that build up two orthogonal cavity modes. The total cavity photon number is now given by $\bar{n}_{\mathrm{c}} = |\alpha_1|^2 + |\alpha_2|^2$ taking into account the first and second cavity mode average displacements α_1 and α_2, see Eq. (2.16). The new resonant cavity number is expressed as

$$\bar{n}_0 = \frac{4}{\kappa}\Big[\alpha_{\mathrm{in}}^2 + (\sqrt{\eta}\alpha_{\mathrm{in}} - \sqrt{1-\eta}\cos\phi\alpha_{\mathrm{aux}})^2 + \sin\phi^2(1-\eta)\alpha_{\mathrm{aux}}^2\Big], \tag{5.2}$$

and depends on the phase ϕ between the two intracavity field. Taking into account this redefinition of $\bar{n}_0$, the solutions of the cavity steady state occupation numbers are presented in Fig. 5.5 for different phases ϕ and the additional powers P_{aux} of the auxiliary local oscillator. The experimentally set loop phase ϕ modifies the total light power sent to the cavity during the second pass through the interference between the outgoing light beam of the first interaction and the auxiliary beam, thereby impacting the onset of bistability. However for our experimental parameters, where the cavity is operated close to resonance and with the ingoing powers $P_1 = 600\,\mu\mathrm{W}$ and $P_{\mathrm{aux}} = 1.2\,\mathrm{mW}$, we are far below the critical power of the onset of the bistability. Consequently we can exclude an optical instability due to the static effect to be the reason for instabilities when we add $\hat{a}_2^{\mathrm{in}}$ for the coherent feedback loop.

5.5.2 Fiber Phase-Noise

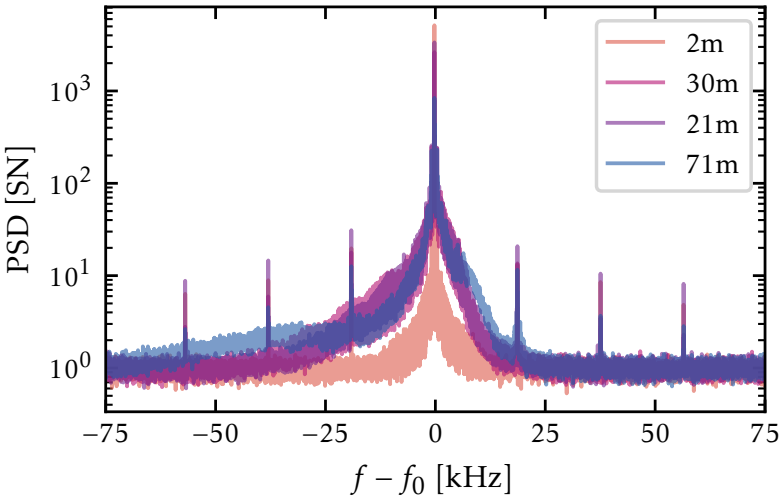

Figure 5.6: Fiber phase noise acquired with a heterodyne detection scheme, with the modulation frequency f_0, detected at the beatnote frequency $f - f_0$, for the fiber lengths used in the coherent feedback double pass experiments.

In our coherent feedback loop, phase noise plays an amplified role, as can be seen from the explicit expression of the mechanical displacement operator in terms of the

ingoing light quadratures, stated in Eq. (2.25). Due to the quadrature rotation implemented by the loop phase, the original phase quadrature of the ingoing light directly couples to the mechanical motion, even with a resonant cavity drive. The optical fibers used in our coherent feedback experiments to set the time delay between the two interactions introduce an additional source of phase noise. In fact, minor variations in the length of the optical fiber caused by thermal and pressure fluctuations can alter the phase of the outgoing light. Here we investigate whether the fiber length significantly affects the magnitude of the introduced phase noise. To measure phase noise, we employ a self-heterodyne detection scheme, as described in App. A, by overlapping the light that is passed through the fiber with a frequency-shifted reference beam. We record the noise spectra via direct detection of the light on a photodiode around the beatnote frequency for different fiber lengths, as shown in Fig. 5.6. We observe that phase noise increases for fiber lengths beyond 2 m. However, there is no significant increase in phase noise for fiber lengths ranging from 21 m to 80 m.

So far, the effect of phase noise has been mostly investigated in the literature in the context of cooling, where an off-resonant cavity drive transduces noise from the ingoing phase quadrature onto the cavity amplitude quadrature that can consequently drive the mechanical motion [176]. In this context, phase noise at the mechanical frequency can be modelled as a sinusoidal modulation [174, 175, 192] . In the off-resonant case, this results in a modulation of the cavity amplitude quadrature generated by $S_{\mathrm{ph}} = \Gamma_1(\kappa^2/2)|C_-|^2 S_{PP}^{\mathrm{in}}$, where we recall that $C_- \propto \Delta$. This modulation can be associated to an optical bath temperature $T_{\mathrm{ph}} = S_{\mathrm{ph}}/(2k_{\mathrm{B}} T m \gamma_{\mathrm{m}})$, which increases the effective mechanical bath temperature [175]. The additional mechanical displacement due to the excess phase noise can be determined using Eq. (1.37) and is given by

$$\delta\hat{X}_{\mathrm{m}}(\omega) = -\kappa\chi_{\mathrm{m}}\sqrt{\Gamma_1}(\omega)C_-(\omega)\hat{P}_{\mathrm{in}}. \tag{5.3}$$

However, the situation becomes more complicated in the presence of the double pass, where the contributions to the mechanical displacement [cf. Eq. (2.25)] from the ingoing phase noise result in

$$\begin{aligned}\delta\hat{X}_{\mathrm{m}}(\omega) = -\kappa\chi_{\mathrm{m}}(\omega)\Bigg\{&\sqrt{1-\eta}\,\kappa\Gamma_2\chi_{\mathrm{m}}(\omega)C_-\hat{P}_{\mathrm{aux}} \\ &+ \hat{P}_1^{\mathrm{in}}\Bigg[\sqrt{\Gamma_1}C_- + \sqrt{\eta\Gamma_2}\mathrm{e}^{\mathrm{i}\omega\tau}\Big(\cos\varphi\Big[C_- - 2\kappa C_+C_-\Big] + \sin\varphi\Big[C_+ - \kappa(C_+^2 - C_-^2)\Big]\Big)\Bigg]\Bigg\}\end{aligned} \tag{5.4}$$

and are also present for a resonant optical drive. For optimal cooling parameters $\Omega_{\mathrm{m}}\tau = \varphi = \pi/2$ the corresponding power spectral density reads

$$\bar{S}_{\delta\hat{X}_{\mathrm{m}}\delta\hat{X}_{\mathrm{m}}}(\omega) = \kappa^2|\chi_{\mathrm{m}}(\omega)|^2\eta\Gamma_2|C_+|^2\Big(\kappa^2|C_+|^2+1\Big)\bar{S}_{P_{\mathrm{in}}P_{\mathrm{in}}}(\omega). \tag{5.5}$$

Hence in the future, phase noise has to be considered as a serious threat to ground state cooling for the mechanical oscillator in the double pass configuration, and should be investigated quantitatively in more detail.

5.6 Conclusions & Outlook

We implemented an all-optical coherent feedback platform to control the motion of a mechanical oscillator and demonstrated full control via the parameters of the feedback loop, namely the phase and the delay. We showed theoretically that this scheme can be used for ground-state cooling in the unresolved sideband regime without the need for measurements. We demonstrated experimentally that even with a moderate mechanical Q–factor, we can beat the theoretical lowest-phonon number limit of cavity dynamical backaction cooling in the unresolved sideband regime, with only 1% of the optical power required for the latter. In contrast to previous proposals, where feedback is performed on the optical cavity mode [112, 42], we perform feedback directly on a mechanical oscillator mode , using orthogonal polarizations for first and second passes. But our scheme does not rely on the availability of same-frequency orthogonal cavity modes: When experimentally possible, one could use another longitudinal mode of the cavity. Alternatively, the scheme could also be implemented via a loop that is opened or closed by an optical switch, with a switching rate $1/(2\tau)$, in such a way that first and second passes are never at the same time in the cavity. As such, the double-pass scheme can be adapted to a variety of different physical systems and is not restricted to optomechanics. In the present configuration, ground state cooling would be achievable by improving the thermal conductivity of the membrane support to ensure thermalization at 4.2 K. However, the most straightforward improvement would consist in using a mechanical resonator with a higher quality factor [63].

The beauty of coherent feedback lies in its potential for processing non-commuting observables [24]. In the unresolved sideband regime, coherent feedback opens up the possibility to generate self-interactions and mechanical squeezing [27], photon-phonon entanglement [42], or to enhance optical nonlinearities at the single-photon level [184]. Our scheme could also be exploited in the sideband resolved regime, where optomechanical couplings of the form $\hat{c}_j\hat{B} + \hat{B}^\dagger\hat{c}_j^\dagger$ can be designed, with $\hat{B}$ being a raising or lowering operator of the mechanical oscillator. Such couplings are sensitive to both quadratures and potentially allow for creating non-classical mechanical states using coherent feedback [22].

In contrast to measurement-based control, coherent feedback avoids the incoherent addition of feedback and measurement noise, making it a key technique in the low phonon-number regime [24]. In particular, the interference of optical input noise can be tuned to realize backaction cancellation [27, 26]. This makes coherent feedback a promising candidate for sensing applications, where such backaction cancellation is highly desirable.

Coherent feedback thus opens up new approaches for engineering the dynamics of quantum systems with potential applications for quantum technology, measurement and control as well as quantum thermodynamics.

Chapter 6

Outlook

In this thesis, I report on the first implementation of an all-optical coherent feedback loop, which we used to control the motion of a mechanical oscillator in an optomechanical setup. We demonstrated the control offered by the parameters of the feedback loop, namely the phase and the delay, which we used to cool the mechanical mode close to the ground state. Our coherent feedback scheme is advantageous for cooling an optomechanical system in the unresolved sideband regime, which we demonstrated by cooling to an occupation number of the mechanical mode below the dynamical backaction limit. Furthermore we developed a theoretical description that is in excellent agreement with the experimental data and that gives an intuitive understanding of the underlying working principle of the coherent feedback scheme. We also derived an expression for the minimal achievable phonon number, showing that our scheme allows for ground-state cooling. Compared to measurement-based techniques, the lower bounds for the cooling processes result in analogous limits determined by the optical efficiency in our case and the measurement efficiency for the latter. Additionally, we described and characterized the next generation of mechanical oscillators that will be used in our experiment, namely the soft-clamped membranes that provide a remarkable reduction in thermal decoherence. The union of the presented elements paves the way towards exploring quantum coherent control of optomechanical oscillators using coherent feedback.

In terms of its cooling performance, the coherent feedback experiment still has room for improvement to actually meet the theoretically predicted limitations and provide ground-state cooling. Besides the obvious technical improvements such as an improved thermalization to cryogenic temperatures, also the operation of the coherent feedback close to cavity resonance would be advantageous for optimal cooling and quantum-limited readout. To avoid potential cavity instabilities, it would be beneficial to have a red-detuned cooling beam for precooling, and resonant beams dedicated to feedback, and potentially also to read-out. This could for instance be achieved by frequency shifting the additional beam to occupy another longitudinal cavity mode, using a separate laser beam. The additional beam could be stabilized at an arbitrary number of free spectral ranges by locking it to a frequency comb available in our department and optically connected to our laboratory.

Our coherent feedback scheme uses same-frequency orthogonal polarizations cavity modes to distinguish and avoid interference between the first and second cavity fields. Alternatively, for systems where the use of two orthogonal polarizations is not possible, like for electro- or magnetomechanical systems or microwave circuits, one could consider using two longitudinal modes of the cavity and frequency shift the light between the two interactions, if experimentally feasible. However, for many systems, the free spectral range of the cavity exceeds the frequency shifting technologies. In such cases, instead of a continuous scheme relying on two orthogonal cavity modes, one can resort to separating

the two cavity fields in the time domain by employing a stroboscopic coupling scheme. To achieve this, an optical deflector, such as an AOM, can be inserted into the feedback loop to open and close the loop stroboscopically. Alternatively one can use two distinct input ports, which can be selected via a switch, that flips from the initial input port to a port connected to the leaking light after the first interaction. The required switching rate is $1/(2\tau)$, which is inversely proportional to the propagation time of the light through the system. By ensuring that the first and second passes are never simultaneously in the cavity, optical interferences can be avoided.

Furthermore, a significant improvement of the experimental setup would involve using a membrane with a lower thermal dissipation rate. Mechanical oscillators with high quality factors facilitate the preparation of mechanical states close to the ground state, owing to the reduced coupling to the thermal environment and the lower heating rates that must be counteracted by cooling. By implementing a membrane-cavity containing a soft-clamped membrane with a high quality factor $Q > 10^7$, the reduced coupling to the thermal reservoir facilitates the access to the quantum backaction-dominated regime.

The preparation of the mechanical oscillator in its ground state and in the backaction dominated regime enabled by our coherent feedback scheme offers a starting point for numerous exciting opportunities, especially in the context of coupling the mechanical system in a hybrid setup. We can for instance consider the concrete example of the hybrid system composed of a mechanical oscillator coupled to the spin of an atomic ensemble, as described in [127]. Once the mechanical oscillator is not saturated with thermal excitations, we can envision quantum coherent coupling, involving the controlled exchange of single excitations between the two strongly coupled systems. Promoting the coupled setup into the quantum-limited regime allows to establish the transfer of nonclassical spin-squeezed states onto the mechanics. However, the verification of the presence of quantum states leads to additional detrimental backaction. It has been shown that looped interactions, enabling the repetition of a given interaction in its exact time-reversed manner, leads to the cancellation of its backaction [27]. In this scenario, the signal of the system's interaction is erased from the outgoing beam and can hardly be used for read-out. However, one could implement a strong light interaction and cancel the associated backaction while adding a weak auxiliary beam for verification. In general for such hybrid coupling experiment, it would thus be advantageous to incorporate double-pass interactions on its individual systems. This has been done for an atomic system before [127], and could be extended to the optomechanical module with the coherent feedback loop we have described here. Erasing the signal about both systems from the outgoing light effectively closes the coupled system as a whole with respect to the environment and allows for coherent exchange of information between the systems within the loop.

Our coherent feedback scheme provides tools not only for enhancing motional state control, but also for a more efficient usage of available optical power and backaction evasion. These capabilities are highly desirable for quantum sensing and communication [26]. Applying this scheme to optomechanical quantum sensors and combining it with ingoing squeezed light could lead to measurement sensitivities below the standard quantum limit, bringing the already remarkable ultrasensitive force and displacement detection capabilities offered by optomechanical systems into the realm of quantum-enhanced sensing [26, 21, 193]. This could, for instance, lead to improved strain sensitivity in gravitational waves detectors [194, 195] and enable the verification of different dark matter models [196, 197, 198].

In addition, the noise reduction properties of the coherent feedback enable the coherent coupling strength to exceed the noise terms, leading to the generation and enhancement of entanglement between different mechanical modes [110, 42, 185, 199]. As such, coherent feedback could facilitate the study of macroscopic mechanically entangled states [88, 87, 89], and lead to insights into fundamental questions related to gravity and quantum mechanics [200, 201, 202, 203, 204].

Moreover, the coherent feedback loop in our optomechanical setup presents exciting opportunities for further studies. The tunable loop phase allows us to switch between two different coupling regimes, namely Hamiltonian interaction, as well as non-Hamiltonian scenarios [27].

In the Hamiltonian case, the feedback loop has the ability not only to cancel noise but also to produce self-interactions. By adjusting the loop phase during the second interaction, an interaction term proportional to $\hat{X}_{\mathrm{m}}^2$ can be created. This leads to a one-axis twisting interaction generating mechanical squeezing that is maximal when the loop phase is set to $\varphi = \pm\pi/2$, as shown in Eq. (2.90). However, it should be noted that the squeezing and the backaction rates cannot be simultaneously optimized, as they require different loop phases. Therefore, significant squeezing can only be achieved once the squeezing rate exceeds the thermal decoherence rate.

In contrast to the Hamiltonian regime, the loop phase can be chosen to favour the dissipative coupling of the interaction. The presence of a dissipation channel and resulting non-reciprocal interactions provide opportunities to explore non-Hermitian physics.

The non-Hermitian dynamics that are inherent to our optomechanical coherent feedback scheme provide a fruitful platform to investigate the so-called exceptional points (EP) through the dynamics of an open, non-conservative system that exchanges energy with its environment [205, 206]. By varying one parameter, the non-Hermitian Hamiltonian may exhibit a singularity where the eigenvalues become degenerate, and the eigenvectors coalesce [207], corresponding to an exceptional point. Such EPs can lead to various exotic phenomena related to the sudden jump in the eigenvalue phase, including unidirectional invisibility [208], absorption enhanced transmission [209], enhanced sensitivity [210, 211], and topological non-reciprocal energy transfer [212]. The remarkable opportunities for sensing and topological operations provided in the vicinity of EPs make the study of dissipative dynamics in the quantum regime highly attractive [206]. One approach to accessing this regime involves modulating the coupling strength between two modes, such as two mechanical modes [212], a combination of optical-mechanical modes, or spin-mechanical modes in a hybrid setup. The tunability of the pump lasers and the resulting ability to control gain and losses, combined with the additional parameters of the coherent loop, makes coherent feedback on cavity optomechanics an ideal platform to investigate parity-time symmetries, exceptional points and the specifics of unknown dynamics in the dissipative regime [206].

Additionally, in the context of quantum thermodynamics, since optomechanical systems provide coherent conversion between photons and phonons, these are highly interesting to study the transformation between mechanical energy and heat, and could be used to engineer quantum heat engine [213]. Equipped with coherent feedback, the system contains an enhanced controllability of the mechanical susceptibility and additional control knobs to tune the coupling regime and the dissipative dynamics that remain experimentally mostly unexplored so far [213, 214, 215, 216].

In the long run, remote quantum coherent coupling of disparate systems could enable the establishment of a quantum internet, by extending phononic and photonic quantum networks and leveraging the benefits of coherent feedback to reduce noise and enhance

the coupling strength and thus boost efficiencies and quantum performance [217, 218, 219, 220, 221].

The coherent feedback scheme presented in this work has the potential to facilitate state preparation through the generation of QND variables, that are immune to the input field used for measurement, while keeping their signature appearing in the output signal, which would be extremely valuable for state stabilization [21, 22]. Moreover, the ability of coherent feedback to produce decoherence-free subsystems (DFS) [122, 21], encompassing variables that are completely isolated from the environment, could generate promising states for quantum computation and improving the lifetime of optomechanical quantum memories [134, 222, 223].

The exploration of coherent feedback holds great promise and excitement, particularly in utilizing both light quadratures, instead of solely relying on the detection of one quadrature while disregarding the orthogonal one [24], potentially leading to the generation of non-classical mechanical states using the parametric gain interaction [22]. In conclusion, numerous unanswered questions remain about harnessing the advantages of coherent feedback, and we have only scratched the surface of the possibilities it presents.

Moreover, the simplicity of the employed feedback protocol makes it highly versatile and applicable to various configurations beyond membrane-cavities, including other optomechanical and hybrid setups, for applications that produce a phase-sensitive measurement whenever a strong light-matter interface is present.Therefore, the presented experiment provides a valuable platform to explore the potential of coherent feedback, and also offers concepts to extend the given feedback scheme to numerous other physical systems.

Appendices

A Heterodyne Detection

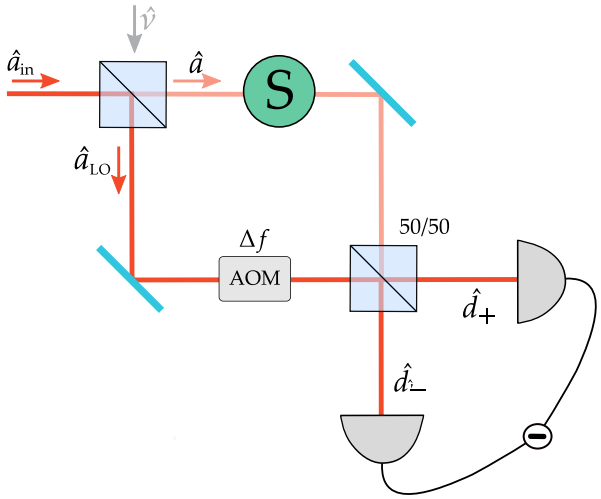

FIGURE 1: Sketch of the Mach-Zehnder interferometer used for heterodyne detection.

Heterodyne detection is, besides homodyne detection another commonly used method to detect the phase quadrature of a light mode $\hat{a}$. In this case, the signal beam is overlapped with a local oscillator $\hat{b}e^{i\Delta_{\text{het}}}$ that is shifted in frequency by Δ_{het}. The phase of the combined field, containing both the detected field and the local oscillator and thus the acquired optical quadrature is oscillating in time. In the case where frequency offset Δ_{het} is smaller than the center frequencies, we obtain in analogy to the section about homodyne detection, that the fields at the output ports of the beamsplitter

$$\hat{d}_{\pm} = \frac{1}{\sqrt{2}}(\hat{b}e^{i(\theta+\Delta_{\text{het}}t)} \pm \hat{a}), \tag{1}$$

such that the expression for the detector signal reads

$$\hat{D} \approx \beta(e^{i(\theta+\Delta_{\text{het}}t)}\hat{a}^{\dagger} + e^{-i(\theta+\Delta_{\text{het}}t)}\hat{a}). \tag{2}$$

In the heterodyne detection, the acquisition of alternating optical quadrature oscillating in time at the frequency of the detuning Δ_{het} contains information about both the amplitude and the phase quadratures. Consequently the power spectral density results in an expression in photon number, containing frequency components at the frequencies

$\Delta_{\rm het} \pm \omega$ [114]

$$S_{DD}(\omega) = \beta^2 \Big[S_{aa}(\Delta_{\rm het} + \omega) + S_{a^\dagger a^\dagger}(\Delta_{\rm het} - \omega) \Big], \tag{3}$$

which can be written in terms of the optical quadratures

$$\begin{aligned} S_{DD}(\omega) = &\frac{1}{4}\Big[S_{X_{\rm out}X_{\rm out}}(\Delta_{\rm LO} + \omega) + S_{P_{\rm out}P_{\rm out}}(\Delta_{\rm LO} + \omega) \\ &+ S_{X_{\rm out}X_{\rm out}}(\Delta_{\rm LO} - \omega) + S_{P_{\rm out}P_{\rm out}}(\Delta_{\rm LO} - \omega) \Big], \end{aligned} \tag{4}$$

which illustrates that the detection is not sensitive to a specific light quadrature, but the measurement effectuates a time-averaging over both quadratures. The detected power spectral density is given in terms of the the mechanical position as

$$\begin{aligned} S_{DD}(\omega) = &\frac{1}{2} + \Big[\Gamma_{\rm eff}(\Delta_{\rm het} + \omega) S_{X_{\rm m}X_{\rm m}}(\Delta_{\rm het} + \omega) \\ &+ \Gamma_{\rm eff}(\Delta_{\rm het} - \omega) S_{X_{\rm m}X_{\rm m}}(\Delta_{\rm het} - \omega) \Big], \end{aligned} \tag{5}$$

where the first term can be attributed to the shot noise contributions, and $\Gamma_{\rm eff}$ the effective measurement rate. Considering each sideband individually, in the limit where $\gamma_{\rm m} \ll \Delta_{\rm het}$, we obtain

$$\begin{aligned} S_{DD}(\Delta_{\rm het} + \omega) &= \frac{1}{2} + 2\gamma_{\rm m}\Gamma_{\rm eff}|\chi_{\rm m}(\omega)|^2 \bar{n}_{\rm th}, \\ S_{DD}(\Delta_{\rm het} - \omega) &= \frac{1}{2} + 2\gamma_{\rm m}\Gamma_{\rm eff}|\chi_{\rm m}(\omega)|^2 (\bar{n}_{\rm th} + 1). \end{aligned} \tag{6}$$

As such a heterodyne measurement provides the possibility for independent and simultaneous detection of the positive and negative mechanical sidebands, offering a direct access to the sideband asymmetry which can be used for temperature estimation and is described in Sec. 1.5.

Furthermore, self-heterodyne measurements are also frequently used for estimating the laser linewidth, by introducing a delay in one of the interferometer arms that is longer than the coherence time of laser or for measuring the phase noise of optical fibres [cf. Sec. 5.5.2].

B Double Pass Optical Output Quadratures

We recall that the outgoing light quadratures after a single optomechanical interaction, written in terms of the ingoing light quadratures are given by

$$\hat{X}_1^{\rm out}(\omega) = \Big[1 - \eta_1 \kappa C_+(\omega) \Big] \hat{X}_{\rm in}(\omega) + \eta_1 \kappa C_-(\omega) \hat{P}_{\rm in}(\omega) + 2\sqrt{\eta_1 \kappa} C_-(\omega) \hat{X}_{\rm m}(\omega), \tag{7}$$

$$\hat{P}_1^{\rm out}(\omega) = -\eta_1 \kappa C_-(\omega) \hat{X}_{\rm in}(\omega) + \Big[1 - \eta_1 \kappa C_+(\omega) \Big] \hat{P}_{\rm in}(\omega) - 2\sqrt{\eta_1 \kappa} C_+(\omega) \hat{X}_{\rm m}(\omega). \tag{8}$$

In the case of the coherent feedback scheme, these expression remain the same, except for the mechanical displacement that now contains the contributions from both the first and the second interactions, as stated in Eq. (2.25). After the double pass interaction, the resulting outgoing light quadratures are obtained from the expression of the outgoing

light mode as stated in Eq. (2.78), which in the frequency domain is given by

$$\hat{a}_2^{\mathrm{out}}(\omega) = \sqrt{\eta}\mathrm{e}^{\mathrm{i}\varphi}\mathrm{e}^{\mathrm{i}\omega\tau}\Big(1-\kappa\chi_{\mathrm{c}}(\omega)\Big)^2\hat{a}_1^{\mathrm{in}}(\omega) + [1-\kappa\chi_{\mathrm{c}}(\omega)]\sqrt{1-\eta}\hat{a}_{\mathrm{aux}}(\omega) - \mathrm{i}\sqrt{2\kappa}\chi_{\mathrm{c}}\Big(g_2 + \sqrt{\eta}g_1\mathrm{e}^{\mathrm{i}\varphi}\mathrm{e}^{\mathrm{i}\omega\tau}\Big[1-\kappa\chi_{\mathrm{c}}(\omega)\Big]\Big)\hat{X}_{\mathrm{m}}(\omega). \tag{9}$$

The complete expressions for the resulting outgoing light quadratures in terms of the mechanical displacement turn into

$$\begin{aligned}
\hat{X}_2^{\mathrm{out}}(\omega) = {}& \sqrt{\eta}\mathrm{e}^{\mathrm{i}\omega\tau}\hat{X}_{\mathrm{in}}(\omega)\Big\{\cos(\varphi)\Big(1-\kappa C_+ + \kappa^2(C_+^2-C_-^2)\Big) + 2\sin(\varphi)\kappa\Big(C_- - \kappa C_+C_-\Big)\Big\} \\
&+ \sqrt{\eta}\mathrm{e}^{\mathrm{i}\omega\tau}\hat{P}_{\mathrm{in}}(\omega)\Big\{2\cos(\varphi)\kappa\Big(C_- - \kappa C_+C_-\Big) - \sin(\varphi)\Big(1-\kappa C_+ + \kappa^2(C_+^2-C_-^2)\Big)\Big\} \\
&+ 2\sqrt{\kappa}\hat{X}_{\mathrm{m}}(\omega)\Big\{C_-g_2 + \sqrt{\eta}g_1\mathrm{e}^{\mathrm{i}\omega\tau}\Big[\cos(\varphi)\Big(-C_- + 2\kappa C_+C_-\Big) - \sin(\varphi)\Big(C_+ - \kappa(C_+^2-C_-^2)\Big)\Big]\Big\} \\
&+ \sqrt{1-\eta}\Big((1-\kappa C_+)\hat{X}_{\mathrm{aux}} + C_-\hat{P}_{\mathrm{aux}}\Big),
\end{aligned} \tag{10}$$

$$\begin{aligned}
\hat{P}_2^{\mathrm{out}}(\omega) = {}& \sqrt{\eta}\mathrm{e}^{\mathrm{i}\omega\tau}\hat{X}_{\mathrm{in}}(\omega)\Big\{2\kappa\cos(\varphi)\Big(-C_- + \kappa C_+C_-\Big) + \sin(\varphi)\Big(1-\kappa C_+ + \kappa^2(C_+^2-C_-^2)\Big)\Big\} \\
&+ \sqrt{\eta}\mathrm{e}^{\mathrm{i}\omega\tau}\hat{P}_{\mathrm{in}}(\omega)\Big\{\cos(\varphi)\Big(1-\kappa C_+ + \kappa^2(C_+^2-C_-^2)\Big) - \sin(\varphi)\Big(-C_- + \kappa C_+C_-\Big)\Big\} \\
&- 2\sqrt{\kappa}\hat{X}_{\mathrm{m}}(\omega)\Big\{C_+g_2 + \sqrt{\eta}g_1\mathrm{e}^{\mathrm{i}\omega\tau}\Big[\cos(\varphi)\Big(C_+ - \kappa(C_+^2-C_-^2)\Big) + \sin(\varphi)\Big(-C_- + 2\kappa C_+C_-\Big)\Big]\Big\} \\
&+ \sqrt{1-\eta}\Big(\kappa C_-\hat{X}_{\mathrm{aux}} + (1-\kappa C_+)\hat{P}_{\mathrm{aux}}\Big)
\end{aligned} \tag{11}$$

For the resonant cavity drive ($C_- = 0$), the expressions for the mechanical displacement simplifies to

$$\begin{aligned}
\hat{X}_{\mathrm{m}}(\omega) = \sqrt{2}\chi_{\mathrm{m}}(\omega)\Big\{{}& \hat{\xi}_{\mathrm{th}} + \hat{X}_{\mathrm{in}}(\omega)\sqrt{2\kappa}\Big[g_1C_+(\omega) + \sqrt{\eta}g_2\mathrm{e}^{\mathrm{i}\omega\tau}\cos(\varphi)\Big(C_+(\omega) - \kappa C_+(\omega)^2\Big)\Big] \\
&- \hat{P}_{\mathrm{in}}(\omega)\sqrt{2\eta\kappa}g_2\mathrm{e}^{\mathrm{i}\omega\tau}\sin(\varphi)\Big(C_+(\omega) - \kappa C_+(\omega)^2\Big) \\
&+ \sqrt{1-\eta}\sqrt{2\kappa}g_2C_+(\omega)\hat{X}_{\mathrm{aux}}(\omega)\Big\}
\end{aligned} \tag{12}$$

and thus the outgoing quadratures become

$$\begin{aligned}\hat{X}_2^{\mathrm{out}}(\omega) &= \sqrt{\eta}\mathrm{e}^{\mathrm{i}\omega\tau}\Big(1-\kappa C_+ + \kappa^2 C_+^2\Big)\Big(\cos(\varphi)\hat{X}_{\mathrm{in}}(\omega) - \sin(\varphi)\hat{P}_{\mathrm{in}}(\omega)\Big)\\ &\quad - 2\sqrt{\eta\kappa}g_1\mathrm{e}^{\mathrm{i}\omega\tau}\hat{X}_{\mathrm{m}}(\omega)\sin(\varphi)\Big(C_+ - \kappa C_+^2\Big)\\ &\quad + \sqrt{1-\eta}(1-\kappa C_+)\hat{X}_{\mathrm{aux}}, \qquad (13)\\ \hat{P}_2^{\mathrm{out}}(\omega) &= \sqrt{\eta}\mathrm{e}^{\mathrm{i}\omega\tau}\Big(1-\kappa C_+ + \kappa^2 C_+^2\Big)\Big(\sin(\varphi)\hat{X}_{\mathrm{in}}(\omega) + \cos(\varphi)\hat{P}_{\mathrm{in}}(\omega)\Big)\\ &\quad - 2\sqrt{\eta\kappa}g_1\mathrm{e}^{\mathrm{i}\omega\tau}\hat{X}_{\mathrm{m}}(\omega)\cos(\varphi)\Big(C_+ - \kappa C_+^2\Big)\\ &\quad + \sqrt{1-\eta}(1-\kappa C_+)\hat{P}_{\mathrm{aux}}. \qquad (14)\end{aligned}$$

C Complete Phonon Occupation Number

In Sec. 1.5 we have derived the direct relation between the integration of the mechanical spectral density and the average phonon occupation number. For the coherent feedback loop, the integration of the complete mechanical displacement power spectral density as stated in Eq. (2.46), leads to the explicit expression for the phonon occupation number

$$\begin{aligned}\bar{n}_{\mathrm{m}} = \frac{\gamma_{\mathrm{m}}}{\gamma_{\mathrm{m}}+\Gamma_{\mathrm{m}}}\Big(\bar{n}_{\mathrm{th}}+\frac{1}{2}\Big) - \frac{1}{2} + \frac{\kappa}{8(\gamma_{\mathrm{m}}+\Gamma_{\mathrm{m}})}\Bigg[\frac{g_1^2+g_2^2}{(\kappa/2)^2+(\Delta+\Omega_{\mathrm{m}})^2} + \frac{g_1^2+g_2^2}{(\kappa/2)^2+(\Delta-\Omega_{\mathrm{m}})^2}\\ + 2g_1g_2\sqrt{\eta}\frac{[(\Delta+\Omega_{\mathrm{m}})^2-(\kappa/2)^2]\cos(\varphi+\Omega_{\mathrm{m}}\tau)+\kappa(\Delta+\Omega_{\mathrm{m}}\sin(\varphi+\Omega_{\mathrm{m}}\tau)}{[(\kappa/2)^2+(\Delta+\Omega_{\mathrm{m}})^2]^2}\\ + 2g_1g_2\sqrt{\eta}\frac{[(\Delta-\Omega_{\mathrm{m}})^2-(\kappa/2)^2]\cos(\varphi-\Omega_{\mathrm{m}}\tau)+\kappa(\Delta-\Omega_{\mathrm{m}}\sin(\varphi-\Omega_{\mathrm{m}}\tau)}{[(\kappa/2)^2+(\Delta-\Omega_{\mathrm{m}})^2]^2}\Bigg], \qquad (15)\end{aligned}$$

where the different terms correspond in sequential order to the contribution from the thermal bath, the zero-point fluctuations, the dynamical backaction, and the coherent feedback loop.

D More on the Loop Phase

Driving the optical cavity with a detuned light beam adds a phase shift on the outgoing light beam with respect to the ingoing beam, which is contributing to the total loop phase. Therefore the values of φ that maximize the light-induced damping term Γ_m as stated in Eq. (2.29) are plotted in Fig. 2 (a), and differ from $\varphi = \pi/2$ if $\Delta \neq 0$. Furthermore, in Fig. 2 (b) we plot the loop phase φ that minimizes the force power spectral density generated by the light S_{fb} as stated in Eq. (2.41), assuming $\Omega_m \tau = \varphi$. In case of finite detuning the ideal phase for backaction cancellation differs from $\varphi = 0$. It is worth noting that the values required for the loop phase to minimize the average occupation number and the optical backaction and do not necessarily coincide.

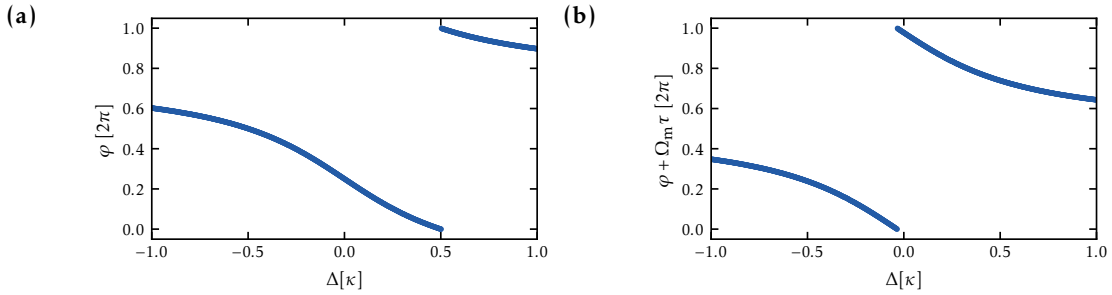

FIGURE 2: **(a)**: The loop phase φ that maximizes the damping rate Γ_m as stated in Eq. (2.29) . **(b)**: The argument $\varphi + \Omega_m \tau$ that maximizes the feedback noise PSD S_{fb} (right)

Acknowledgements

I am happy to express my gratitude to all the people who have supported and contributed to this work, without them, this project would not have been possible.

First and foremost, I am immensely grateful to Philipp Treutlein for providing me with the opportunity and trust to build the optomechanical setup. I would like to thank him for all the insightful discussions, the effort he put into explaining complex concepts in an intuitive and understandable manner, and his relentless enthusiasm and fascination for our experiment.

I would like to express my gratitude to Albert Schliesser for dedicating his time to review my thesis.

I extend my thanks to Patrick Maletinsky for serving as a second supervisor to my thesis.

A very big thank you to the members of the membrane team, namely Manel Bosch Aguilera, Gian-Luca Schmid, Chun Tat Ngai, and Thomas Karg, for their invaluable contributions and tireless dedication in the lab. Thomas, thank you for introducing me to the art of cavity assembly and membrane handling. James and Gian-Luca, I appreciate all the hard work you put into making things work in the lab, working together to troubleshoot, and patience with my music choices. It was really fun! Most importantly, I want to thank Manel for bearing with me through all the steps and iterations to make the membrane setup work, and for helping me to transform it from "my" setup to "our" setup, which I consider an uttermost very fortunate turning point. Everything is awesome if you are part of a team!

I would like to thank the coffee office members, and the whole group for countless insightful discussions.

I would also like to give a special thanks to our theory collaborators, Patrick Potts, Matteo Brunelli and Christoph Bruder, for their invaluable insights and contributions to the development and our understanding of the coherent feedback loop. It was always a pleasure to discuss!

A big thank you also to our fabrication collaborators, Simon Gröblacher and especially Claus Gärtner and Jin Chang for all the effort they put in the clean room fabrication and supply us with membranes.

Furthermore, I want to acknowledge the technical workshop staff, including Sascha Martin, Dominik Sifrig, and Patrick Stöcklin, for their exceptional work in handling our fabrication and Helium requirements. I am also thankful to Gabriel Gisin for his work on the membrane raster scan setup.

Shout out to Manel for proof-reading the entire whole complete full thesis!

Finally, I express my heartfelt gratitude to my family, flatmates and friends and in particular André Weis, for their unwavering support and encouragement throughout this journey. Thank you all once again for your immense contributions, without which this work would not have been possible.

Bibliography

[1] K. J. Åström and R. M. Murray. *Feedback systems: an introduction for scientists and engineers*. en. OCLC: ocn183179623. Princeton: Princeton University Press, 2008 (cit. on p. 1).

[2] W. S. Warren, H. Rabitz, and M. Dahleh. "Coherent Control of Quantum Dynamics: The Dream Is Alive". In: *Science* 259.5101 (Mar. 1993). Publisher: American Association for the Advancement of Science, pp. 1581–1589. DOI: 10.1126/science.259.5101.1581 (cit. on p. 1).

[3] A. C. Doherty et al. "Quantum feedback control and classical control theory". In: *Phys. Rev. A* 62.1 (June 2000). Publisher: American Physical Society, p. 012105. DOI: 10.1103/PhysRevA.62.012105 (cit. on p. 1).

[4] J. Bechhoefer. "Feedback for physicists: A tutorial essay on control". en. In: *Rev. Mod. Phys.* 77.3 (Aug. 2005), pp. 783–836. DOI: 10.1103/RevModPhys.77.783 (cit. on p. 1).

[5] A. A. Clerk et al. "Introduction to quantum noise, measurement, and amplification". In: *Rev. Mod. Phys.* 82 (2 2010), pp. 1155–1208. DOI: 10.1103/RevModPhys.82.1155 (cit. on pp. 1, 7, 13, 14, 17, 18, 31, 45, 51, 52, 61, 103).

[6] J. Zhang et al. "Quantum feedback: Theory, experiments, and applications". In: *Phys. Rep.* 679 (2017), pp. 1–60. DOI: https://doi.org/10.1016/j.physrep.2017.02.003 (cit. on pp. 1–3, 115).

[7] Y. Yamamoto, N. Imoto, and S. Machida. "Amplitude squeezing in a semiconductor laser using quantum nondemolition measurement and negative feedback". en. In: *Phys. Rev. A* 33.5 (May 1986), pp. 3243–3261. DOI: 10.1103/PhysRevA.33.3243 (cit. on p. 1).

[8] R. Inoue et al. "Unconditional Quantum-Noise Suppression via Measurement-Based Quantum Feedback". In: *Phys. Rev. Lett.* 110.16 (Apr. 2013). Publisher: American Physical Society, p. 163602. DOI: 10.1103/PhysRevLett.110.163602 (cit. on p. 1).

[9] M. Rossi et al. "Measurement-based quantum control of mechanical motion". In: *Nature* 563.7729 (Nov. 2018), pp. 53–58. DOI: 10.1038/s41586-018-0643-8 (cit. on pp. 1, 4–6, 54, 116, 118).

[10] C. Monroe et al. "Demonstration of a Fundamental Quantum Logic Gate". en. In: *Phys. Rev. Lett.* 75.25 (Dec. 1995), pp. 4714–4717. DOI: 10.1103/PhysRevLett.75.4714 (cit. on p. 1).

[11] R. Vijay et al. "Stabilizing Rabi oscillations in a superconducting qubit using quantum feedback". In: *Nature* 490.7418 (Oct. 2012). Number: 7418 Publisher: Nature Publishing Group, pp. 77–80. DOI: 10.1038/nature11505 (cit. on p. 1).

[12] G. G. Gillett et al. "Experimental Feedback Control of Quantum Systems Using Weak Measurements". en. In: *Phys. Rev. Lett.* 104.8 (Feb. 2010), p. 080503. DOI: 10.1103/PhysRevLett.104.080503 (cit. on p. 1).

[13] C. Sayrin et al. "Real-time quantum feedback prepares and stabilizes photon number states". In: *Nature* 477.7362 (Sept. 2011). Number: 7362 Publisher: Nature Publishing Group, pp. 73–77. DOI: 10.1038/nature10376 (cit. on p. 1).

[14] G. de Lange et al. "Reversing Quantum Trajectories with Analog Feedback". en. In: *Phys. Rev. Lett.* 112.8 (Feb. 2014), p. 080501. DOI: 10.1103/PhysRevLett.112.080501 (cit. on p. 1).

[15] A. Vepsäläinen et al. "Improving qubit coherence using closed-loop feedback". en. In: *Nat Commun* 13.1 (Apr. 2022). Number: 1 Publisher: Nature Publishing Group, p. 1932. DOI: 10.1038/s41467-022-29287-4 (cit. on p. 1).

[16] D. Ristè et al. "Deterministic entanglement of superconducting qubits by parity measurement and feedback". en. In: *Nature* 502.7471 (Oct. 2013). Number: 7471 Publisher: Nature Publishing Group, pp. 350–354. DOI: 10.1038/nature12513 (cit. on p. 1).

[17] N. Roch et al. "Observation of Measurement-Induced Entanglement and Quantum Trajectories of Remote Superconducting Qubits". en. In: *Phys. Rev. Lett.* 112.17 (Apr. 2014), p. 170501. DOI: 10.1103/PhysRevLett.112.170501 (cit. on p. 1).

[18] J. Cramer et al. "Repeated quantum error correction on a continuously encoded qubit by real-time feedback". en. In: *Nat Commun* 7.1 (May 2016). Number: 1 Publisher: Nature Publishing Group, p. 11526. DOI: 10.1038/ncomms11526 (cit. on p. 1).

[19] W. P. Livingston et al. "Experimental demonstration of continuous quantum error correction". en. In: *Nat Commun* 13.1 (Apr. 2022). Number: 1 Publisher: Nature Publishing Group, p. 2307. DOI: 10.1038/s41467-022-29906-0 (cit. on p. 1).

[20] S. Lloyd. "Coherent quantum feedback". In: *Phys. Rev. A* 62 (2 2000), p. 022108. DOI: 10.1103/PhysRevA.62.022108 (cit. on pp. 1, 2, 115).

[21] N. Yamamoto. "Coherent versus Measurement Feedback: Linear Systems Theory for Quantum Information". In: *Phys. Rev. X* 4.4 (Nov. 2014), p. 041029. DOI: 10.1103/PhysRevX.4.041029 (cit. on pp. 1, 2, 31, 115, 128, 130).

[22] H. M. Wiseman and G. J. Milburn. "All-optical versus electro-optical quantum-limited feedback". In: *Phys. Rev. A* 49.5 (May 1994), pp. 4110–4125. DOI: 10.1103/PhysRevA.49.4110 (cit. on pp. 1–3, 115, 126, 130).

[23] H. M. Wiseman and G. J. Milburn. *Quantum Measurement and Control*. Cambridge University Press, 2009. DOI: 10.1017/CBO9780511813948 (cit. on pp. 1, 2, 115).

[24] R. Hamerly and H. Mabuchi. "Advantages of Coherent Feedback for Cooling Quantum Oscillators". In: *Phys. Rev. Lett.* 109 (17 2012), p. 173602. DOI: 10.1103/PhysRevLett.109.173602 (cit. on pp. 1–3, 5, 32, 116, 126, 130).

[25] K. Jacobs, X. Wang, and H. M. Wiseman. "Coherent feedback that beats all measurement-based feedback protocols". In: *New J. Phys.* 16.7 (July 2014), p. 073036. DOI: 10.1088/1367-2630/16/7/073036 (cit. on pp. 1, 2, 115).

[26] M. Tsang and C. M. Caves. "Coherent Quantum-Noise Cancellation for Optomechanical Sensors". In: *Phys. Rev. Lett.* 105.12 (Sept. 2010), p. 123601. DOI: 10.1103/PhysRevLett.105.123601 (cit. on pp. 1, 2, 28, 58, 115, 126, 128).

[27] T. M. Karg et al. "Remote Hamiltonian interactions mediated by light". In: *Phys. Rev. A* 99.6 (June 2019), p. 063829. DOI: 10.1103/PhysRevA.99.063829 (cit. on pp. 2, 3, 32, 43, 56–58, 60, 62, 116, 126, 128, 129).

[28] R. Hamerly and H. Mabuchi. "Coherent controllers for optical-feedback cooling of quantum oscillators". In: *Phys. Rev. A* 87.1 (Jan. 2013). Publisher: American Physical Society, p. 013815. DOI: 10.1103/PhysRevA.87.013815 (cit. on pp. 2, 3, 5).

[29] K. Jacobs et al. "Comparing resolved-sideband cooling and measurement-based feedback cooling on an equal footing: Analytical results in the regime of ground-state cooling". In: *Physical Review A* 91.4 (Apr. 2015), p. 043812. DOI: 10.1103/PhysRevA.91.043812 (cit. on p. 2).

[30] S. Iida et al. "Experimental Demonstration of Coherent Feedback Control on Optical Field Squeezing". In: *IEEE Trans. Autom. Control* 57.8 (Aug. 2012). Conference Name: IEEE Transactions on Automatic Control, pp. 2045–2050. DOI: 10.1109/TAC.2012.2195831 (cit. on pp. 2, 115).

[31] Y. Zhou et al. "Quantum Coherent Feedback Control for Generation System of Optical Entangled State". In: *Sci. Rep.* 5.1 (June 2015), p. 11132. DOI: 10.1038/srep11132 (cit. on pp. 2, 115).

[32] H. Rohde et al. "Sympathetic ground-state cooling and coherent manipulation with two-ion crystals". In: *J. Opt. B: Quantum Semiclass. Opt.* 3.1 (Jan. 2001), S34–S41. DOI: 10.1088/1464-4266/3/1/357 (cit. on pp. 2, 5, 115, 118).

[33] M. Frimmer, J. Gieseler, and L. Novotny. "Cooling Mechanical Oscillators by Coherent Control". In: *Phys. Rev. Lett.* 117.16 (Oct. 2016), p. 163601. DOI: 10.1103/PhysRevLett.117.163601 (cit. on pp. 2, 3, 115).

[34] G.-L. Schmid et al. "Coherent feedback cooling of a nanomechanical membrane with atomic spins". In: *Phys. Rev. X* 12.1 (Jan. 2022), p. 011020. DOI: 10.1103/PhysRevX.12.011020 (cit. on pp. 2, 5, 6, 31, 59–61, 115, 116, 118).

[35] S. Shankar et al. "Autonomously stabilized entanglement between two superconducting quantum bits". In: *Nature* 504.7480 (Dec. 2013), pp. 419–422. DOI: 10.1038/nature12802 (cit. on pp. 2, 115).

[36] M. Hirose and P. Cappellaro. "Coherent feedback control of a single qubit in diamond". In: *Nature* 532.7597 (Apr. 2016), pp. 77–80. DOI: 10.1038/nature17404 (cit. on pp. 2, 115).

[37] R. Blatt and D. Wineland. "Entangled states of trapped atomic ions". en. In: *Nature* 453.7198 (June 2008), pp. 1008–1015. DOI: 10.1038/nature07125 (cit. on p. 3).

[38] J. Zhang et al. "Quantum Coherent Nonlinear Feedback With Applications to Quantum Optics on Chip". In: *IEEE Trans. Autom. Control* 57.8 (2012), pp. 1997–2008. DOI: 10.1109/TAC.2012.2195871 (cit. on pp. 3, 115).

[39] M. Hirose and P. Cappellaro. "Coherent feedback control of a single qubit in diamond". In: *Nature* 532.7597 (Apr. 2016), pp. 77–80. DOI: 10.1038/nature17404 (cit. on p. 3).

[40] H. J. Kimble. "The quantum internet". In: *Nature* 453.7198 (June 2008), pp. 1023–1030. DOI: 10.1038/nature07127 (cit. on p. 3).

[41] D. Lee et al. "Topical review: spins and mechanics in diamond". In: *J. Opt.* 19.3 (Mar. 2017), p. 033001. DOI: 10.1088/2040-8986/aa52cd (cit. on p. 3).

[42] J. Guo and S. Gröblacher. "Coherent feedback in optomechanical systems in the sideband-unresolved regime". In: *Quantum* 6 (2022), p. 848. DOI: 10.22331/q-2022-11-03-848 (cit. on pp. 3, 5, 6, 32, 34, 62, 116, 118, 126, 129).

[43] D. Mansouri et al. "Cavity-assisted coherent feedback cooling of a mechanical resonator to the ground-state in the unresolved sideband regime". In: *J. Phys. B: At. Mol. Opt.* 55.16 (Aug. 2022), p. 165501. DOI: 10.1088/1361-6455/ac7d27 (cit. on pp. 3, 5, 116, 118).

[44] M. Aspelmeyer, T. J. Kippenberg, and F. Marquardt. "Cavity optomechanics". In: *Rev. Mod. Phys.* 86.4 (Dec. 2014), pp. 1391–1452. DOI: 10.1103/RevModPhys.86.1391 (cit. on pp. 3–5, 7, 10, 12, 16, 18, 28, 46, 50–54, 58, 68, 69, 76, 116, 119, 121, 123).

[45] A. Bachtold, J. Moser, and M. Dykman. "Mesoscopic physics of nanomechanical systems". en. In: *Rev. Mod. Phys.* 94.4 (Dec. 2022), p. 045005. DOI: 10.1103/RevModPhys.94.045005 (cit. on pp. 3, 4, 7, 31, 68, 69).

[46] V. B. Braginskii and A. B. Manukin. "Ponderomotive effects of electromagnetic radiation". en. In: (1967) (cit. on p. 4).

[47] C. M. Caves. "Quantum-Mechanical Radiation-Pressure Fluctuations in an Interferometer". In: *Phys. Rev. Lett.* 45.2 (July 1980). Publisher: American Physical Society, pp. 75–79. DOI: 10.1103/PhysRevLett.45.75 (cit. on pp. 4, 28).

[48] A. Gillespie and F. Raab. "Thermally excited vibrations of the mirrors of laser interferometer gravitational-wave detectors". en. In: *Phys. Rev. D* 52.2 (July 1995), pp. 577–585. DOI: 10.1103/PhysRevD.52.577 (cit. on pp. 4, 95).

[49] P. F. Cohadon, A. Heidmann, and M. Pinard. "Cooling of a Mirror by Radiation Pressure". en. In: *Phys. Rev. Lett.* 83.16 (Oct. 1999), pp. 3174–3177. DOI: 10.1103/PhysRevLett.83.3174 (cit. on p. 4).

[50] A. Dorsel et al. "Optical Bistability and Mirror Confinement Induced by Radiation Pressure". en. In: *Phys. Rev. Lett.* 51.17 (Oct. 1983), pp. 1550–1553. DOI: 10.1103/PhysRevLett.51.1550 (cit. on p. 4).

[51] A. Abramovici et al. "LIGO: The Laser Interferometer Gravitational-Wave Observatory". In: *Science* 256.5055 (Apr. 1992). Publisher: American Association for the Advancement of Science, pp. 325–333. DOI: 10.1126/science.256.5055.325 (cit. on p. 4).

[52] T. Corbitt et al. "An All-Optical Trap for a Gram-Scale Mirror". en. In: *Phys. Rev. Lett.* 98.15 (Apr. 2007), p. 150802. DOI: 10.1103/PhysRevLett.98.150802 (cit. on p. 4).

[53] T. Corbitt et al. "Optical Dilution and Feedback Cooling of a Gram-Scale Oscillator to 6.9 mK". en. In: *Phys. Rev. Lett.* 99.16 (Oct. 2007), p. 160801. DOI: 10.1103/PhysRevLett.99.160801 (cit. on p. 4).

[54] J. D. Thompson et al. "Strong dispersive coupling of a high-finesse cavity to a micromechanical membrane". In: *Nature* 452.7183 (Mar. 2008), pp. 72–75. DOI: 10.1038/nature06715 (cit. on pp. 4, 118).

[55] D. J. Wilson et al. "Cavity Optomechanics with Stoichiometric SiN Films". In: *Phys. Rev. Lett.* 103.20 (Nov. 2009). Publisher: American Physical Society, p. 207204. DOI: 10.1103/PhysRevLett.103.207204 (cit. on pp. 4, 66, 78, 87, 88).

[56] H. Zeng and F. Lin. "Quantum conversion between the cavity fields and the center-of-mass motion of ions in a quantized trap". In: *Phys. Rev. A* 50.5 (Nov. 1994). Publisher: American Physical Society, R3589–R3592. DOI: 10.1103/PhysRevA.50.R3589 (cit. on p. 4).

[57] K. W. Murch et al. "Observation of quantum-measurement backaction with an ultracold atomic gas". In: *Nature Phys* 4.7 (July 2008). Number: 7 Publisher: Nature Publishing Group, pp. 561–564. DOI: 10.1038/nphys965 (cit. on pp. 4, 10).

[58] F. Brennecke et al. "Cavity Optomechanics with a Bose-Einstein Condensate". In: *Science* 322.5899 (Oct. 2008). Publisher: American Association for the Advancement of Science, pp. 235–238. DOI: 10.1126/science.1163218 (cit. on pp. 4, 10).

[59] D. E. Chang et al. "Cavity opto-mechanics using an optically levitated nanosphere". In: *Proceedings of the National Academy of Sciences* 107.3 (Jan. 2010). Publisher: Proceedings of the National Academy of Sciences, pp. 1005–1010. DOI: 10.1073/pnas.0912969107 (cit. on p. 4).

[60] P. F. Barker and M. N. Shneider. "Cavity cooling of an optically trapped nanoparticle". In: *Phys. Rev. A* 81.2 (Feb. 2010). Publisher: American Physical Society, p. 023826. DOI: 10.1103/PhysRevA.81.023826 (cit. on p. 4).

[61] I. Wilson-Rae et al. "High- Q Nanomechanics via Destructive Interference of Elastic Waves". en. In: *Phys. Rev. Lett.* 106.4 (Jan. 2011), p. 047205. DOI: 10.1103/PhysRevLett.106.047205 (cit. on pp. 4, 69, 71, 72).

[62] C. Reinhardt et al. "Ultralow-Noise SiN Trampoline Resonators for Sensing and Optomechanics". en. In: *Phys. Rev. X* 6.2 (Apr. 2016), p. 021001. DOI: 10.1103/PhysRevX.6.021001 (cit. on p. 4).

[63] Y. Tsaturyan et al. "Ultracoherent nanomechanical resonators via soft clamping and dissipation dilution". In: *Nat. Nanotechnol.* 12.8 (Aug. 2017), pp. 776–783. DOI: 10.1038/nnano.2017.101 (cit. on pp. 4, 65, 66, 73, 74, 81, 98, 126).

[64] C. Reetz et al. "Analysis of Membrane Phononic Crystals with Wide Band Gaps and Low-Mass Defects". In: *Phys. Rev. Appl.* 12.4 (Oct. 2019), p. 044027. DOI: 10.1103/PhysRevApplied.12.044027 (cit. on pp. 4, 65, 66, 72–75, 81).

[65] A. H. Ghadimi et al. "Elastic strain engineering for ultralow mechanical dissipation". In: *Science* 360.6390 (May 2018). Publisher: American Association for the Advancement of Science Section: Report, pp. 764–768. DOI: 10.1126/science.aar6939 (cit. on pp. 4, 65, 73).

[66] Y. Seis et al. "Ground state cooling of an ultracoherent electromechanical system". In: *Nat Commun* 13.1 (Mar. 2022). Number: 1 Publisher: Nature Publishing Group, p. 1507. DOI: 10.1038/s41467-022-29115-9 (cit. on p. 4).

[67] S. Gigan et al. "Self-cooling of a micromirror by radiation pressure". In: *Nature* 444.7115 (Nov. 2006). Number: 7115 Publisher: Nature Publishing Group, pp. 67–70. DOI: 10.1038/nature05273 (cit. on p. 4).

[68] D. Kleckner et al. "Optomechanical trampoline resonators". eng. In: *Opt Express* 19.20 (Sept. 2011), pp. 19708–19716. DOI: 10.1364/OE.19.019708 (cit. on p. 4).

[69] S. Gröblacher et al. "Observation of strong coupling between a micromechanical resonator and an optical cavity field". In: *Nature* 460.7256 (Aug. 2009). Number: 7256 Publisher: Nature Publishing Group, pp. 724–727. DOI: 10.1038/nature08171 (cit. on pp. 4, 43).

[70] K. J. Vahala. "Optical microcavities". en. In: *Nature* 424.6950 (Aug. 2003). Number: 6950 Publisher: Nature Publishing Group, pp. 839–846. DOI: 10.1038/nature01939 (cit. on p. 4).

[71] G. Anetsberger et al. "Ultralow-dissipation optomechanical resonators on a chip". en. In: *Nature Photon* 2.10 (Oct. 2008), pp. 627–633. DOI: 10.1038/nphoton.2008.199 (cit. on p. 4).

[72] S. G. Hofer et al. "Quantum entanglement and teleportation in pulsed cavity optomechanics". en. In: *Phys. Rev. A* 84.5 (Nov. 2011), p. 052327. DOI: 10.1103/PhysRevA.84.052327 (cit. on pp. 4, 61).

[73] L. Ding et al. "Wavelength-sized GaAs optomechanical resonators with gigahertz frequency". In: *Applied Physics Letters* 98.11 (Mar. 2011), p. 113108. DOI: 10.1063/1.3563711 (cit. on p. 4).

[74] Y. Akahane et al. "Fine-tuned high-Q photonic-crystal nanocavity". EN. In: *Opt. Express, OE* 13.4 (Feb. 2005). Publisher: Optica Publishing Group, pp. 1202–1214. DOI: 10.1364/OPEX.13.001202 (cit. on p. 4).

[75] R. H. Olsson and I. El-Kady. "Microfabricated phononic crystal devices and applications". en. In: *Meas. Sci. Technol.* 20.1 (Nov. 2008), p. 012002. DOI: 10.1088/0957-0233/20/1/012002 (cit. on p. 4).

[76] M. Eichenfield et al. "Optomechanical crystals". en. In: *Nature* 462.7269 (Nov. 2009). Number: 7269 Publisher: Nature Publishing Group, pp. 78–82. DOI: 10.1038/nature08524 (cit. on p. 4).

[77] A. H. Safavi-Naeini et al. "Optomechanics in an ultrahigh-Q two-dimensional photonic crystal cavity". In: *Applied Physics Letters* 97.18 (Nov. 2010), p. 181106. DOI: 10.1063/1.3507288 (cit. on p. 4).

[78] J. Chan et al. "Laser cooling of a nanomechanical oscillator into its quantum ground state". In: *Nature* 478.7367 (Oct. 2011), pp. 89–92. DOI: 10.1038/nature10461 (cit. on pp. 4, 5).

[79] S. Barzanjeh et al. "Optomechanics for quantum technologies". In: *Nat. Phys.* 18.1 (Jan. 2022), pp. 15–24. DOI: 10.1038/s41567-021-01402-0 (cit. on pp. 4, 5, 7, 31, 65, 69, 116).

[80] A. D. O'Connell et al. "Quantum ground state and single-phonon control of a mechanical resonator". In: *Nature* 464.7289 (Apr. 2010). Number: 7289 Publisher: Nature Publishing Group, pp. 697–703. DOI: 10.1038/nature08967 (cit. on pp. 4, 62).

[81] D. Mason et al. "Continuous force and displacement measurement below the standard quantum limit". In: *Nat. Phys.* 15.8 (Aug. 2019). Number: 8 Publisher: Nature Publishing Group, pp. 745–749. DOI: 10.1038/s41567-019-0533-5 (cit. on p. 4).

[82] E. E. Wollman et al. "Quantum squeezing of motion in a mechanical resonator". In: *Science* 349.6251 (Aug. 2015). Publisher: American Association for the Advancement of Science, pp. 952–955. DOI: 10.1126/science.aac5138 (cit. on p. 4).

[83] F. Lecocq et al. "Quantum nondemolition measurement of a nonclassical state of a massive object". In: *Physical Review X* 5.4 (2015), p. 041037 (cit. on pp. 4, 28).

[84] T. P. Purdy et al. "Strong optomechanical squeezing of light". In: *Physical Review X* 3.3 (2013), p. 031012 (cit. on p. 4).

[85] A. H. Safavi-Naeini et al. "Squeezed light from a silicon micromechanical resonator". en. In: *Nature* 500.7461 (Aug. 2013). Number: 7461 Publisher: Nature Publishing Group, pp. 185–189. DOI: 10.1038/nature12307 (cit. on p. 4).

[86] V. Sudhir et al. "Quantum Correlations of Light from a Room-Temperature Mechanical Oscillator". In: *Phys. Rev. X* 7.3 (Sept. 2017). Publisher: American Physical Society, p. 031055. DOI: 10.1103/PhysRevX.7.031055 (cit. on p. 4).

[87] C. F. Ockeloen-Korppi et al. "Stabilized entanglement of massive mechanical oscillators". In: *Nature* 556.7702 (Apr. 2018), pp. 478–482. DOI: 10.1038/s41586-018-0038-x (cit. on pp. 4, 62, 129).

[88] R. Riedinger et al. "Remote quantum entanglement between two micromechanical oscillators". In: *Nature* 556.7702 (Apr. 2018), pp. 473–477. DOI: 10.1038/s41586-018-0036-z (cit. on pp. 4, 62, 129).

[89] S. Kotler et al. "Direct observation of deterministic macroscopic entanglement". In: *Science* 372.6542 (May 2021). Publisher: American Association for the Advancement of Science, pp. 622–625. DOI: 10.1126/science.abf2998 (cit. on pp. 4, 65, 129).

[90] E. A. Wollack et al. "Quantum state preparation and tomography of entangled mechanical resonators". en. In: *Nature* 604.7906 (Apr. 2022). Number: 7906 Publisher: Nature Publishing Group, pp. 463–467. DOI: 10.1038/s41586-022-04500-y (cit. on pp. 4, 62, 66).

[91] T. A. Palomaki et al. "Entangling Mechanical Motion with Microwave Fields". In: *Science* 342.6159 (Nov. 2013). Publisher: American Association for the Advancement of Science, pp. 710–713. DOI: 10.1126/science.1244563 (cit. on pp. 4, 61).

[92] R. Riedinger et al. "Non-classical correlations between single photons and phonons from a mechanical oscillator". In: *Nature* 530.7590 (Feb. 2016), pp. 313–316. DOI: 10.1038/nature16536 (cit. on p. 4).

[93] I. Marinković et al. "Optomechanical Bell Test". en. In: *Phys. Rev. Lett.* 121.22 (Nov. 2018), p. 220404. DOI: 10.1103/PhysRevLett.121.220404 (cit. on pp. 4, 10, 61).

[94] S. Barzanjeh et al. "Stationary entangled radiation from micromechanical motion". In: *Nature* 570.7762 (June 2019). Number: 7762 Publisher: Nature Publishing Group, pp. 480–483. DOI: 10.1038/s41586-019-1320-2 (cit. on p. 4).

[95] K. Stannigel et al. "Optomechanical Transducers for Long-Distance Quantum Communication". en. In: *Phys. Rev. Lett.* 105.22 (Nov. 2010), p. 220501. DOI: 10.1103/PhysRevLett.105.220501 (cit. on p. 4).

[96] M. Forsch et al. "Microwave-to-optics conversion using a mechanical oscillator in its quantum ground state". en. In: *Nat. Phys.* 16.1 (Jan. 2020). Number: 1 Publisher: Nature Publishing Group, pp. 69–74. DOI: 10.1038/s41567-019-0673-7 (cit. on p. 4).

[97] M. Mirhosseini et al. "Superconducting qubit to optical photon transduction". en. In: *Nature* 588.7839 (Dec. 2020). Number: 7839 Publisher: Nature Publishing Group, pp. 599–603. DOI: 10.1038/s41586-020-3038-6 (cit. on p. 4).

[98] C. Genes et al. "Ground-state cooling of a micromechanical oscillator: Comparing cold damping and cavity-assisted cooling schemes". In: *Phys. Rev. A* 77.3 (Mar. 2008), p. 033804. DOI: 10.1103/PhysRevA.77.033804 (cit. on p. 5).

[99] J. D. Teufel et al. "Sideband cooling of micromechanical motion to the quantum ground state". In: *Nature* 475.7356 (July 2011), pp. 359–363. DOI: 10.1038/nature10261 (cit. on p. 5).

[100] R. Peterson et al. "Laser Cooling of a Micromechanical Membrane to the Quantum Backaction Limit". In: *Phys. Rev. Lett.* 116.6 (Feb. 2016), p. 063601. DOI: 10.1103/PhysRevLett.116.063601 (cit. on p. 5).

[101] B. Brubaker et al. "Optomechanical Ground-State Cooling in a Continuous and Efficient Electro-Optic Transducer". In: *Phys. Rev. X* 12.2 (June 2022), p. 021062. DOI: 10.1103/PhysRevX.12.021062 (cit. on p. 5).

[102] P. Treutlein et al. "Hybrid Mechanical Systems". In: *Cavity Optomechanics: Nano- and Micromechanical Resonators Interacting with Light*. Ed. by M. Aspelmeyer, T. J. Kippenberg, and F. Marquardt. Berlin: Springer, 2014, pp. 327–351 (cit. on pp. 5, 31, 116).

[103] J. B. Clark et al. "Sideband cooling beyond the quantum backaction limit with squeezed light". In: *Nature* 541.7636 (Jan. 2017). DOI: 10.1038/nature20604 (cit. on pp. 5, 6, 28, 118).

[104] C. Schäfermeier et al. "Quantum enhanced feedback cooling of a mechanical oscillator using nonclassical light". In: *Nat. Commun.* 7.1 (Nov. 2016). DOI: 10.1038/ncomms13628 (cit. on pp. 5, 118).

[105] S. Mancini, D. Vitali, and P. Tombesi. "Optomechanical Cooling of a Macroscopic Oscillator by Homodyne Feedback". In: *Phys. Rev. Lett.* 80 (4 1998), pp. 688–691. DOI: 10.1103/PhysRevLett.80.688 (cit. on pp. 5, 54, 116, 118, 121).

[106] U. Delić et al. "Cooling of a levitated nanoparticle to the motional quantum ground state". In: *Science* 367.6480 (Feb. 2020), pp. 892–895. DOI: 10.1126/science.aba3993 (cit. on pp. 5, 116, 118).

[107] F. Tebbenjohanns et al. "Quantum control of a nanoparticle optically levitated in cryogenic free space". In: *Nature* 595.7867 (July 2021), pp. 378–382. DOI: 10.1038/s41586-021-03617-w (cit. on pp. 5, 54, 116, 118).

[108] C. Whittle et al. "Approaching the motional ground state of a 10-kg object". In: *Science* 372.6548 (June 2021), pp. 1333–1336. DOI: 10.1126/science.abh2634 (cit. on pp. 5, 116, 118).

[109] P. Christoph et al. "Combined feedback and sympathetic cooling of a mechanical oscillator coupled to ultracold atoms". In: *New J. Phys.* 20.9 (Sept. 2018), p. 093020. DOI: 10.1088/1367-2630/aadf20 (cit. on pp. 5, 118).

[110] J. Li et al. "Enhanced entanglement of two different mechanical resonators via coherent feedback". In: *Phys. Rev. A* 95.4 (Apr. 2017), p. 043819. DOI: 10.1103/PhysRevA.95.043819 (cit. on pp. 5, 32, 62, 116, 129).

[111] S. Huang and A. Chen. "Cooling of a Mechanical Oscillator and Normal Mode Splitting in Optomechanical Systems with Coherent Feedback". In: *Appl. Sci.* 9.16 (Jan. 2019), p. 3402. DOI: 10.3390/app9163402 (cit. on pp. 5, 116, 118).

[112] A. Harwood, M. Brunelli, and A. Serafini. "Cavity optomechanics assisted by optical coherent feedback". In: *Phys. Rev. A* 103 (2021), p. 023509. DOI: 10.1103/physreva.103.023509 (cit. on pp. 5, 32, 116, 118, 126).

[113] M. Ernzer et al. "Optical Coherent Feedback Control of a Mechanical Oscillator". In: *Phys. Rev. X* 13.2 (May 2023). Publisher: American Physical Society, p. 021023. DOI: 10.1103/PhysRevX.13.021023 (cit. on pp. 6, 31, 115).

[114] W. Bowen and G. Milburn. *Quantum Optomechanics*. CRC Press, Oct. 2015 (cit. on pp. 8, 14, 18, 19, 23, 28, 33, 45, 132).

[115] D. Zoepfl et al. "Single-Photon Cooling in Microwave Magnetomechanics". en. In: *Phys. Rev. Lett.* 125.2 (July 2020), p. 023601. DOI: 10.1103/PhysRevLett.125.023601 (cit. on p. 10).

[116] C. Meng et al. "Measurement-based preparation of multimode mechanical states". In: *Science Advances* 8.21 (May 2022). Publisher: American Association for the Advancement of Science, eabm7585. DOI: 10.1126/sciadv.abm7585 (cit. on p. 10).

[117] C. W. Gardiner and P. Zoller. *Quantum Noise*. Springer, 2000 (cit. on p. 11).

[118] C. W. Gardiner and M. J. Collett. "Input and output in damped quantum systems: Quantum stochastic differential equations and the master equation". en. In: *Phys. Rev. A* 31.6 (June 1985), pp. 3761–3774. DOI: 10.1103/PhysRevA.31.3761 (cit. on p. 11).

[119] V. Giovannetti and D. Vitali. "Phase-noise measurement in a cavity with a movable mirror undergoing quantum Brownian motion". In: *Phys. Rev. A* 63 (2 2001), p. 023812. DOI: 10.1103/PhysRevA.63.023812 (cit. on p. 17).

[120] M. Brunelli et al. "Stroboscopic quantum optomechanics". In: *Phys. Rev. Research* 2.2 (May 2020), p. 023241. DOI: 10.1103/PhysRevResearch.2.023241 (cit. on p. 28).

[121] V. B. Braginsky, Y. I. Vorontsov, and K. S. Thorne. "Quantum Nondemolition Measurements". In: *Science* 209.4456 (Aug. 1980). Publisher: American Association for the Advancement of Science, pp. 547–557. DOI: 10.1126/science.209.4456.547 (cit. on pp. 28, 58).

[122] M. Tsang and C. M. Caves. "Evading Quantum Mechanics: Engineering a Classical Subsystem within a Quantum Environment". en. In: *Phys. Rev. X* 2.3 (Sept. 2012), p. 031016. DOI: 10.1103/PhysRevX.2.031016 (cit. on pp. 28, 130).

[123] M. H. Wimmer et al. "Coherent cancellation of backaction noise in optomechanical force measurements". en. In: *Phys. Rev. A* 89.5 (May 2014), p. 053836. DOI: 10.1103/PhysRevA.89.053836 (cit. on p. 28).

[124] M. Xiao, L.-A. Wu, and H. J. Kimble. "Precision measurement beyond the shot-noise limit". en. In: *Phys. Rev. Lett.* 59.3 (July 1987), pp. 278–281. DOI: 10.1103/PhysRevLett.59.278 (cit. on p. 28).

[125] C.-W. Lee, J. H. Lee, and H. Seok. "Squeezed-light-driven force detection with an optomechanical cavity in a mach–zehnder interferometer". In: *Scientific Reports* 10.1 (2020), p. 17496 (cit. on p. 28).

[126] E. Gavartin, P. Verlot, and T. J. Kippenberg. "A hybrid on-chip optomechanical transducer for ultrasensitive force measurements". In: *Nature Nanotech* 7.8 (Aug. 2012). Number: 8 Publisher: Nature Publishing Group, pp. 509–514. DOI: 10.1038/nnano.2012.97 (cit. on p. 29).

[127] T. M. Karg et al. "Light-mediated strong coupling between a mechanical oscillator and atomic spins 1 meter apart". In: *Science* 369.6500 (July 2020), pp. 174–179. DOI: 10.1126/science.abb0328 (cit. on pp. 31, 59–61, 128).

[128] C. Genes et al. "Ground-state cooling of a micromechanical oscillator: Comparing cold damping and cavity-assisted cooling schemes". In: *Phys. Rev. A* 77 (3 2008), p. 033804. DOI: 10.1103/PhysRevA.77.033804 (cit. on pp. 55, 61, 121).

[129] J. B. Hertzberg et al. "Back-action-evading measurements of nanomechanical motion". In: *Nature Phys* 6.3 (Mar. 2010). Number: 3 Publisher: Nature Publishing Group, pp. 213–217. DOI: 10.1038/nphys1479 (cit. on p. 58).

[130] G. Vasilakis et al. "Generation of a squeezed state of an oscillator by stroboscopic back-action-evading measurement". en. In: *Nature Phys* 11.5 (May 2015). Number: 5 Publisher: Nature Publishing Group, pp. 389–392. DOI: 10.1038/nphys3280 (cit. on p. 58).

[131] C. Ockeloen-Korppi et al. "Quantum Backaction Evading Measurement of Collective Mechanical Modes". en. In: *Phys. Rev. Lett.* 117.14 (Sept. 2016), p. 140401. DOI: 10.1103/PhysRevLett.117.140401 (cit. on pp. 58, 62).

[132] C. B. Møller et al. "Quantum back-action-evading measurement of motion in a negative mass reference frame". In: *Nature* 547.7662 (July 2017), pp. 191–195. DOI: 10.1038/nature22980 (cit. on p. 58).

[133] I. Shomroni et al. "Optical backaction-evading measurement of a mechanical oscillator". en. In: *Nat Commun* 10.1 (May 2019). Number: 1 Publisher: Nature Publishing Group, p. 2086. DOI: 10.1038/s41467-019-10024-3 (cit. on p. 58).

[134] L. Mercier de Lépinay et al. "Quantum mechanics–free subsystem with mechanical oscillators". In: *Science* 372.6542 (May 2021). Publisher: American Association for the Advancement of Science, pp. 625–629. DOI: 10.1126/science.abf5389 (cit. on pp. 58, 130).

[135] C. T. Ngai. "Coherent feedback cooling of a nanomechanical membrane with atomic spins". PhD thesis. Klingelbergstrasse 82 4058 Basel: University of Basel, Department of Physics, 2022 (cit. on p. 59).

[136] K. Hammerer, A. S. Sørensen, and E. S. Polzik. "Quantum interface between light and atomic ensembles". In: *Rev. Mod. Phys.* 82 (2 2010), pp. 1041–1093. DOI: 10.1103/RevModPhys.82.1041 (cit. on p. 59).

[137] W. H. P. Nielsen et al. "Multimode optomechanical system in the quantum regime". In: *Proceedings of the National Academy of Sciences* 114.1 (Jan. 2017). Company: National Academy of Sciences Distributor: National Academy of Sciences Institution: National Academy of Sciences Label: National Academy of Sciences Publisher: Proceedings of the National Academy of Sciences, pp. 62–66. DOI: 10.1073/pnas.1608412114 (cit. on pp. 61, 90).

[138] D. Vitali, S. Mancini, and P. Tombesi. "Stationary entanglement between two movable mirrors in a classically driven Fabry–Perot cavity". en. In: *J. Phys. A: Math. Theor.* 40.28 (July 2007), pp. 8055–8068. DOI: 10.1088/1751-8113/40/28/S14 (cit. on pp. 61, 62).

[139] C. Galland et al. "Heralded Single-Phonon Preparation, Storage, and Readout in Cavity Optomechanics". en. In: *Phys. Rev. Lett.* 112.14 (Apr. 2014), p. 143602. DOI: 10.1103/PhysRevLett.112.143602 (cit. on pp. 61, 62).

[140] C. Gut et al. "Stationary optomechanical entanglement between a mechanical oscillator and its measurement apparatus". en. In: *Phys. Rev. Research* 2.3 (Aug. 2020), p. 033244. DOI: 10.1103/PhysRevResearch.2.033244 (cit. on p. 62).

[141] H. Miao et al. "Probing macroscopic quantum states with a sub-Heisenberg accuracy". In: *Phys. Rev. A* 81.1 (Jan. 2010). Publisher: American Physical Society, p. 012114. DOI: 10.1103/PhysRevA.81.012114 (cit. on p. 62).

[142] J. D. Jost et al. "Entangled mechanical oscillators". In: *Nature* 459.7247 (June 2009). Number: 7247 Publisher: Nature Publishing Group, pp. 683–685. DOI: 10.1038/nature08006 (cit. on p. 62).

[143] R. A. Thomas et al. "Entanglement between distant macroscopic mechanical and spin systems". In: *Nat. Phys.* 17.2 (Feb. 2021), pp. 228–233. DOI: 10.1038/s41567-020-1031-5 (cit. on p. 62).

[144] M. J. Woolley and A. A. Clerk. "Two-mode back-action-evading measurements in cavity optomechanics". en. In: *Phys. Rev. A* 87.6 (June 2013), p. 063846. DOI: 10.1103/PhysRevA.87.063846 (cit. on p. 62).

[145] S. A. Fedorov et al. "Generalized dissipation dilution in strained mechanical resonators". In: *Phys. Rev. B* 99.5 (Feb. 2019). Publisher: American Physical Society, p. 054107. DOI: 10.1103/PhysRevB.99.054107 (cit. on pp. 65, 71, 73, 76).

[146] G. S. MacCabe et al. "Nano-acoustic resonator with ultralong phonon lifetime". In: *Science* 370.6518 (Nov. 2020). Publisher: American Association for the Advancement of Science, pp. 840–843. DOI: 10.1126/science.abc7312 (cit. on p. 65).

[147] J. Güttinger et al. "Energy-dependent path of dissipation in nanomechanical resonators". en. In: *Nature Nanotech* 12.7 (July 2017). Number: 7 Publisher: Nature Publishing Group, pp. 631–636. DOI: 10.1038/nnano.2017.86 (cit. on p. 65).

[148] C. Urgell et al. "Cooling and self-oscillation in a nanotube electromechanical resonator". In: *Nat. Phys.* 16.1 (Jan. 2020). Number: 1 Publisher: Nature Publishing Group, pp. 32–37. DOI: 10.1038/s41567-019-0682-6 (cit. on p. 66).

[149] P.-L. Yu, T. P. Purdy, and C. A. Regal. "Control of Material Damping in High-Q Membrane Microresonators". In: *Phys. Rev. Lett.* 108.8 (Feb. 2012). Publisher: American Physical Society, p. 083603. DOI: 10.1103/PhysRevLett.108.083603 (cit. on pp. 66, 69–72).

[150] A. W. Leissa. *Vibration of plates*. Vol. 160. Scientific and Technical Information Division, National Aeronautics and ..., 1969 (cit. on p. 67).

[151] L. D. Landau et al. *Theory of elasticity: volume 7*. Vol. 7. Elsevier, 1986 (cit. on p. 67).

[152] Q. P. Unterreithmeier, T. Faust, and J. P. Kotthaus. "Damping of Nanomechanical Resonators". In: *Phys. Rev. Lett.* 105.2 (July 2010). Publisher: American Physical Society, p. 027205. DOI: 10.1103/PhysRevLett.105.027205 (cit. on pp. 67, 70).

[153] M. Bao et al. "Energy transfer model for squeeze-film air damping in low vacuum". In: *J. Micromech. Microeng.* 12.3 (Apr. 2002), p. 341. DOI: 10.1088/0960-1317/12/3/322 (cit. on p. 69).

[154] H. D. Goodfellow and E. Tahti. *Industrial ventilation design guidebook*. Academic press, 2001 (cit. on p. 69).

[155] S. Schmid et al. "Damping mechanisms in high-Q micro and nanomechanical string resonators". In: *Phys. Rev. B* 84.16 (Oct. 2011). Publisher: American Physical Society, p. 165307. DOI: 10.1103/PhysRevB.84.165307 (cit. on pp. 69–71).

[156] S. Chakram et al. "Dissipation in Ultrahigh Quality Factor SiN Membrane Resonators". In: *Phys. Rev. Lett.* 112.12 (Mar. 2014). Publisher: American Physical Society, p. 127201. DOI: 10.1103/PhysRevLett.112.127201 (cit. on p. 69).

[157] S. Ghaffari et al. "Quantum Limit of Quality Factor in Silicon Micro and Nano Mechanical Resonators". In: *Sci Rep* 3.1 (Nov. 2013). Number: 1 Publisher: Nature Publishing Group, p. 3244. DOI: 10.1038/srep03244 (cit. on pp. 69, 70).

[158] T. Faust et al. "Signatures of two-level defects in the temperature-dependent damping of nanomechanical silicon nitride resonators". In: *Phys. Rev. B* 89.10 (Mar. 2014). Publisher: American Physical Society, p. 100102. DOI: 10.1103/PhysRevB.89.100102 (cit. on p. 70).

[159] L. Villanueva and S. Schmid. "Evidence of Surface Loss as Ubiquitous Limiting Damping Mechanism in SiN Micro- and Nanomechanical Resonators". In: *Phys. Rev. Lett.* 113.22 (Nov. 2014). Publisher: American Physical Society, p. 227201. DOI: 10.1103/PhysRevLett.113.227201 (cit. on pp. 70, 71).

[160] S. A. Fedorov et al. "Thermal intermodulation noise in cavity-based measurements". In: *Optica, OPTICA* 7.11 (Nov. 2020). Publisher: Optica Publishing Group, pp. 1609–1616. DOI: 10.1364/OPTICA.402449 (cit. on pp. 71, 104).

[161] T. P. Purdy et al. "Cavity optomechanics with Si_3N_4 membranes at cryogenic temperatures". In: *New J. Phys.* 14.11 (Nov. 2012), p. 115021. DOI: 10.1088/1367-2630/14/11/115021 (cit. on p. 71).

[162] S. Mohammadi et al. "Complete phononic bandgaps and bandgap maps in two-dimensional silicon phononic crystal plates". In: *Electron. Lett.* 43.16 (2007), p. 898. DOI: 10.1049/el:20071159 (cit. on p. 74).

[163] M. Pinard, Y. Hadjar, and A. Heidmann. "Effective mass in quantum effects of radiation pressure". en. In: *Eur. Phys. J. D* 7.1 (Aug. 1999), pp. 107–116. DOI: 10.1007/s100530050354 (cit. on p. 77).

[164] G. Gysin. "Characterization of soft clamped membranes". MA thesis. Klingelbergstrasse 82 4058 Basel: University of Basel, Department of Physics, 2022 (cit. on p. 81).

[165] A. M. Jayich et al. "Dispersive optomechanics: a membrane inside a cavity". In: *New J. Phys.* 10.9 (Sept. 2008), p. 095008. DOI: 10.1088/1367-2630/10/9/095008 (cit. on pp. 87, 88).

[166] C. Genes and A. Dantan. "Light–matter interactions in multi-element resonators". In: *J. Phys. B: At. Mol. Opt. Phys.* 50.10 (May 2017), p. 105502. DOI: 10.1088/1361-6455/aa6a74 (cit. on p. 88).

[167] B. E. Saleh and M. C. Teich. *Fundamentals of photonics*. john Wiley & sons, 2019 (cit. on p. 88).

[168] V. Dumont et al. "Flexure-tuned membrane-at-the-edge optomechanical system". In: *Opt. Express, OE* 27.18 (Sept. 2019). Publisher: Optica Publishing Group, pp. 25731–25748. DOI: 10.1364/OE.27.025731 (cit. on p. 89).

[169] T. Karg. "Strong light-mediated coupling between a membrane oscillator and an atomic spin ensemble". PhD thesis. Klingelbergstrasse 82 4058 Basel: University of Basel, Department of Physics, 2020 (cit. on pp. 95, 96).

[170] A. Ryou and J. Simon. "Active cancellation of acoustical resonances with an FPGA FIR filter". en. In: *Review of Scientific Instruments* 88.1 (Jan. 2017), p. 013101. DOI: 10.1063/1.4973470 (cit. on p. 95).

[171] M. Yuan, M. A. Cohen, and G. A. Steele. "Silicon nitride membrane resonators at millikelvin temperatures with quality factors exceeding 10^8". en. In: *Appl. Phys. Lett.* 107.26 (Dec. 2015), p. 263501. DOI: 10.1063/1.4938747 (cit. on p. 98).

[172] R. W. P. Drever et al. "Laser phase and frequency stabilization using an optical resonator". In: *Appl. Phys. B* 31.2 (June 1983), pp. 97–105. DOI: 10.1007/BF00702605 (cit. on p. 101).

[173] E. D. Black. "An introduction to Pound–Drever–Hall laser frequency stabilization". In: *American Journal of Physics* 69.1 (Jan. 2001). Publisher: American Association of Physics Teachers, pp. 79–87. DOI: 10.1119/1.1286663 (cit. on p. 101).

[174] L. Diósi. "Non-Markovian continuous quantum measurement of retarded observables". In: *Physical review letters* 100.8 (2008), p. 080401 (cit. on pp. 103, 125).

[175] A. Schliesser et al. "Resolved-sideband cooling of a micromechanical oscillator". In: *Nature Phys* 4.5 (May 2008). Number: 5 Publisher: Nature Publishing Group, pp. 415–419. DOI: 10.1038/nphys939 (cit. on pp. 103, 125).

[176] P Rabl et al. "Phase-noise induced limitations on cooling and coherent evolution in optomechanical systems". en. In: *PHYSICAL REVIEW A* (2009) (cit. on pp. 103, 125).

[177] T. Briant et al. "Optomechanical characterization of acoustic modes in a mirror". In: *Phys. Rev. A* 68.3 (Sept. 2003). Publisher: American Physical Society, p. 033823. DOI: 10.1103/PhysRevA.68.033823 (cit. on p. 103).

[178] S. A. Saarinen et al. "Laser cooling a membrane-in-the-middle system close to the quantum ground state from room temperature". In: *Optica, OPTICA* 10.3 (Mar. 2023). Publisher: Optica Publishing Group, pp. 364–372. DOI: 10.1364/OPTICA.468590 (cit. on p. 103).

[179] L. Neuhaus et al. "PyRPL (Python Red Pitaya Lockbox) — An open-source software package for FPGA-controlled quantum optics experiments". In: *2017 Conference on Lasers and Electro-Optics Europe & European Quantum Electronics Conference (CLEO/Europe-EQEC)*. June 2017, pp. 1–1. DOI: 10.1109/CLEOE-EQEC.2017.8087380 (cit. on p. 105).

[180] M. L. Gorodetksy et al. "Determination of the vacuum optomechanical coupling rate using frequency noise calibration". In: *Optics Express* 18.22 (Oct. 2010), pp. 23236–23246. DOI: 10.1364/OE.18.023236 (cit. on p. 106).

[181] H. Mabuchi. "Coherent-feedback quantum control with a dynamic compensator". In: *Phys. Rev. A* 78.3 (Sept. 2008), p. 032323. DOI: 10.1103/PhysRevA.78.032323 (cit. on p. 115).

[182] J. E. Gough and S. Wildfeuer. "Enhancement of field squeezing using coherent feedback". In: *Phys. Rev. A* 80.4 (Oct. 2009), p. 042107. DOI: 10.1103/PhysRevA.80.042107 (cit. on p. 115).

[183] R. J. Nelson et al. "Experimental Demonstration of Fully Coherent Quantum Feedback". In: *Phys. Rev. Lett.* 85.14 (Oct. 2000), pp. 3045–3048. DOI: 10.1103/PhysRevLett.85.3045 (cit. on p. 115).

[184] Z. Wang and A. H. Safavi-Naeini. "Enhancing a slow and weak optomechanical nonlinearity with delayed quantum feedback". In: *Nat. Commun.* 8 (July 2017), p. 15886. DOI: 10.1038/ncomms15886 (cit. on pp. 115, 126).

[185] M. Amazioug, B. Maroufi, and M. Daoud. "Using coherent feedback loop for high quantum state transfer in optomechanics". In: *Physics Lett. A* 384.27 (Sept. 2020), p. 126705. DOI: 10.1016/j.physleta.2020.126705 (cit. on pp. 116, 129).

[186] J. Kerckhoff et al. "Tunable Coupling to a Mechanical Oscillator Circuit Using a Coherent Feedback Network". In: *Phys. Rev. X* 3.2 (June 2013), p. 021013. DOI: 10.1103/PhysRevX.3.021013 (cit. on p. 116).

[187] A. Metelmann and A. A. Clerk. "Nonreciprocal Photon Transmission and Amplification via Reservoir Engineering". In: *Phys. Rev. X* 5 (2 2015), p. 021025. DOI: 10.1103/PhysRevX.5.021025 (cit. on p. 116).

[188] A. Metelmann and A. A. Clerk. "Nonreciprocal quantum interactions and devices via autonomous feedforward". In: *Phys. Rev. A* 95 (1 2017), p. 013837. DOI: 10.1103/PhysRevA.95.013837 (cit. on p. 116).

[189] Y. Chu and S. Gröblacher. "A perspective on hybrid quantum opto- and electromechanical systems". In: *Appl. Phys. Lett.* 117 (Oct. 2020), p. 150503. DOI: 10.1063/5.0021088 (cit. on p. 116).

[190] J. Monsel et al. "Optomechanical cooling with coherent and squeezed light: The thermodynamic cost of opening the heat valve". In: *Phys. Rev. A* 103 (6 2021), p. 063519. DOI: 10.1103/PhysRevA.103.063519 (cit. on pp. 116, 118).

[191] A. Rogalski. "Next decade in infrared detectors". In: *Electro-Optical and Infrared Systems: Technology and Applications XIV*. Ed. by D. A. Huckridge, R. Ebert, and H. Bürsing. SPIE, 2017, p. 104330L (cit. on p. 118).

[192] P. Rabl et al. "Strong magnetic coupling between an electronic spin qubit and a mechanical resonator". en. In: *Phys. Rev. B* 79.4 (Jan. 2009), p. 041302. DOI: 10.1103/PhysRevB.79.041302 (cit. on p. 125).

[193] C. Degen, F. Reinhard, and P. Cappellaro. "Quantum sensing". en. In: *Rev. Mod. Phys.* 89.3 (July 2017), p. 035002. DOI: 10.1103/RevModPhys.89.035002 (cit. on p. 128).

[194] L. McCuller et al. "Frequency-Dependent Squeezing for Advanced LIGO". In: *Phys. Rev. Lett.* 124.17 (Apr. 2020). Publisher: American Physical Society, p. 171102. DOI: 10.1103/PhysRevLett.124.171102 (cit. on p. 128).

[195] M. A. Page et al. "Gravitational wave detectors with broadband high frequency sensitivity". en. In: *Commun Phys* 4.1 (Feb. 2021). Number: 1 Publisher: Nature Publishing Group, pp. 1–8. DOI: 10.1038/s42005-021-00526-2 (cit. on p. 128).

[196] D. Carney et al. "Ultralight dark matter detection with mechanical quantum sensors". en. In: *New J. Phys.* 23.2 (Feb. 2021), p. 023041. DOI: 10.1088/1367-2630/abd9e7 (cit. on p. 128).

[197] J. Manley et al. "Searching for Vector Dark Matter with an Optomechanical Accelerometer". In: *Phys. Rev. Lett.* 126.6 (Feb. 2021). Publisher: American Physical Society, p. 061301. DOI: 10.1103/PhysRevLett.126.061301 (cit. on p. 128).

[198] F. Monteiro et al. "Search for Composite Dark Matter with Optically Levitated Sensors". en. In: *Phys. Rev. Lett.* 125.18 (Oct. 2020), p. 181102. DOI: 10.1103/PhysRevLett.125.181102 (cit. on p. 128).

[199] R. Peng et al. "Enhancement of mechanical entanglement and asymmetric steering with coherent feedback". en. In: *Phys. Rev. A* 107.1 (Jan. 2023), p. 013507. DOI: 10.1103/PhysRevA.107.013507 (cit. on p. 129).

[200] O. Romero-Isart et al. "Large Quantum Superpositions and Interference of Massive Nanometer-Sized Objects". In: *Phys. Rev. Lett.* 107.2 (July 2011), p. 020405. DOI: 10.1103/PhysRevLett.107.020405 (cit. on p. 129).

[201] C. Marletto and V. Vedral. "Gravitationally Induced Entanglement between Two Massive Particles is Sufficient Evidence of Quantum Effects in Gravity". In: *Phys. Rev. Lett.* 119.24 (Dec. 2017), p. 240402. DOI: 10.1103/PhysRevLett.119.240402 (cit. on p. 129).

[202] S. Bose et al. "Spin Entanglement Witness for Quantum Gravity". In: *Phys. Rev. Lett.* 119.24 (Dec. 2017). Publisher: American Physical Society, p. 240401. DOI: 10.1103/PhysRevLett.119.240401 (cit. on p. 129).

[203] F. Fröwis et al. "Macroscopic quantum states: Measures, fragility, and implementations". en. In: *Rev. Mod. Phys.* 90.2 (May 2018), p. 025004. DOI: 10.1103/RevModPhys.90.025004 (cit. on p. 129).

[204] T. Krisnanda et al. "Observable quantum entanglement due to gravity". In: *npj Quantum Information* 6.1 (Jan. 2020), pp. 1–6. DOI: 10.1038/s41534-020-0243-y (cit. on p. 129).

[205] H. Pichler et al. "Quantum optics of chiral spin networks". In: *Phys. Rev. A* 91.4 (Apr. 2015). Publisher: American Physical Society, p. 042116. DOI: 10.1103/PhysRevA.91.042116 (cit. on p. 129).

[206] M.-A. Miri and A. Alù. "Exceptional points in optics and photonics". In: *Science* 363.6422 (Jan. 2019). Publisher: American Association for the Advancement of Science, eaar7709. DOI: 10.1126/science.aar7709 (cit. on p. 129).

[207] W. D. Heiss. "The physics of exceptional points". In: *J. Phys. A: Math. Theor.* 45.44 (Oct. 2012). Publisher: IOP Publishing, p. 444016. DOI: 10.1088/1751-8113/45/44/444016 (cit. on p. 129).

[208] Z. Lin et al. "Unidirectional Invisibility Induced by P T -Symmetric Periodic Structures". en. In: *Phys. Rev. Lett.* 106.21 (May 2011), p. 213901. DOI: 10.1103/PhysRevLett.106.213901 (cit. on p. 129).

[209] A. Guo et al. "Observation of P T -Symmetry Breaking in Complex Optical Potentials". en. In: *Phys. Rev. Lett.* 103.9 (Aug. 2009), p. 093902. DOI: 10.1103/PhysRevLett.103.093902 (cit. on p. 129).

[210] Y. Ashida, Z. Gong, and M. Ueda. "Non-Hermitian physics". In: *Advances in Physics* 69.3 (July 2020). Publisher: Taylor & Francis _eprint: https://doi.org/10.1080/00018732.2021.1876991, pp. 249–435. DOI: 10.1080/00018732.2021.1876991 (cit. on p. 129).

[211] L. Bao, B. Qi, and D. Dong. "Exponentially Enhanced Quantum Non-Hermitian Sensing via Optimized Coherent Drive". In: *Phys. Rev. Appl.* 17.1 (Jan. 2022). Publisher: American Physical Society, p. 014034. DOI: 10.1103/PhysRevApplied.17.014034 (cit. on p. 129).

[212] H. Xu et al. "Topological energy transfer in an optomechanical system with exceptional points". en. In: *Nature* 537.7618 (Sept. 2016). Number: 7618 Publisher: Nature Publishing Group, pp. 80–83. DOI: 10.1038/nature18604 (cit. on p. 129).

[213] K. Zhang, F. Bariani, and P. Meystre. "Theory of an optomechanical quantum heat engine". In: *Phys. Rev. A* 90.2 (Aug. 2014). Publisher: American Physical Society, p. 023819. DOI: 10.1103/PhysRevA.90.023819 (cit. on p. 129).

[214] V. Blickle and C. Bechinger. "Realization of a micrometre-sized stochastic heat engine". en. In: *Nature Phys* 8.2 (Feb. 2012). Number: 2 Publisher: Nature Publishing Group, pp. 143–146. DOI: 10.1038/nphys2163 (cit. on p. 129).

[215] A. Dechant, N. Kiesel, and E. Lutz. "All-Optical Nanomechanical Heat Engine". en. In: *Phys. Rev. Lett.* 114.18 (May 2015), p. 183602. DOI: 10.1103/PhysRevLett.114.183602 (cit. on p. 129).

[216] N. E. Abari et al. "An optomechanical heat engine with feedback-controlled in-loop light". en. In: *New J. Phys.* 21.9 (Sept. 2019). Publisher: IOP Publishing, p. 093051. DOI: 10.1088/1367-2630/ab41e7 (cit. on p. 129).

[217] H. J. Kimble. "The quantum internet". en. In: *Nature* 453.7198 (June 2008). Number: 7198 Publisher: Nature Publishing Group, pp. 1023–1030. DOI: 10.1038/nature07127 (cit. on p. 130).

[218] B. Vermersch et al. "Quantum State Transfer via Noisy Photonic and Phononic Waveguides". en. In: *Phys. Rev. Lett.* 118.13 (Mar. 2017), p. 133601. DOI: 10.1103/PhysRevLett.118.133601 (cit. on p. 130).

[219] R. N. Patel et al. "Single-Mode Phononic Wire". en. In: *Phys. Rev. Lett.* 121.4 (July 2018), p. 040501. DOI: 10.1103/PhysRevLett.121.040501 (cit. on p. 130).

[220] A. H. Safavi-Naeini et al. "Controlling phonons and photons at the wavelength scale: integrated photonics meets integrated phononics". EN. In: *Optica, OPTICA* 6.2 (Feb. 2019). Publisher: Optica Publishing Group, pp. 213–232. DOI: 10.1364/OPTICA.6.000213 (cit. on p. 130).

[221] W. Chen et al. "Scalable and programmable phononic network with trapped ions". en. In: *Nat. Phys.* (Feb. 2023). Publisher: Nature Publishing Group, pp. 1–7. DOI: 10.1038/s41567-023-01952-5 (cit. on p. 130).

[222] A. Wallucks et al. "A quantum memory at telecom wavelengths". en. In: *Nat. Phys.* 16.7 (July 2020). Number: 7 Publisher: Nature Publishing Group, pp. 772–777. DOI: 10.1038/s41567-020-0891-z (cit. on p. 130).

[223] D. P. Lake et al. "Processing light with an optically tunable mechanical memory". en. In: *Nat Commun* 12.1 (Jan. 2021). Number: 1 Publisher: Nature Publishing Group, p. 663. DOI: 10.1038/s41467-021-20899-w (cit. on p. 130).